

# **Wheat straw ash and its use as a silica source**

**Jennifer Ruth Dodson**

**PhD**

**University of York**

**Chemistry**

**September 2011**



# Abstract

The overall aim of this project was to study the reutilisation of the major ash components, predominantly silica and potassium, in wheat straw combustion residues to form alkali silicate binders for novel inorganic composite boards.

Wheat straw of one variety and year was studied in detail on a lab-scale. Studies on the effects of combustion time and temperature show, for the first time, that the inherent alkali in the wheat straw is sufficient to solubilise up to 25% of the silica in the ash at room temperature. Combustion at temperatures below 600 °C gives the highest silica extraction by producing the most alkaline solutions, preventing calcium solubility and maintaining silica in a more reactive form. The first detailed comparisons of the effect of wheat straw variety and growth year on the properties of its combustion residues show that their mineralogical composition, leaching of inorganic components, silica structure and alkalinity can be correlated to the initial elemental composition.

Pretreatment of wheat straw by ethanol extraction indicates that this can reduce the potassium and chloride content similar to that achieved by water washing, potentially producing a less problematic material for combustion, without significantly reducing the alkalinity of the combustion residues. This is believed to be the first reported observation of this effect.

Pyrolysis of the wheat straw followed by char washing prior to combustion demonstrates improved extractability of the silica present utilising the inherent alkalinity, compared to extraction of the ashes. The leached chars display a lower ash content, lower potassium content, lower chloride content and higher calorific value, making them more suitable for combustion than the initial straw.

Finally, the formation of alkali silicate solutions from commercial biomass combustion residues is demonstrated. Biosilicate solutions comparable to commercial potassium silicate solutions are formed by extraction of the bottom ashes. These show potential as binders for inorganic composite boards.



# Table of contents

<b>List of tables.....</b>	<b>10</b>
<b>List of figures.....</b>	<b>12</b>
<b>Acknowledgements.....</b>	<b>19</b>
<b>Declaration.....</b>	<b>21</b>
<b>Chapter 1: Introduction.....</b>	<b>23</b>
1.1 Scope of the project	25
1.2 The Challenge: Climate Change, Peak Oil and Green Chemistry	26
1.3 Energy from biomass	29
1.3.1 Potential biomass sources	31
1.3.2 Agricultural residue availability in the UK	32
1.3.3 Biomass composition	33
1.4 Combustion of biomass and the impact of inorganic species	36
1.4.1 Combustion technologies	36
1.4.2 Impact of inorganics during grate-firing of herbaceous biomass	38
1.4.3 Reducing fouling and slagging	41
1.5 Current uses of residues from thermochemical conversion of biomass	42
1.5.1 Agriculture	42
1.5.2 Construction	43
1.6 Silica from biomass	45
1.6.1 Silicon's presence in biomass	45
1.6.2 Composition and inorganic distribution	47
1.7 Alkali silicates – chemistry and uses	48
1.7.1 Alkali silicates	48
1.7.2 Structure of alkali silicates	49
1.7.3 Setting processes	53
1.8 Utilising silica from biomass	54
1.8.1 Dissolution of silica	55
1.8.2 Silica from Rice Hull Ashes (RHAs)	56
1.9 Composite materials	57
1.9.1 Environmental impacts and challenges	58
1.9.2 Alternative resins	59

1.9.3	Alternative substrates	60
1.10	Project vision and thesis content	60
1.11	References for Chapter 1	61

## **Chapter 2: Lab-scale combustion of wheat straw and extraction of residues..... 67**

2.1	Chapter 2 – Summary	69
2.2	Wheat straw properties	69
2.2.1	Proximate and ultimate analysis	69
2.2.2	Thermogravimetric analysis	73
2.3	Mineralogical changes occurring during combustion	75
2.3.1	X-Ray Diffraction	77
2.3.2	Infrared	82
2.4	Aqueous extraction of Cl07 wheat straw combustion residues	85
2.4.1	Potassium and chloride	89
2.4.2	Silica	93
2.5	Higher temperatures of extraction and added alkali	99
2.5.1	Effect of extraction temperature	99
2.5.2	Effect of KOH concentration	101
2.6	Kinetics	102
2.7	Varying wheat straw variety	103
2.8	Incomplete combustion – effect of water quenching vs air cooling	107
2.9	Textural properties	112
2.9.1	10 min combustion	115
2.9.2	2 h combustion	120
2.10	Conclusions and Further Work	122
2.11	References for Chapter 2	123

## **Chapter 3: The impact of pretreatment processes on inorganic species during the combustion and extraction of wheat straw..... 127**

3.1	Chapter 3 – Summary	128
3.2	Pretreatment options	128
3.3	Wax extraction optimisation	129
3.3.1	Soxhlet extraction	129
3.3.2	Supercritical CO <sub>2</sub> extraction	131
3.3.3	Extract composition and properties	137

3.4	Inorganic leaching optimisation	141
3.5	Impact of pretreatment on mineralogical changes during combustion	145
3.5.1	Fuel analysis	145
3.5.2	Mineralogical changes	149
3.5.3	Thermochemical changes	151
3.5.4	Decomposition characteristics of pretreated straw ash	154
3.5.5	Aqueous extraction of ash	164
3.6	Conclusions and further work	167
3.7	References for Chapter 3	169

## **Chapter 4: Lab-scale pyrolysis of wheat straw and extraction of chars.....173**

4.1	Chapter 4 – Summary	175
4.2	Pyrolysis	175
4.3	Low temperature microwave pyrolysis	177
4.4	Conventional pyrolysis	181
4.4.1	Aqueous extraction	181
4.4.2	Char analysis	193
4.5	Extraction at higher temperatures and with added alkali	209
4.6	Conclusions and Further Work	210
4.7	References for Chapter 4	211

## **Chapter 5: Biosilicate formation and binder application using power station combustion residues.....215**

5.1	Chapter 5 - Summary	217
5.2	Power station ashes	217
5.3	Fuel analysis	218
5.4	Combustion-extraction trends	220
5.5	Power station ashes	224
5.5.1	Mineral analysis of ashes	224
5.5.2	Chemical analysis of ashes	228
5.6	Silicate analysis development	231
5.7	Biosilicate solution	236
5.7.1	Effect of alkali concentration	236
5.7.2	Reproducibility	242
5.7.3	Effect of time	246

5.7.4	Using fly ash solution for extraction	248
5.8	Board formation	249
5.8.1	Biosilicate	249
5.8.2	Board making	251
5.9	Residual solids	254
5.9.1	Analysis of residue	254
5.9.2	Test hardened blocks	257
5.10	Conclusions and Further Work	260
5.11	References for Chapter 5	261

## **Chapter 6: Materials and Methods.....265**

6.1	Chemicals	267
6.2	Experimental details and instrumentation for Chapters 2, 3 and 4	267
6.2.1	Straw collection and processing	267
6.2.2	Thermogravimetric analysis of wheat straw	267
6.2.3	Simultaneous Thermal Analysis of wheat straw and chars	268
6.2.4	Calorific value of wheat straw	268
6.2.5	CHN analysis	269
6.2.6	Typical combustion and extraction procedure	269
6.2.7	pH measurements	270
6.2.8	Atomic Absorption Spectroscopy (AAS)	270
6.2.9	Transmission Electron Microscopy (TEM)	271
6.2.10	Nitrogen adsorption studies	271
6.2.11	X-Ray Fluorescence	271
6.2.12	Powder X-Ray Diffraction	272
6.2.13	Infrared Spectroscopy	272
6.2.14	Ion Chromatography	272
6.2.15	Inductively Coupled Plasma Atomic Emission Spectroscopy	272
6.2.16	Solution Nuclear Magnetic Resonance	273
6.2.17	Solid State Nuclear Magnetic Resonance	273
6.3	Experimental details and instrumentation for Chapter 3	273
6.3.1	Typical Soxhlet extraction of wheat straw	273
6.3.2	Typical supercritical carbon dioxide extraction	273
6.3.3	Acid and water leaching of wheat straw	274
6.3.4	Differential Scanning Calorimetry of lipids	274
6.3.5	Fusion tests	274
6.4	Experimental details and instrumentation for Chapter 4	275

6.4.1	Microwave pyrolysis procedure	275
6.4.2	Microwave char demineralisation	275
6.4.3	Convection heating pyrolysis procedure	275
6.5	Experimental details and instrumentation for Chapter 5	275
6.5.1	Collection of residues from combustion boilers	275
6.5.2	Water leaching of ashes	276
6.5.3	Typical alkali extraction of bottom ashes	276
6.5.4	Extraction of bottom ashes using fly ash extract	276
6.5.5	Typical board formation procedure	276
6.5.6	Internal bond strength test	277
6.5.7	Water swelling test	277
6.5.8	Block formation procedure for extraction residue	277
<b>Chapter 7: Conclusions and further work.....</b>		<b>279</b>
7.1	Concluding remarks	281
7.2	Further Work	283
7.3	Outcomes of the PhD	284
7.3.1	Published work	284
7.3.2	Patents	284
7.3.3	Oral Presentations	284
7.3.4	Selected Poster Presentations	285
<b>Appendix A: XRD spectra.....</b>		<b>287</b>
<b>Glossary.....</b>		<b>297</b>

# List of tables

## Chapter 1

**Table 1.1:** Energy potential of UK biomass feedstocks

**Table 1.2:** Ash, elemental composition and calorific value data for a variety of biomass materials and coal

**Table 1.3:** Recommendations of the Swedish Forest Agency on threshold values for constituents in ash aimed for recycling on forest soils

**Table 1.4:** Percentage of silica found in different parts of the wheat plant.

**Table 1.5:** Relative silica concentration in the shoots of several agricultural and energy crops.

**Table 1.6:** Main element concentrations of initial dry biomass and silica:alkali ratios.

**Table 1.7:** Assigned  $^{29}\text{Si}$  NMR shifts for silicate species with different connectivity in solution (with respect to tetramethylsilane)

**Table 1.8:** Bass and Turner's assignments of components of main sodium silicate infrared band to different silicate anion types.

## Chapter 2

**Table 2.1:** Ultimate and proximate analyses for all wheat straw varieties used during this study

**Table 2.2:** Peak and ignition temperatures for all wheat straw samples under pyrolysis and combustion conditions

**Table 2.3:** Mass remaining and CHN analysis of combustion residues of Cl07 formed under varying combustion conditions

**Table 2.4:** Concentration of main inorganic species in aqueous extracts from Cl07 combusted and quenched under varying conditions

**Table 2.5:** Percentage of main inorganic species in aqueous extracts from Cl07 combusted and quenched under varying conditions

**Table 2.6:** Porosimetry data of Cl07 combustion residues before (I) and after leaching (Q/NQ)

## Chapter 3

**Table 3.1:**  $2^2$  factorial design - experimental and coded values

**Table 3.2:** Concentrations of ions in water leached solution

**Table 3.3:** Fuel analysis of pretreated Cl07 wheat straw

**Table 3.4:** Normalised oxide content of ash following pretreatment processes (all wt%)

**Table 3.5:** Peak and ignition temperatures for pretreated straw samples under pyrolysis and combustion conditions

**Table 3.6:** Mass losses from straw ashes pretreated by different methods showing the rate of mass loss in various temperature ranges and identification of the inorganic species associated with the mass loss

**Table 3.7:** Normalised content of SiO<sub>2</sub>, K<sub>2</sub>O and CaO in ashes of pretreated straw

## **Chapter 4**

**Table 4.1:** Concentrations of inorganic species in aqueous extracts of pyrolysis chars formed at various temperatures

**Table 4.2:** Moisture, ash and CHN analysis of the char formed before and after leaching. The numbers indicate the temperature of pyrolysis, and the second number the time of pyrolysis (e.g. 400-2 = 400 °C for 2 h)

**Table 4.3:** Infrared band assignments for ATR-IR spectra of pyrolysis chars

## **Chapter 5**

**Table 5.1:** Fuel analysis of wood chip and miscanthus fuels

**Table 5.2:** Levels of extraction of Si, K, Ca and Cl from miscanthus and wood chip ash

**Table 5.3:** Elemental composition of fly ash and bottom ashes from two biomass power plants analysed by XRF, all in wt%

**Table 5.4:** Elemental composition of solutions formed from the water leaching of power station ashes. All concentrations in ppm.

**Table 5.5:** Details of commercial silicate solutions used for silicate analysis development

**Table 5.6:** Slope, intercept and R<sup>2</sup> values for the correlation between Si concentration analysed by AAS and silicate IR band area for different silicate solutions

**Table 5.7:** Results of silica extraction from Ely-BA1 using KOH solutions of different concentrations (based on AAS analysis)

**Table 5.8:** Peak frequencies and identification in the ATR-IR spectra of Ely-BA1 silicate solutions

**Table 5.9:** Analysis of biosilicate solutions from Ely-BA1 ash using constant KOH solution concentrations and ash:liquid ratios with extraction occurring under reflux over 24 h

**Table 5.10:** Elemental analysis of two potassium silicate solutions formed from Ely-BA1

**Table 5.11:** Characterisation of silicate solutions used for binder tests

**Table 5.12:** Strawboard composite properties using different silicate binders (tested at Bangor University)

**Table 5.13:** Strawboard composite properties using different silicate binders (tested at the University of York)

**Table 5.14:** Elemental composition of Ely-BA1-15 solid residue after extraction and the percentage of each element solubilised

**Table 5.15:** Initial 3-point bending test results

# List of figures

## Chapter 1

**Figure 1.1:** Concept for the formation of inorganic composite boards utilising waste materials throughout (Originally in colour)

**Figure 1.2:** UK 2008 CO<sub>2</sub> emissions by sector attributed either to the source of the emissions or the end user<sup>16</sup> (Originally in colour)

**Figure 1.3:** The potential of biomass for creating energy, fuels, materials and chemicals (developed from Ref 20) (Originally in colour)

**Figure 1.4:** Basic grate-fired biomass combustion plant design (Originally in colour)

**Figure 1.5:** Proposed mechanism for the condensation of silicic acid<sup>96</sup>

**Figure 1.6:** The structure of a few species identified in silicate solutions by <sup>29</sup>Si NMR

**Figure 1.7:** Changes in silicate species distribution with changing SiO<sub>2</sub>:Na<sub>2</sub>O molar ratio at a SiO<sub>2</sub> concentration of 0.4 M.<sup>100</sup>

**Figure 1.8:** Silica phase transformations

**Figure 1.9:** Distribution of wood-based panelling used in the UK in 2009 (a) and production of wood-based panelling in the UK in 2009 (b)<sup>125</sup>

**Figure 1.10:** Main steps in the manufacture of particle board and MDF

## Chapter 2

**Figure 2.1:** a) The locations where wheat straw was collected are circled in red b) collecting straw from fields near Castle Howard in 2008

**Figure 2.2:** Cumulative rainfall for North East England in August of 2007 – 2009

**Figure 2.3:** Thermogravimetric analyses under pyrolysis conditions of wheat straw, variety Claire, harvested in different years

**Figure 2.4:** Thermogravimetric analyses under combustion conditions of wheat straw, variety Claire, harvested in different years

**Figure 2.5:** XRD patterns of Claire 07 wheat straw ashes after (a) 10 minutes combustion and (b) 2 h combustion from 400 °C to 800 °C. The phases present are indicated by numbers: 1 = Sylvite (KCl); 2 = Calcite (CaCO<sub>3</sub>); 3 = Arcanite (K<sub>2</sub>SO<sub>4</sub>); 4 = Anhydrite (CaSO<sub>4</sub>); 5 = Quartz (SiO<sub>2</sub>); 6 = Calcium silicate (CaSiO<sub>3</sub>); sh = sample holder

**Figure 2.6:** Diffractograms of wheat straw, variety Claire, harvested over 3 years combusted at 500 °C for 2 h: 1 = Sylvite (KCl); 2 = Calcite (CaCO<sub>3</sub>); 3 = Arcanite (K<sub>2</sub>SO<sub>4</sub>); 4 = Anhydrite (CaSO<sub>4</sub>); 5 = Quartz (SiO<sub>2</sub>)

**Figure 2.7:** Diffractograms of wheat straw harvested in 2008 combusted at 500 °C for 2 h: 1 = Sylvite (KCl); 2 = Calcite (CaCO<sub>3</sub>); 4 = Anhydrite (CaSO<sub>4</sub>); 5 = Quartz (SiO<sub>2</sub>)

**Figure 2.8:** Diffractograms of wheat straw harvested in 2009 combusted at 500 °C for 2 h: 1 = Sylvite (KCl); 2 = Calcite (CaCO<sub>3</sub>); 3 = Arcanite (K<sub>2</sub>SO<sub>4</sub>); 5 = Quartz (SiO<sub>2</sub>); 7 = Fairchildite (K<sub>2</sub>Ca(CO<sub>3</sub>)<sub>2</sub>)

**Figure 2.9:** Diffractograms of Cl07 and Cl08 combusted at 800 °C for 2 h: 5 = Quartz (SiO<sub>2</sub>); 6 = CaSiO<sub>3</sub>; 8 = α-cristobalite (SiO<sub>2</sub>)

**Figure 2.10:** ATR-IR spectra of Cl07 ashes from combusted for 2 h at different temperatures

**Figure 2.11:** ATR-IR spectra of all wheat straw ashes combusted at 500 °C for 2 h – dotted line 2007, dashed line 2008, solid line 2009

**Figure 2.12:** Cumulative extraction of different species from Cl07 combustion residues following water quenching after a) 10 min combustion and b) 2 h combustion

**Figure 2.13:** Percentage potassium (solid lines) and chloride (dashed lines) extracted from Cl07 combustion residues with varying combustion and quenching conditions a) 10 min combustion, b) 120 min combustion

**Figure 2.14:** Correlation between potassium concentration and chloride and sulfate concentration in Cl07 combustion residue extracts

**Figure 2.15:** Change in potassium and chloride in Cl07 2 h ashes before and after aqueous extraction relative to the silicon content before extraction and the calcium content after extraction (based on XRF analysis)

**Figure 2.16:** Silica extraction from Cl07 ashes under varying combustion and cooling conditions from AAS analysis of extract

**Figure 2.17:** Relationship between the pH of the extract solution and silica extraction across all combustion and cooling conditions. Red dots – initial pH of 120-Q/NQ solutions; black dots – final pH of 120-Q/NQ solutions; Red stars - initial pH of 10-Q solutions; Black stars - final pH of 10-Q solutions; Blue stars – final pH of solutions formed from ashes combusted for 10 min between 400–600 °C and cooled in air before extraction

**Figure 2.18:** Correlation between pH and silica concentration for pure amorphous silica in an alkaline solution (black)<sup>37</sup> and wheat straw ash extracts after 10 min combustion and air cooling (red)

**Figure 2.19:** Solid state <sup>29</sup>Si NMR of Cl07 wheat straw ashes combusted between 400 – 700 °C for 2 h (a) before and (b) after extraction

**Figure 2.20:** Influence of extraction temperature on Si extraction from Cl07 wheat straw combusted at 500 °C for 2 h extracted in water (solid line) or a 0.1M KOH solution (dashed line)

**Figure 2.21:** Concentrations of other elements in solutions from extractions of Cl07 wheat straw ash combusted at 500 °C for 2 h extracted in water (solid line) or a 0.1M KOH solution (dashed line) at different temperatures

**Figure 2.22:** Effect of KOH solution concentration on the extraction of various elements from Cl07 500-120-Q ashes

**Figure 2.23:** Extraction of potassium and silicon from Cl07 ash (500-120-Q) at 40 °C (red) and 100 °C (black) over time

**Figure 2.24:** Effect of water and KOH solutions on silica extraction from wheat straw varieties all combusted at 500 °C for 2 h

**Figure 2.25:** Correlation between the Si concentration of the water extract solution and potassium concentration and initial pH following the extraction of 500-120-Q ashes of various wheat straw varieties

**Figure 2.26:** Inorganic species extracted from different wheat straw ashes combusted at 500 °C 2h and extracted under reflux in water a) cumulative concentration and b) percentage extracted

**Figure 2.27:** All wheat straw varieties combusted at 400 °C for 10 min showing the effect of water quenching (Q) versus air cooling (NQ) on silica extraction

**Figure 2.28:** All wheat straw varieties combusted at 400 °C for 10 min showing the effect of water quenching (Q) versus air cooling (NQ) on the initial (solid) and final (hashed) pH of the extraction solution

**Figure 2.29:** Effect of a) time and b) cooling method on the silica extraction from Cl07 400-10-Q/NQ combustion residues

**Figure 2.30:** a) Colour of Cl07 400-10-Q/NQ solutions before and after oxidation by H<sub>2</sub>O<sub>2</sub> b) colour of residue following the evaporation of extraction solutions from 400-10 combustion residues cooled under different conditions before extraction

**Figure 2.31:** <sup>1</sup>H NMR spectra of Cl07 400-10 a) Q and b) NQ solution residues dissolved in D<sub>2</sub>O

**Figure 2.32:** Classification of adsorption isotherms according to IUPAC classifications

**Figure 2.33:** Adsorption isotherms of Cl07 residues following 10 min combustion at different temperatures before (I) and after (Q) leaching

**Figure 2.34:** BET surface area of Cl07 ashes after 10 minutes combustion before leaching (black), and following extraction with water quenching (red) or air cooling (blue)

**Figure 2.35:** TEM images of Cl07 ashes after 10 minutes combustion at (a) 400 °C and (b) 800 °C

**Figure 2.36:** Pore size distribution of Cl07 ashes after 10 min combustion before (dashed line) and after (solid line) extraction

**Figure 2.37:** BET surface area of Cl07 ashes after 2 h combustion before leaching (black), and following extraction with water quenching (red) or air cooling (blue)

**Figure 2.38:** Adsorption isotherms of Cl07 residues following 120 min combustion before (I) and after leaching (Q)

## **Chapter 3**

**Figure 3.1:** Soxhlet extractor set-up

**Figure 3.2:** Yield of crude extracts from Soxhlet extraction of Cl07 straw using hexane and ethanol with different extraction times

**Figure 3.3:** Variation of density with pressure along different isotherms for supercritical carbon dioxide

**Figure 3.4:** Carbon dioxide densities over experimental range

**Figure 3.5:** Extraction yield from Cl07 wheat straw using scCO<sub>2</sub> over factorial design conditions compared to hexane Soxhlet extraction

**Figure 3.6:** Wax extraction by scCO<sub>2</sub>, yield and trend

**Figure 3.7:** Colour of waxes extracted from Cl07 under different conditions

**Figure 3.8:** DSC plots of extracts from (a) Soxhlet extraction and (b) supercritical carbon dioxide extraction

**Figure 3.9:** Infrared spectra of extracts by ethanol and hexane Soxhlet extraction and scCO<sub>2</sub> extraction at 100 °C and 300 bar

**Figure 3.10:** Percentage potassium leached from Cl07 wheat straw with varying temperature, time and leaching solution. Based on AAS analysis of extract

**Figure 3.11:** Percentage potassium leached from Cl07 wheat straw using different acids after extraction for 1 h at 50 °C. Based on AAS analysis of extract

**Figure 3.12:** Concentration of various anionic species in wheat straw leachates after extraction for 1 h at 50 °C using acetic acid or water

**Figure 3.13:** Percentage of various anionic species extracted by leaching Cl07 wheat straw in acetic acid and water for 1 h at 50 °C

**Figure 3.14:** X-ray diffraction of wheat straw ash following different pretreatment methods. All combusted at 500 °C for 2 h. 1 = Sylvite (KCl); 2 = Calcite (CaCO<sub>3</sub>); 3 = Arcanite (K<sub>2</sub>SO<sub>4</sub>); 4 = Anhydrite (CaSO<sub>4</sub>); 5 = Quartz (SiO<sub>2</sub>)

**Figure 3.15:** Pyrolysis profiles of pretreated Cl07 wheat straw

**Figure 3.16:** Combustion profiles of pretreated Cl07 wheat straw

**Figure 3.17:** Comparison of mass loss of ashes from pretreated wheat straw previously combusted at 550 °C

**Figure 3.18:** Mass loss from ashes between 0 – 250 °C

**Figure 3.19:** TG, DTG and DSC of ash of initial wheat straw

**Figure 3.20:** TG, DTG and DSC of ash of scCO<sub>2</sub> extracted wheat straw

**Figure 3.21:** TG, DTG and DSC of ash of EtOH extracted wheat straw

**Figure 3.22:** TG, DTG and DSC of ash of H<sub>2</sub>O leached wheat straw

**Figure 3.23:** TG, DTG and DSC of ash of CH<sub>3</sub>COOH leached wheat straw

**Figure 3.24:** Changes in the shape of pellets of ash formed from pretreated Cl07 wheat straw previously combusted to 550 °C and heated to 1000 °C at 5 °C min<sup>-1</sup>

**Figure 3.25:** K<sub>2</sub>O-SiO<sub>2</sub>-CaO phase diagram displaying some of the solidus temperatures and the position of the pretreated wheat straw samples

**Figure 3.26:** Cumulative concentration of inorganic species in the aqueous extracts of pretreated Cl07 straw ash

**Figure 3.27:** Silica extraction from pretreated Cl07 straw ash using water and KOH solutions, showing the molar concentration of the KOH solutions used

**Figure 3.28:** Proposed scheme for the pretreatment of wheat straw by ethanol extraction prior to combustion

## **Chapter 4**

**Figure 4.1:** Proposed general mechanism for cellulose pyrolysis

**Figure 4.2:** STA profiles of char before and after washing showing the changes in energy on combustion and the mass loss profile (inset)

**Figure 4.3:** Elemental content of Cl07 straw and microwave chars before and after leaching. Based on XRF analysis of solid material

**Figure 4.4:** Calorific values of straw and chars initially and after washing

**Figure 4.5:** Gas chromatograms of silylated compounds in leached microwave char solution

**Figure 4.6:** Potassium and chloride concentrations in aqueous extracts of pyrolysis chars

**Figure 4.7:** Si extraction trends for pyrolysis chars and combustion ashes following aqueous leaching at room temperature

**Figure 4.8:** Initial pH and final pH after 24 h leaching of pyrolysis char extracts

**Figure 4.9:** Effect of pyrolysis time on silica extraction and the pH of the extract of wheat straw char pyrolysed at 400 °C

**Figure 4.10:** a) Turbostratic carbon sheets showing the lack of 3-dimensional order. b) Growth of turbostratic sheets with increasing pyrolysis temperature

**Figure 4.11:** Proposed mechanism for the increasing alkalinity of wheat straw char extracts with increasing combustion temperature and time

**Figure 4.12:** Na,  $\text{SO}_3^{2-}$  and  $\text{NO}_3^-$  concentration in char extracts with pyrolysis temperature

**Figure 4.13:** Changing char yield with pyrolysis temperature and time (Originally in colour)

**Figure 4.14:** Van Krevelen diagram of changing atomic ratios of char on a  $\text{H}_2\text{O}$  free basis

**Figure 4.15:** X-ray diffractograms of chars formed at different temperatures after 2 h: 1 = Sylvite (KCl); 2 = Calcite ( $\text{CaCO}_3$ ); 3 = Arcanite ( $\text{K}_2\text{SO}_4$ ); 9 = Calcium silicate ( $\text{Ca}_2\text{SiO}_4$ ) or Potassium carbonate ( $\text{K}_2\text{CO}_3$ ); sh = sample holder

**Figure 4.16:** ATR-IR spectra of pyrolysis chars formed at different temperatures before leaching

**Figure 4.17:** ATR-IR spectra of pyrolysis chars formed at 400 °C with different heating times following leaching

**Figure 4.18:** Comparison of infrared spectra before and after leaching of char for pyrolysis treatment of 400 °C for 2 h

**Figure 4.19:** Calorific value of chars before and after extraction based on STA analysis

**Figure 4.20:** Change in ash content of chars before and after extraction based on thermogravimetric analysis

**Figure 4.21:** DSC profiles of chars before (solid line) and after (dashed line) leaching

**Figure 4.22:** Temperature of maximum energy release during combustion of chars with changing HTT before and after leaching

**Figure 4.23:** Carbon-oxygen complexes suggested to be formed during the catalytic decomposition of graphite

**Figure 4.24:** Percentage Si removed from pyrolysis chars and combustion ashes formed at 500 °C after 2 h under different extraction conditions. Based on AAS analysis of extract

## **Chapter 5**

**Figure 5.1:** Basic layout and collection points of material from power stations burning wood chip and miscanthus biomass

**Figure 5.2:** Concentration of various elements in extracts of miscanthus ash formed at different combustion temperatures

**Figure 5.3:** Concentration of various elements in extracts of wood chip ash formed at different combustion temperatures

**Figure 5.4:** Diffractograms of miscanthus ashes formed at different combustion temperatures: 1 = Sylvite (KCl); 2 = Calcite ( $\text{CaCO}_3$ ); 3 = Arcanite ( $\text{K}_2\text{SO}_4$ ); 5 = Quartz ( $\text{SiO}_2$ ); 6 = Calcium silicate ( $\text{CaSiO}_2$ ); 7 = Fairchildite ( $\text{K}_2\text{Ca}(\text{CO}_3)_2$ ); 9 = Calcium silicate ( $\text{Ca}_2(\text{SiO}_4)$ ); 10 = Calcium oxide (CaO)

**Figure 5.5:** Diffractograms of wood chip ashes formed at different combustion temperatures: 2 = Calcite ( $\text{CaCO}_3$ ); 3 = Arcanite ( $\text{K}_2\text{SO}_4$ ); 5 = Quartz ( $\text{SiO}_2$ ); 7 = Fairchildite ( $\text{K}_2\text{Ca}(\text{CO}_3)_2$ ); 9 = Calcium silicate ( $\text{Ca}_2(\text{SiO}_4)$ ); 11 = Portlandite ( $\text{Ca}(\text{OH})_2$ )

**Figure 5.6:** XRD of Ely-BA1 and Ely-FA1 - fly ash and bottom ash from a combustion facility primarily using miscanthus: 1 = Sylvite ( $\text{KCl}$ ); 3 = Arcanite ( $\text{K}_2\text{SO}_4$ ); 8 = Cristobalite ( $\text{SiO}_2$ ); 11 = Portlandite ( $\text{Ca}(\text{OH})_2$ ); 12 = Potassium sodium sulfate ( $\text{K}_3\text{Na}(\text{SO}_4)_2$ )

**Figure 5.7:** XRD of Ecc-BA1 and Ecc-FA1 - fly ash and bottom ash from a primarily wood chip combustion facility: 1 = Sylvite ( $\text{KCl}$ ); 4 = Anhydrite ( $\text{CaSO}_4$ ); 5 = Quartz ( $\text{SiO}_2$ ); 9 = Calcium silicate ( $\text{Ca}_2(\text{SiO}_4)$ ); 10 = Calcium oxide ( $\text{CaO}$ ); 12 = Potassium sodium sulfate ( $\text{K}_3\text{Na}(\text{SO}_4)_2$ )

**Figure 5.8:** pH of solutions during the leaching of power station bottom ashes and fly ashes with time

**Figure 5.9:** Infrared spectra of K120 solution at various concentrations relative to the original solution

**Figure 5.10:** Infrared spectra of various commercial silicate solutions diluted to 32% of the original concentration

**Figure 5.11:** Correlation between the Si concentration of three sodium silicate solutions analysed by AAS and the area of the silicate band in their IR spectra

**Figure 5.12:** Correlation between the Si concentration of three sodium silicate solutions analysed by AAS and the area of the silicate band in their IR spectra

**Figure 5.13:** Correlation between the Si concentration of several potassium and sodium silicate solutions analysed by AAS and the area of the silicate band in their IR spectra

**Figure 5.14:** Comparison of Si concentration analysed by AAS and using the IR integral for Ely-BA1 extraction solutions formed with different KOH solution concentrations

**Figure 5.15:** IR spectra of silicate solutions formed by the extraction of Ely-BA1 using different KOH concentrations

**Figure 5.16:** Correlation between the IR integral and Si AAS analysis for several silicate solutions formed from the extraction of Ely-BA1. The points in blue indicate solutions calculated from the linear fitting

**Figure 5.17:** Area of silicate peak vs time during the extraction of Ely-BA1 ash

**Figure 5.18:** IR spectra of silicate solutions formed during the extraction of Ely-BA1 for different lengths of time

**Figure 5.19:** IR spectra of silicate solutions formed during the extraction of Ely-BA1 using a 1M KOH solution and a concentrated solution from the extraction of Ely-FA1

**Figure 5.20:** IR spectra of K120 and Ely-BA1 biosilicate solutions used as binders for board formation testing

**Figure 5.21:** Procedure for formation of test boards using a wheat straw substrate with different potassium silicate binders

**Figure 5.22:**  $^{29}\text{Si}$  NMR of Ely-BA1 before and after extraction

**Figure 5.23:** XRD of initial Ely-BA1 and Ely-BA1-15 residue following silica extraction and washing to remove residual silicate

**Figure 5.24:** XRD of residual Ely-BA1 material after silicate extraction and drying with or without washing

**Figure 5.25:** Blocks formed from biosilicate ash residue showing samples where cracks have formed on drying after A: 2 days; B and C: 7 days; D 9 days air drying

**Figure 5.26:** 3-point bending test set-up

## **Appendix A**

**Figure A1:** Powder XRD spectrum of sylvite from the ICSD database<sup>1</sup> compared to Cl07 wheat straw ash combusted at 500 °C for 2 h (as shown in Figure 2.5b)

**Figure A2:** Powder XRD spectrum of calcite from the ICSD database compared to wood chip ash combusted at 400 °C for 2 h (as shown in Figure 5.5)

**Figure A3:** Powder XRD spectrum of arcanite from the ICSD database compared to wood chip ash combusted at 400 °C for 2 h (as shown in Figure 5.5)

**Figure A4:** Powder XRD spectrum of anhydrite from the ICSD database compared to Eccleshall fly ash (as shown in Figure 5.7)

**Figure A4:** Powder XRD spectrum of quartz from the ICSD database compared to Eccleshall bottom ash (as shown in Figure 5.7)

**Figure A6:** Powder XRD spectrum of calcium silicate from the ICSD database compared to Cl07 wheat straw ash combusted at 800 °C for 2 h (as shown in Figure 2.5b)

**Figure A7:** Powder XRD spectrum of fairchildite from the ICSD database compared to Viscount 09 wheat straw ash combusted at 500 °C for 2 h (as shown in Figure 2.8)

**Figure A8:** Powder XRD spectrum of  $\alpha$ -cristobalite from the ICSD database compared to Claire 08 wheat straw ash combusted at 800 °C for 2 h (as shown in Figure 2.9)

**Figure A9:** Powder XRD spectrum of calcium silicate from the ICSD database compared to extracted Ely-BA1 ash dried at 120 °C (as shown in Figure 5.24)

**Figure A10:** Powder XRD spectrum of potassium carbonate from the ICSD database compared to Claire 07 wheat straw pyrolysed at 800 °C for 2 h (as shown in Figure 4.15)

**Figure A11:** Powder XRD spectrum of calcium oxide from the ICSD database compared to Ecc-FA1 (as shown in Figure 5.7)

**Figure A12:** Powder XRD spectrum of portlandite from the ICSD database compared to Ely-FA1 (as shown in Figure 5.6)

**Figure A13:** Powder XRD spectrum of apthitalite from the ICSD database compared to Ely-FA1 (as shown in Figure 5.7)

**Figure A14:** Powder XRD spectrum of aluminium from the ICSD database compared to Claire 07 wheat straw combusted at 400 °C for 10 min (as shown in Figure 2.5)

# Acknowledgements

Firstly, I would like to thank Professor James Clark for providing the opportunity to carry out this research. Thank you to both James and Dr. Andrew Hunt for your support, guidance, interesting discussions and the opportunity to attend and speak at conferences both in the UK and abroad.

Thank you to Defra for providing the funding for this project and to the rest of the Defra LINK team for your help and ideas – Kris, Avtar, Mario and Andy. To everyone else in the Green Chemistry Centre a huge thanks for the camaraderie, the energy, enthusiasm and fun times. I want to particularly thank Vitaly and Andy for inspirational discussions, collaborations and bringing the excitement back into labwork. Also, to my silica buddies Jenny, Emma and Duncan...where would we be without silica - I'm expecting a song about it soon!

Thanks must also go to Charlie Parker at G & H Cholmley farms for providing the straw and helping with its collection, Alan Minihan at PQ Corporation for providing samples of many types of alkali silicate solutions, Graham Ormondroyd and Morwenna Spear at the University of Bangor with information about board-making and testing our 'bioboards' and the staff at Ely Power Station and Eccleshall Power Station for providing samples of their ashes. I would also like to thank Meg Stark for her invaluable help with SEM and TEM, Rebecca Sutton for helping me with ion chromatography measurements, Robert Burton at Sheffield Hallam University for carrying out XRF analyses and Heather Fish for her training to use the NMR. I couldn't have completed this work without Dave Lyndsey and Phil Halliwell allowing me the use of the AA spectrometer in the undergraduate labs almost every week – thank you so much for all your time and help.

To the rest of the outreach team – Louise, Odette, Elisa, Jo and Helen. The past four years just wouldn't have been the same without dressing up as a green frog, trips to Bristol and Glasgow to make bubbles, dry ice and limonene and the rest of the fabulous times.

I have met so many wonderful other people in York that have made life beautiful and helped me keep a wider perspective on why I chose to carry out research in Green

Chemistry in the first place. Special thanks to Peter – I wish you and your house could move with us wherever we live in the future.

Finally to my family. Thank you for all the love and support that allowed me to get to this point, the Dodson debates, the pep talks, proof reading, endless supplies of chutney and jam...I can't put it all in one sentence. And to Tom, thank you for being there through it all and keeping me laughing.

# Declaration

I hereby declare that the work presented in this thesis is my own, except where otherwise acknowledged, and has not previously been submitted for a degree at this or any other university.

Jennifer Ruth Dodson

September 2011



# **Chapter 1:**

# **Introduction**



## 1.1 Scope of the project

The work contained within this thesis was part of a larger project, which aimed to develop sustainable materials utilising indigenous UK renewable materials at all stages of production. A biorefinery approach was envisioned to produce general purpose boards utilising waste biomass derived substituents as both the substrate and the binder (Figure 1.1).

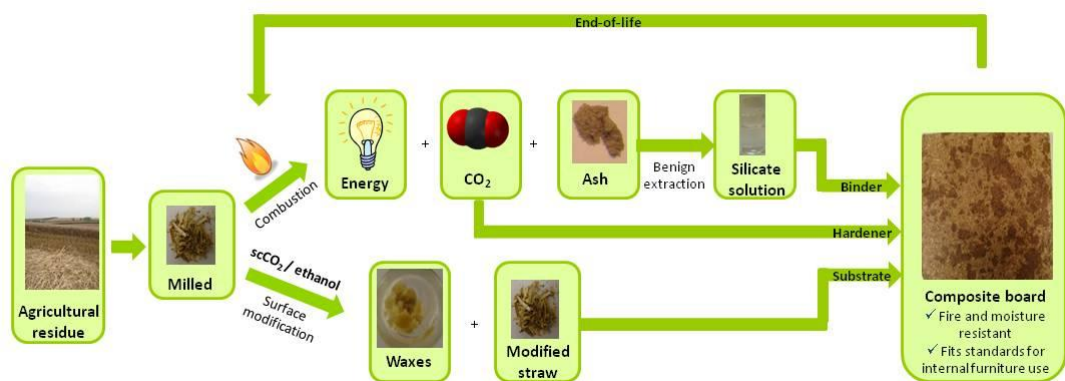


**Figure 1.1: Concept for the formation of inorganic composite boards utilising waste materials throughout (Originally in colour)**

The work within this thesis focused on one aspect of this project; understanding the formation of combustion residues from agricultural wastes and the production of alkali silicate solutions from those wastes as a binder for composite boards. To this end several avenues of research were explored.

**The impacts of the combustion process on the inorganic species within the combustion material.** One variety of wheat straw was investigated in detail to understand the impact of combustion conditions on the mineralogical, physical and chemical characteristics of the ashes and chars formed. Work focused on the extraction and aqueous solubility of all elements and their interdependency, with a particular emphasis on silicon and potassium. Previous work has concentrated on the impact of inorganic species, mostly alkali metals and halogens, on combustion properties.<sup>1</sup> However, understanding of the formation of combustion residues and specifically how this impacts on their utilisation as a valuable material has received limited attention in the scientific literature.

**Variation between wheat straw varieties and different biomass materials.** Several varieties of wheat straw collected over three years, along with wood chips and miscanthus straw, were compared to understand the impact of the initial elemental composition on the physico-chemical characteristics of the ashes formed and the extraction of elements. This is vital for understanding how the wheat straw variety, growing conditions and biomass species affect the use of the combustion residues formed.

**Pretreatment of wheat straw.** The negative impacts of alkali metals and halogens on combustion in large scale boilers has led to research studies into the extraction of these elements prior to combustion.<sup>2</sup> Other researchers have looked at the valorisation of wheat straw by the extraction of high value epicuticular waxes.<sup>3</sup> However, the impact of these pretreatment processes on the mineralogical composition and extraction of combustion residues was previously unstudied.

**Alkali silicate from biomass-fired combustion boiler residues as a binder in composite boards.** The formation of an alkali silicate solution from biomass-fired boiler combustion residues was investigated and utilised as a binder to form particleboards. The use of alkali silicates hasn't previously been demonstrated as a binder at low concentrations for lignocellulosic substrates.

## **1.2 The Challenge: Climate Change, Peak Oil and Green Chemistry**

The concept of sustainability has developed as a key idea for how all human needs can be met within the boundaries of the finite resources available on earth, such that in the future these needs could be met indefinitely. The key definition of sustainable development was coined by the Brundtland Commission in 1987 as development that “meets the needs of the present without compromising the ability of future generations to meet their own needs”.<sup>4</sup> It links environmental, social and economic sustainability.

The need to incorporate sustainability into all aspects of our lives has never been greater at a time when we face two great challenges: the end of cheap and abundant petroleum sources and the impact of climate change from the unsustainable use of fossil fuels.

Over the past 50 years the economies of the most industrialised and more-economically developed countries have rapidly expanded, based on cheap and abundant fossil fuels as the lifeblood for everything from agriculture to consumer products, energy and transport. Demand for oil is continuing to grow as many of the least-economically developed countries, particularly China, the Middle East and Brazil, follow the same developmental route.<sup>5</sup> As the available, and easily extractable, oil reserves are depleted and as demand continues to grow we will reach a global point of 'peak oil', where demand will overtake the ability to increase total production.<sup>6</sup> This could result in extremely high oil prices, with detrimental impacts for everyone in society, unless alternative solutions are found in anticipation of these problems. The chemical industries are particularly dependent on petrochemicals as the building block for almost all products developed over the past century, with 98% of organic chemicals produced in the United States coming from petroleum feedstocks in 1998.<sup>7</sup> This makes these industries highly susceptible to changes in the economics of oil supply and demand and therefore they must be at the forefront of finding sustainable alternatives.

In addition, our use of fossil fuels has had a major impact on the wider environment, increasing the amount of atmospheric carbon dioxide from 280 ppm at pre-industrial levels to 379 ppm in 2005, and exceeding the measured natural range over the past 650,000 years.<sup>8</sup> The mean global temperature has increased by  $0.74\text{ °C} \pm 0.18\text{ °C}$  over the past 100 years, with scientific evidence indicating that it is extremely likely that there has been a substantial contribution from anthropogenic induced warming.<sup>9</sup> The probable result will be large changes to the global climate system over the coming centuries, resulting in challenges for ecosystems, including human, across the world.<sup>8</sup>

This combination of peak oil and climate change, relating to our unsustainable use of fossil fuels, along with the political, economic and social pressure to 'do something about it' has created a driving force which demands that the current 'business as usual' model for energy production and the chemical industries must change.

An additional important, but frequently neglected, issue is the increasing scarcity and cost of a wide range of elements.<sup>10</sup> The price of indium, used for LCD screens and solar cells, stayed relatively stable from the 1980s up to the year 2000, at between  $\$85\text{-}200\text{ kg}^{-1}$ , but has since dramatically increased to a maximum of  $\$918\text{ kg}^{-1}$  in 2006, reducing to  $\$500\text{ kg}^{-1}$

in 2009 due to the global recession.<sup>11</sup> It is predicted that indium could be depleted within 5-10 years.<sup>10</sup> Even the price of potash, the soluble source of the vital plant nutrient potassium, has been steadily increasing from \$280 t<sup>-1</sup> in 2005 to \$820 t<sup>-1</sup> in 2009.<sup>12</sup> With 93% of the worldwide production being used as a fertiliser, this is a vital concern for the agricultural industry. This underscores the necessity to ensure complete recovery, recycling and reuse of all elements; 'elemental sustainability', not just carbon in a biorefinery approach.

A green chemistry approach aims to tackle these challenges by utilising renewable resources and developing new techniques and tools that will enable innovative and novel sustainable chemicals for human needs to be manufactured. In 1996, the International Union of Pure and Applied Chemistry (IUPAC) defined Green Chemistry as "the invention, design and application of chemical products and processes to reduce or to eliminate the use and generation of hazardous substances".<sup>13</sup> Anastas and Warner described 12 fundamental principles setting out how this can be achieved:<sup>7</sup>

1. It is better to prevent waste than to treat or clean up waste after it is formed.
2. Synthetic methods should be designed to maximize the incorporation of all materials used in the process into the final product.
3. Wherever practicable, synthetic methodologies should be designed to use and generate substances that possess little or no toxicity to human health and the environment.
4. Chemical products should be designed to preserve efficacy of function while reducing toxicity.
5. The use of auxiliary substances (e.g. solvents, separation agents, etc) should be made unnecessary wherever possible and, innocuous when used.
6. Energy requirements should be recognized for their environmental and economic impacts and should be minimized. Synthetic methods should be conducted at ambient temperature and pressure.
7. A raw material of feedstock should be renewable rather than depleting wherever technically and economically practicable.

8. Unnecessary derivatisation (blocking group, protection/deprotection, temporary modification of physical/chemical processes) should be avoided whenever possible.
9. Catalytic reagents (as selective as possible) are superior to stoichiometric reagents.
10. Chemical products should be designed so that at the end of their function they do not persist in the environment and break down into innocuous degradation products.
11. Analytical methodologies need to be further developed to allow for real-time, in-process monitoring and control prior to the formation of hazardous substances.
12. Substances and the form of a substance used in a chemical process should be chosen so as to minimize the potential for chemical accidents.

The overall concept that integrates all of these principles is 'benign by design'; incorporating these principles at the beginning of the design and research process. The wider project that this work is part of exemplifies these principles by aiming to utilise waste and renewable feedstocks (principles 1 and 7), incorporate all parts of the initial material into the final product (principle 2), reduce energy use during manufacturing (principle 6) and design for utilisation at end-of-life (principle 10), whilst also taking into account the broader aspects of sustainability.

### **1.3 Energy from biomass**

In order to tackle these sustainability challenges, several pieces of legislation have been implemented globally and nationally. The Climate Change Act commits the UK to cutting levels of greenhouse gas emissions by 80% by 2050 on the 1990 baseline.<sup>14</sup> In the shorter term, the UK is also legally bound to produce 15% of all energy and 10% of road energy from renewable resources by 2020 under the EU Renewable Energy Directive (RED).<sup>15</sup>

In 2008, the UK produced 533 million tonnes of CO<sub>2</sub>, 10% below the 1990 baseline.<sup>16</sup> The majority of these emissions were produced during energy generation and transportation and attributed to transportation, electricity and heating, particularly by businesses and domestic dwellings (Figure 1.2). Of these emissions, 43% came from the use of gas, 30% from oil, 22% from coal, 2% from other solid fuels and 3% from non-solid fuel sources.<sup>16</sup>

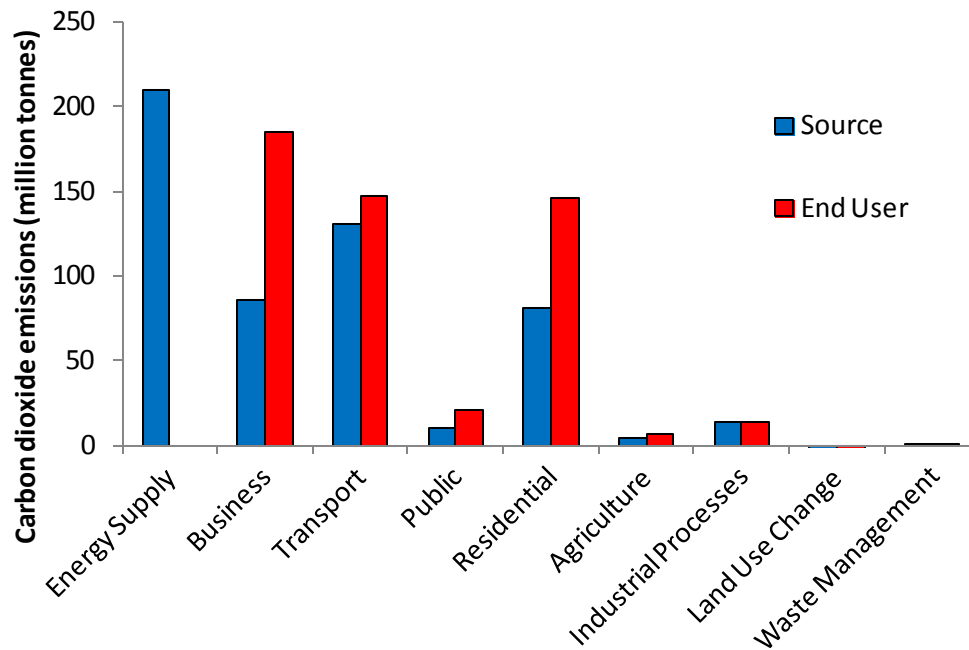


**Figure 1.2: UK 2008 CO<sub>2</sub> emissions by sector attributed either to the source of the emissions or the end user<sup>16</sup> (Originally in colour)**

This highlights the huge challenge faced in switching the UK away from its current dependence on fossil fuels and reducing greenhouse gas emissions by the level required. The necessity for this is noticeably acute in energy production.

Biomass is a carbon source that is renewable over a short timescale, by fixing CO<sub>2</sub> during growth via photosynthesis and releasing it during decomposition. Biomass is potentially the only globally distributed indigenous material capable of replacing all aspects of fossil fuel usage to produce electricity, heat, solid, liquid and gaseous fuels and materials (Figure 1.3).

Both Defra's 2007 'UK Biomass Strategy' and the Department for Energy and Climate Change's 'Renewable Energy Strategy 2009' demonstrate varied opportunities for the utilisation of biomass to help meet the UK's legislative demands.<sup>17, 18</sup> The UK Government predicts that 5% of the nation's heat and power (70 TWh) could be cost-effectively generated from indigenous biomass by 2020.<sup>17</sup> Currently, combustion remains the default technology for energy production from biomass and wastes due to the lower technological hurdles.<sup>19</sup> However, other technologies such as anaerobic digestion, gasification and pyrolysis are being extensively explored.

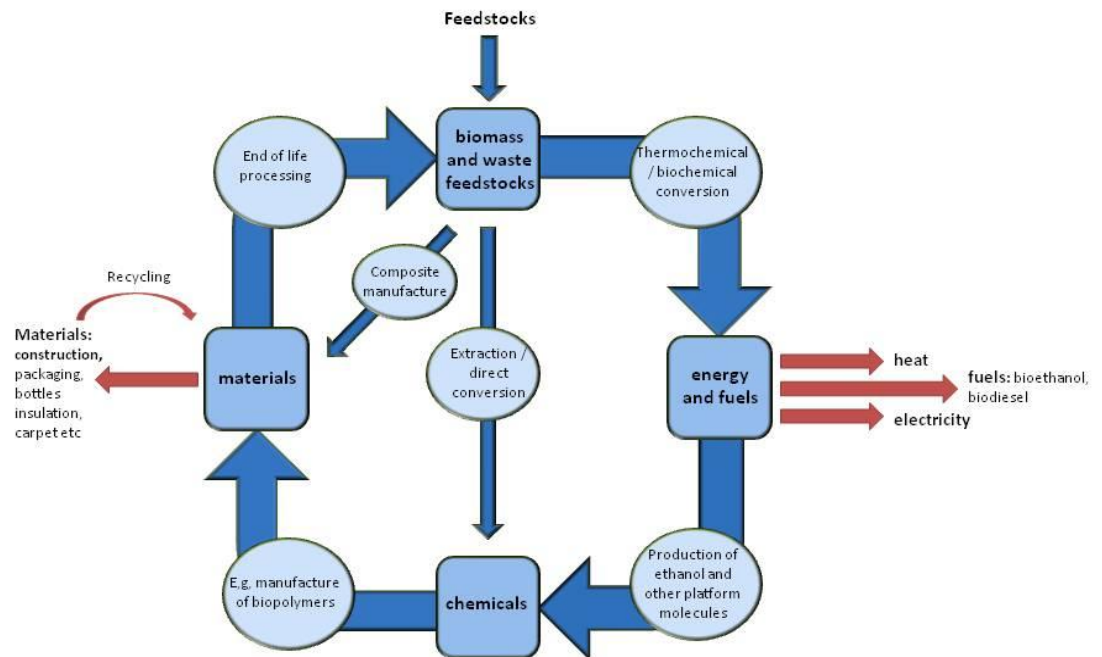


**Figure 1.3: The potential of biomass for creating energy, fuels, materials and chemicals (developed from Ref 20) (Originally in colour)**

### 1.3.1 Potential biomass sources

The potential of different indigenous biomass feedstocks to contribute to energy production in the UK are listed in Table 1.1 from modelling taking into account competing resource demands and technical, environmental and supply constraints.<sup>21</sup> This data indicates that agricultural crop residues and wood wastes currently offer the largest potential source of biomass for energy via thermochemical conversion, particularly when unsuitable wet organic materials are excluded. Miscanthus and short rotation coppice (SRC) have the potential to provide a large energy resource in the future on environmentally sustainable land.<sup>21</sup> UK and EU Governments are incentivising the planting of these perennial biomass crops due to their high yields, low fertiliser requirements and predicted high greenhouse gas emissions savings.<sup>22</sup>

Worldwide an estimated 95-115 EJ  $\gamma^{-1}$  of energy could be extracted sustainably from forestry and crop residues by 2050, with 53-61% of this coming from crop residues.<sup>23</sup> An additional 232-1349 EJ  $\gamma^{-1}$  could be available from dedicated energy crops on surplus agricultural land.<sup>23</sup> This compares to a total global primary energy demand of 517 EJ in 2010.<sup>24</sup> The variation in potential energy production from biomass particularly depends

on land-use requirements for animal products (using more than 70% of global agricultural land in 2002), and technological advancements in food production.<sup>23</sup>

This investigation focuses on crop residues as one of the largest, most widely available and least studied sources of biomass for energy production. In addition, comparisons are made to waste wood and energy crops as alternative current and future sources of biomass for energy.

**Table 1.1: Energy potential of UK biomass feedstocks<sup>21</sup>**

Feedstock	Sources	Energy potential 2009 (PJ y <sup>-1</sup> )	Energy potential 2020 (PJ y <sup>-1</sup> )
Energy crops	Short rotation coppice (SRC) willow or poplar, and miscanthus	0-20	150-180
Crop residues	Straw from crops including wheat and oil seed rape	69 (not all collected)	69 (100% collected)
Stemwood	Hardwood and softwood tree trunks	4.5	17.5
Forestry residues	Wood chips from branches, tips and poor quality stemwood	0	19.3
Sawmill co-product	Wood chips, sawdust and bark made when sawing stemwood	2.4	19.5
Arboricultural arisings	Stemwood, wood chips, branches, foliage from municipal tree surgery operations	1.5 (+4.6 currently landfilled)	3.2
Waste wood	Clean and contaminated waste wood	19	149 (in 2030)
Organic waste	Paper/card; food/kitchen; garden/plant and textiles wastes	40 (13; 10; 16; 1 respectively)	40
Sewage sludge	From Waste Water Treatment Works	15.2	24.6
Animal manures	Manures and slurries from cattle, pigs, sheep and poultry	0.27	5.8
<b>Total maximum energy potential (PJ)</b>		<b>171.9</b>	<b>527.9</b>

### 1.3.2 Agricultural residue availability in the UK

In 2008 James Copeland and David Turley studied the national and regional supply/demand balance of agricultural straws in the UK.<sup>25</sup> They found a potential total annual straw yield of 11.9 million tonnes from wheat (54%), oilseed rape (21%), barley (20%), oats (4%), other cereals (1%) and linseed (0.1%).<sup>25</sup> After calculating the current straw use in the livestock and mushroom industries they estimated that there is a 3 million tonne annual cereal straw surplus (mainly wheat), concentrated in the East of England. In

addition, 2.5 million tonnes of oilseed rape straw could be available that isn't presently recovered. However, the report also stressed the nutrient value, particularly of potassium, of the straw that is removed.<sup>25</sup> The study by Copeland and Turley clearly identified wheat straw as the most abundant agricultural residue available in the UK. The decision to focus on an understanding of the utilisation of indigenous agricultural residues therefore led to the choice of wheat straw as the main focus of this investigation, with some comparisons to other crop residues. As one of the main staple crops grown across the world, the results and lessons learnt from this study may also be applicable more widely.

### 1.3.3 Biomass composition

The composition of biomass varies depending both on the species and the geographic location in which it has been grown. Nevertheless, in general, crop residues, such as cereal straws, consist of five main components: cellulose, hemicellulose, lignin, extractives and ash. Typical values for herbaceous plants range from 40-50% cellulose, 20-40% hemicellulose, 15-20% lignin and 5-10% extractives.<sup>26</sup> Woody biomass generally has a higher lignin but lower hemicellulose content.

In terms of energy production, the polysaccharide content of biomass makes the material much more oxygen rich than coal, with materials with a higher lignin content having a lower O/C ratio and a corresponding higher calorific value.<sup>27</sup> Additionally, in comparison to coal, biomass contains more moisture, has a lower density, contains less sulfur, less nitrogen, more silica, potassium and chlorine, less aluminium and iron and has a lower heating value.<sup>28</sup> Some of these differences are beneficial, whilst others create technological challenges. High moisture contents reduce the thermal efficiency of combustion, can cause problems during ignition and lower the maximum flame temperature.<sup>29</sup> The optimal moisture content is around 15%, although furnaces can usually cope with a maximum of 65% moisture.<sup>30</sup> Chopped straw has a bulk density of 50-120 kg m<sup>-3</sup> compared to 800-900 kg m<sup>-3</sup> for bituminous coals.<sup>31</sup> This increases both the carbon and monetary costs of transportation, reduces the heating value per unit volume, and makes it difficult to continuously feed the straw and control the rate of burning.<sup>29, 31</sup> Densification of biomass to 500-1000 kg m<sup>-3</sup> is possible using several different technologies, such as pelletisation, however it increases the production cost.<sup>30</sup> A more

decentralised system of smaller energy facilities is therefore attractive to reduce transportation distances, despite the increased capital costs and labour requirements.<sup>31</sup> Increasing job creation in rural areas is, however, beneficial and is an argument in the UK Government's desire to create a 'greener' economy.

A wide variation in the ash content and distribution of inorganic species can be observed both within agricultural residue types and between them (Table 1.2). Irrigation and fertiliser usage in the growth of herbaceous plants leads to higher contents for almost every inorganic species in comparison to wood.<sup>2</sup> The alkali content is, in particular, much higher in the herbaceous materials in comparison to the woody and coal sources. Silica and potassium are the two major ash forming species for all of the agricultural residues, excluding rape straw. The mix of inorganic species within each material affects both the combustion properties of the fuel and the design and operation of combustion systems. These issues are discussed in more detail in section 1.4.2.

Table 1.2: Ash content, elemental composition and calorific value data for a variety of biomass materials and coal

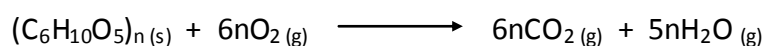
Residue type	Ash (wt% dry basis)	SiO <sub>2</sub>	Al <sub>2</sub> O <sub>3</sub>	Fe <sub>2</sub> O <sub>3</sub>	CaO	MgO	Na <sub>2</sub> O	K <sub>2</sub> O	SO <sub>3</sub>	P <sub>2</sub> O <sub>5</sub>	Cl	HHV (MJ / kg dry basis)	Alkali index (kg M <sub>2</sub> O / GJ)	Ref	
<b>Wheat straw</b>	Imperial Valley (USA)	12.8	35.8	2.5	1.0	4.7	2.5	10.5	18.4	5.5	1.5	14.7	17.2	2.15	2
	(China)	10.0	36.9	8.0	6.3	8.1	3.0	9.2	17.4	4.5	2.0	5.2	16.2	1.64	32
	2000 (Denmark)	4.8	35.3	1.1	0.1	10.2	2.4	0.5	30.1	6.2	2.6	3.4	16.8	0.88	33
	Soisson (Spain)	5.7	64.0	0.3	0.2	5.4	1.8	0.1	17.0	1.8	1.6	2.8	16.3	0.60	33
	2001 (Denmark)	4.8	67.0	0.2	0.2	8.7	2.2	0.1	14.0	2.2	2.4	2.1	17.4	0.39	33
	Marius (Spain)	4.9	65.0	0.8	0.6	11.0	1.7	0.1	9.1	2.5	2.3	1.2	17.1	0.26	33
<b>Other agricultural straws available in UK</b>	Winter barley	6.9	25.2	0.2	0.1	6.9	2.2	5.1	40.2	5.1	1.9	6.9	16.5	1.89	33
	Spring barley	5.7	37.2	nd	nd	12.5	1.0	0.9	17.8	2.7	1.4	1.4	nd		33
	Oat straw	3.8	15.2	0.3	0.1	26.5	3.3	4.5	17.4	6.4	6.7	0.8	17.4	0.48	33
	Rape straw	2.7	2.4	4.2	1.6	48.7	3.1	0.2	15.2	3.8	1.4	0.5	17.0	0.24	33
<b>Agricultural residues around the world</b>	Rice straw	20.9	72.3	0.1	0.3	2.1	2.1	2.7	11.8	1.1	1.8	4.1	14.7	2.05	2
	Cotton straw	7.4	17.7	10.8	2.4	9.0	7.3	6.8	30.2	5.8	4.3	4.9	15.9	1.73	32
	Maize	7.1	33.0	3.7	1.6	17.0	4.4	0.4	22.0	1.7	1.9	5.4	16.4	0.97	33
	Sugarcane bagasse	8.5	42.6	23.2	16.2	3.0	2.0	0.6	3.0	0.5	1.3	0.1	17.7	0.17	2
	Switchgrass	3.8	62.8	0.3	0.9	6.2	1.7	0.4	11.7	1.5	4.2	0.1	18.7	0.24	2
<b>Wood</b>	Wood fuel	4.5	37.5	14.1	0.6	7.6	17.0	3.6	1.4	2.2	6.0	2.2	18.7	0.12	2
	Red Oak	1.2	38.3	8.1	7.6	12.8	1.0	0.4	8.6	1.8	1.0	<0.01	19.0	0.06	34
<b>Macroalgae</b>	<i>Laminara digitata</i>	25.8	0.4	0.1	1.0	5.0	5.2	19.6	14.8	-	6.7	-	17.6	3.23	35
<b>Coal</b>	Eastern Kentucky	7.6	51.6	32.5	4.5	1.1	0.4	0.2	1.3	1.3	0.3	2.3	31.0	0.04	34

## 1.4 Combustion of biomass and the impact of inorganic species

The process of burning biomass is one of the oldest and simplest chemical conversions carried out by mankind. Globally, biomass still provides around 14% of the world's energy requirement, and 35% of the energy in developing countries.<sup>28</sup> But as described by Petterson *et al.*:<sup>36</sup>

*“It is easy to start a fire, but to burn a fuel at optimal conditions regarding complete combustion, clean exhaust gases with respect to NO<sub>x</sub>, SO<sub>x</sub>, HCl, HF and trace element emissions as well as to achieve reliable operation conditions is altogether a challenge.”*

The stoichiometric equation for the combustion of biomass using the basic empirical formula for cellulose can be represented as:



Thermogravimetric analysis has been used to identify the stages of biomass combustion.<sup>26</sup> An initial mass loss up to 120 °C is caused by evaporation of the contained moisture along with high-energy volatiles. The main mass loss occurs between 180 – 375 °C as the solid lignocellulosic material begins to decompose and devolatilise releasing organic compounds that burn in the gas phase.<sup>30</sup> This step is similar to the processes occurring during pyrolysis. Research within the latter area has given rise to a 3-component model: hemicellulose and cellulose decompose in parallel and are mainly responsible for the mass loss, whilst lignin decomposes over a broader temperature range and is responsible for the majority of the char formed.<sup>26</sup> At higher temperatures (375 – 525 °C), in an oxygen-rich atmosphere, the residual chars combust at a slower rate.<sup>30</sup>

### 1.4.1 Combustion technologies

The main aims in combustion systems are to maximise boiler efficiency for the production of steam and to minimise undesirable gas emissions.<sup>30</sup> The two main biomass combustion technologies in use are grate-fired and fluidised bed combustion (FBC) boilers.<sup>37</sup>

#### 1.4.1.1 Grate fired combustion

Grate-fired boilers vary in capacity from around 4-200 MW and consist of (Figure 1.4):

1. A fuel feeding system
2. Grate assembly
3. Secondary air supply
4. Ash discharge system
5. Heat exchange system

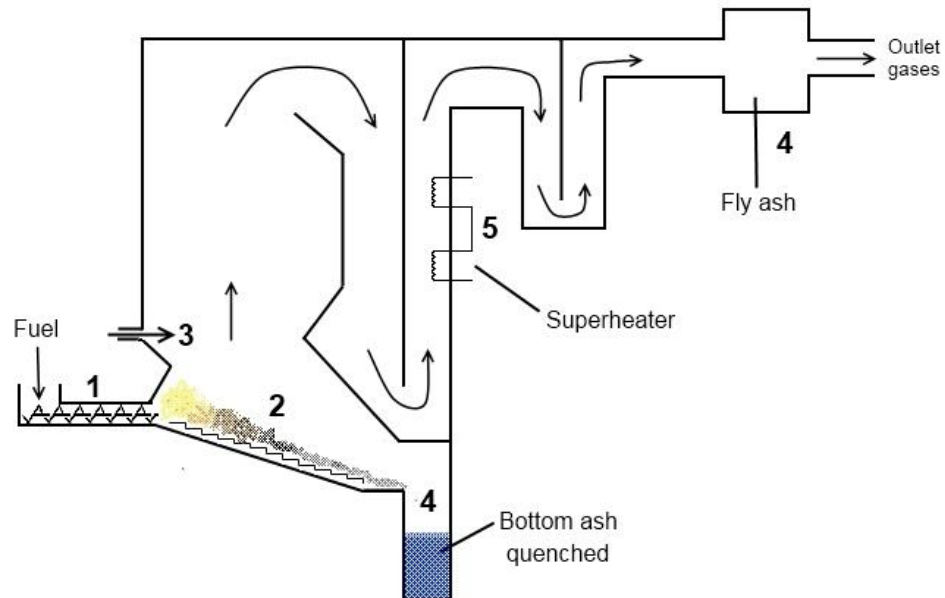


**Figure 1.4: Basic grate-fired biomass combustion plant design (Originally in colour)**

The grate assembly is responsible for ensuring good mixing of the fuel and that there is a sufficient air flow and residence time for the complete combustion of slower burning chars.<sup>29</sup> Generally a residence time of 20-40 minutes is required.<sup>38</sup> The top layer of the fuel ignites due to radiant heat from the furnace and flames above the bed.<sup>39</sup> The flame front moves down through the bed against the primary air supply. After reaching the grate a char burnout front moves in the opposite direction. Primary air is injected up through the grate. In modern systems a substoichiometric amount of air is likely to be added, with a secondary air supply added higher up in the furnace box.<sup>30, 40</sup> This helps to ensure complete combustion to prevent emissions of pollutants such as hydrocarbons ( $C_xH_y$ ), CO, particulates and polyaromatic hydrocarbons.<sup>41</sup> It can also prevent  $NO_x$  emissions and volatilisation of inorganic species by enabling a lower temperature and less air to be used at the fuel bed.<sup>42</sup>

The hot flue gases transfer heat to water cooled tubes in the superheaters. Additional economisers capture the waste heat by heating the boiler feedwater. The bottom ash that falls through the grate is discharged to an ash receptacle and is often quenched in water.<sup>43</sup> Fine particulate fly ash, which has followed the flue gases, is collected in bag filters.<sup>43</sup>

Few studies indicate the actual grate temperature in industrial combustion units, however, furnace gas exit temperatures and furnace temperatures are typically between 800 – 900 °C; flame temperatures above the grate may be higher.<sup>44</sup> In Denmark, the Government's requirement to burn large volumes of straw since 2004, has led to the development of dedicated straw-fired co-generation plants which can operate at lower furnace exit gas temperatures of 640 - 760 °C.<sup>45</sup> An additional superheater, utilising gases from straw pyrolysis, can be used to superheat the steam for power generation.

#### **1.4.1.2 Fluidised bed combustion**

In fluidised bed combustion (FBC) an inert refractory material, usually silica sand,<sup>36</sup> is used as the bed material, with the fuel suspended within it. Air is added through a hole under the bed, which increases the volume of the bed, causing it to become 'fluidised'.<sup>30</sup> The constant movement of the bed material improves the temperature distribution, ensures intimate mixing of the fuel and oxidant and enables the addition of additives, such as limestone, to minimise pollutants.<sup>30</sup>

Both of these technologies are flexible to a wide variety of fuels and are used at dedicated biomass facilities around the world, with FBC a more recent technological development. However, despite some advantages, the latter is prone to bed agglomeration when using high alkali fuels, such as straw, and the initial capital and maintenance costs are higher.<sup>37</sup> The research contained within this thesis did not study fluidised bed combustion as the travelling grate boiler is the most common design for biomass combustion and produces an ash material based only on the initial elemental composition of the fuel is formed.<sup>46</sup>

#### **1.4.2 Impact of inorganics during grate-firing of herbaceous biomass**

Within the past decade, extensive investigations have been undertaken into the combustion of wheat straw.<sup>1, 32, 40, 45, 47-52</sup> This has been due to both an explosion of

interest in the production of energy from renewable fuels and the realisation of the difficulties in utilising straw in traditional combustion boilers.<sup>1, 42</sup> The combustion of wheat straw has been found to differ greatly to coal and woody biomass sources. This is primarily due to its distinct ash chemistry, including higher total ash content, alkalinity, chlorine and silica content (Table 1.2), resulting in lower ash melting points.<sup>53</sup> The impact of this can be severe slagging, fouling and corrosion.

Fouling is the deposition of solid materials on heat transfer zones, such as superheaters, beyond the furnace cavity.<sup>54</sup> Slagging is the formation of fused or sintered materials on radiant heat transfer surfaces within the furnace cavity, or of agglomeration of fluidised-bed materials.<sup>37</sup> These problems have been found to occur extensively during the combustion of wheat straw, in particular, decreasing the thermal efficiency of the system and at its worse causing the shutdown of boilers.<sup>33, 44-46, 55, 56</sup> In California, none of the biomass power plants built have been able to burn straw due to these problems.<sup>1</sup>

The main causes of fouling, slagging and corrosion from herbaceous materials are:

1. The reaction of potassium with silica, with chlorine as a facilitator causing the formation of low temperature eutectics.<sup>44</sup>
2. The reaction of potassium with sulfur to form potassium sulfates on superheater surfaces.<sup>1</sup>
3. High gas phase concentrations of KCl deposited by condensation on heat-transfer surfaces.<sup>33</sup>
4. Corrosion induced by chlorine on superheater surfaces.

The impacts of the three main ash forming components in wheat straw are discussed in more detail below.

#### **1.4.2.1 Potassium**

Studies indicate that potassium is present in biomass as cations associated with oxygen-containing functional groups or precipitated as chloride, carbonate, oxalate or sulfate salts.<sup>52</sup> Chemical fractionation suggests that 70-80% of the potassium present is either water soluble or ion exchangeable.<sup>46</sup> In comparison, in coal the alkali metal is usually bound within stable minerals.<sup>57</sup>

In laboratory studies, potassium losses during wheat straw combustion positively correlate with temperature.<sup>56</sup> Evolution has been observed to occur over two stages: a small amount at lower temperatures (180-500 °C), suggested to be due to release of potassium associated with organic species;<sup>52</sup> and 50-90% at higher temperatures (> 700 °C).<sup>38</sup> Correlation with chlorine losses intimates that the majority of this is due to the vaporisation of sylvite, with KCl amongst the most stable gas-phase alkali containing species,<sup>1</sup> however, some of the potassium is still retained in the ashes.<sup>56</sup> STA studies imply that this is a result of the reaction of  $K_2CO_3$  with  $SiO_2$ ,<sup>33</sup> with more potassium captured in the bottom ashes in higher silica content straws.<sup>38,50</sup>

Potassium can also influence the combustion and pyrolysis processes, with the onset of devolatilisation and the char burnout phase observed to occur at lower temperatures when even a small amount of potassium is present.<sup>52</sup>

#### **1.4.2.2 Chlorine**

The high chlorine content of wheat straw can cause corrosion on the surface of superheater tubes.<sup>28</sup> Lab-scale studies differ in their observations of the temperature of chlorine loss. Some have noted 25-70% of chlorine to be released at < 500 °C with the remainder above 700 °C.<sup>38</sup> Others have only detected chlorine losses to occur above 770 °C due to the vaporisation of sylvite.<sup>56</sup> Many researchers have highlighted that chlorine, rather than alkali concentration in fuels, can be the limiting factor in controlling the total amount of alkali volatilised by supporting the transfer of alkali to the surface of the fuel.<sup>46</sup>

#### **1.4.2.3 Silicates**

Potassium silicate eutectics formed in the combustion bed can melt or soften at temperatures as low as 700 °C.<sup>1</sup> Ternary silicates, containing a small quantity of sodium, can have liquidus temperatures as low as 540 °C.<sup>40</sup> Equilibrium calculations of the combustion of wheat straw indicate the presence of liquid silicates from 500 - 1200 °C.<sup>40</sup> By studying the solubility of potassium from wheat straw chars at 700 – 900 °C, significant amounts of potassium silicate were hypothesised to be formed above 700 °C.<sup>58</sup> As mentioned previously, these low melting silicates can cause bed agglomeration in FBC or, if present on refractory surfaces, can capture flyash through inertial impaction and sticking, leading to the build-up of deposits.<sup>44</sup>

All of these issues depend on the melting point and evaporation of inorganic species within the solid fuel. Ash fusion tests are therefore frequently used to try and predict the behaviour of biomass ash during combustion.<sup>53</sup> The slagging index, which measures the mass of alkali within the material as a ratio of the calorific value, was developed for coal to predict the risk of problems during combustion of different coals. Levels of  $< 0.17 \text{ kg GJ}^{-1}$  indicate a low slagging risk and levels  $> 0.34 \text{ kg GJ}^{-1}$  indicate that the fuel is virtually certain to cause melting, vaporisation and condensation of deposits on surfaces.<sup>30</sup> High slagging indices are observed in wheat straw samples from around the world (Table 1.2).

### 1.4.3 Reducing fouling and slagging

There are two main methods to resolve the issues caused by the inorganic composition of the fuel. The first is to control the combustion conditions, reducing the furnace exit temperature to below the initial deformation temperature of the ash, this may need to be as low as  $680 \text{ }^\circ\text{C}$  for herbaceous biomass fuels.<sup>54</sup> The alternative is to remove the offending inorganic species, specifically potassium and chlorine, prior to combustion.

Several researchers have studied the leaching of wheat straw with water, by rain washing before harvesting, manual washing after harvesting, or with acid.<sup>2, 44, 59</sup> Typically  $> 80\%$  of the alkali metal and  $> 90\%$  of the chlorine concentration in the initial fuel can be removed with water washing, particularly via complete immersion,<sup>2</sup> with a substantial reduction within 2 minutes.<sup>44</sup> This was found to enormously reduce the release of HCl and KCl during combustion and increase the fusion temperature from  $800 \text{ }^\circ\text{C}$  to a maximum of  $1300 \text{ }^\circ\text{C}$ .<sup>2, 44</sup> Acid washing was found to remove even greater amounts of alkali material.<sup>59</sup> However, some organic material, and its calorific value, was also removed during both water and acid washing.<sup>59</sup> Analysis of the cost effectiveness of reducing the inorganic content of rice straw indicated additional costs were  $\$13 \text{ t}^{-1}$  for rain leached straw collected in the spring or  $\$18 \text{ t}^{-1}$  for industrially leached straw.<sup>60</sup> This compares to the price of wheat straw collected and stored following harvesting which has varied between  $\text{£}37\text{-}73 \text{ t}^{-1}$  in the UK during the past decade.<sup>61</sup>

Jensen *et al* suggested an alternative pretreatment option by studying the pyrolysis of straw at  $550 \text{ }^\circ\text{C}$  followed by char washing.<sup>62, 63</sup> 80-95% of the potassium was released within 120 min, slower than for straw washing, whilst 90% of the chlorine was released

within 20 minutes. However, variations of pyrolysis temperature and time, leaching of other inorganic species or the impacts of leaching on the combustion of the char were not studied.

Despite the research described above, the challenges of the influence of inorganic species on the combustion of herbaceous biomass have yet to be completely solved, and whilst many studies have focused on the combustion processes and gas-phase release of inorganics, few have studied the mineralogical changes occurring within the ashes, and importantly how this impacts on the reutilisation of the inorganic species.

## **1.5 Current uses of residues from thermochemical conversion of biomass**

The large-scale utilisation of wheat straw, and similar biomass materials, in combustion systems will result in the formation of a significant quantity of new waste: biomass fly ash and bottom ash. The valorisation of these waste materials is vital to ensure recovery and reuse of the inorganic species, in line with an elemental sustainability and biorefinery vision, and to add economic value.

The issue of the disposal and utilisation of the ash from biomass combustion has been highlighted as a major issue.<sup>30</sup> In large-scale combustion tests on wheat straw the total ash produced has been found to be as much as 12% by weight of the initial straw, with fly ash making up 28% of the ash.<sup>43</sup> In countries where the utilisation of biomass residues is more developed, particularly in Scandinavia where wood is widely used, the increasing amount of ash residue is leading to the search for utilisation methods other than landfilling.<sup>64</sup>

The most frequently cited alternative applications for biomass ashes are in: 1) agriculture, as a fertiliser or soil amendment; and 2) construction, by partly replacing cement or as an aggregate in road building.<sup>65</sup>

### **1.5.1 Agriculture**

The return of biomass ashes to soils is considered invaluable to reduce fertiliser usage and recycle the nutrients removed with the plant. Nutrients of particular importance are

phosphorus, potassium, magnesium and calcium. Nitrogen is almost totally lost during combustion. However, landfilling is currently the primary disposal method for combustion residues.<sup>66</sup> In the US, currently 90% of ash from the combustion of paper production residues goes to landfill.<sup>67</sup> The overwhelming majority of research on the reutilisation of ash has been carried out on wood ash, particularly in the US, Sweden, Finland and Denmark, specifically to return it to forest soils. This has led to the development of standards for threshold values of components in ash for recycling on forest floors (Table 1.3).<sup>64</sup> Combustion ashes are also considered as potential liming agents to reduce acidity in soils.<sup>68</sup>

The specific mineral and organic content of the ashes formed affects its use, with these varying even between wood species.<sup>67</sup> The mineral content of herbaceous biomass is higher than wood and therefore produces a proportionally larger amount of ash following combustion, and also has a significantly different elemental distribution. However, very little work has studied the changes in nutrient content and availability with combustion conditions from these types of ash, particularly within the UK. Lab-scale studies in Germany have recently shown that rye straw ash can have a beneficial impact on yields of ryegrass and maize.<sup>69</sup> Rape straw ash contains more calcium and has been observed to have a higher liming effect than wheat straw ash.<sup>43</sup> However, the heavy metal concentrations of ashes can cause concern. In Denmark, the limiting concentration for Cd in ashes is  $5.0 \text{ mg kg}^{-1}$ , which has been found to be exceeded in some straw ashes.

### 1.5.2 Construction

The vast quantities of coal fly ash produced have led to the development of its use as a standard additive in concrete as a pozzolan;<sup>70</sup> approximately 6.7 million tonnes of coal fly ash were used in this way in the US in 1994.<sup>71</sup> A pozzolan is a siliceous material that by itself has little or no cementitious property, but will react with calcium hydroxide in the presence of water to form a material with cementing properties.<sup>72</sup> However, fly ash from biomass doesn't meet the current standards,<sup>70</sup> due to the high alkali and chloride concentrations and lower alumina levels in the ashes.<sup>65</sup> Therefore, further research is required to study the use of biomass ashes for this application and others. Researchers have found that several agricultural waste ashes are suitable for use as a component of

**Table 1.3: Recommendations of the Swedish Forest Agency on threshold values for constituents in ash aimed for recycling on forest soils (Data from Ref 64)**

	Minimum	Maximum
<b>Macronutrients</b>		
<b>(% ash db)</b>		
Ca	12.5	
Mg	1.5	
K	3.0	
P	0.7	
<b>Micronutrients</b>		
<b>(mgkg<sup>-1</sup> db)</b>		
B		800
Cu		400
Zn	500	7000
As		30
Pb		300
Cd		30
Cr		100
Hg		3
Ni		70
V		70

concrete including rice husk ash,<sup>73</sup> sugarcane ash,<sup>74</sup> palm oil fuel ash,<sup>75</sup> and wheat ash.<sup>76</sup> However, most of these studies were carried out on ashes produced at the lab-scale, combusted at lower temperature than normally used in power plants and did not study the effects of a range of parameters.

Olive and bone meal ash have also been used to make fire-resistant lightweight construction boards and clay bricks in combinations with other materials,<sup>65, 77</sup> and several biomass ashes have been shown to be effective adsorbents for the removal of dyes from waste streams on a lab scale.<sup>71, 78, 79</sup>

This highlights several potential opportunities for the utilisation of wheat straw and other agricultural ashes. However, no studies have investigated the full impacts of combustion conditions on the physical, chemical and textural changes occurring during the combustion of wheat straw and how these affect, influence and direct the applications of

the unique waste ashes formed. In addition, most studies have focused on the utilisation of fly ashes and not approached utilisation from a holistic viewpoint. The inorganic composition of the waste ashes should be the starting point for directing the potential applications, with silicon and potassium the most abundant elements in wheat straw ash (Table 1.2).

## 1.6 Silica from biomass

### 1.6.1 Silicon's presence in biomass

Silicon is one of the most abundant minerals present in plant tissues.<sup>80</sup> Within soil, silicon is mostly found in the form of insoluble crystalline silica and silicates with soluble silicic acid present at around 0.1 - 2.0 mM.<sup>81</sup> The conversion of silicon in the soil to deposited silica within plant tissues is an incredibly efficient, though little understood, process and there is currently very little utilisation of this vast resource. As Currie and Perry eloquently express:<sup>82</sup>

*“Plants, diatoms and sponges are capable of accumulating, storing and processing Si to create ornate hierarchical patterned biosilicas. The production of silica by organisms is carried out in an aqueous environment from under-saturated solutions of silicic acid, at atmospheric pressure and with temperatures ranging between 4 and 40 °C, and this production, amounting to gigatons per annum, vastly outweighs that produced industrially.”*

The ability of plants to accumulate silica to a higher concentration than that of the soluble silica in the soil is not uniform throughout the plant kingdom and neither are the silica structures formed and the location of them within the plant.<sup>81</sup> Silica accumulation ability appears to be highly dependent on the high-level phylogenetic position of the plant, with this ability mainly present in primitive land plants and monocot angiosperms, particularly the family *Poaceae*, also known as grasses.<sup>80</sup> This family includes the major agricultural species such as rice, wheat and other important plants such as bamboo. Studies have shown that of various different grass species, uptake of silicon from a solution of silicic acid is in the order rice >> wheat > triticale > sorghum > rye > maize > barley.<sup>83</sup> In these plants, silicon is actively taken up by the roots in the form of silicic acid, although efflux

and influx transporter genes have so far only been identified for rice.<sup>84, 85</sup> Once in the root, the silicic acid is transported to the xylem and then to the shoot, stem and leaves by the transpiration stream, where it becomes concentrated due to evaporation and polymerisation and is deposited as a thin layer of amorphous silica in the cell walls below the cuticle layer.<sup>86, 87</sup> The effect of the strong pull of the transpiration stream is that the silicon concentration is higher in older tissues, leaves and the shoot than in the stem (Table 1.4).<sup>88</sup>

**Table 1.4: Percentage of silica found in different parts of the wheat plant.<sup>88</sup>**

Wheat organ	SiO <sub>2</sub> (%)
Culm/stem	1.5 ± 0.2
Leaf sheath	5.8 ± 0.9
Leaf blade	5.7 ± 1.4
Rachis	1.1
Influorescence	3.8 ± 0.9
Bulk	2.3 ± 0.3

Although silicon is not classified as an essential mineral for plants, except for certain algae and *Equisetaceae*,<sup>89</sup> benefits due to the presence of Si include: increased resistance to chemical (high levels of salt or toxic metals) and physical stresses (drought and high temperature);<sup>89</sup> added strength and stiffness of the stems and leaf blades thereby increasing light interception;<sup>90</sup> and increased pest and fungal resistance.<sup>85</sup> This has led to the utilisation of silicon fertilisers for sugarcane and rice, which show decreased yields when silicon accumulation is low.<sup>86, 90</sup>

The relative Si shoot concentrations vary across different agricultural and energy crops (Table 1.5).<sup>80</sup> Of the species cultivated in the UK, miscanthus and wheat display the highest uptake of silica.

**Table 1.5: Relative silica concentration in the shoots of several agricultural and energy crops.<sup>80</sup>**

Species	Common name	Mean relative shoot Si concentration
<i>Oryza sativa</i>	Rice	4.12
<i>Equisetum arvense</i>	Horsetail	3.99
<i>Miscanthus sinensis</i>	Miscanthus / Elephant grass	2.86
<i>Triticum aestivum</i>	Wheat	2.46
<i>Panicum virgatum</i>	Switchgrass	2.01
<i>Hordeum vulgare</i>	Barley	1.82
<i>Quercus robur</i>	English oak	1.54
<i>Saccharum officinarum</i>	Sugarcane	1.51
<i>Avena sativa</i>	Oat	1.51
<i>Secale cereal</i>	Rye	1.26
<i>Brassica napus</i>	Oilseed rape	-0.12

### 1.6.2 Composition and inorganic distribution

The levels of silica in shoot concentrations are matched by the concentration of silica in the biomass following harvest (Table 1.2): *Poaceae* species contain the highest concentrations; oilseed rape, of the *Brassicaceae* family, has a particularly low level.

Potassium is generally also present at high levels, and at a much higher level than sodium. This results in a varying  $\text{SiO}_2:\text{K}_2\text{O}$  molar ratio for each different biomass source, both between different species and from different studies of the same species (Table 1.6). The results for wheat straw show a ratio generally in the range of commercially produced alkali silicates. Where they are not, this is probably due to the loss of potassium by rain leaching prior to harvesting.<sup>91</sup> This data indicates the potential for the production of alkali silicates from the ashes of these biomass materials using only the inherent inorganic species. The variability in the elemental composition within the same species in different studies highlights the dependence of the mineral content of the plant on many other factors. This underpins the need for any technology that is developed to utilise biomass sources to be extremely robust to variations in the source materials. However, the wide variation of the ratio of silica and alkali minerals in different biomass ashes could

potentially allow a degree of controllability to the molar ratio of the final silicate solution formed.

**Table 1.6: Main element concentrations of initial dry biomass and silica:alkali ratios.**

	SiO <sub>2</sub> (%)	K <sub>2</sub> O (%)	SiO <sub>2</sub> :K <sub>2</sub> O (wt)	Cl (%)	CaO (%)	Ref
Wheat straw	4.6	2.4	1.9	1.9	0.6	2
Wheat straw	3.7	1.7	2.1	0.5	0.8	32
Wheat (Marius)	3.6	1.0	3.8	0.2	0.3	33
Wheat Denmark 2001	3.2	0.7	4.8	0.1	0.4	33
Wheat (Soisson) Spain	3.2	0.4	7.1	0.1	0.5	33
Wheat Denmark 2000	1.7	1.4	1.2	0.2	0.5	33
Winter barley	1.7	2.8	0.6	0.5	0.5	33
Spring barley	2.1	1.0	2.1	0.1	0.7	33
Oat straw	0.6	0.7	0.9	0.03	1.0	33
Rape straw	0.1	0.4	0.2	0.01	1.3	33
Rice straw	15.1	2.5	6.1	0.8	0.4	2
Sugarcane bagasse	3.6	0.3	14.4	0.009	0.2	2
Switchgrass	2.4	0.4	5.4	0.004	0.2	2
Wood fuel	1.7	0.1	26.4	0.1	0.3	2
Macroalgae ( <i>Laminara digitata</i> )	0.1	3.8	0.03	-	1.3	34
Eastern Kentucky Coal	3.9	0.1	39.7	0.2	0.1	35

## 1.7 Alkali silicates – chemistry and uses

Alkali silicates have been known since the seventeenth century and by 1855 were being manufactured commercially.<sup>92</sup> However, many aspects of alkali silicates are still not well understood, in particular regarding their structure and reactivity in solution. Nevertheless, alkali silicates do have several known chemical and physical properties that make them useful to study as a potential binder for lignocellulosic systems, with silicate solutions having been utilised as adhesives in many applications.

### 1.7.1 Alkali silicates

Alkali silicates are solutions or solids of silicate anions and alkali metal cations. These systems can be expressed as M<sub>2</sub>SiO<sub>3</sub> but are more usually defined by the molar ratio or

$x\text{SiO}_2:\text{M}_2\text{O}$ , where  $\text{M} = \text{Li}, \text{Na}$  or  $\text{K}$ . It is this molar ratio together with the solids concentration in solution and the alkali metal used that defines the physical and chemical properties of the alkali silicate system. Since the molar ratio and solids concentration is highly variable and can be controlled, this produces a system with a wide variety of applications.

## 1.7.2 Structure of alkali silicates

A wide variety of different silicate structures are formed in solution. Evidence indicates that the species are all compact and tetrahedrally co-ordinated with many similar species in dynamic equilibrium.<sup>93</sup> The condensation processes that occur to form polymeric species are still not fully understood and are of particular interest for researchers understanding sol-gel chemistry and zeolite synthesis.<sup>94</sup> Condensation is generally believed to be catalysed by hydroxyl ions from both theoretical and experimental studies.<sup>92, 95, 96</sup> The mechanism suggested involves deprotonation by a hydroxyl ion followed by a two-step condensation reaction with silicic acid via a five-coordinate reaction intermediate stabilised by three strong hydrogen bonds, followed by loss of water (Figure 1.5).<sup>95</sup> The anionic species formed may be charge stabilised by an alkali cation. Computer modelling is increasingly being used to try and understand the reactions that may be occurring due to the complexity of the different species present and the difficulty of accurately gathering thermodynamic information for individual species using experimental methods.

### 1.7.2.1 Analysis by $^{29}\text{Si}$ NMR

The specific species that are formed in solution and during polymerisation under different conditions are also still not well understood. A  $\text{Q}^i$  description was developed by Engelhardt *et al* to describe the connectivity of silicon atoms and help identification by  $^{29}\text{Si}$  NMR.<sup>97</sup>  $\text{Q}^0$  represents silicate structures in which the silicon atom is not connected to any other silicon atoms through an oxygen bridge (monomeric species), whilst  $\text{Q}^4$  denotes a silicon atom that is connected to four other silicon atoms at each tetrahedral linkage (Figure 1.6).  $^{29}\text{Si}$  NMR peaks have been assigned to the different  $\text{Q}^i$  species in solution (Table 1.7).<sup>98</sup>

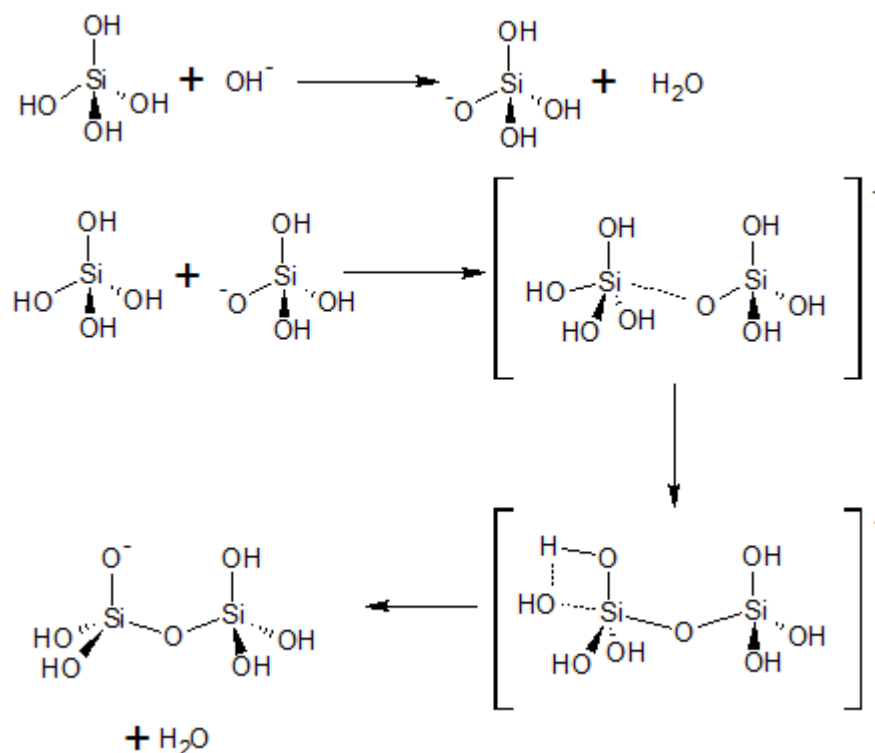


Figure 1.5: Proposed mechanism for the condensation of silicic acid<sup>95</sup>

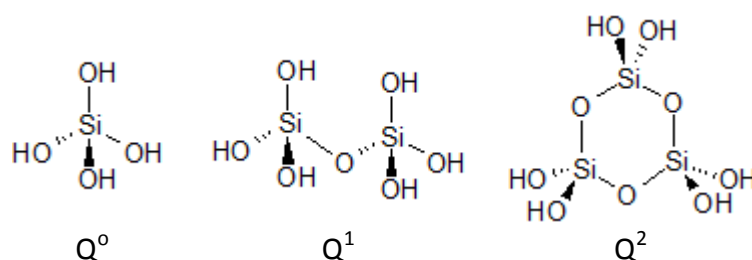
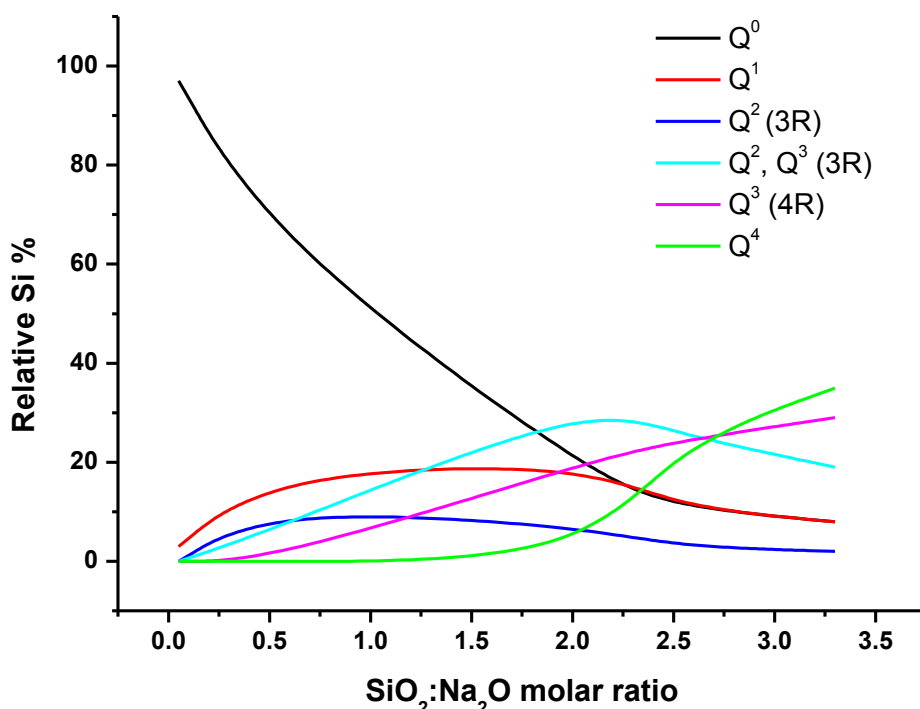


Figure 1.6: The structure of a few species identified in silicate solutions by <sup>29</sup>Si NMR

Table 1.7: Assigned <sup>29</sup>Si NMR shifts for silicate species with different connectivities in solution (with respect to tetramethylsilane)<sup>98</sup>

Q <sup>i</sup> connectivity	-δ(ppm)
Q <sup>0</sup>	~ 72
Q <sup>1</sup>	~ 79
Q <sup>2</sup> <sub>(3R)</sub> (cyclic trimer)	~ 82
Q <sup>2</sup> <sub>(4R)</sub> and Q <sup>3</sup> <sub>(3R)</sub> (three ring)	~ 87 – 92
Q <sup>3</sup> <sub>(4R)</sub> (four ring)	~ 96 – 98
Q <sup>4</sup>	~ 108 (broad)

Identifying specific species in solution using  $^{29}\text{Si}$  NMR is made difficult due to the presence of many similar species in dynamic equilibrium and due to the low abundance of  $^{29}\text{Si}$  which prevents the visibility of  $^{29}\text{Si}$ - $^{29}\text{Si}$  coupling.<sup>93</sup> Greater success has been achieved by studying the changes in the integrated band intensities of the different  $Q^i$  peaks with changing silicon concentration,<sup>99</sup> cation type,<sup>98</sup> pH,<sup>100</sup> and molar ratio (Figure 1.7).<sup>99, 101, 102</sup> These indicate that at a pH above  $\sim 10.7$  and as solutions become more siliceous, more complex polymeric species,  $Q^3$  and  $Q^4$ , are formed at the expense of the monomer and dimer.<sup>102</sup> It is also noticeable that cyclic species are favourably formed during condensation processes. In addition, it has been found that decreasing the concentration of the solution decreases the degree of polymerisation and vice versa.<sup>98</sup>



**Figure 1.7: Changes in silicate species distribution with changing  $\text{SiO}_2:\text{Na}_2\text{O}$  molar ratio at a  $\text{SiO}_2$  concentration of 0.4 M. (Data from Ref 99)**

### 1.7.2.2 Analysis by infrared

Although  $^{29}\text{Si}$  NMR can provide extremely useful, detailed and quantitative information about silicate solutions, other researchers have used cheaper and less time intensive techniques, such as infrared (IR) spectroscopy, to gain an understanding of silicate solutions. IR can enable the characterisation of silicate solutions, albeit at a much lower resolution and with some controversy remaining around assignments of bands to specific vibrational modes.<sup>103, 104</sup>

The main infrared absorption bands of alkali silicates are observed between 1250 and 700  $\text{cm}^{-1}$  with a strong broad band due to asymmetric Si-O-Si stretching vibrations, usually centred around 1000  $\text{cm}^{-1}$ . Bass and Turner have correlated the changes in silicate speciation observed by  $^{29}\text{Si}$  NMR with the changing peak structure observed in the IR spectra by deconvolution (Table 1.8).<sup>99</sup> They suggest that higher wavenumber sections of the band correspond to more complex anionic species. They then observe that as the molar ratio decreases the high frequency edge of the band shifts to lower frequency, suggesting a reduction in the complexity of the anionic species present. Bands in the range 950-1020  $\text{cm}^{-1}$  appear to more sensitive to the local silicate environment.<sup>105</sup> However, band assignment was undertaken by comparing low concentration solutions due to better resolution of the  $^{29}\text{Si}$  NMR peaks at 0.4 M concentrations.

**Table 1.8: Bass and Turner's assignments of components of main sodium silicate infrared band to different silicate anion types.<sup>99</sup>**

Assignment	Wavenumber ( $\text{cm}^{-1}$ )
SiO- small anions	850-900
Monomer + dimer	910-950
Linear $\text{Q}^1$	965-985, 995-1005
$\text{SiO}^-$ cyclic anions	1010-1020
$\text{Q}^2_{(3\text{R})}$ rings	1020-1050
$\text{Q}^3_{(3\text{R})}$ , $\text{Q}^2_{(4\text{R})}$ rings, linear $\text{Q}^2$	1030-1070
$\text{Q}^3_{(4\text{R})}$ rings	1050-1120
Polymer	1100-1300

Osswald and Fehr attempted to assign IR bands of concentrated potassium silicate solutions based on a comparison with IR studies of silica gels.<sup>106</sup> They correlated the shift of the frequency of the main band to the presence of surface Si-O-K groups, weakening neighbouring Si-O-Si bonds, and the high frequency shoulder of the main band to the situation where neighbouring oxygen atoms asymmetrically vibrate 180° out of phase with each other, rather than to the presence of more highly polymerised species.<sup>107</sup> Halasz *et al* tried to distinguish between bands related to monomeric and polymeric silicate species by using aqueous solutions of  $\text{Na}_2\text{SiO}_3$ , which almost exclusively contain monosilicate ions at pH's > 10.<sup>104</sup> Their aqueous ATR FTIR spectra showed broad bands, without a high frequency shoulder, that shifted to lower wavenumbers with increasing

concentration or increasing alkali content, which they related to the degree of dissociation in the solution.

### **1.7.3 Setting processes**

The chemical and physical properties of alkali silicates vary depending on their molar ratio and solids concentration. Of particular interest with respect to this project are the properties relating to the use of alkali silicates as a binder. There are three setting reactions that alkali silicates can undergo, which each impart different characteristics on the final material. In addition, compatibility with the substrate material must be considered, with the solutions performing most effectively on hydrophilic, non-oily surfaces, where they can achieve proper wetting and, hence, maximum adhesion.

#### **1.7.3.1 Dehydration**

Viscosity increases rapidly as moisture is removed and more rapidly for higher ratio silicate solutions.<sup>108</sup> The glassy nature of the bond formed imparts strength and rigidity, however, the insolubility of the bond is dependent on the ambient temperature and humidity.<sup>109</sup> Heating to around 250 °C is required to cross-link the silicate species and impart a high moisture resistance.<sup>110</sup>

#### **1.7.3.2 Precipitation**

Soluble silicates react almost instantly with multivalent metal cations such as  $\text{Ca}^{2+}$  and  $\text{Mg}^{2+}$  to form either insoluble metal silicate networks or hydrated silica with adsorbed metal oxides or hydroxides.<sup>108</sup> This mechanism is used to form pigments and surface coatings.

#### **1.7.3.3 Gelation**

Silicate solutions are stable to condensation above pH  $\sim 10.7$ , due to the presence of repulsive highly charged anionic silicate species or stabilised ion-paired species.<sup>92</sup> As the pH decreases fewer silicate anions are supported in solution, and the polymerisation of these species occurs with the expulsion of water due to a reduction in electrostatic repulsive forces.<sup>111</sup> There are three stages recognised in the polymerisation process:<sup>92</sup>

1. Polymerisation of the monomer to form small particles

2. Growth of particles
3. Linking of particles into chains and then networks which extend through the solution, thickening it to a gel.

The extent of polymerisation is dependent on the solids concentration, salt content, the temperature and the pH of gelation. In general, the rate of gelation increases as the pH decreases to a maximum at pH 6-7.<sup>92</sup> Initially small polymerised species are formed, maximising the number of internal siloxane bonds and minimising the number of surface silanol groups. The resulting small particles are the nuclei for larger particles which form the backbone of the silica gel. A dynamic equilibrium is present in which smaller more soluble particles dissolve releasing silica which can react with the nucleating particles resulting in growth of the particles in a process known as Ostwald ripening.<sup>92</sup> The main driving force for this is the reduction in surface free energy. Both simultaneously with and following particle growth, aggregation of the particles may occur dependent on diffusion rates and electrostatic forces between the particles until a gel network is formed. During this process the gel continues on a macroscopic scale to have the same concentration of silica and water as the surrounding sol. However, if coagulants, such as polyvalent metal ions or substantial amounts of salts are present, a white precipitate or opaque gel will be formed.

The bond formed via gelation is usually not as strong as that caused by dehydration but can have a higher degree of water resistance.<sup>112</sup> A wide variety of different setting agents are available that can be used to induce gelation by reducing the pH of the solution. For controlled gelation a chemical that will be hydrolysed over time to induce acidity is often used.<sup>109</sup> For binding purposes a higher ratio silicate solution is often particularly valuable since less additional chemical is required to neutralise the solution to a pH below 10.7 and begin to induce gelation.

## **1.8 Utilising silica from biomass**

Sodium silicate is generally formed by the fusing of sand ( $\text{SiO}_2$ ) with sodium carbonate or 'soda ash' at around 1100-1200 °C. The resulting glass is then dissolved using high pressure steam.<sup>92</sup> A large amount of energy is used during this process and there are environmental issues associated with the extraction of sand from mining or dredging, as

well as the release of CO<sub>2</sub> due to carbonate decomposition. It is only in the past few years that the extraction and use of silicon present in biomass has seriously been considered. The main resource studied has been rice husk ash (RHA) due its high content of relatively pure silica.

### 1.8.1 Dissolution of silica

Silica can either be dissolved by strong alkaline solutions or by HF. In alkaline solutions, the reaction that is occurring during dissolution is essentially depolymerisation, the reverse of the polymerisation reaction described in section 1.7.2. This reaction is also catalysed by hydroxyl ions which can react with silica to form a five co-ordinate centre, thereby weakening the other oxygen linking bonds. The rate at which dissolution occurs depends on the ability of the hydroxyl ion to catalyse this reaction, particularly the silica structure and the pH of the solution. At atmospheric pressure, the main crystalline silica phases formed are quartz, tridymite, cristobalite, with the transformation between them fully reversibly if the temperature change is slow (Figure 1.8).<sup>92</sup> The structures of tridymite, cristobalite and silica melts (glass) will be preserved at low temperatures if they are quickly cooled beyond their transition temperature. Interestingly, as silica glass is heated it is transformed directly to  $\beta$ -cristobalite rather than quartz.<sup>92</sup> Amorphous unstructured silicas, including glass, opal and biogenic silica, have much greater dissolution rates than the crystalline phases due to the openness of the structure, enabling greater access to hydroxyl ions.<sup>92</sup> The dissolution rate and maximum saturation level for all silica phases increases with increasing alkalinity, particularly above a pH of 9, due to the increasing presence of silicate ions influencing the silica saturation equilibrium, with the rate of dissolution correlated to the density of the material.<sup>113</sup> The dissolution rate and total solubility are also affected by surface area,<sup>113</sup> temperature and pressure.<sup>114</sup>

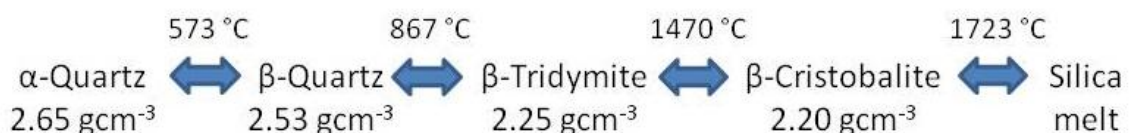


**Figure 1.8: Silica phase transformations**

### 1.8.2 Silica from Rice Hull Ashes (RHAs)

Most silica in biomass is thought to exist in inorganic linkages as amorphous silica. X-ray diffraction studies and solid state  $^{29}\text{Si}$  NMR have identified amorphous silica in rice hull ashes (RHAs) up to 800 °C, with cristobalite and tridymite phases present at higher temperatures.<sup>72</sup> Therefore, generally extraction of silica from RHAs uses material combusted, gasified or pyrolysed below 800 °C. By boiling RHAs in 1M NaOH for 1 h, Kalapathy *et al* demonstrated that 91% of the silica present could be extracted.<sup>115</sup> This methodology is now being used by AgriTec Systems to produce sodium silicate solutions from gasified rice hulls with a high value activated carbon co-product.<sup>116</sup> It has also been used to study the production of silicate thermal insulation material and the formation of flexible silicate films from RHAs.<sup>117, 118</sup>

By purely heating RHAs to 700 °C for 6 h, Della *et al* found that they could produce a material that contained 95% amorphous silica with a surface area of 54 – 81 m<sup>2</sup> g<sup>-1</sup>.<sup>119</sup> This method was also used by Rodrigues to create a pozzolanic material for cement production.<sup>120</sup>

Silica has also been formed from rice hulls, rice straw and wheat straw by chemical pulping of the material with H<sub>2</sub>SO<sub>4</sub> followed by combustion of the residue at 500 °C. The materials formed contained 99% SiO<sub>2</sub> and had BET surface areas ranging from 186 – 291 m<sup>2</sup> g<sup>-1</sup>.<sup>121</sup> The only other studies that have examined the utilisation of silica in wheat residues have investigated, briefly, the use of ashes as an additive in cement production and for the formation of autoclaved mortar.<sup>76, 122, 123</sup>

These studies found that wheat straw ash (WSA) or wheat hull ash can produce a pozzolanic material. However, once again these studies have not looked at the utilisation of WSA from a holistic and elemental sustainability perspective, understanding the interaction of all inorganic species and their use during combustion or other thermochemical processes. Specifically, the formation of alkali silicates utilising the inherent inorganic species has not been explored.

## 1.9 Composite materials

Alkali silicates have been utilised as adhesives in many applications including cardboard packaging and foil laminate.<sup>110</sup> However, the use of alkali silicates in composite materials would be a novel application, particularly via the use of waste ash. There are additionally further environmental imperatives for the development of new binders.

Wood based panels are an ubiquitous part of office and home design with just over 6 million  $\text{m}^3 \text{y}^{-1}$  used in the UK every year (Figure 1.9a).<sup>124</sup> The major types used are plywood, MDF and particleboard, with only the latter two produced in the UK (Figure 1.9b). These two materials are, therefore, most relevant to this study.

Particleboard has been defined as a “sheet material manufactured from small pieces of wood or other ligno-cellulosic materials (e.g. chips, flakes, splinters, strands, shreds etc.) agglomerated by use of an organic binder together with one or more of the following agents: heat, pressure, humidity, a catalyst, etc”.<sup>124</sup> MDF is defined as a “type of fibreboard with a density exceeding  $0.50 \text{ g cm}^{-3}$  but not exceeding  $0.80 \text{ g cm}^{-3}$ ”.<sup>124</sup> Fibreboard is “a panel manufactured from fibres of wood or other lignocellulosic materials with the primary bond deriving from the felting of the fibres and their inherent adhesive properties. Bonding materials and/or additives may be added. It is usually flat pressed but may also be moulded.”<sup>124</sup>

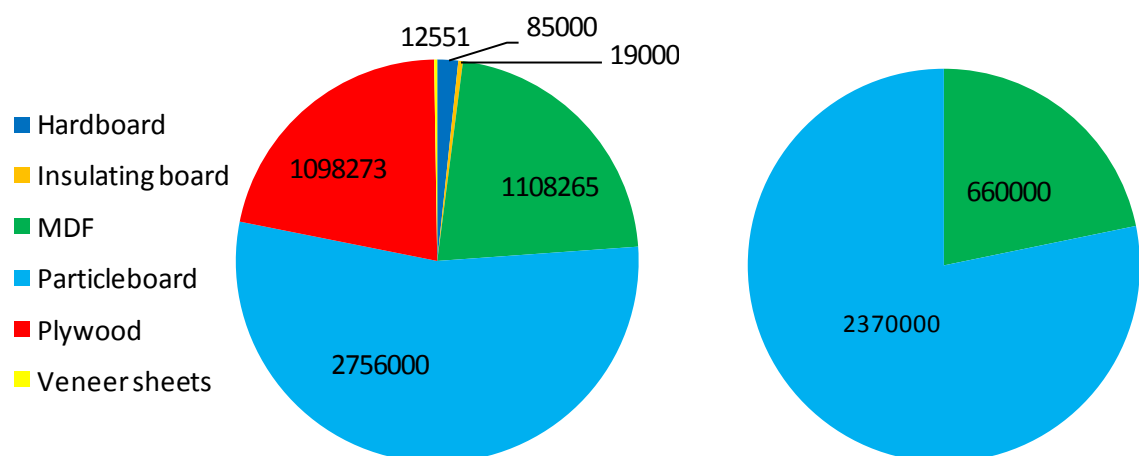


**Figure 1.9: Volume ( $\text{m}^3$ ) of wood-based panelling (a) used in the UK in 2009 and (b) produced in the UK in 2009 (Data from Ref 124) (Originally in colour)**

The manufacturing methods for MDF and particleboard are shown in Figure 1.10. Although the overall processes are similar for both products, the manufacturing process for MDF requires the production of fine fibres prior to pressing.

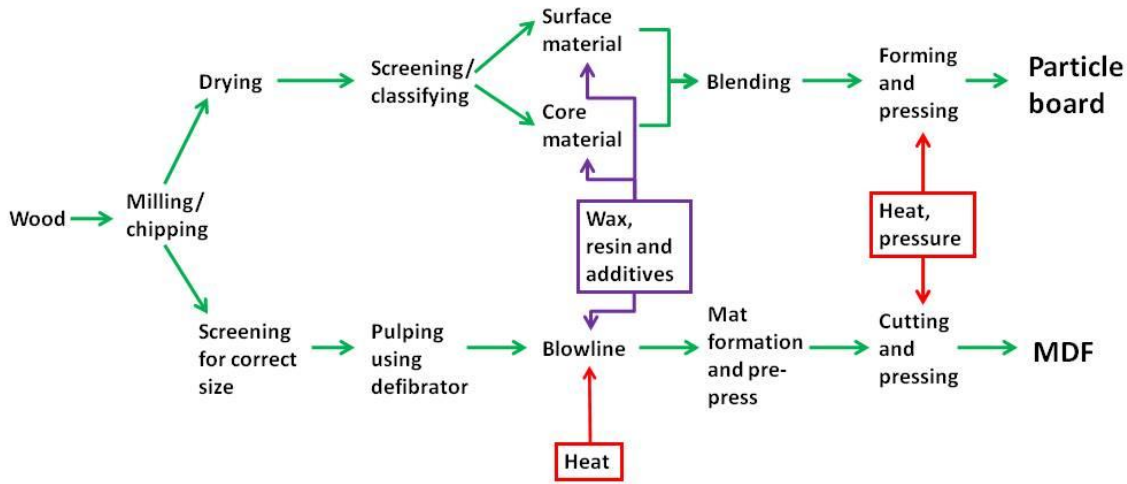


Figure 1.10: Main steps in the manufacture of particle board and MDF (Originally in colour)

### 1.9.1 Environmental impacts and challenges

There are three major environmental issues related to the current manufacture of these lignocellulosic construction materials: the binder; the use of wood as the substrate; and inefficiencies in the manufacturing process.

Urea formaldehyde (UF) is used as the binder for over 90% of particleboard and is also the main binder for many other wood-based panels due to the strong bonds formed at low cost.<sup>125</sup> However, formaldehyde has been classified as a ‘probable carcinogen’ by the International Agency for Research on Cancer,<sup>126</sup> is linked to eye, nose and respiratory irritation and can cause contact dermatitis,<sup>127</sup> thereby posing a significant health risk to people working in the composite board manufacturing industry. In addition, formaldehyde emissions continue to be released following manufacture due to the presence of free formaldehyde,<sup>125</sup> which has resulted in many countries applying stringent limits on formaldehyde release from composite boards.<sup>128</sup> Urea formaldehyde is also manufactured from fossil fuel sources.<sup>129</sup> With around 10% of urea formaldehyde

present in particleboard by weight,<sup>125</sup> and a higher content in MDF,<sup>130</sup> the production of boards worldwide puts pressure on the dwindling fossil fuel resources.

Currently, both particleboard and MDF are overwhelmingly made from wood-based material, usually waste from sawmills, although some virgin wood is used. However, with an estimated increase of MDF production of 4% year-on-year from 2006-2010 in Europe,<sup>131</sup> competition from other products for the same raw material and environmental imperatives to reduce virgin wood consumption, the demand for non-wood lignocellulosic substrates will increase.

### 1.9.2 Alternative resins

Due to these challenges with conventional production, many researchers have been searching for alternative binders or production methods. Melamine modified urea formaldehyde,<sup>132</sup> phenol formaldehyde,<sup>133</sup> and methylenediphenyl isocyanate all show reduced formaldehyde emissions. However, similar concerns remain as for UF since they are fossil-fuel derived and often require corrosive or irritating starting materials.

In search of sustainable alternatives, other researchers have looked to renewable binders based on for instance soy flour,<sup>134</sup> forest-floor biomass (depolymerised lignin),<sup>126</sup> cashew nut shell liquid,<sup>135</sup> and sugarcane bagasse lignin.<sup>136</sup> Mostly these are phenolic substitutes, although they usually cannot entirely replace the fossil fuel phenol source. An alternative approach is to eradicate the need for binders altogether. High strength-high density low cost binderless boards have been formed from coconut husk via the melting of the high lignin content pith residue binding the coir fibres.<sup>137</sup>

Wood-plastic composites are a relatively new material based on a combination of a lignocellulosic substrate with either virgin or recycled thermosetting plastics.<sup>138</sup> However, around 40-50% of the composite by weight needs to be the thermoplastic in order to achieve good tensile and flexural strength, with these properties still worse than that of commercial MDF and particleboard.<sup>139</sup>

Inorganic composites that are highly resistant to fire and insects have been developed using gypsum and Portland Cement.<sup>140</sup> These boards usually contain between 10-70wt%

wood particles and consequentially require 30-90wt% binder due to the high viscosity of the inorganic binders.<sup>140, 141</sup> They can also require long cure times, although they are often set at ambient conditions. Research using potassium aluminosilicate as an alternative binder showed that with 70% binder by weight and curing at ambient temperature and pressure, highly fire-resistant materials could be formed.<sup>142</sup>

### **1.9.3 Alternative substrates**

In the past two decades interest in using alternative lignocellulosic material to replace wood-derived substrates has increased. The main focus of interest has been on the use of wheat straw for particleboards, but other alternatives are now beginning to be studied including cornstalks, corncobs,<sup>139</sup> Scottish pine needles,<sup>143</sup> and even aubergine stalks,<sup>144</sup> dependent on the particular renewable resources available locally. The composition and surface properties of these materials can be very different to wood, for instance straw has a very waxy surface.<sup>3</sup> This can affect the binding of the substrate with the adhesive, so requiring additional research and development to produce boards with the same properties as traditional wood-based particleboard and MDF.

### **1.10 Project vision and thesis content**

This project aims to draw together the different themes discussed above by approaching the study of the inorganic species within wheat straw and other biomass materials from a holistic perspective. This requires the study of the interrelation and interaction of all species during combustion and other treatment processes and how that can lead to recommendations and directions for the reutilisation of the inorganic species to ensure elemental sustainability. There is a particular focus on silica as it is the main inorganic species within wheat straw and has been relatively unstudied. In addition, there is a central motivation to study whether the hypothesised production of alkali silicates from biomass ashes and their utilisation as a novel inorganic binder for composite board manufacture is feasible. The latter process is significantly different from other attempts to produce inorganic composite boards, with the aspiration of utilising low levels of binder, similar to the concentrations of organic binders currently used for MDF production, whilst utilising only waste and renewable feedstocks throughout. This thesis therefore covers four main areas:

1. The lab-scale combustion of wheat straw and the impacts of wheat straw variety, year and combustion conditions on the mineralogical, chemical and textural properties of combustion residues.
2. The pretreatment of wheat straw by organic solvent, supercritical CO<sub>2</sub>, water and acid and the impacts on the mineralogical and chemical properties of the combustion residues.
3. The lab-scale pyrolysis of wheat straw and the impacts on the mineralogical and chemical properties of the chars, and the impacts of inorganic removal on the combustion properties of chars.
4. The utilisation of combustion residues – fly ash and bottom ash – from commercial biomass facilities. The analysis of their composition, extraction and utilisation for the formation of alkali silicate binders for inorganic composite boards.

### **1.11 References for Chapter 1**

1. L. L. Baxter, T. R. Miles, T. R. Miles, B. M. Jenkins, T. Milne, D. Dayton, R. W. Bryers and L. L. Oden, *Fuel Process. Technol.*, 1998, 54, 47-78.
2. D. C. Dayton, B. M. Jenkins, S. Q. Turn, R. R. Bakker, R. B. Williams, D. Belle-Oudry and L. M. Hill, *Energ. Fuel.*, 1999, 13, 860-870.
3. F. E. I. Deswarte, J. H. Clark, J. J. E. Hardy and P. M. Rose, *Green Chem.*, 2006, 8, 39-42.
4. United Nations, Report of the World Commission on Environment and Development, General Assembly Resolution 42/187, 11 December 1987.
5. Energy Information Administration, Short-Term Energy Outlook—January 2011, [http://www.eia.doe.gov/steo/steo\\_full.pdf](http://www.eia.doe.gov/steo/steo_full.pdf), Accessed 17/01/10.
6. R. L. Hirsch, R. Bezdek and R. Wendling, *Peaking of World Oil Production: Impacts, Mitigating and Risk Management*, Science Applications International Corporation, 2005.
7. P. Anastas and J. Warner, *Green Chemistry: Theory and Practice*, Oxford University Press, Oxford, 1998.
8. Intergovernmental Panel on Climate Change, IPCC Fourth Assessment Report (AR4): The AR4 Synthesis Report, 17 November 2007.
9. S. Smith, Postnote No. 295: Climate Change Science, Parliamentary Office of Science and Technology, 2007.
10. D. Cohen, *New Scientist*, 2007.
11. C. A. DiFrancesco, M. W. George, J. F. Carlin Jr. and A. C. Tolcin, *Indium Statistics*, U.S. Geological Survey, 2010.
12. S. M. Jasinski, *Potash: Mineral Commodities Summary*, U.S. Geological Survey, January 2010.
13. P. Anastas and P. Tundo, *Green Chemistry: Challenging Perspectives.*, Oxford University Press, Oxford, 2000.
14. Great Britain, *Climate Change Act 2008: Elizabeth II, Chapter 27*, The Stationary Office, London, 2008.
15. European Parliament, *Promotion of the use of energy from renewable sources*, 2009/28/EC, 2009.

16. Department of Energy & Climate Change, 2008 final UK greenhouse gas emissions: data tables, London, 14 April 2010.
17. Department for Environment Food and Rural Affairs, UK Biomass Strategy, 2007.
18. Department of Energy & Climate Change, The UK Renewable Energy Strategy 2009, 2009.
19. L. Evans, S. Okamura, J. Poll and N. Barker, Evaluation of Opportunities for Converting Indigenous UK Wastes to Fuels and Energy, AEA report for the NNFFCC, July 2009.
20. G. Evans and L. Nattrass, Advanced Thermochemical Biofuels Roadmap and Challenge, NNFFCC Project 09/014, NNFFCC, York, 2009.
21. E4tech, Biomass supply curves for the UK, For DECC, March 2009.
22. A. J. Houghton, A. J. Bond, A. A. Lovett, T. Dockerty, G. Sünnerberg, S. J. Clark, D. A. Bohan, R. B. Sage, M. D. Mallott, V. E. Mallott, M. D. Cunningham, A. B. Riche, I. F. Shield, J. W. Finch, M. M. Turner and A. Karp, *J. Appl. Ecol.*, 2009, 46, 315–322.
23. E. M. W. Smeets, A. P. C. Faaij, I. M. Lewandowski and W. C. Turkenburg, *Prog. Energy Combust. Sci.*, 2007, 33, 56-106.
24. International Energy Agency, Key World Energy Statistics 2010, Paris, 2010.
25. J. Copeland and D. Turley, National and Regional Supply/Demand balance for agricultural straw in Great Britain, Central Sciences Laboratory, 2008.
26. A. Barneto, J. Carmona, J. E. Alfonso and L. Alcaide, *Bioresour. Technol.*, 2009, 100, 3963-3973.
27. J. M. Jones, M. Nawaz, L. I. Darvell, A. B. Ross, M. Pourashanian and A. Williams, in *Science in Thermal and Chemical Biomass Conversion*, ed. A. Bridgewater, Blackwell Science Ltd, Oxford, Editon edn., 2006, pp. 331-339.
28. A. Demirbas, *Prog. Energy Combust. Sci.*, 2004, 30, 219-230.
29. A. A. Khan, W. de Jong, P. J. Jansens and H. Spliethoff, *Fuel Process. Technol.*, 2009, 90, 21-50.
30. D. L. Klass, *Biomass for Renewable Energy, Fuels and Chemicals*, Academic Press, California, 1998.
31. J. Werther, M. Saenger, E. U. Hartge, T. Ogada and Z. Siagi, *Prog. Energy Combust. Sci.*, 2000, 26, 1-27.
32. Y. Q. Wu, S. Y. Wu, Y. Li and J. S. Gao, *Energ. Fuel.*, 2009, 23, 5144-5150.
33. S. Arvelakis, P. A. Jensen and M. Dam-Johansen, *Energ. Fuel.*, 2004, 18, 1066-1076.
34. D. Belle-Oudry and D. Dayton, in *Impact of Mineral Impurities in Solid Fuel Combustion*, ed. R. Gupta, Kluwer Academic / Plenum Publishers, New York, Editon edn., 1999, pp. 569-579.
35. A. B. Ross, J. M. Jones, M. L. Kubacki and T. Bridgeman, *Bioresour. Technol.*, 2008, 99, 6494-6504.
36. A. Pettersson, L. E. Amand and B. M. Steenari, *Fuel*, 2009, 88, 1758-1772.
37. C. Yin, L. A. Rosendahl and S. K. Kaer, *Prog. Energy Combust. Sci.*, 2008, 34, 725-754.
38. J. N. Knudsen, P. A. Jensen and K. Dam-Johansen, *Energ. Fuel.*, 2004, 18, 1385-1399.
39. R. P. van der Lans, L. T. Pedersen, A. Jensen, P. Glarborg and K. Dam-Johansen, *Biomass Bioenerg.*, 2000, 19, 199-208.
40. M. Blander and A. D. Pelton, *Biomass Bioenerg.*, 1997, 12, 295-298.
41. I. Obernberger, T. Brunner and G. Barnthaler, *Biomass Bioenerg.*, 2006, 30, 973-982.
42. B. Staiger, S. Unterberger, R. Berger and K. R. G. Hein, *Energy*, 2005, 30, 1429-1438.
43. M. L. Sander and O. Andren, *Water Air Soil Pollut.*, 1997, 93, 93-108.
44. B. M. Jenkins, R. R. Bakker and J. B. Wei, *Biomass Bioenerg.*, 1996, 10, 177-200.
45. B. Olanders and B.-M. Steenari, *Biomass Bioenerg.*, 1995, 8, 105-115.
46. T. R. Miles, T. R. Miles, L. L. Baxter, R. W. Bryers, B. M. Jenkins and L. L. Oden, *Biomass Bioenerg.*, 1996, 10, 125-138.

47. R. Gupta, T. Wall and L. Baxter, *Impact of Mineral Impurities in Solid Fuel Combustion*, Kluwer Academic / Plenum Publishers, New York, 1999.
48. N. O. Knudsen, P. A. Jensen, B. Sander and K. Dam-Johansen, in *Biomass for Energy and Industry*, eds. H. Kopetz, T. Weber, W. Palz, P. Chartier and G. L. Ferrero, *Centrales Agrar Rohstoff Mkt & Entwicklung Netzwerk*, Rimpär, Editon edn., 1998, pp. 224-228.
49. S. Arvelakis, H. Gehrman, M. Beckmann and E. G. Koukios, *J. Therm. Anal. Calorim.*, 2003, 72, 1019-1030.
50. P. Thy, B. M. Jenkins, C. E. Lesher and S. Grundvig, *Fuel Process. Technol.*, 2006, 87, 383-408.
51. D. Vamvuka, S. Troulinos and E. Kastanaki, *Fuel*, 2006, 85, 1763-1771.
52. J. M. Jones, L. I. Darvell, T. G. Bridgeman, M. Pourkashanian and A. Williams, *P. Combust. Inst.*, 2007, 31, 1955-1963.
53. M. J. F. Llorente and J. E. C. Garcia, *Fuel*, 2005, 84, 1893-1900.
54. R. W. Bryers, in *Impact of Mineral Impurities in Solid Fuel Combustion*, eds. R. Gupta, T. Wall and L. Baxter, Kluwer Academic / Plenum Publishers, New York, Editon edn., 1999, pp. 105-131.
55. S. Arvelakis, F. J. Frandsen and K. Dam-Johansen, *J. Therm. Anal. Calorim.*, 2003, 72, 1005-1017.
56. P. Thy, B. M. Jenkins, S. Grundvig, R. Shiraki and C. E. Lesher, *Fuel*, 2006, 85, 783-795.
57. A. Zolin, A. Jensen, P. A. Jensen, F. Frandsen and K. Dam-Johansen, *Energ. Fuel.*, 2001, 15, 1110-1122.
58. P. A. Jensen, F. J. Frandsen, K. Dam-Johansen and B. Sander, *Energ. Fuel.*, 2000, 14, 1280-1285.
59. D. N. Thompson, P. G. Shaw and J. A. Lacey, *Appl. Biochem. Biotechnol.*, 2003, 105, 205-218.
60. R. R. Bakker and B. M. Jenkins, *Biomass Bioenerg.*, 2003, 25, 597-614.
61. Defra, *Commodity Prices: Hay and Straw*, 7 July 2011.
62. P. A. Jensen, B. Sander and K. Dam-Johansen, *Biomass Bioenerg.*, 2001, 20, 431-446.
63. P. A. Jensen, B. Sander and K. Dam-Johansen, *Biomass Bioenerg.*, 2001, 20, 447-457.
64. S. Sarenbo, *Biomass Bioenerg.*, 2009, 33, 1212-1220.
65. A. Gómez-Barea, L. F. Vilches, C. Leiva, M. Campoy and C. Fernández-Pereira, *Chem. Eng. J.*, 2009, 146, 227-236.
66. A. Elliott and T. Mahmood, *Tappi J.*, 2006, 5, 9-16.
67. R. M. Pitman, *Forestry*, 2006, 79, 563-588.
68. P. Vesterinen, *Wood Ash Recycling: State of the Art in Finland and Sweden*, <http://www.cti2000.it/solidi/WoodAshReport%20VTT.pdf>, Accessed 01/02/2011.
69. K. Schiemenz and B. Eichler-Lobermann, *Nutr. Cycl. Agroecosyst.*, 2010, 87, 471-482.
70. S. Wang and L. Baxter, in *Science in Thermal and Chemical Biomass Conversion*, ed. A. Bridgewater, Blackwell Science Ltd., Oxford, Editon edn., 2006, pp. 325-330.
71. P. Janos, H. Buchtová and M. Rýznarová, *Water Res.*, 2003, 37, 4938-4944.
72. D. G. Nair, A. Fraaij, A. A. K. Klaassen and A. P. M. Kentgens, *Cement Concrete Res.*, 2008, 38, 861-869.
73. P. Chindaprasirt and S. Rukzon, *Constr. Build. Mater.*, 2008, 22, 1601-1606.
74. M. Frías, E. Villar-Cociña and E. Valencia-Morales, *Waste Manage.*, 2007, 27, 533-538.
75. W. Tangchirapat, T. Saeting, C. Jaturapitakkul, K. Kiattikomol and A. Siripanichgorn, *Waste Manage.*, 2007, 27, 81-88.
76. H. Biricik, F. Aköz, I. I. Berktaş and A. N. Tulgar, *Cement Concrete Res.*, 1999, 29, 637-643.
77. C. Leiva, A. Gomez-Barea, L. F. Vilches, P. Ollero, J. Vale and C. Fernandez-Pereira, *Energ. Fuel.*, 2006, 21, 361-367.

78. V. K. Gupta, I. Ali, V. K. Saini, T. Van Gerven, B. Van der Bruggen and C. Vandecasteele, *Ind. Eng. Chem. Res.*, 2005, 44, 3655-3664.
79. V. K. Gupta, A. Mittal, V. Gajbe and J. Mittal, *J. Colloid Interface Sci.*, 2008, 319, 30-39.
80. M. J. Hodson, P. J. White, A. Mead and M. R. Broadley, *Annal. Bot.-London*, 2005, 96, 1027-1046.
81. W. H. Casey, S. D. Kinrade, C. T. G. Knight, D. W. Rains and E. Epstein, *Plant Cell Environ.*, 2004, 27, 51-54.
82. H. A. Currie and C. C. Perry, *Annal. Bot.-London*, 2007, 100, 1383-1389.
83. K. Tamai and J. F. Ma, *New Phytol.*, 2003, 158, 431-436.
84. J. F. Ma, K. Tamai, N. Yamaji, N. Mitani, S. Konishi, M. Katsuhara, M. Ishiguro, Y. Murata and M. Yano, *Nature*, 2006, 440, 688-691.
85. J. F. Ma, N. Yamaji, N. Mitani, K. Tamai, S. Konishi, T. Fujiwara, M. Katsuhara and M. Yano, *Nature*, 2007, 448, 209-212.
86. J. F. Ma and N. Yamaji, *Trends Plant Sci.*, 2006, 11, 392-397.
87. M. J. Hodson, A. G. Parker, M. J. Leng and H. J. Sloane, *J. Quaternary Sci.*, 2008, 23, 331-339.
88. J. Mecfel, S. Hinke, W. A. Goedel, G. Marx, R. Fehlhaber, E. Bäucker and O. Wienhaus, *J. Plant Nutr. Soil Sci.*, 2007, 170, 769-772.
89. E. Epstein, *Annu. Rev. Plant. Physiol. Plant. Mol. Biol.*, 1999, 50, 641-664.
90. K. Tamai and J. F. Ma, *Plant Soil*, 2008, 307, 21-27.
91. P. Hald, Technical University of Denmark, 1994.
92. R. K. Iler, *The Chemistry of Silica*, Wiley & Sons, New York, 1979.
93. C. T. G. Knight, R. J. Balec and S. D. Kinrade, *Angew. Chem., Int. Ed.*, 2007, 46, 8148-8152.
94. M. J. Mora-Fonz, C. R. A. Catlow and D. W. Lewis, *J. Phys. Chem. C*, 2007, 111, 18155-18158.
95. T. T. Trinh, A. P. J. Jansen and R. A. van Santen, *J. Phys. Chem. B*, 2006, 110, 23099-23106.
96. M. J. Munoz Aguado and M. Gregorkiewitz, *J. Colloid Interface Sci.*, 1997, 185, 459-465.
97. G. Engelhardt, D. Zeigan, H. Jancke, D. Hoebbel and W. Wieker, *A. Anorg. Allg. Chem.*, 1975, 418, 17-28.
98. G. Engelhardt and D. Michel, *High-Resolution Solid-State NMR of Silicates and Zeolites*, John Wiley, New York, 1987.
99. J. L. Bass and G. L. Turner, *J. Phys. Chem. B*, 1997, 101, 10638-10644.
100. C. F. Weber and R. D. Hunt, *Ind. Eng. Chem. Res.*, 2003, 42, 6970-6976.
101. I. L. Svensson, S. Sjoberg and L. O. Ohman, *J. Chem. Soc. Farad. T. 1*, 1986, 82, 3635-3646.
102. J. L. Provis, P. Duxson, G. C. Lukey, F. Separovic, W. M. Kriven and J. S. J. van Deventer, *Ind. Eng. Chem. Res.*, 2005, 44, 8899-8908.
103. I. Halasz, M. Agarwal, R. Li and N. Miller, *Catal. Today*, 2007, 126, 196-202.
104. I. Halasz, M. Agarwal, R. Li and N. Miller, *Catal. Lett.*, 2007, 117, 34-42.
105. J. S. Falcone Jr, J. L. Bass, P. H. Krumrine, K. Brensinger and E. R. Schenk, *J. Phys. Chem. A*, 2010, 114, 2438-2446.
106. J. Osswald and K. T. Fehr, *J. Mater. Sci.*, 2006, 41, 1335-1339.
107. C. T. Kirk, *Phys. Rev. B*, 1988, 38, 1255.
108. PQ Corporation, *Sodium Silicates: Liquids and Solids*, PQ Corporation, USA, 2004.
109. P. M. Gill, *Bulletin 9: Environmentally Safe Binders for Agglomeration*, PQ Corporation, USA, 1997.
110. PQ Corporation, *Bulletin 12-31: Bonding and Coating Applications of PQ Soluble Silicates*, PQ Corporation, 2006.

111. H. A. Nasr-El-Din and K. C. Taylor, *J. Pet. Sci. Eng.*, 2005, 48, 141-160.
112. M. McDonald and J. LaRosa Thompson, *Sodium Silicate a Binder for the 21st Century*, PQ Corporation.
113. W. Vogelsberger, A. Seidel and G. Rudakoff, *J. Chem. Soc. Faraday T.*, 1992, 88, 473-476.
114. N. Zotov and H. Keppler, *Chem. Geol.*, 2002, 184, 71-82.
115. U. Kalapathy, A. Proctor and J. Shultz, *Bioresource Technol.*, 2000, 73, 257-262.
116. USA Pat., 6524543, 1998.
117. U. Kalapathy, A. Proctor and J. Shultz, *Ind. Eng. Chem. Res.*, 2003, 42, 46-49.
118. U. Kalapathy, A. Proctor and J. Shultz, *Bioresource Technol.*, 2000, 72, 99-106.
119. V. P. Della, I. Kuhn and D. Hotza, *Mater. Lett.*, 2002, 57, 818-821.
120. F. A. Rodrigues, *Cement Concrete Res.*, 2003, 33, 1525-1529.
121. M. Ubukata, S. Mitsuhashi, A. Ueki, Y. Sano, N. Iwasa, S. Fujita and M. Arai, *J. Agr. Food Chem.*, 2010, 58, 6312-6317.
122. J. Zhang, J. M. Khatib, C. Booth and R. Siddique, in *Excellence in Concrete Construction through Innovation*, eds. M. C. Limbachiya and H. Y. Kew, Crc Press-Taylor & Francis Group, Boca Raton, Editon edn., 2009, pp. 517-521.
123. N. M. Al-Akhras and B. A. Abu-Alfoul, *Cement Concrete Res.*, 2002, 32, 859-863.
124. FAOSTAT, ForesSTAT, <http://faostat.fao.org/site/630/default.aspx>, Accessed 03/02/11.
125. G. Nemli and I. Öztürk, *Build. Environ.*, 2006, 41, 770-774.
126. A. Ghosh and M. Sain, *Polym. Polym. Compos.*, 2006, 14, 217-227.
127. Z. E. Isaksson M, Bruze M, *J. Occup. Environ. Med.*, 1999, 41, 261-266.
128. California Air Resources Board, Fact Sheet: Airborne Toxic Control Measure (ATCM) to Reduce Formaldehyde Emissions from Composite Wood Products.
129. H. Xu, Q. Li, L. F. Shen, W. Wang and J. P. Zhai, *J. Hazard. Mater.*, 175, 198-204.
130. Environment Protection Agency, An Introduction to Indoor Air Quality, <http://www.epa.gov/iaq/formalde.html>, Accessed 03/02/2011.
131. S. Halvarsson, H. Edlund and M. Norgren, *Ind. Crop. Prod.*, 2008, 28, 37-46.
132. H. Chung-Yun, F. Feng and P. Hui, *Forest Prod. J.*, 2008, 58, 56-61.
133. R. M. Rammon, in *Proc. 31st Inter. Particleboard and Composite Materials Symp.*, Washington State Univ., Pullman, Washington, Editon edn., 1997, pp. 177-181.
134. Columbia Forest Products, PureBond: Formaldehyde-Free Hardwood Plywood <http://www.columbiaforestproducts.com/products/prodpb.aspx>, Accessed 12/08/08, 2008.
135. M. Lubi and E. T. Thachil, *Polym-Plast. Technol.*, 2007, 46, 393-400.
136. W. Hoareau, F. B. Oliveira, S. Grelier, B. Siegmund, E. Frollini and A. Castellan, *Macromol. Mater. Eng.*, 2006, 291, 829-839.
137. J. E. G. van Dam, M. J. A. van den Oever and E. R. P. Keijsers, *Ind. Crop. Prod.*, 2004, 20, 97-101.
138. A. Ashori, *Bioresource Technol.*, 2008, 99, 4661-4667.
139. S. Panthapulakkal and M. Sain, *Compos. Pt. A-Appl. Sci. Manuf.*, 2007, 38, 1445-1454.
140. B. English, *The National Institute of Environmental Health Sciences (NIEHS)*, Editon edn., 1994, vol. 102, pp. 168-170.
141. M. H. Simatupang and R. L. Geimer, *Wood Adhesives*, Wisconsin, 1990.
142. J. Giancaspro, C. Papakonstantinou and P. Balaguru, *Compos. Sci. Technol.*, 2008, 68, 1895-1902.
143. G. Nemli, S. Yildiz and E. D. Gezer, *Bioresource Technol.*, 2008, 99, 6054-6058.

144. E. Guntekin and B. Karakus, *Ind. Crop. Prod.*, 2008, 27, 354-358.

## Chapter 2:

# Lab-scale combustion of wheat straw and extraction of residues

Some of the work detailed in this chapter is published in: Jennifer R. Dodson, Andrew J. Hunt, Vitaly L. Budarin, Avtar S. Matharu and James H. Clark, 'The chemical value of wheat straw combustion residues', *RSC Adv.*, 2011, DOI: 10.1039/C1RA00271F



## **2.1 Chapter 2 – Summary**

The mineralogical changes occurring during the combustion of several varieties of wheat straw are studied, including the physical, chemical and textural properties of the ashes. Particular focus is placed on the effects on potassium and silica, as the major species in the ashes, and the extraction of silica utilising the inherent alkalinity to understand whether the formation of alkali silicates from wheat straw combustion residues might be feasible. In addition, the textural properties of one variety of wheat straw throughout the combustion process and following leaching are examined.

## **2.2 Wheat straw properties**

Several varieties of wheat straw were collected over three years from two locations in the vicinity of York (Figure 2.1). In 2007 and 2009 these were collected a few weeks after harvesting from straw bales, whilst in 2008 the straw was collected directly from the fields. All of the materials studied are/were winter wheat varieties on the Homegrown Cereal Association (HGCA) recommended growing lists (Nijinsky was removed in 08/09).<sup>1</sup> Claire, Robigus and Nijinsky are all Group 3 (suitable for biscuit making) varieties, with Claire the benchmark for this group. Viscount is a Group 4 variety (suitable for distilling). All of the varieties are soft wheats, with a low protein content and high starch content in the grain. Claire is the tallest variety, with an average height of 91 cm, indicating a higher yield of straw.<sup>1</sup> All of the straws were air dried following collection, stored in breathable materials to prevent decomposition and milled to the same particle size for use in all experiments. Visual observation indicated little surface soil contamination.

### **2.2.1 Proximate and ultimate analysis**

Proximate and ultimate analyses of all the wheat straws studied were undertaken (Table 2.1). Ash and moisture content analyses were carried out in triplicate, whilst the CHN analyses and oxide composition of Claire wheat straw ash from 2007 (Cl07) were examined in duplicate. The average and standard deviation for each is shown. Overall, the ultimate and proximate values are within the ranges of wheat straw harvested in various countries throughout Europe.<sup>3,2-6</sup>



**Figure 2.1: a) The locations where wheat straw was collected are circled in red b) collecting straw from fields near Castle Howard in 2008**

In comparison to other materials frequently used in combustion systems wheat straw has a distinctive composition. The ash content is higher than for woody biomass with, in general, higher potassium and chlorine levels.<sup>7</sup> The wheat straw samples used in this study confirm this trend. The ash content fluctuates between 4.7 – 6.7%, apparently independent of both the wheat straw variety and the year of harvesting. The most striking differences between the straws are found within the ash composition, with the

alkali, silica and chloride concentration highly dependent on the year of harvesting. The alkali, chloride and sulfur levels in the ash are much lower for all straws collected in 2008, with a corresponding increase in the silica concentration. In comparison, Claire 2007 (Cl07) and the varieties studied from 2009 all have similar ash compositions with respect to alkali and silica. The chloride levels of the straws from 2009 are generally lower than that of Cl07, this may be due to the use of low chloride potassium fertiliser or a difference in soil composition reducing chloride uptake. The calcium content remains consistent across all wheat straw varieties and years.

Overall, this signifies that the year of production has a greater impact on the wheat straw characteristics, particularly the ash composition, than the variety. This can be correlated with the rainfall around harvest time, August, in each year (Figure 2.2). There were much higher levels of rainfall across the North East of England during August 2008 than in either 2007 or 2009. In July similar levels of rainfall fell in all years, whilst 2008 also saw higher levels in September. The level of rainfall at harvest time during 2008 is also confirmed by the fact that the straw was extremely wet on removal from the fields and was immediately dried to prevent decomposition. The removal of ash components, particularly potassium, chloride and sulfur has been observed to occur by rain leaching of rice straw and water soaking of wheat straw and other biomass materials.<sup>4, 8</sup> The detected variations in ash composition between wheat straw varieties grown in different years is therefore suggested to be due mainly to the degree of leaching of water soluble components within the fields. This can be beneficial for utilisation of the straw for thermochemical conversion by directly recycling nutrients and reducing the content of low melting slag-forming and corrosive elements. However, the high rainfall in 2008 caused challenging harvesting conditions for farmers and a decrease in income due to reduced wheat grain quality.<sup>9, 10</sup> These variations in the inorganic composition may fundamentally affect the combustion of the material, the nature of the ash formed and therefore its applications.

	Claire 2007 (Cl07)	Claire 2008 (Cl08)	Robigus 2008 (Rob08)	Nijinsky 2008 (Nij08)	Claire 2009 (Cl09)	Robigus 2009 (Rob09)	Viscount 2009 (Vis09)
Moisture (%)	7.10 ± 0.10	7.25 ± 0.11	8.49 ± 0.30	8.64 ± 0.45	9.07 ± 0.42	9.02	9.15 ± 0.43
Volatile carbon (%) <sup>db</sup>	68.4	70.1	69.2	68.4	72.2	70.4	68.7
Fixed carbon (%) <sup>db</sup>	25.6	23.4	24.4	26.5	23.1	24.3	25.8
Ash (%) <sup>db</sup>	6.03 ± 0.04	6.59 ± 0.10	6.41 ± 0.28	5.09 ± 0.29	4.65 ± 0.41	5.29	5.57 ± 0.36
C (%) <sup>db</sup>	45.5 ± 0.29	45.5 ± 0.33	45.9 ± 0.28	46.5 ± 0.04	46.6 ± 0.04	45.2 ± 0.37	46.1 ± 0.09
H (%) <sup>db</sup>	5.19 ± 0.02	5.17 ± 0.10	5.03 ± 0.04	5.27 ± 0.01	5.17 ± 0.01	5.05 ± 0.11	5.06 ± 0.04
N (%) <sup>db</sup>	0.39 ± 0.04	0.61 ± 0.07	0.49 ± 0.03	0.38 ± 0.03	0.53 ± 0.04	0.47 ± 0.06	0.56 ± 0.00
O (%) <sup>db</sup>	42.5 ± 0.35	41.7 ± 0.16	41.6 ± 0.29	42.3 ± 0.00	42.5 ± 0.01	43.4 ± 0.43	42.2 ± 0.06
<b>Ash (%)</b>							
Na <sub>2</sub> O	0.44 ± 0.47	0.10	0.10	0.12	0.72	0.37	0.20
MgO	1.41 ± 0.06	1.87	1.53	1.98	2.19	2.13	2.43
Al <sub>2</sub> O <sub>3</sub>	0.22 ± 0.04	0.07	0.17	0.16	0.37	0.11	0.10
SiO <sub>2</sub>	44.8 ± 0.82	74.6	76.2	78.9	45.3	41.5	44.1
P <sub>2</sub> O <sub>5</sub>	1.76 ± 0.31	1.70	1.73	1.51	2.21	2.02	1.57
SO <sub>3</sub>	3.26 ± 0.59	2.20	1.07	0.81	2.43	4.47	3.13
K <sub>2</sub> O	26.6 ± 2.47	6.24	10.7	5.95	22.6	29.2	29.0
CaO	11.0 ± 2.28	13.0	7.80	10.4	14.7	11.0	14.0
TiO <sub>2</sub>	0.02 ± 0.0	0.01	0.02	0.02	0.03	0.01	0.01
Mn <sub>3</sub> O <sub>4</sub>	0.14 ± 0.0	0.02	0.12	0.05	0.28	0.14	0.36
Fe <sub>2</sub> O <sub>3</sub>	0.21 ± 0.20	0.00	0.05	0.02	0.31	0.16	0.17
ZnO	0.02 ± 0.01	0.04	0.01	0.00	0.02	0.01	0.01
SrO	0.02 ± 0.01	0.00	0.04	0.03	0.06	0.05	0.06
ZrO <sub>2</sub>	0.01 ± 0.01	0.00	0.00	0.00	0.00	0.00	0.01
BaO	0.11 ± 0.02	0.06	0.08	0.07	0.08	0.06	0.08
Cl	8.94 ± 1.07	0.08	0.43	0.00	1.08	6.04	1.25
<b>SUM</b>	<b>99.4</b>	<b>100.0</b>	<b>100.0</b>	<b>100.0</b>	<b>93.1</b>	<b>97.8</b>	<b>97.2</b>
<b>SiO<sub>2</sub>:K<sub>2</sub>O (wt ratio)</b>	<b>1.69</b>	<b>11.9</b>	<b>7.12</b>	<b>13.3</b>	<b>2.01</b>	<b>1.42</b>	<b>1.52</b>

db = dry basis

Table 2.1 : Ultimate and proximate analyses for all wheat straw varieties used during this study

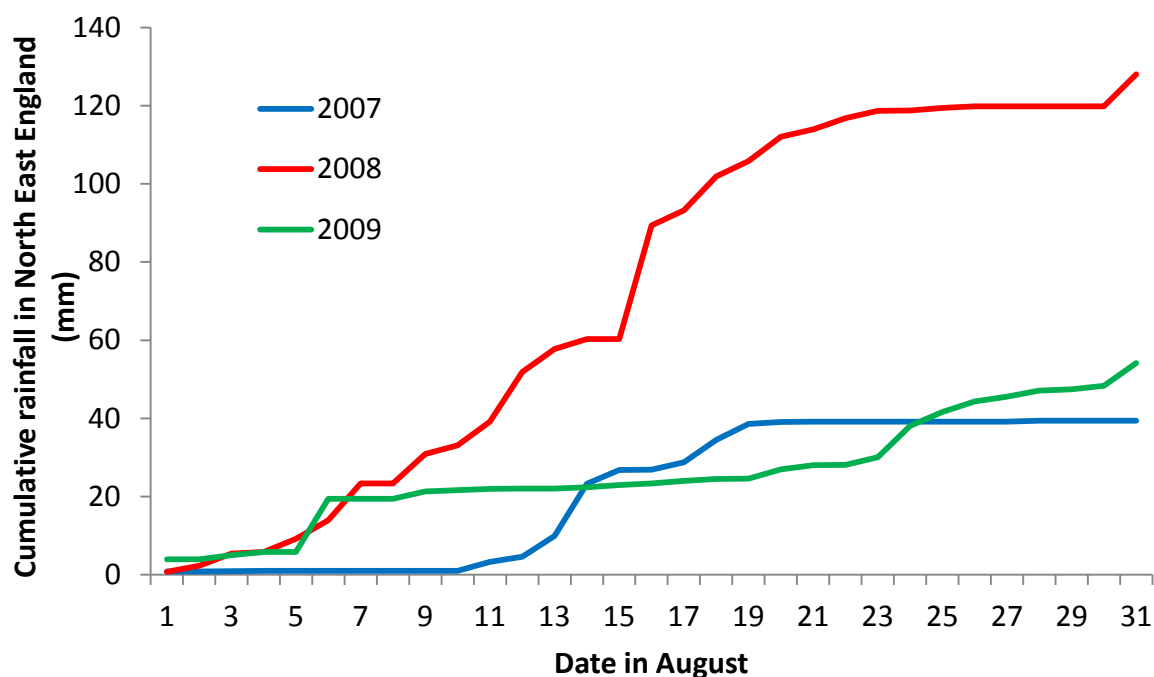


Figure 2.2: Cumulative rainfall for North East England in August 2007 – 2009<sup>11</sup>

### 2.2.2 Thermogravimetric analysis

Thermogravimetric profiles of each wheat straw under pyrolysis (Figure 2.3) and combustion (Figure 2.3) conditions underscores the impact of the differing straw composition on its thermochemical conversion. The pyrolysis profiles, in particular, demonstrate an increase in decomposition onset temperature, peak temperature and maximum rate of decomposition (Table 2.2) in the 2008 samples, indicative of a lower reactivity.<sup>7</sup> These changes are generally attributed to the impact of minerals present in the ash, particularly potassium, and a catalytic influence on decomposition processes, principally on cellulose.<sup>12</sup> This may not be directly due to the activity of elemental potassium, but rather the formation of basic species, causing base-catalysed decomposition.<sup>13-15</sup> A decrease in potassium levels within the different straws does correlate with a shift of the peak temperature to higher temperatures. Interestingly, whilst the straws collected in 2007 and 2008 both display a distinct low temperature shoulder, generally attributed to the decomposition of hemicellulose, and a higher temperature main peak due to cellulose, all of the 2009 samples exhibit only one broad decomposition profile. Previous studies have observed the separation of pyrolysis decomposition into two distinct peaks upon water washing, with both decomposition

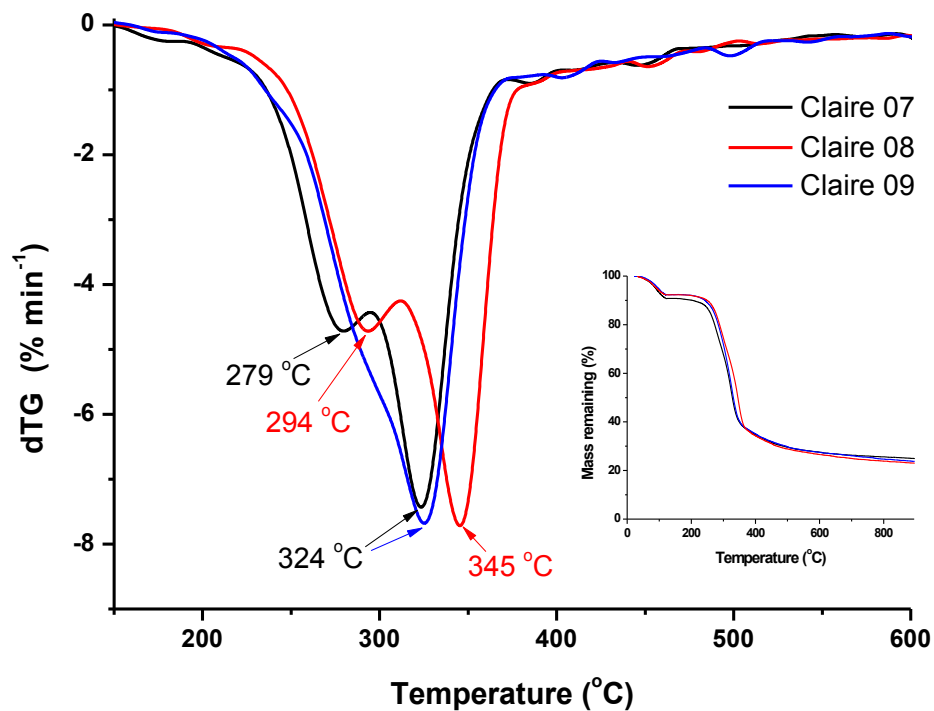


Figure 2.3: Thermogravimetric analyses under pyrolysis conditions of wheat straw, variety Claire, harvested in different years (Originally in colour)

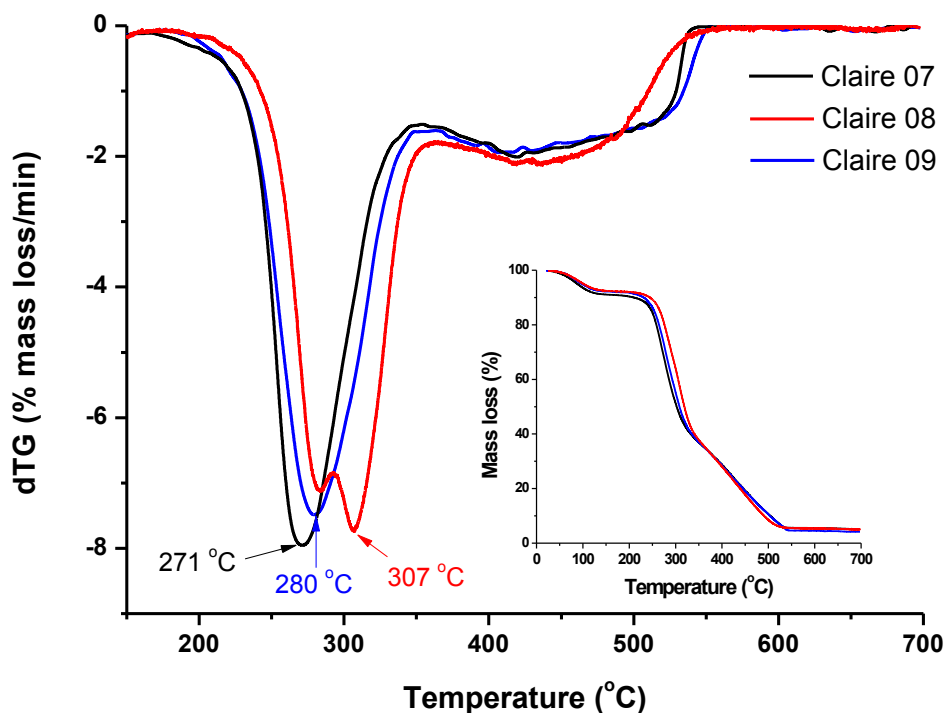


Figure 2.4: Thermogravimetric analyses under combustion conditions of wheat straw, variety Claire, harvested in different years (Originally in colour)

**Table 2.2: Peak and ignition temperatures for all wheat straw samples under pyrolysis and combustion conditions**

		Cl07	Cl08	Rob08	Nij08	Cl09	Rob09	Vis09
Pyrolysis	Onset T (°C)	214	233	228	234	217	214	213
	Peak T (°C)	324	345	338	348	324	319	319
	Max mass loss rate (% min <sup>-1</sup> )	-7.79	-8.02	-7.07	-8.89	-7.86	-7.52	-7.06
Combustion	Ignition T (°C)	213	228	221	226	216	207	210
	Peak T (°C)	271	306	281	313	280	272	270
	Max mass loss rate (% min <sup>-1</sup> )	-7.96	-7.65	-7.94	-8.49	-7.50	-9.32	-8.97

bands remaining separate and shifting to lower temperatures following the addition of KCl to the washed straw.<sup>16</sup> This suggests that it is not only the mineral content, but also its distribution and interaction with the different biopolymers, which influences decomposition.

The combustion profiles (Figure 2.4) display a broad volatile combustion peak, with the peak temperature occurring at lower temperatures than under pyrolysis conditions, as observed by researchers studying other biomass materials.<sup>17</sup> The samples from 2008 still display higher ignition and peak temperatures as detected under pyrolysis conditions. The profiles are typical of lignocellulosic materials, showing the onset of an initial volatilisation stage around 220 °C followed by a char oxidation stage at higher temperatures.<sup>7</sup>

### **2.3 Mineralogical changes occurring during combustion**

Claire 07 was initially studied to analyse the impact of varying combustion parameters on the physical, chemical and textural properties of the ashes formed and to study the optimisation of the extraction of silica. The wheat straw was combusted between 400 °C and 800 °C, for a set time (10 minutes or 2 hours). The combustion conditions chosen ranged from the onset of char combustion of the wheat straw to complete combustion and ash melting to enable a complete exploration of the interaction between the physical, chemical and textural properties of the residues formed throughout the combustion range. The ashes formed after 10 minutes combustion were black, whilst after 2 hours the samples were a continuum of colour ranging from dark grey at 400 °C to creamy-orange at 800 °C. The presence of darker particles within ashes has previously

been suggested to be due to the inclusions of carbon or carbonates, particularly those of potassium.<sup>8</sup> Indeed, ashes formed from 2008 wheat straws, with lower potassium levels, were all lighter in colour. CHN analyses of the CI07 residues demonstrate a low, but continued, carbon content up to 700 °C, correlating with the onset of lightening of the ashes (Table 2.3). The CHN analysis method determines both organic and inorganic carbon and therefore cannot be used to directly determine whether the remaining carbon content is due to carbonates or organic carbon. At 800 °C after 2 h combustion the ash of CI07 had begun to melt.

After two hours combustion the percentage solid remaining up to 500 °C (Table 2.3) was similar to the ash content found in the initial wheat straw (i.e. after combustion at 550 °C to constant weight), indicating that complete combustion had occurred. At higher combustion temperatures there was a small but continued mass loss, probably due to the devolatilisation of inorganic species, consistent with previously reported data.<sup>18</sup> After only 10 minutes combustion significant proportions of organic material still remain, although combustion rates increase with temperature. Incomplete combustion would obviously not be ideal in a commercial furnace, however, it allows insight into the changes occurring amongst the inorganic species during the volatilisation and char oxidation stage. Nitrogen levels within the residues do not appear to be significantly reduced during the first 10 minutes of combustion, whilst complete devolatilisation has occurred after 2 h combustion at all temperatures.

**Table 2.3: Mass remaining and CHN analysis of combustion residues of CI07 formed under varying combustion conditions**

Temp (°C)	Time (min)	Mass remaining (%)	CHN			Rest (%)
			C (%)	H (%)	N (%)	
400	10	26.4	65.1	2.83	0.60	31.5
500	10	24.4	67.3	2.33	0.57	29.8
600	10	19.3	65.5	1.57	0.56	32.4
700	10	14.1	60.9	1.19	0.50	37.4
800	10	14.3	58.1	1.01	0.60	40.3
400	120	5.1	4.18	0.76	0.00	95.1
500	120	5.1	5.99	0.78	0.00	93.2
600	120	4.7	3.93	0.60	0.00	95.5
700	120	4.5	0.54	0.24	0.00	99.2
800	120	4.3	0.89	0.18	0.00	98.9

### 2.3.1 X-Ray Diffraction

The mineralogical changes occurring in the ashes as a function of time and temperature were identified by X-Ray Diffraction (XRD) (Figure 2.5). The mineral phases identified in the residues are shown in Appendix A. Figure 2.5a illustrates a broad background region between 20-30° 2 $\theta$  in the XRD patterns of Cl07 wheat straw ashes combusted for 10 minutes. This feature is observed in biomass chars and corresponds to the aromatic lamellae of the remaining carbon.<sup>19</sup> The reduction in the area of this background halo coincides with the reduction in carbon content of the residues with increasing temperature (Table 2.3) and is no longer present in the diffractograms of the residues after 2 h combustion (Figure 2.5b). Sylvite (KCl) is the main crystalline phase observed, present at all temperatures. Peaks due to calcite (CaCO<sub>3</sub>) increase in intensity with increasing combustion temperature, assumed to be due to the increasing relative inorganic concentration of the ashes. However, they are significantly reduced at 800 °C, presumably due to the decomposition of calcite, which indicates that this occurs rapidly. The presence of arcanite (K<sub>2</sub>SO<sub>4</sub>) is also observed. The other intense peaks present, due to the aluminium sample holder, reduce in intensity with increasing temperature. This could indicate increasing crystallinity of the combustion residues.

Similar crystalline phases are observed after 2 h combustion (Figure 2.5b). The intensity of the sylvite peaks decrease at 700 °C and are absent at 800 °C, in agreement with previous observations regarding the loss of KCl during the combustion of wheat straw.<sup>20</sup> Above 500 °C calcite is no longer detected. This is at a lower temperature than would be predicted by its decomposition temperature (848 °C). However, STA analyses of the ashes (shown in Chapter 3) indicate the loss of CO<sub>2</sub> from calcium carbonate, even at a slow heating rate, between 600 – 700 °C (section 3.5.4). The breakdown of calcite and loss of sylvite correlate well with the decrease in the remaining mass of the residue at 600 °C and above (Table 2.3). Arcanite (K<sub>2</sub>SO<sub>4</sub>) is present in the ashes at all temperatures. The minor presence of quartz is discerned in all of the ashes, peaking in intensity at 700 °C, whilst calcium silicate appears at 700 °C, indicating the transformation of the silica phase. Cristobalite is not observed, contrasting with previous research on rice hull ashes in which this was the major silica phase at higher temperatures.<sup>18</sup> Potassium carbonate is not identified unambiguously, although its presence may be indicated by small peaks between 31.5 – 32.5° 2 $\theta$ .

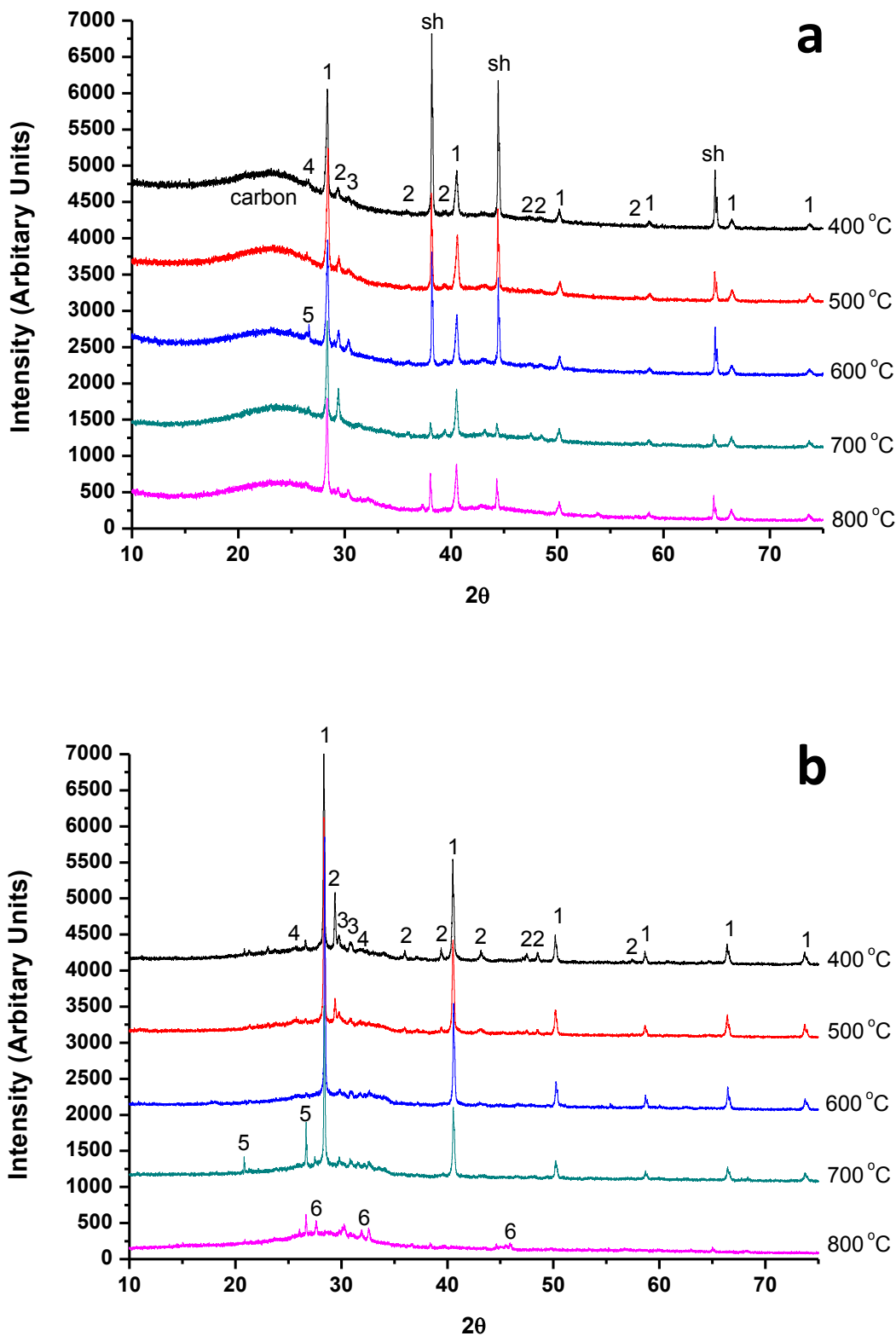


Figure 2.5: XRD patterns of Claire 07 wheat straw ashes after (a) 10 minutes combustion and (b) 2 h combustion from 400 °C to 800 °C. The phases present are indicated by numbers: 1 = Sylvite (KCl); 2 = Calcite ( $\text{CaCO}_3$ ); 3 = Arcanite ( $\text{K}_2\text{SO}_4$ ); 4 = Anhydrite ( $\text{CaSO}_4$ ); 5 = Quartz ( $\text{SiO}_2$ ); 6 = Calcium silicate ( $\text{CaSiO}_3$ ); sh = sample holder (Originally in colour)

The other varieties of wheat straw collected in different years were all combusted at 500 °C for 2 h and analysed by XRD (Figure 2.6 – 2.8). The diffractograms highlight the dependence of the mineralogical changes occurring during combustion on the initial elemental distribution of the ash. Although some of the minor crystalline phases are difficult to identify due to their low abundance, overall both Cl07 and Cl09 (Figure 2.6) display a similar speciation. Cl09 contains very little sylvite and higher concentrations of calcite, supporting the XRF analysis of the initial ash composition (Table 2.1). However, both display a flat baseline with a broader background region between 25 – 35° 2 $\theta$ . This observation correlates with the higher potassium, chlorine and calcium content of these wheat straws, intimating at the formation of glassy alkali silicates rather than the conversion of amorphous silica into other silica polymorphs. In contrast, Cl08 displays a large background halo between 15 – 35° 2 $\theta$  with a maxima around 22° 2 $\theta$ . The low carbon content of the ashes formed at this temperature suggests that it is not due to the carbon species identified in the residues formed after 10 min. Instead this feature can be attributed to amorphous silica, in particularly disordered  $\alpha$ -cristobalite, as previously identified in rice hull ashes.<sup>21-23</sup>

The ashes of different varieties of straws collected in the same year display a strong resemblance in their diffractograms. All of the 2008 ashes (Figure 2.7) have low or non-apparent KCl signals with the same background halo centred at 22° 2 $\theta$ . The presence of a small sylvite peak for Rob08 supports the minor Cl concentration observed in this sample by XRF. The intensity of the CaCO<sub>3</sub> peaks decrease in intensity with decreasing Ca content of the initial material: Cl08 > Nij08 > Rob08 (Table 2.1). The ashes from different wheat straw varieties collected in 2009 are also similar (Figure 2.8), although the sylvite intensity increases in accordance with the Cl content of the initial straw, with a corresponding decrease in the calcite intensity. This highlights the variability in mineralogical changes dependent on the initial inorganic content of the straw, but also hints at the sensitivity and usefulness of XRD in indicating the initial elemental composition of the straw. It also supports the XRF analyses of the elemental composition of the straw ash.

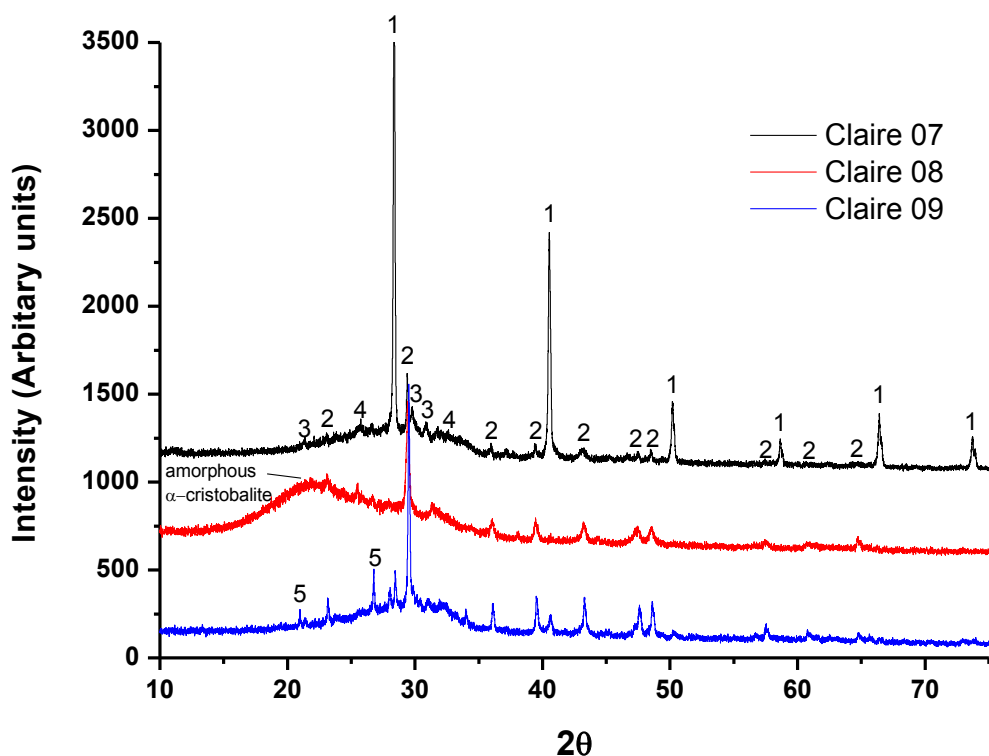


Figure 2.6: Diffractograms of wheat straw, variety Claire, harvested over 3 years combusted at 500 °C for 2 h: 1 = Sylvite (KCl); 2 = Calcite ( $\text{CaCO}_3$ ); 3 = Arcanite ( $\text{K}_2\text{SO}_4$ ); 4 = Anhydrite ( $\text{CaSO}_4$ ); 5 = Quartz ( $\text{SiO}_2$ ) (Originally in colour)

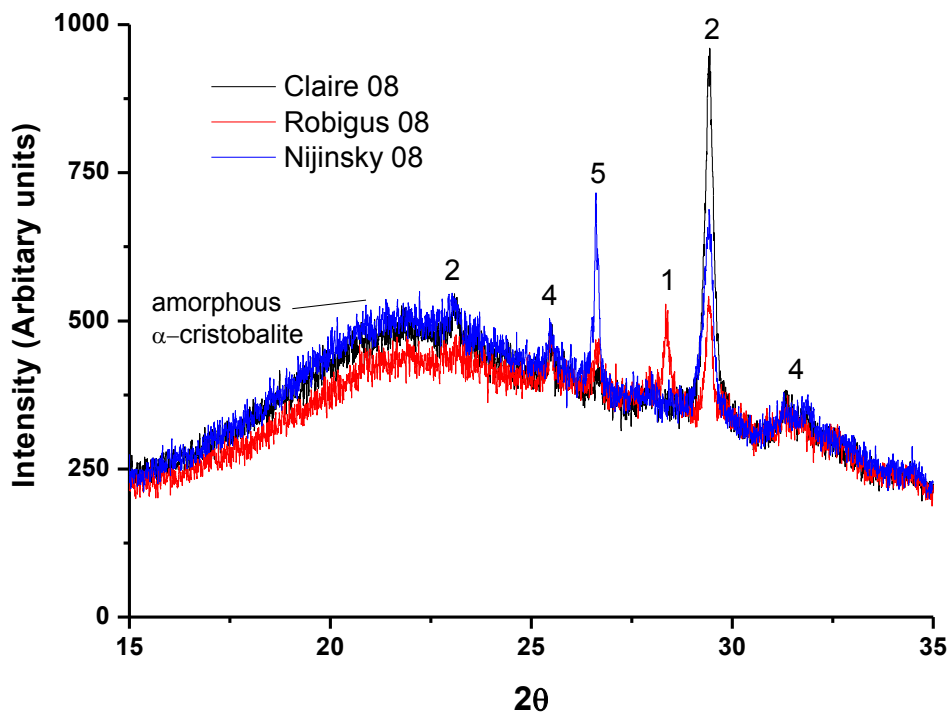


Figure 2.7: Diffractograms of wheat straw harvested in 2008 combusted at 500 °C for 2 h: 1 = Sylvite (KCl); 2 = Calcite ( $\text{CaCO}_3$ ); 4 = Anhydrite ( $\text{CaSO}_4$ ); 5 = Quartz ( $\text{SiO}_2$ ) (Originally in colour)

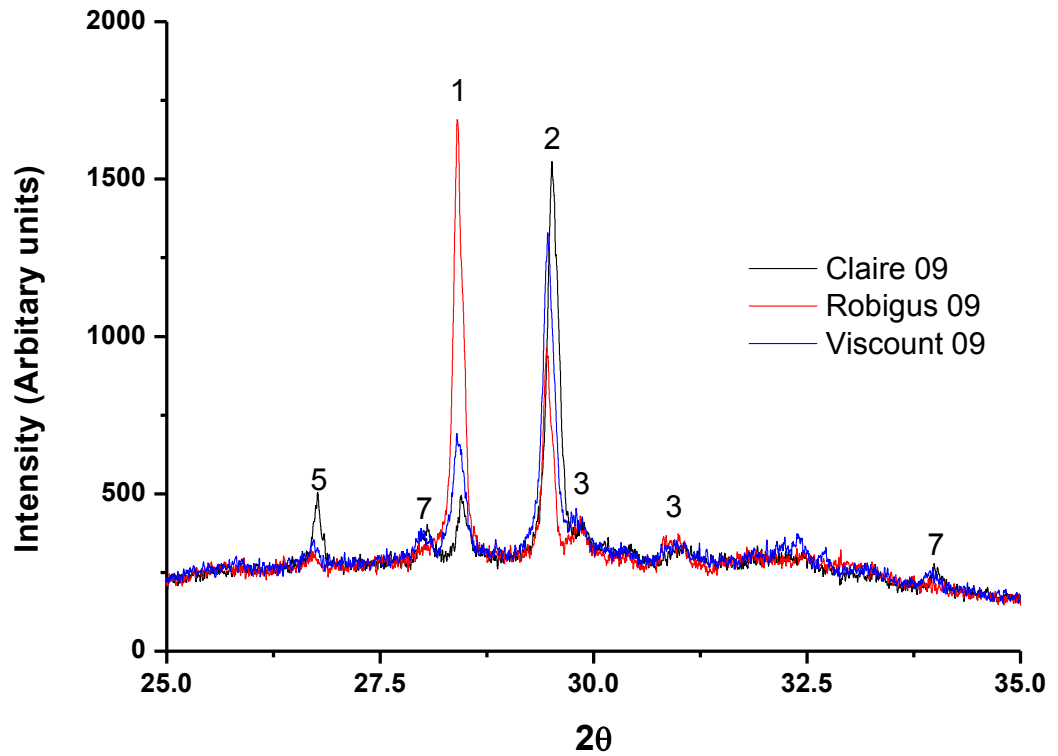


Figure 2.8: Diffractograms of wheat straw harvested in 2009 combusted at 500 °C for 2 h: 1 = Sylvite (KCl); 2 = Calcite ( $\text{CaCO}_3$ ); 3 = Arcanite ( $\text{K}_2\text{SO}_4$ ); 5 = Quartz ( $\text{SiO}_2$ ); 7 = Fairchildite ( $\text{K}_2\text{Ca}(\text{CO}_3)_2$ ) (Originally in colour)

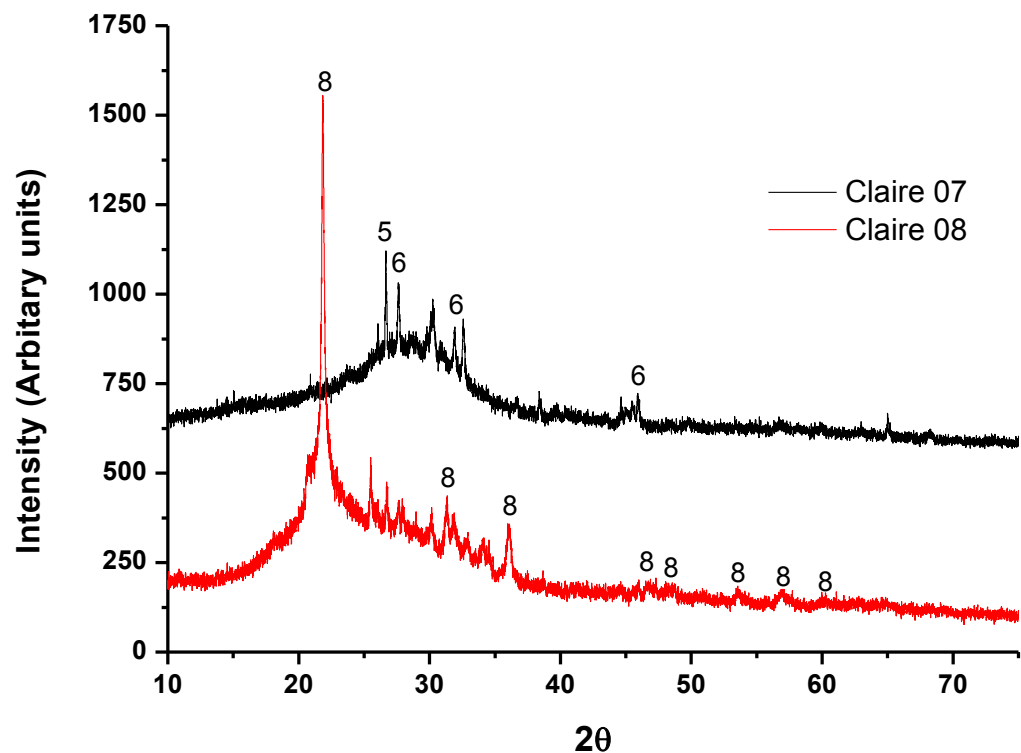


Figure 2.9: Diffractograms of CI07 and CI08 combusted at 800 °C for 2 h: 5 = Quartz ( $\text{SiO}_2$ ); 6 =  $\text{CaSiO}_3$ ; 8 =  $\alpha$ -cristobalite ( $\text{SiO}_2$ ) (Originally in colour)

Following combustion at 800 °C, the difference in the mineral speciation between the low and high potassium concentration straws is even more striking, here highlighted for CI07 and CI08 (Figure 2.9). Although unambiguous identification of all of the minor peaks has proven difficult, ordering of the silica in CI08 is manifested by the sharp and intense peaks at 21.8° and 36.1° 2 $\theta$ , amongst others, due to crystalline  $\alpha$ -cristobalite, as also observed with increasing heat treatment temperature for rice hull ashes.<sup>21</sup> These peaks are not at all apparent in ashes with higher potassium and chloride contents, where a broad background region between 25 – 35° 2 $\theta$  and the formation of calcium silicate is observed.

### 2.3.2 Infrared

Further information about the mineralogical nature of the ashes can be garnered from infrared analysis, specifically about the silica or silicate structures, as these are mostly obscured in XRD due to their amorphous nature. Only the ashes formed after 2 h combustion are shown, due to the difficulty of obtaining good IR spectra of black materials. The bands in the main silica range are shown for CI07 combusted between 400 – 800 °C in Figure 2.10 and for all of the straws combusted at 500 °C in Figure 2.11. The spectra are analogous depending mainly on the year of harvesting and therefore the inorganic composition.

Carbonate species are identified by peaks between 1490 - 1410 and at 875 cm<sup>-1</sup>, all of which decrease with increasing combustion temperature correlating, with the observed decrease in calcite content based on XRD analysis (Figure 2.5).<sup>24, 25</sup> Only CI07 shows the splitting of the high frequency band into two peaks at 1463 and 1416 cm<sup>-1</sup>, whilst the other ashes display a broad band covering the same range centred at 1440 cm<sup>-1</sup>. The latter assignment correlates well with that found for calcium carbonate.<sup>24</sup> However, the low relative intensity of the carbonate peaks in the 2008 ashes suggests that these peaks may also be due to other carbonate species, perhaps particularly potassium carbonate,<sup>26</sup> although this species could not be identified in the XRD diffractograms.

For CI07, as the combustion temperature increases the shape of the silica band alters considerably (Figure 2.10). A shoulder at 1105 cm<sup>-1</sup> remains, the peak at 1021 cm<sup>-1</sup> decreases in relative intensity with new bands appearing at 983 and 935 cm<sup>-1</sup>, whilst the peak at 785 cm<sup>-1</sup> shifts to lower frequency. Similar peaks and band shapes are observed

for all of the 2009 ashes (Figure 2.11). The 2008 ashes display one broad peak centred at a higher wavenumber,  $1040\text{ cm}^{-1}$ , with a shoulder between  $1250\text{--}1150\text{ cm}^{-1}$ . All of the bands within this region are associated with the silica structure, with bands between  $1200\text{--}900\text{ cm}^{-1}$  due to Si-O stretching modes. The shape of the 2008 ashes is very similar to K60 silica gel with the main peak generally attributed to in-phase asymmetric Si-O-Si stretching and the high frequency shoulder due to the situation when oxygen atoms move  $180^\circ$  out-of-phase with one another.<sup>27, 28</sup> The greater contribution of lower frequencies to this band than is normally observed for amorphous silica is potentially due to a greater concentration of surface silanol groups.<sup>29</sup> The shoulder at  $1105\text{ cm}^{-1}$  and the peak at  $1021\text{ cm}^{-1}$  in Cl07 and the 2009 ashes can also be ascribed to the asymmetric Si-O-Si stretching modes. However, the rest of the spectra, particularly at higher combustion temperatures, appear to more similar to those of bulk silicate glasses,<sup>25, 30</sup> which frequently display a maximum or more developed shoulder at lower frequencies than observed in pure silica.<sup>30</sup> In studies of solid alkali silicate glasses by IR, lower frequency vibrations have been assigned to those of non-bridging O atoms ( $O_{nb}$ ) adjacent to alkali or alkaline earth cations,<sup>30</sup> with the concentrations of  $O_{nb}$  increasing as progressive amounts of alkali and alkaline earth metals are added.<sup>31</sup> Potassium and sodium silicates have been observed to cause a splitting of the Si- $O_{nb}$  stretching mode into two peaks whilst calcium and aluminium silicate glasses display just one broad peak at lower frequencies. Overall, this data supports the hypothesis, intimated from the differences in the background halo in the diffractograms of the different ashes, that the higher potassium, chlorine and calcium content of the 2007 and 2009 wheat straws cause the formation of alkali silicates, rather than the conversion of amorphous silica into other silica polymorphs at increased combustion temperatures. The differences in the inorganic composition appear to cause variations in the inorganic speciation at combustion temperatures as low as  $500\text{ }^\circ\text{C}$ . The potassium content, in particular, appears to have the most significant influence on the changes occurring, since the 2009 straws with lower chlorine contents display the same changes as Cl07, whilst purer silica polymorphs remain in the 2008 ashes despite similar levels of calcium to both the Cl07 and the 2009 straws.

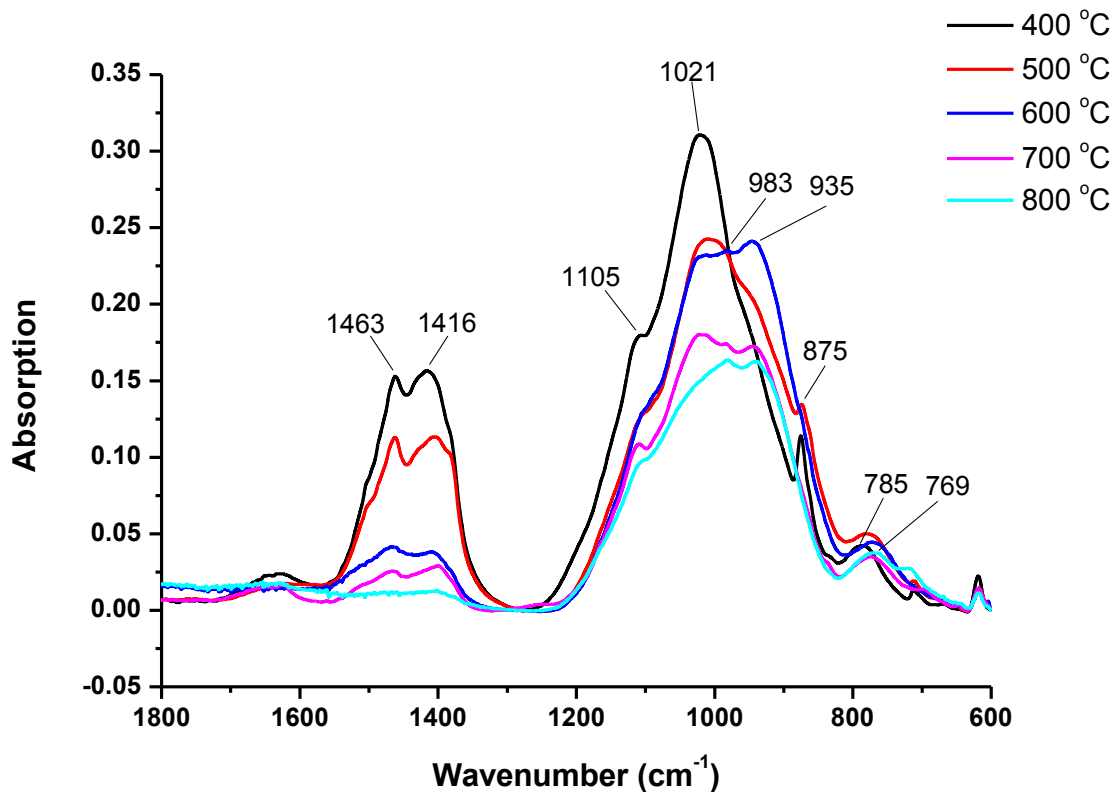


Figure 2.10: ATR-IR spectra of CI07 ashes combusted for 2 h at different temperatures (Originally in colour)

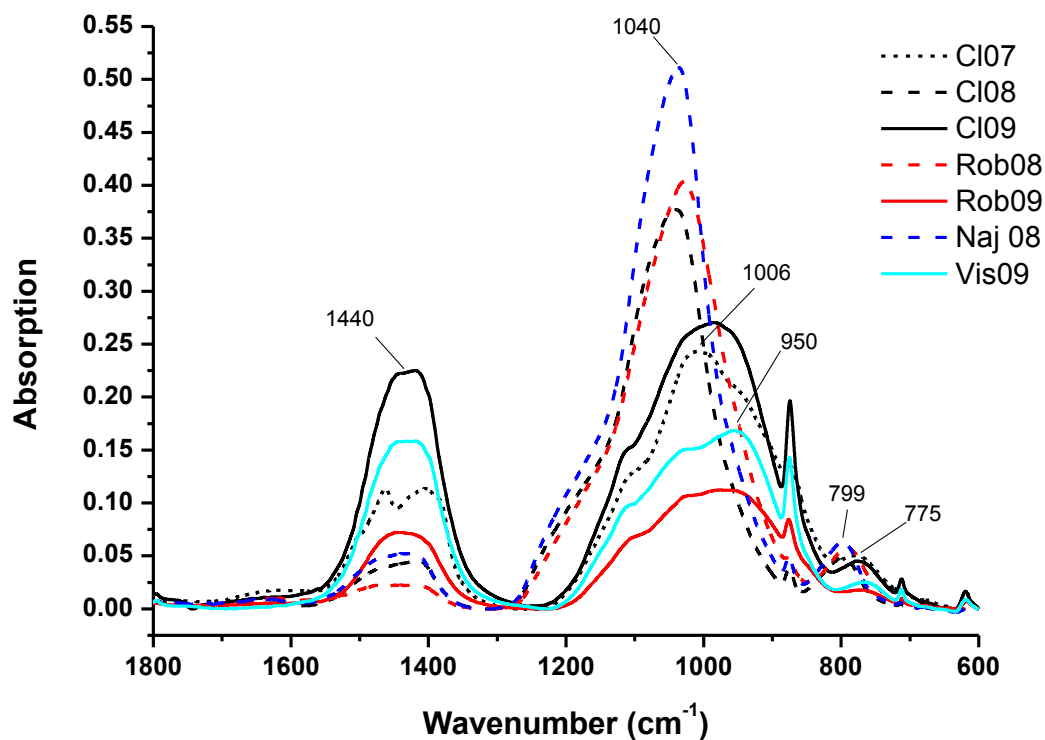


Figure 2.11: ATR-IR spectra of all wheat straw ashes combusted at 500 °C for 2 h – dotted line 2007, dashed line 2008, solid line 2009 (Originally in colour)

## **2.4 Aqueous extraction of Cl07 wheat straw combustion residues**

The chemical changes occurring within the ashes during the combustion of Cl07 were studied by ambient aqueous extraction, using a batch method similar to the Swedish standard ash leaching technique.<sup>32</sup> Following combustion the ashes were either directly quenched in water (Q) or air cooled (NQ) before adding to water to study whether the cooling conditions affected the aqueous solubility of inorganic species. In the descriptions below, shorthand labels are frequently used to express the conditions under which the solution was formed: the first number refers to the combustion temperature, the second to the combustion time in minutes and the letters to whether the ash was directly quenched in water or air cooled before extraction. For instance 400-10-Q refers to a solution formed from straw combusted at 400 °C for 10 min and then quenched in water.

The total aqueous solubility of the main inorganic species for Cl07 are shown in Table 2.4 for the absolute concentration and in Table 2.5 for the percentage of each element or species extracted. Potassium and silicon were analysed by Flame Atomic Absorption Spectroscopy (AAS), anions by Ion Chromatography (IC) and Ca, Na and Mg by Inductively Coupled Plasma – Atomic Emission Spectroscopy (ICP-AES). The main focus was on the interaction between the solubility of silica and potassium combined with the impact of other species on the solubility of K and Si. Where errors are shown these are based on triplicate extractions. These generally indicate that the values are reproducible within  $\pm 10\%$ . The errors associated with the analysis of each element in a single solution are generally in the range of 1-2%.

A gradual decline in total inorganic solubility is observed with increasing combustion temperature after only 10 minutes combustion (Figure 2.12a), indicating that immediate chemical changes are occurring in the residues, as observed by XRD. Above 500 °C there is a sharp decline in the aqueous solubility of inorganic species following 2 hours combustion (Figure 2.12b). The main species in all of these solutions are potassium, silicon, chloride, sulfate and sodium. Studying the solubility of the five major elements present in the ash, the majority of the reduction in total inorganic species extracted is due to the decreasing removal of potassium, chloride and silicon. In contrast, a slight increase in calcium solubility is detected under 800-120-Q/NQ conditions. The extraction of each of these elements individually and their interaction is discussed in more detail below.

Table 2.4: Concentration of main inorganic species in aqueous extracts from CI07 combusted and quenched under varying conditions

Time (min)	Temp (°C)	Water quenched (Q) / Air cooled (NQ)	AAS (ppm)		IC (ppm)				ICP-AES (ppm)			Total concentration (ppm)	
			K	Si	Cl	NO <sub>3</sub>	SO <sub>4</sub>	PO <sub>4</sub>	Ca	Mg	Na		
10	400	Q	3809 ± 371	1126 ± 107	1931	9	424	20	10.3	1.80	29.6	7838	
		NQ	3464 ± 33	314 ± 91	1931	4	424	39	16.5	1.48	35.0	6354	
	500	Q	3876	1324	2018	4	399	15	4.65	1.25	79.0	7605	
		NQ	3400	559									
	600	Q	3662 ± 302	919 ± 129	1664	43	242	7	1.53	0.68	71.3	7041	
		NQ	3766 ± 232	637 ± 68	1960	9	223	10	12.0	1.28	44.6	6964	
	700	Q	3185	462	1662	28	191	-	1.62	0.07	75.4	5605	
		NQ	2882	562									
	800	Q	2720 ± 90	476 ± 46	1175	11	153	-	-	-	35.7	4707	
		NQ	2926 ± 28	533 ± 7	1407	15	136	4	10.8	0.18	34.7	5101	
	120	400	Q	3679	797 ± 153	1716	3	162	23	1.83	0.43	73.5	5585
			NQ	3600	957 ± 84	1739	2	609	25	1.99	0.52	78.2	7096
500		Q	3743	776	1661	-	612	9	2.31	0.38	65.7	6869	
		NQ	3361	605									
550		Q	2762	368									
600		Q	2669	294 ± 14	1609	-	437	-	1.89	0.02	73.2	5097	
		NQ	2662	199 ± 54	1760	2	319	-	3.23	0.04	81.4	5080	
700		Q	947	142	281	4	354	-	7.43	0.16	40.4	1776	
		NQ	1184	30									
800		Q	286 ± 220	99 ± 74	24	-	290	-	54.5	-	8.35	1057	
		NQ	385 ± 171	58 ± 40	18	-	244	-	125	-	9.78	1052	

Table 2.5: Percentage of main inorganic species in aqueous extracts from CI07 combusted and quenched under varying conditions

Time (min)	Temp (°C)	Water quenched (Q) / Air cooled (NQ)	AAS (%)		IC (%)				ICP-AES (%)			Total inorganic species extracted (%)	
			K	Si	Cl	NO <sub>3</sub>	SO <sub>4</sub>	PO <sub>4</sub>	Ca	Mg	Na		
10	400	Q	76.4 ± 7.4	23.9 ± 2.2	96.3	0.014	48.4	3.74	0.58	0.94	40.4	50.2	
		NQ	70.2 ± 0.5	6.7 ± 2.0	96.3	0.007	48.4	7.38	0.93	0.78	47.8	40.7	
	500	Q	76.6	25.6	101	0.006	45.5	2.75	0.26	0.65	108	48.7	
		NQ	68.6	11.9									
	600	Q	73.1 ± 5.0	19.5 ± 2.7	83.0	0.067	27.6	1.37	0.09	0.35	97.4	45.1	
		NQ	75.9 ± 4.3	13.6 ± 1.4	97.7	0.014	25.4	1.98	0.68	0.67	60.9	44.6	
	700	Q	64.0	9.8	82.9	0.044	21.7	-	0.09	0.04	103	35.9	
		NQ	58.1	11.9									
	800	Q	54.3 ± 0.8	10.0 ± 1.2	58.6	0.018	17.4	-	-	-	48.8	30.1	
		NQ	59.1 ± 0.4	11.3 ± 0.2	70.1	0.023	15.5	0.67	0.61	0.09	47.4	32.7	
	120	400	Q	74.5	17.0 ± 3.3	85.6	0.004	18.4	4.43	0.10	0.23	100	35.8
			NQ	72.3	20.5 ± 2.2	86.7	0.004	69.4	4.67	0.11	0.27	107	45.4
500		Q	75.2	16.4	82.8	-	69.8	1.68	0.13	0.20	89.8	44.0	
		NQ	68.0	12.9									
550		Q	56.1	7.9									
600		Q	53.5	6.2 ± 0.3	80.2	-	49.8	-	0.11	0.01	100	32.6	
		NQ	53.9	4.2 ± 1.2	87.8	0.004	36.4	-	0.18	0.02	111	32.5	
700		Q	19.2	3.0	14.0	0.007	40.4	-	0.42	0.09	55.1	11.4	
		NQ	24.1	0.6									
800		Q	5.9 ± 4.6	2.1 ± 1.6	1.2	-	33.0	-	3.09	-	11.4	6.77	
		NQ	7.7 ± 3.4	1.2 ± 0.9	0.9	-	27.8	-	7.09	-	13.4	6.74	

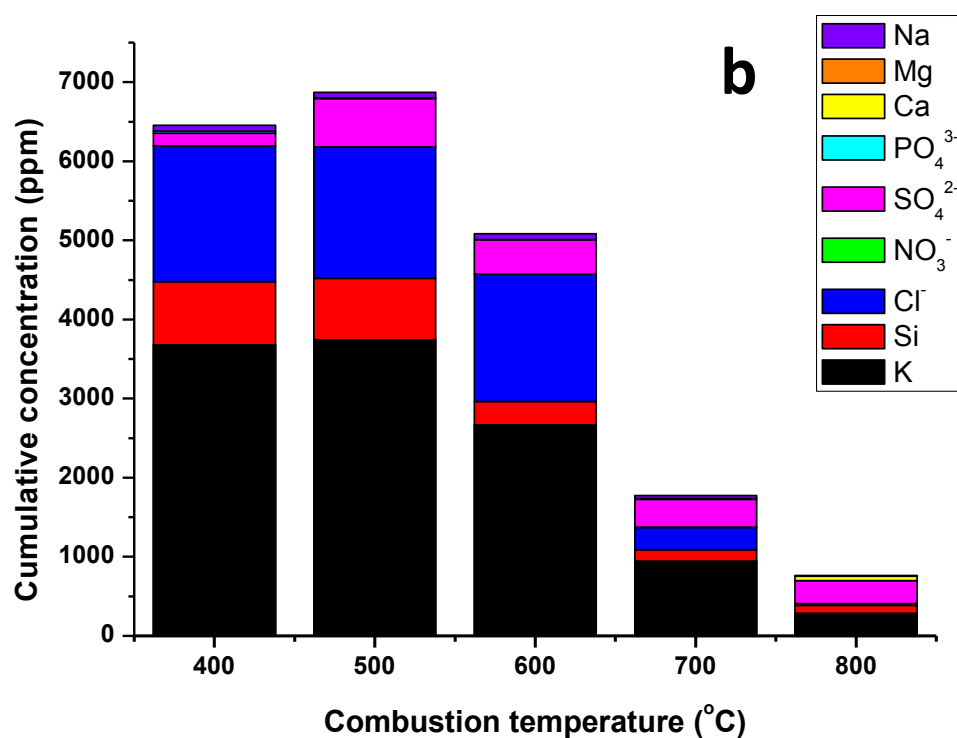
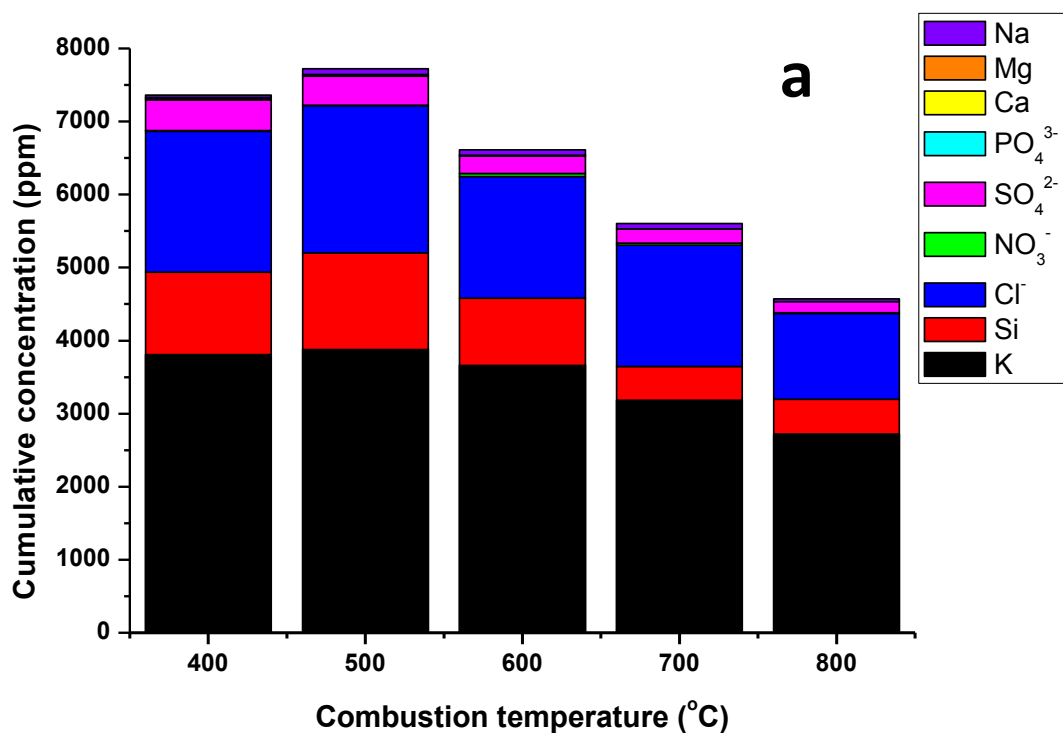


Figure 2.12: Cumulative extraction of different species from Cl07 combustion residues following water quenching (Q) after a) 10 min combustion and b) 2 h combustion (Originally in colour)

### 2.4.1 Potassium and chloride

Up to 500 °C, the solubility of both potassium and chloride remains constant irrespective of the extent of combustion or the cooling condition (Figure 2.13). Potassium extraction levels are between 70-75%, whilst chloride is close to 100% (slightly lower after 120 min combustion), similar to the extraction found for these elements during the leaching of pyrolysis chars formed at 500 °C within this study (Chapter 4) and previously.<sup>2</sup> This implies that these elements are relatively stable and are not interacting with other species at low combustion temperatures. However, the levels of potassium and chloride solubilised are lower than that of the uncombusted wheat straw (Chapter 3). The incomplete potassium extraction may be due to partial volatilisation of potassium bound to the organic matrix at temperatures < 400 °C,<sup>33</sup> although this would also be expected to affect the initial elemental analysis of the wheat straw.

Previous researchers have suggested that aqueous potassium release from pyrolysis char is controlled by diffusion of KCl and K<sub>2</sub>CO<sub>3</sub> from the ash surface, with some fixed insoluble potassium bound in the char or ash. The strong linear correlation between the potassium concentration and levels of chloride ions in solution for all of the aqueous extracts (Figure 2.14) suggests that the presence of both of these elements as KCl within the ashes strongly influences their total concentration in the solution following leaching. Sulfate concentrations, on the other hand, are generally independent of the total potassium concentration. Overall, the solubilisation of potassium as either KCl or K<sub>2</sub>SO<sub>4</sub> can only account for 60-70% of the potassium dissolved. The high pH of the solutions formed suggests that the remainder is in the form of K<sub>2</sub>CO<sub>3</sub>, KOH or K<sub>2</sub>O upon quenching.

At 600 °C and above, the availability of potassium and chloride for extraction decreases substantially with increasing combustion time and temperature, down to 6-8% for potassium and 3-7% for chloride following 2 hours combustion at 800 °C (Figure 2.13b). The reduction after 10 min combustion is not as extensive. However, the trends for each element for both water quenching and air cooling are identical suggesting little impact of the cooling condition on the solubility of these species and highlighting the reproducibility of their extraction. Surface ionisation probe studies of wheat straw pyrolysis showed a dramatic increase in alkali emissions above 500 °C from the ash component.<sup>33</sup> Molecular beam mass spectrometry of switchgrass,<sup>34</sup> another high potassium, high chloride grass,

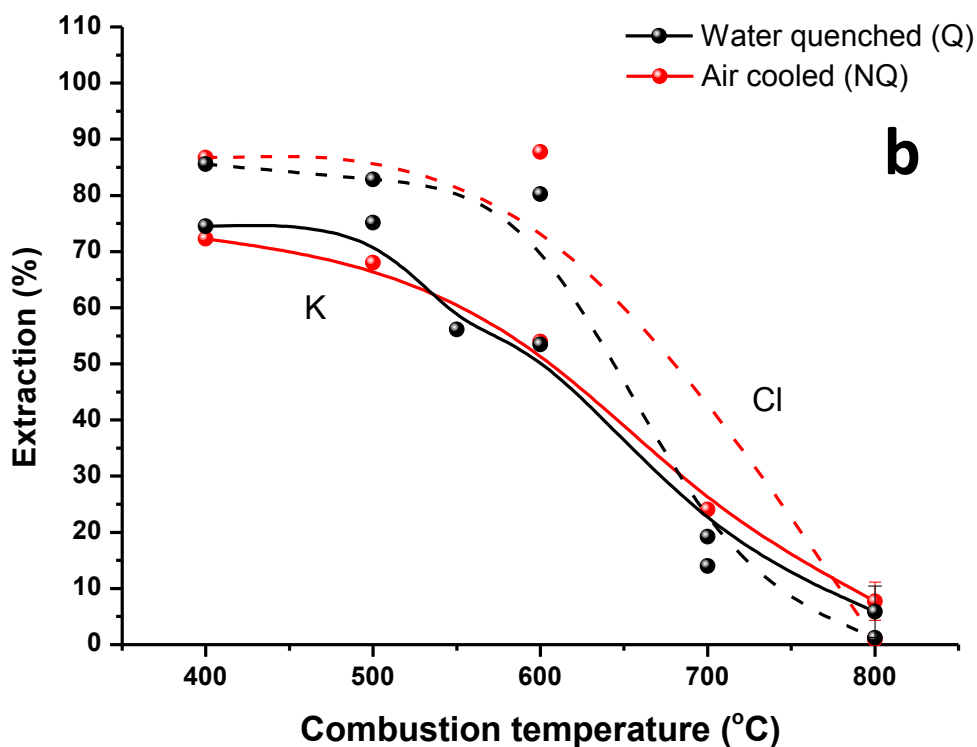
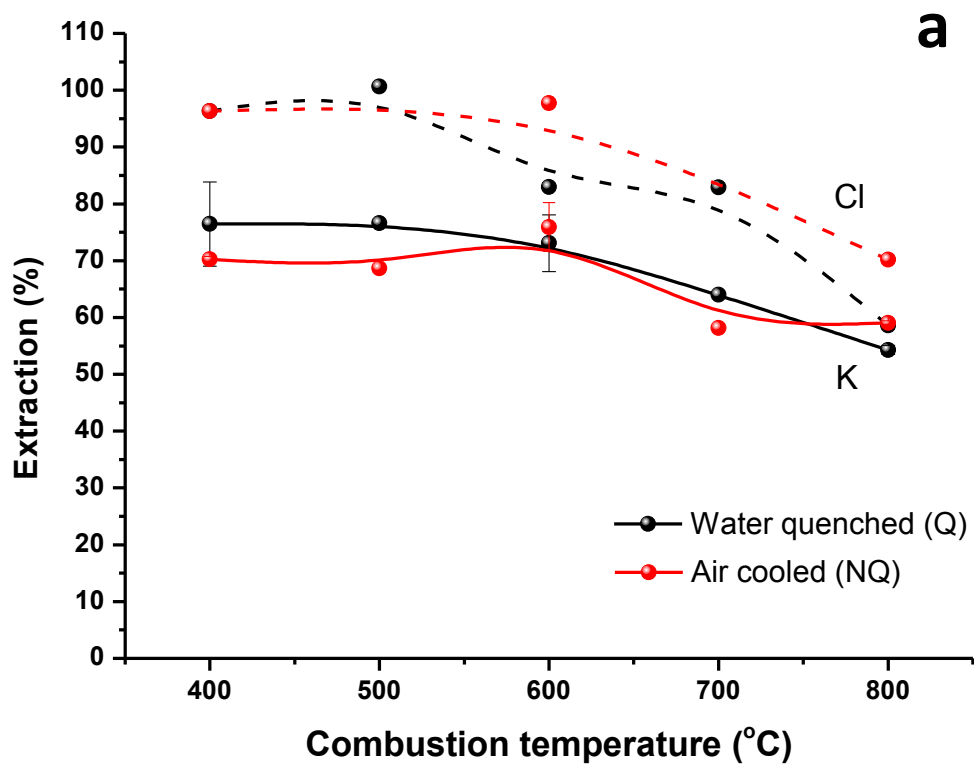
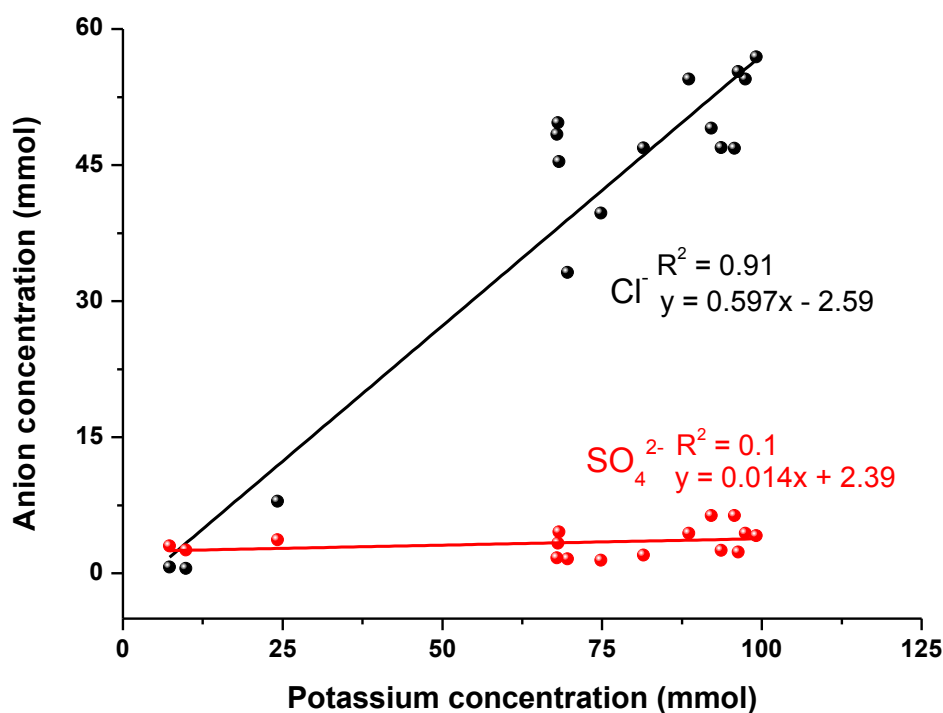


Figure 2.13: Percentage potassium (solid lines) and chloride (dashed lines) extracted from ClO7 combustion residues with varying combustion and quenching conditions a) 10 min combustion, b) 120 min combustion (Originally in colour)



**Figure 2.14: Correlation between potassium concentration and chloride and sulfate concentration in Cl07 combustion residue extracts (Originally in colour)**

identified the predominant alkali metal containing species released at 800 °C during the char combustion stage as KCl. This correlates with XRD observations in this study (Figure 2.5), which indicated a reduction in KCl content in the ashes at 700 °C and above. All of this data leads to the conclusion that potassium and chloride concentrations in the solutions are reducing at higher combustion temperatures due to KCl evaporation from the ashes.

Nevertheless, the data also suggests that not all of the potassium is volatilised as KCl. XRF analysis of the 2 h combustion ashes (Figure 2.15) shows that 67% of the initial potassium content remains in the ashes at 800 °C after 2 h combustion. This analysis is based on the assumption that no silica is volatilised during combustion. Following extraction, potassium levels remaining in the ash increase with combustion temperature, whilst all of the chloride is consistently leached from the ashes. Therefore, the levels of potassium available for extraction are not only affected by evaporation of potassium during combustion but are also due to the formation of less soluble potassium species. The broad amorphous background in the XRD spectra and the development of lower frequency peaks in the IR spectra of ashes combusted at high temperatures indicates that this is due to the formation of glass-like potassium or mixed metal silicate species which

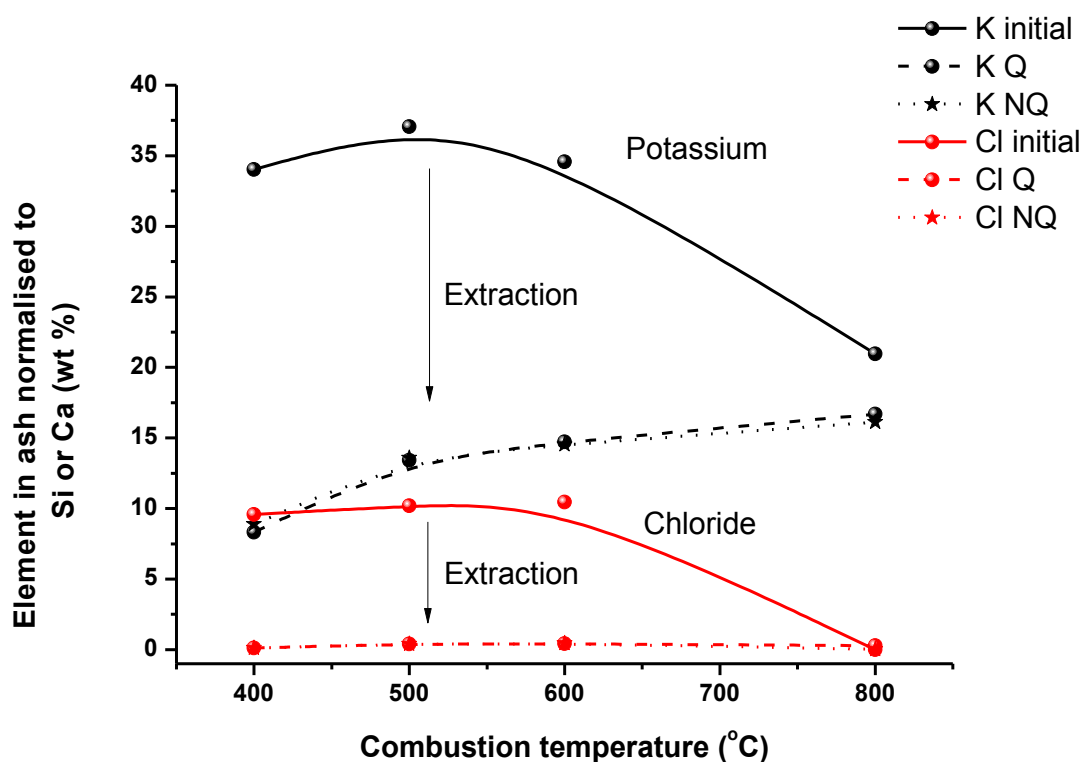


**Figure 2.15: Change in potassium and chloride in CI07 2 h ashes before and after aqueous extraction relative to the silicon content before extraction and the calcium content after extraction (based on XRF analysis) (Originally in colour)**

would be insoluble under ambient conditions. In contrast, the decrease in chloride solubility appears to be entirely due to evaporation at higher temperatures of combustion.

The concentration of sulfur in the solutions is high, with a maximum extraction of 70% after 2 hours combustion at 400 and 500 °C, similar to the extraction observed from uncombusted wheat straw by water leaching.<sup>11</sup> Soluble potassium sulfate was present in the XRD patterns up to 800 °C and has previously been identified as the most stable sulfur compound under oxidising conditions for wheat straw in equilibrium calculations.<sup>35</sup> The decreasing solubilisation of sulfur with temperature was observed by Knudsen *et al* and attributed to the dissociation of  $K_2SO_4$  and release of  $SO_2$  to the gas phase due to the preference of K and Ca to form alkali silicates at higher temperatures.<sup>35</sup> However, in this case the capture of sulfur and extraction from ashes formed at 800 °C remains high, potentially due to melting of the ash particles around the sulfate particles preventing its dissociation.

## 2.4.2 Silica

The extraction of silica varies significantly with combustion conditions. However, as hypothesised, it is possible to solubilise some of the silica present in the wheat straw ash by utilising its inherent alkalinity; up to 25% under ambient conditions (Figure 2.16).

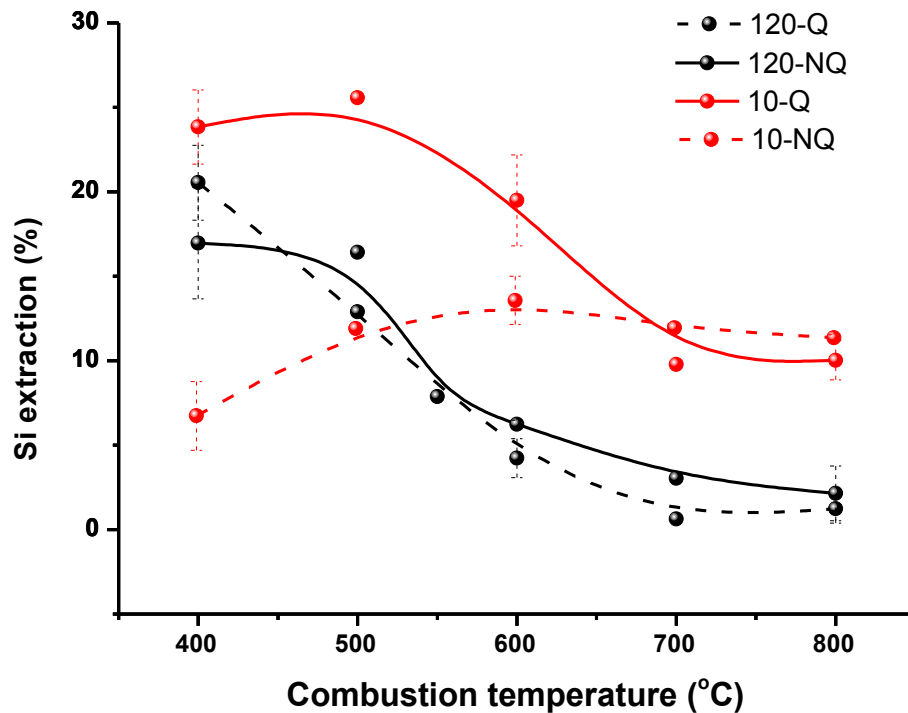


**Figure 2.16: Silica extraction from CI07 ashes under varying combustion and cooling conditions from AAS analysis of extract (Originally in colour)**

After 2 h combustion, the trend with increasing heat treatment temperature is consistent independent of the ash cooling process (black lines in Figure 2.16). However, after 10 min combustion, cooling the ash in air before aqueous extraction significantly reduces the silica solubility at lower combustion temperatures. Excluding the 10-NQ trend, generally the silica extraction decreases with increasing combustion temperature and most dramatically with both temperature and time above 500 °C. The values for the 120 min samples are consistently below those of the 10-Q ashes. A similar trend has been observed for rice hull ashes, with the most reactive silica formed at maximum combustion temperatures of 400 and 500 °C, although for these studies an alkali solution was used to study silica solubility.<sup>36</sup>

The changes in the silica solubility can be correlated with variations in the pH of the extract following the immediate addition of the combustion residues to water (initial pH)

and after 24 h extraction (final pH) (Figure 2.17). Below a combustion temperature of 600 °C, the initial pH of the solution is constant independent of the combustion and quenching conditions (apart from the 10-NQ samples). This suggests that the solubility of alkaline species is high and occurs quickly, within the first 5-10 minutes of addition of the ash to water. In addition, the maximum alkalinity of the residues is reached following combustion at 400 °C for 10 min and does not diminish either with combustion time or temperature up to 600 °C (red dots/stars, 10-30% Si extraction in Figure 2.17). For the solutions formed from low temperature combustion ashes, after 24 h extraction there is an inverse correlation between the final pH and the percentage of silica dissolved (black dots/stars, 10-30% Si extraction in Figure 2.17). This is conjectured to be due to the dissolution of silica neutralising the hydroxide present as silicate ions are formed, resulting in a lowering of the pH. The maximum levels of extraction observed coincide with the pH dropping to levels below which silica saturation concentrations drop off dramatically.<sup>37</sup>

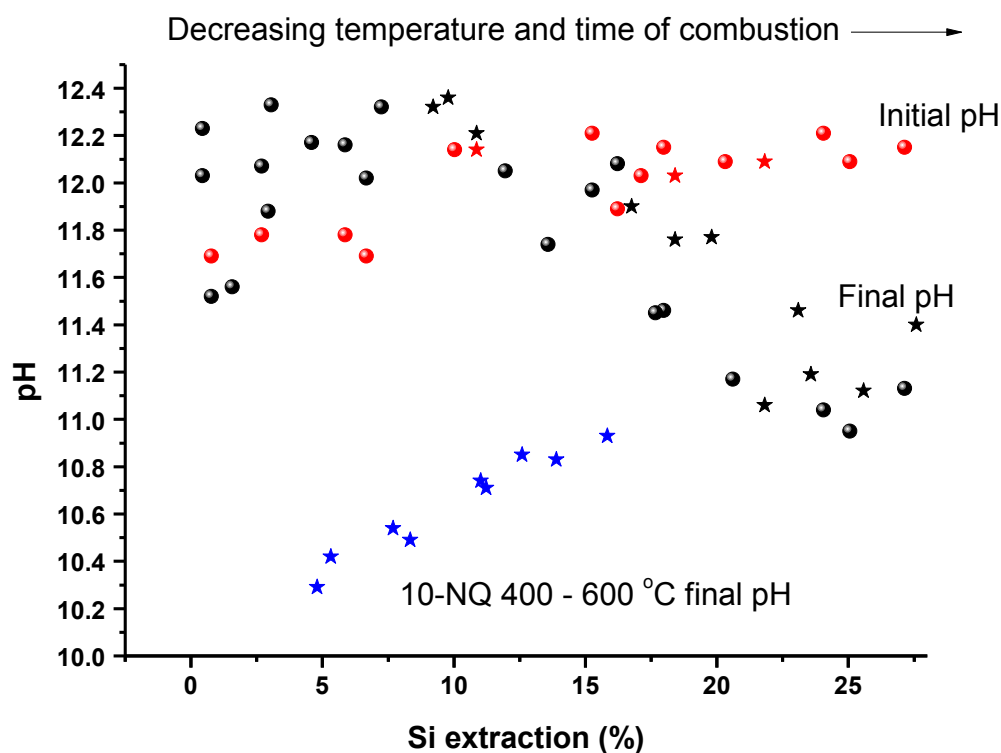


**Figure 2.17: Relationship between the pH of the extract solution and silica extraction across all combustion and cooling conditions. Red dots – initial pH of 120-Q/NQ solutions; black dots – final pH of 120-Q/NQ solutions; Red stars - initial pH of 10-Q solutions; Black stars - final pH of 10-Q solutions; Blue stars – final pH of solutions formed from ashes combusted for 10 min between 400–600 °C and cooled in air before extraction (Originally in colour)**

This trend only breaks down above 600 °C with 2 h combustion. For these solutions the initial pH decreases with increasing combustion temperature (red dots, 0-10 % Si extraction in Figure 2.17), which can be linked to mineralogical changes in the ashes decreasing the concentration of alkaline potassium species (Figure 2.13b). This will lower the maximum dissolution of silica since fewer silicate ions are formed, causing saturation of the solution with monosilicic acid to occur more quickly. However, for these solutions the pH actually increases during extraction. This is proposed to be due to the slower solubilisation of calcium species. Calcium concentrations in the extracts are extremely low for all solutions, but increase marginally above 700 °C for ashes combusted for 2 h (Table 2.4). This can be correlated with the decomposition of calcium carbonate at higher temperatures and longer times of combustion, as observed by XRD (Figure 2.5). However, despite the absence of calcite in the XRD pattern above 600 °C, the low concentration of calcium in these ash solutions could be caused by the reaction of calcium with silica in solution. Insoluble calcium silicate precipitates would be formed, removing both calcium and silicon from the solution and thereby contributing to the lowering of the silica concentration in the solutions of ashes combusted at 600 °C or above.

The 10-NQ silica vs pH trend reveals further details about the reasons for the low solubility of these samples following air cooling. The initial and final pH's of these solutions are much lower than the 10-Q samples (red and black stars in Figure 2.17), with the final pH reducing below the point at which solid amorphous silica can remain in equilibrium with silicic acid and silicate anions (below 700 °C) (blue stars in Figure 2.17). The total solubility is therefore pH limited, with the silica concentration-pH trend correlating well with that observed for pure amorphous silica (Figure 2.18).<sup>37</sup> The explanation for the lower pH of these 10-NQ samples is discussed in more detail below.

This data suggests that the extraction of silica is only pH limited for 10-NQ samples combusted below 700 °C and perhaps towards the maximum extraction levels observed of ~25%. Where the silica solubility is lower, other factors must therefore be influencing the outcome.

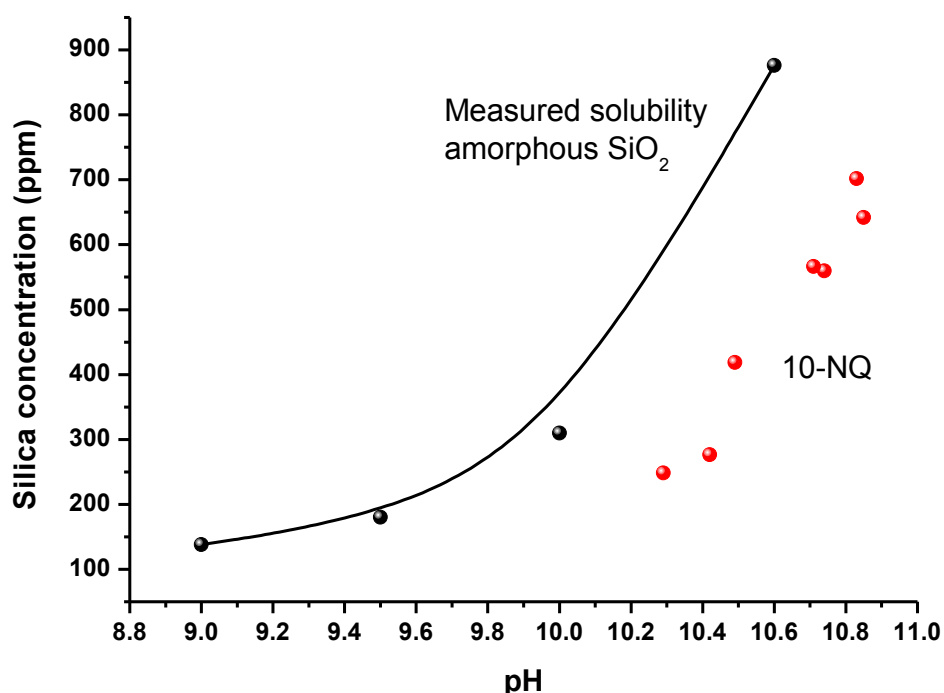


**Figure 2.18: Correlation between pH and equilibrium silica concentration for pure amorphous silica in an alkaline solution (black)<sup>37</sup> and wheat straw ash extracts after 10 min combustion and air cooling (red) (Originally in colour)**

#### 2.4.2.1 <sup>29</sup>Si NMR

The decrease in the solubility of silica can also be linked to changes in the silica structure during combustion. In general, as the temperature of combustion increases amorphous silica becomes more crystalline. Quartz peaks were observed in the XRD patterns above 500 °C (Figure 2.5). This is less soluble than amorphous silica owing to its tightly packed structure, making it more resistant to attack by hydroxide ions.<sup>37</sup> <sup>29</sup>Si MAS NMR can show in greater detail changes occurring in the silica structure within a solid. Spectra were obtained for ashes combusted for 2 h before and after extraction (Figure 2.19). Due to the dilution of silica by the residual carbon, spectra were not obtained after 10 min combustion. With a combustion temperature of 400 °C the spectra are broad, with silica species distributed relatively evenly between Q<sup>2</sup>, Q<sup>3</sup> and Q<sup>4</sup> sites (Figure 2.19a). This suggests an amorphous silica structure with large variations in Si-O-Si bond angles and large numbers of terminal silanol groups around a central silica network. The silanol groups are the reactive sites for OH<sup>-</sup> attack, enabling dissolution to occur with relative ease. As the temperature of combustion increases the Q<sup>4</sup> peak reduces and a broad

uniform peak remains at a lower chemical shift with majority  $Q^3$  character. The peak maxima shifts from -97.4 ppm at 400 °C to -94.4 ppm at 700 °C. This is in contrast to studies on rice hull ashes (RHA).<sup>38</sup>  $^{29}\text{Si}$  NMR of RHA show a similar broad spectra initially that narrows and displays increasing  $Q^4$  character at higher temperatures of combustion as more crystalline cristobalite forms.<sup>38</sup> In this study on wheat straw ashes, the XRD and IR data intimate that the variation is instead due to the formation of glass-like alkali silicates at higher heating temperatures with either K or Ca as the counter ion at the terminating group. The  $^{29}\text{Si}$  NMR spectra further support this proposition. The addition of increasing amounts of alkali and alkaline earth metals to  $\text{SiO}_2$  has previously been shown to cause the progressive formation of non-bonding oxygen sites and therefore a reduction in  $Q^4$  species and consequently a downfield chemical shift.<sup>31, 39</sup> The broad linewidths indicate the presence of a disordered structure with a wide variety of Si-O-Si bond angles rather than the development of crystalline silicate structures.

Following extraction (Figure 2.19b) there is an increase in the concentration of  $Q^4$  sites relative to  $Q^3$  and  $Q^2$  sites. As the combustion temperature increases there is less variation between the spectra before and after extraction, which corresponds to lower levels of silica dissolution. This data indicates that extraction of silica is occurring with attack of hydroxide ions at the terminal silanol sites in agreement with the accepted mechanism of silica dissolution.<sup>37</sup> The continued presence of  $Q^1$ - $Q^3$  sites suggests that further silica is available for dissolution, although the silica at  $Q^4$  sites may need more aggressive conditions and longer time-frames to dissolve.

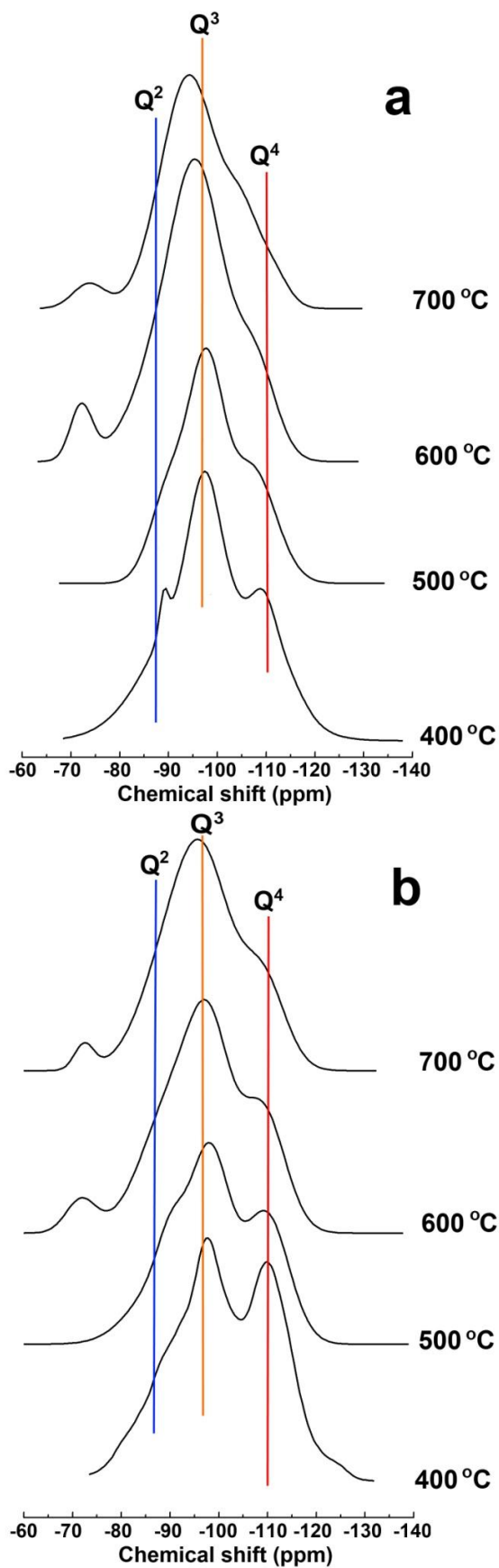


Figure 2.19: Solid state  $^{29}\text{Si}$  NMR of CI07 wheat straw ashes combusted between 400 – 700 °C for 2 h (a) before and (b) after extraction (Originally in colour)

## **2.5 Higher temperatures of extraction and added alkali**

The data laid out above indicates that optimum aqueous silica extraction from CI07 wheat straw ash, using the inherent alkali under ambient conditions, is achieved with temperatures of combustion at or below 500 °C. It was therefore decided to combust wheat straw at 500 °C and study the impact of other factors on the extraction of SiO<sub>2</sub> from wheat straw ashes. Studies were taken forward on straw combusted for 2 h and water quenched (Q) ash. The cooling process was shown not to impact on the dissolution of inorganic species after 2 h combustion. However, since ashes in commercial combustion systems are frequently directly quenched in water, this method was chosen.

### **2.5.1 Effect of extraction temperature**

The marked effect of extraction temperature on silica dissolution is highlighted in Figure 2.20 for 500-120-Q ashes, quenched in either water or a 0.1 M KOH solution. In aqueous solutions the total dissolution increases from  $16.4 \pm 0.1\%$  at room temperature to  $36.1 \pm 1.1\%$  under reflux. This is consistent with the increasing solubility of SiO<sub>2</sub> at higher temperatures.<sup>37</sup> Increasing the extraction temperature within a sealed pressure unit to 160 °C did not increase the silica extraction further, and therefore the influence of higher temperatures was not pursued. In addition, at higher temperatures amorphous silica may begin to crystallise, reducing its solubility.<sup>37</sup> The use of a 0.1 M KOH solution rather than water increases the extraction of silica even further, but follows the same solubility trend as for water with extraction temperature, reaching a maximum silica dissolution of  $60.7 \pm 3.6\%$ .

The temperature of extraction appears to have less impact on the other major species in solution (Figure 2.21). There are some variations in the absolute concentrations but no clear trends. Only nitrate appears to show a steady increase in concentration with increasing extraction temperature for both the water and KOH solvents.

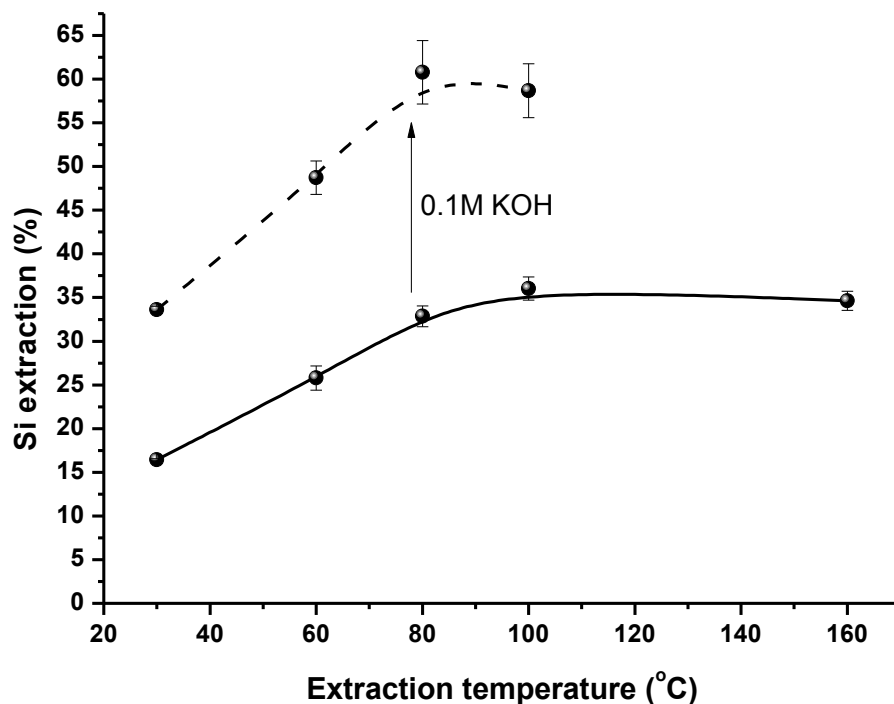


Figure 2.20: Influence of extraction temperature on Si extraction from Cl07 wheat straw combusted at 500 °C for 2 h extracted in water (solid line) or a 0.1M KOH solution (dashed line)

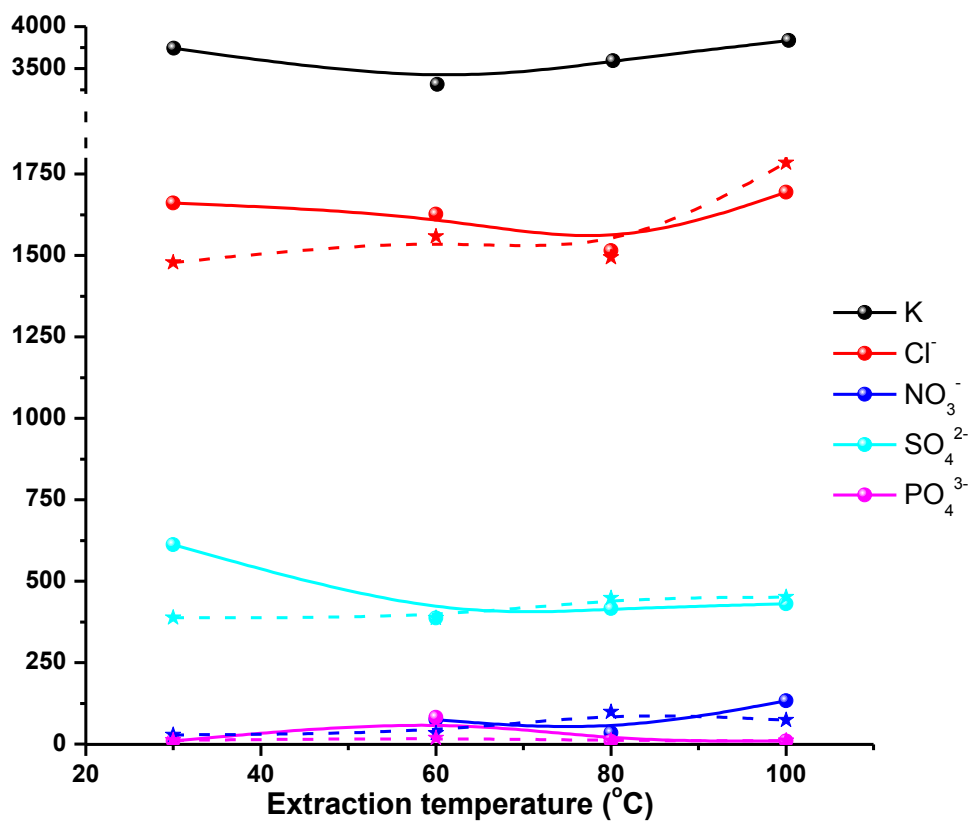


Figure 2.21: Concentrations of other elements in solutions from extractions of Cl07 wheat straw ash combusted at 500 °C for 2 h extracted in water (solid line) or a 0.1M KOH solution (dashed line) at different temperatures (Originally in colour)

## 2.5.2 Effect of KOH concentration

The data above demonstrated that the use of a more alkaline extraction solution increased the silica extraction significantly without affecting the release of the other major species. The variation of Si,  $\text{Cl}^-$ ,  $\text{NO}_3^-$ ,  $\text{SO}_4^{2-}$  and  $\text{PO}_4^{3-}$  with varying KOH concentrations are shown in Figure 2.22 for 500-120-Q ashes extracted under reflux for 24 h.

Silica extraction increases marginally with increasing KOH concentration from ~60% to ~65%, however, this is mainly within the margin of error. The impact on the other species is equally minor, although the concentration of  $\text{NO}_3^-$  does appear to increase with increasing KOH concentration. This data indicates that a portion of the silica present in the ashes is insoluble even under highly alkaline and high temperature conditions.

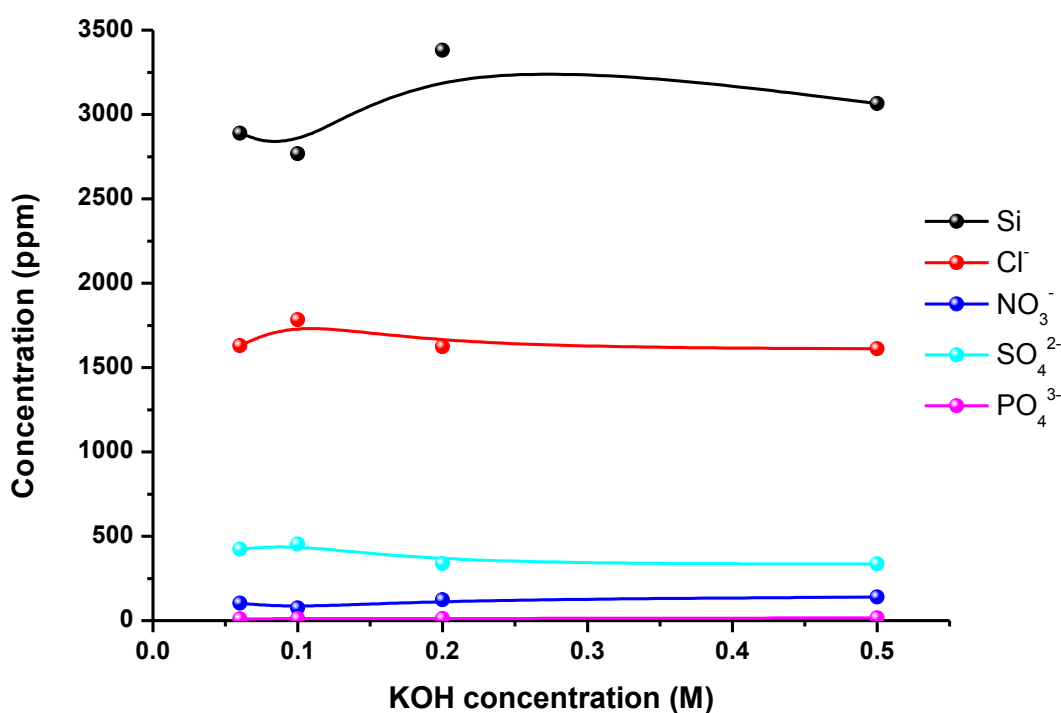


Figure 2.22: Effect of KOH solution concentration on the extraction of various elements from Cl07 500-120-Q ashes (Originally in colour)

## 2.6 Kinetics

A study of 500-120-Q Cl07 ash extracted at room temperature and under reflux over time (Figure 2.23) showed that after 24 h the equilibrium concentrations of both potassium and silicon had been achieved. Potassium extraction was extremely rapid, with the maximum concentration reached within 2 h. The silica removal lagged slightly behind, however, around 70 - 80% of the total silica was leached within 1 h with the remainder extracted over the following few hours. The rate of extraction doesn't appear to alter with leaching temperature, although the maximum levels of extraction do. This data contrasts with that observed for wheat straw char pyrolysed at 500 °C where potassium dissolution was observed to proceed with an initial fast release followed by a secondary slow release mechanism over several hours.<sup>2</sup> The latter was attributed to diffusion limited release from the solid matrix. More data would need to be obtained between 0 – 1 h extraction times in order to develop an accurate kinetic model for dissolution of K and Si from these wheat straw ashes.

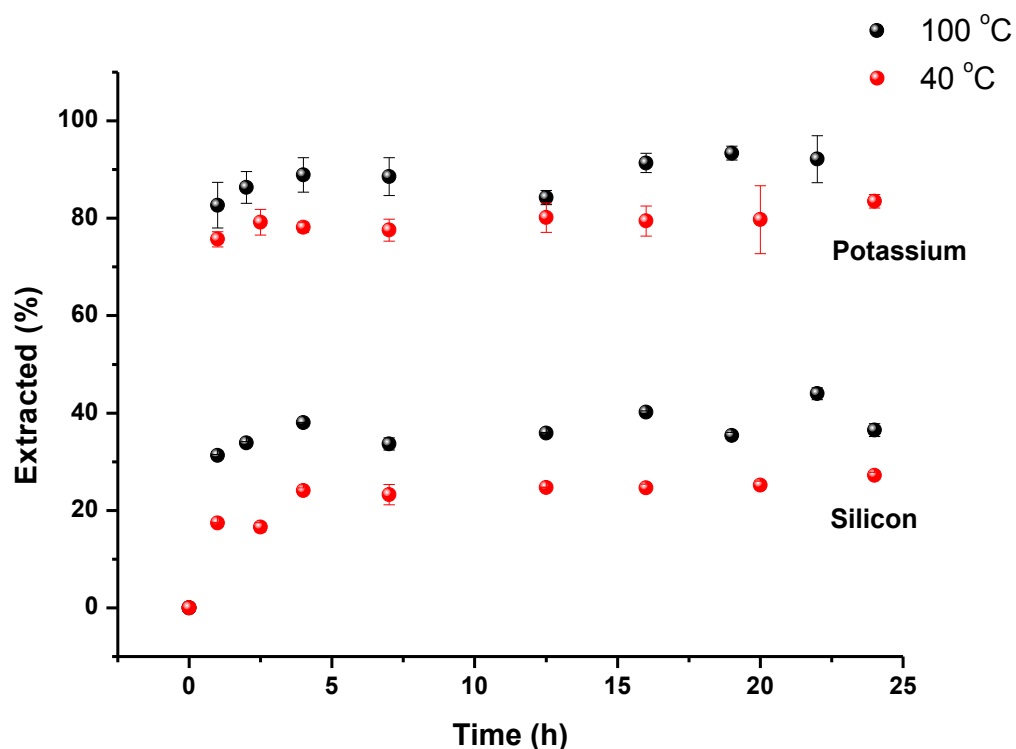


Figure 2.23: Extraction of potassium and silicon from Cl07 ash (500-120-Q) at 40 °C (red) and 100 °C (black) over time using a water solution (Originally in colour)

The data does, however, highlight the reproducibility of the extraction for each element as each point is from a separate batch sample due to the sample size required for analysis, the removal of which would have substantially altered the solid/liquid ratio. For the room temperature samples, above 4 h, the average silica extraction was  $24.8 \pm 1.4\%$  with potassium at  $74.9 \pm 1.8\%$ . Under reflux the values were  $37.7 \pm 3.5\%$  and  $84.2 \pm 3.1\%$  respectively. This more detailed study does, therefore, show a consistent increase in potassium solubility with a higher temperature of extraction compared to the data in Figure 2.21.

## 2.7 Varying wheat straw variety

The optimised silica extraction based on the above data was compared with the extraction of inorganic species obtained from the ashes of the other varieties of wheat straw. The parameters used were: 500 °C combustion for 2 h; quenched in extractant; heated under reflux for 24 h. An initial straw to solvent ratio of 1:2.5 w/v was used in all cases. The solvents tested were water and KOH solutions. The concentrations of the KOH solutions were calculated to determine whether the same percentage of silica could be extracted based on knowledge of the initial elemental content of the straws. The calculation was made on the basis of the additional K<sub>2</sub>O that would need to be added to produce a solution with SiO<sub>2</sub>:K<sub>2</sub>O wt ratio of 1.4 (that of an alkaline commercial potassium silicate solution) assuming that only 70% of the K present was soluble (based on the data presented above) and that all of the Cl and SO<sub>3</sub> analysed in the ashes was present as KCl or K<sub>2</sub>SO<sub>4</sub>, thereby reducing the availability of potassium to form an alkaline solution.

The percentage silica extracted using both water and KOH from the ashes of several varieties of wheat straw are shown in Figure 2.24 (Nijinsky 08 was not tested using a KOH solution). The silica extraction using only water fluctuates extensively, particularly based on the year of harvesting. Direct correlations between the silica concentration and either the potassium concentration (excluding K as KCl, K<sub>2</sub>SO<sub>4</sub>, KNO<sub>3</sub> and K<sub>3</sub>PO<sub>4</sub>) or the pH of the solutions can be drawn when the values for the different wheat straw varieties are combined (Figure 2.25). More points would be needed to show whether both relationships are truly linear, however, they do emphasise that the silica extraction increases with the pH of the initial solution and that this directly links to the concentration of potassium in the solution. The silica extraction can, therefore, be directly

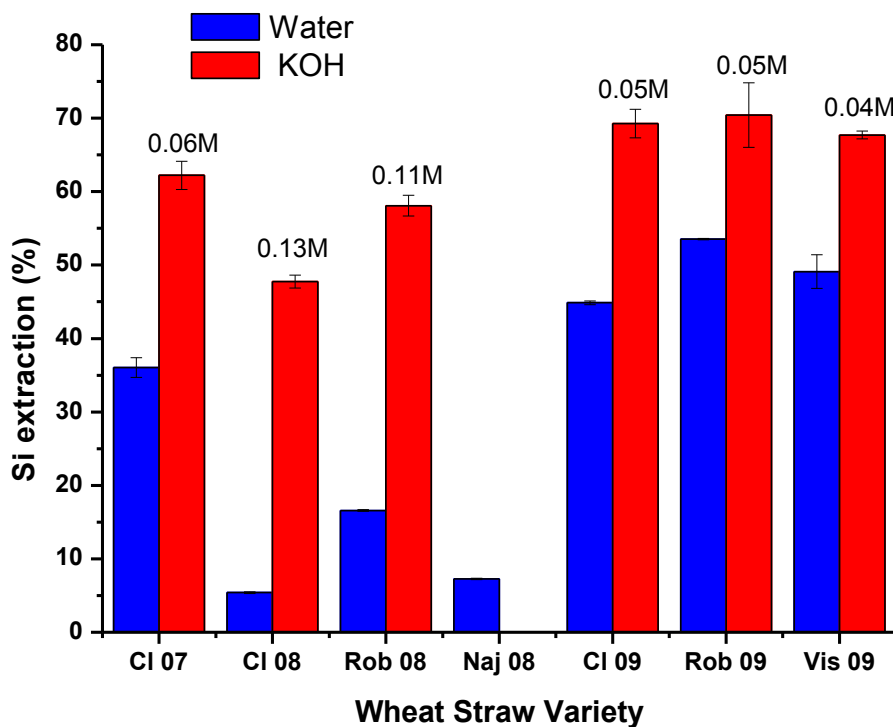


Figure 2.24: Effect of water and KOH solutions on silica extraction from wheat straw varieties all combusted at 500 °C for 2 h (Originally in colour)

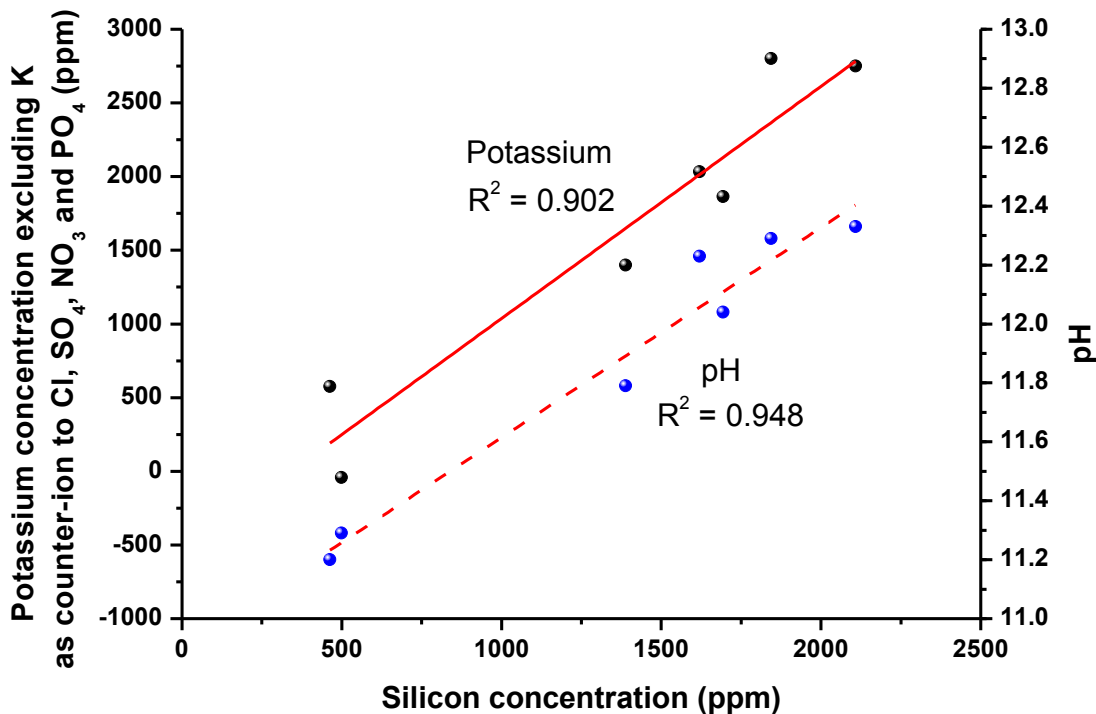


Figure 2.25: Correlation between the Si concentration of the water extract solution and potassium concentration and initial pH following the extraction of 500-120-Q ashes of various wheat straw varieties (Originally in colour)

associated to the inorganic composition of the ashes and the expected extraction could potentially be calculated based on the initial analyses of the ashes.

The extraction of the other major soluble species in the wheat straw ashes (Figure 2.26) also demonstrates a strong correlation with their initial concentrations in the ashes (Table 2.1), particularly identifiable by the relatively stable percentage extraction of K and Cl (Figure 2.26b), despite the large fluctuations in absolute concentration in the solution (Figure 2.26a). The level of potassium extracted from all wheat straw ashes is consistent at between 70 – 80%, supporting the assumption employed for the determination of the concentrations of the KOH solutions to use. The level of chloride removed is also consistently high. The values over 100% are due to the low level of chloride present in the initial ashes and therefore the greater level of error introduced in calculating their percentage dissolution. Sulfate dissolution fluctuates extensively between 20 – 90%. The exact reason for this is unknown. It may be due to differences in the level of sulfur organically associated in the different varieties of wheat straw or the degree of volatilisation of sulfur from the different ashes at 500 °C, which is believed to be dependent on the interaction of K and Ca with other species in the ashes.<sup>35</sup>

Silica extraction increases for all ashes when a solution of KOH is used (Figure 2.24). The calculated KOH solution concentrations increase the extraction to between 60 – 70% for the majority of the straw varieties. It was expected that the 2008 straws might display higher levels of total silica dissolution due to their greater amorphous character as indicated by XRD data (Figure 2.7), however, this was not observed. The 2008 solutions displayed a greater reduction in pH during the extraction, which could hint that insufficient alkalinity was present for complete solubilisation. However, overall this data indicates that from a knowledge of the initial inorganic composition it is possible to calculate the level of additional alkali needed to achieve similar levels of silica solubilisation.

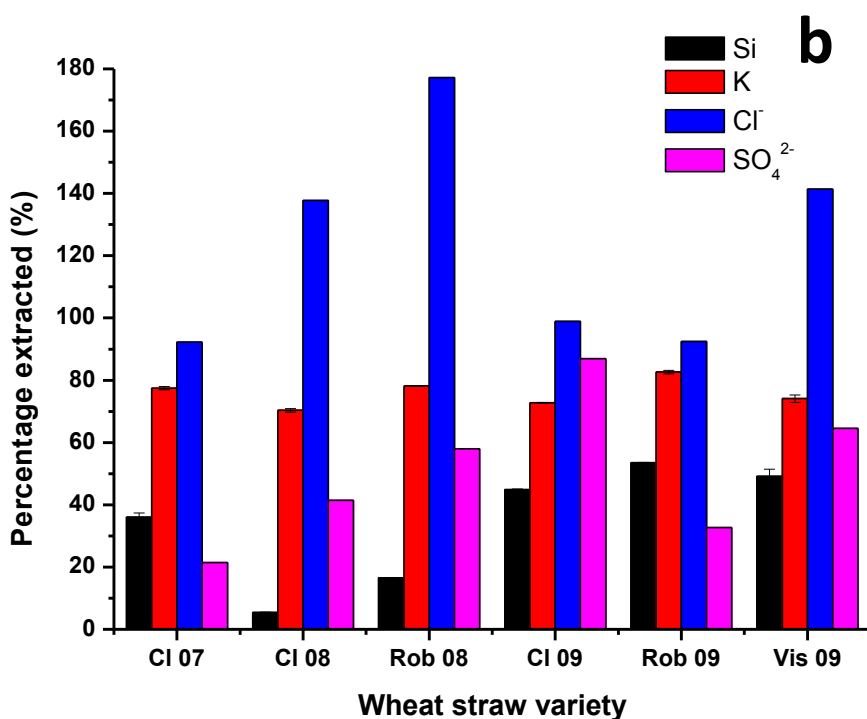
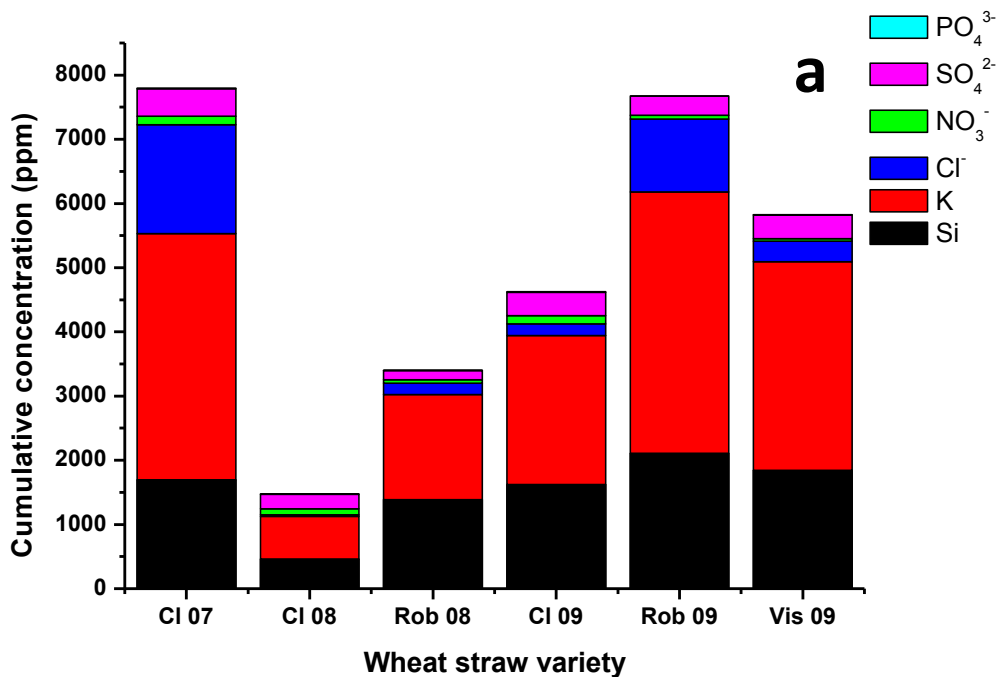
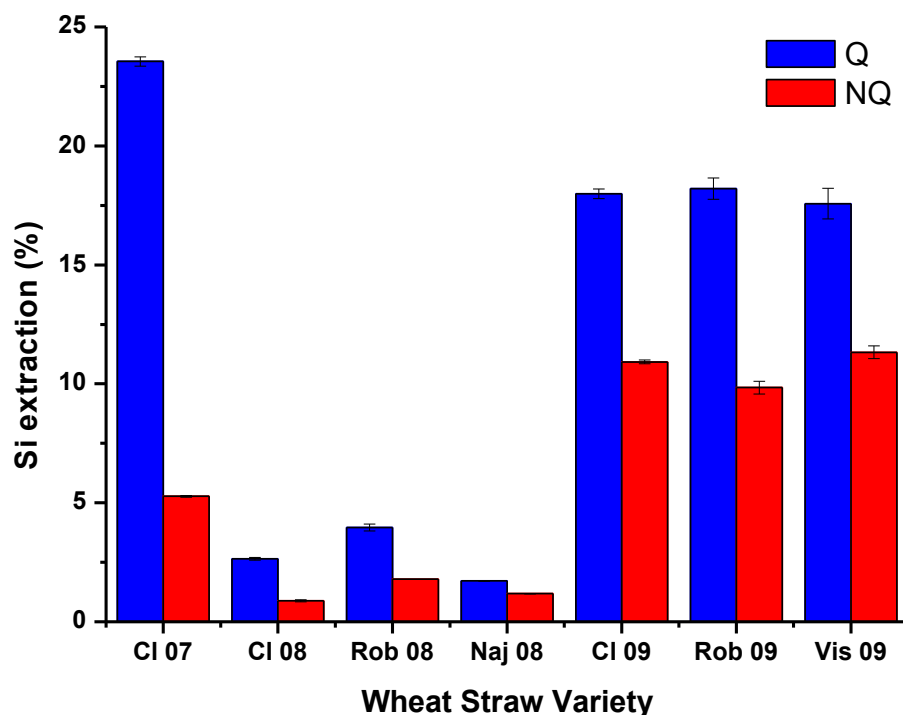


Figure 2.26: Inorganic species extracted from different wheat straw ashes combusted at 500 °C 2h and extracted under reflux in water a) cumulative concentration and b) percentage extracted (Originally in colour)

## 2.8 Incomplete combustion – effect of water quenching vs air cooling

To study the anomalously low silica extraction for wheat straw (WS) combusted for 10 min and cooled in air at low combustion temperatures, a comparison was initially made between all of the wheat straw varieties to study whether this difference was universal (Figure 2.27). From these results it can be observed that all seven wheat straw samples display a reduced silica dissolution when partially combusted at 400 °C for 10 min and cooled in air rather than directly quenched in water. The difference is particularly striking for CI07 with a 78% reduction, however, for the 2008 samples the decrease is between 32 – 67% and for the 2009 straws between 36 – 46%.



**Figure 2.27: All wheat straw varieties combusted at 400 °C for 10 min showing the effect of water quenching (Q) versus air cooling (NQ) on silica extraction (Originally in colour)**

For the majority of these varieties the initial pH on addition of the residue to water is lower in the case of the air cooled samples (Figure 2.28) and reduces further during extraction than for the water quenched samples. For the 2009 WS samples the final NQ pH values do not fall below the threshold (pH 10.7) at which an equilibrium between solid amorphous silica and dissolved monomeric silicic acid exists, enabling a higher silica concentration to be attained than for CI07. Silica solubility is correlated with pH and therefore the lower silica concentrations found in the 400-10-NQ solutions can be

attributed to the lower initial and final pH's of the solutions. However, the cause of this decrease must be examined in more detail.

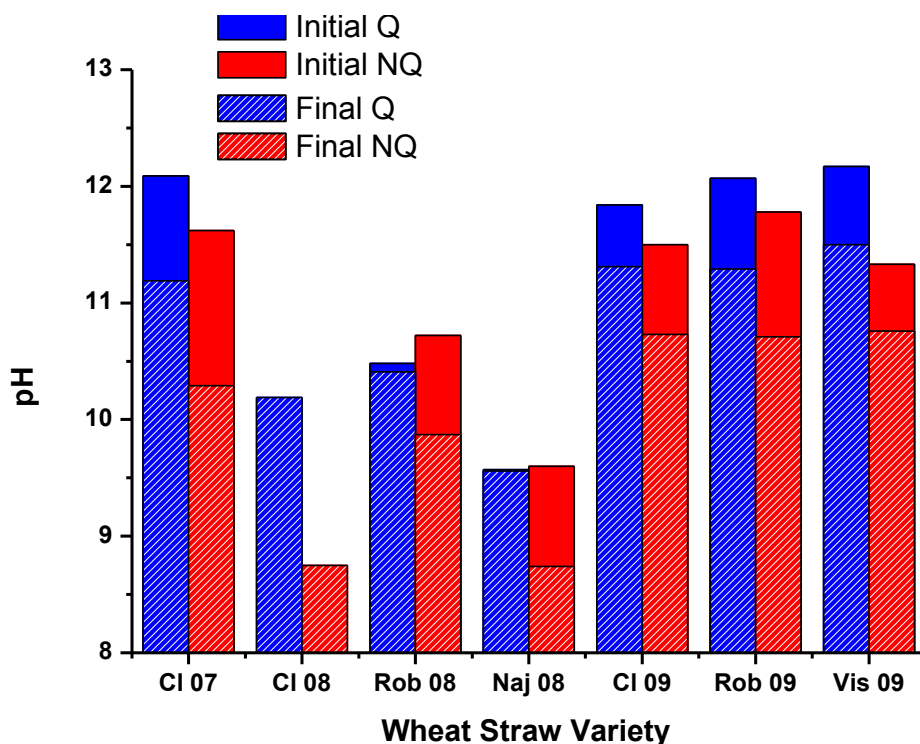


**Figure 2.28: All wheat straw varieties combusted at 400 °C for 10 min showing the effect of water quenching (Q) versus air cooling (NQ) on the initial (solid) and final (hashed) pH of the extraction solution (Originally in colour)**

Focusing on CI07, the data shows that if the combustion time is increased at 400 °C (Figure 2.29a), the difference in the silica dissolution between the Q and NQ samples reduces. Furthermore, cooling under argon as opposed to cooling under air produces the same silica extraction as directly quenching in water (Figure 2.29b). The latter results were obtained by combustion of the straw in a quartz flask to enable control of the atmosphere on cooling. This may have resulted in a slightly different combustion rate and therefore have caused the higher levels of silica extraction compared to combustion in an open vessel.

Consistently, the NQ solutions are characterised by lower initial and final pH's. This indicates that a more acidic/less alkaline residue is formed only in the presence of air, suggesting a continued oxidative process on cooling, with the effect lessening with

increased combustion, suggesting that the effect is due to organic components rather than changes in the inorganic species upon cooling. The NQ solutions are more highly coloured (Figure 2.30a), and a darker coloured residue if formed upon evaporation (Figure 2.30b). The solution colouring is reduced by oxidation with  $H_2O_2$ , indicating the presence of organic species.

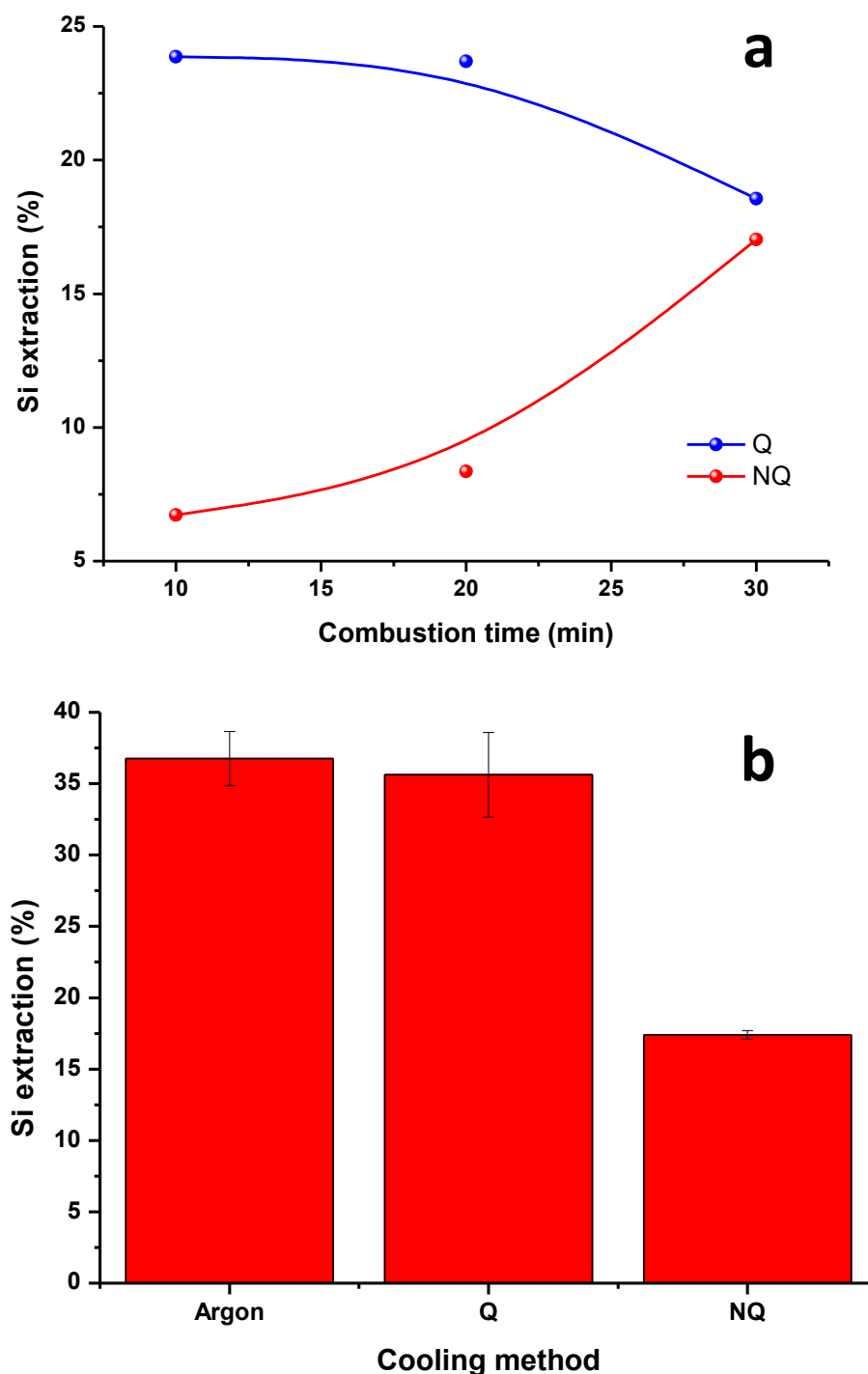
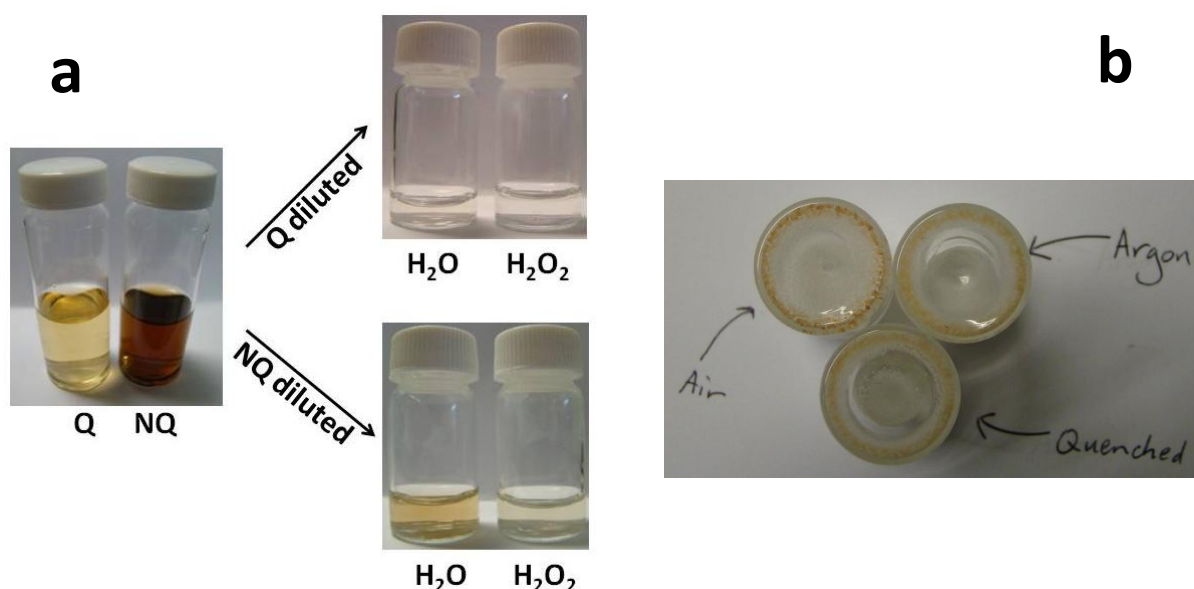


Figure 2.29: Effect of a) time and b) cooling method on the silica extraction from ClO7 400-10-Q/NQ combustion residues (Originally in colour)



**Figure 2.30: a) Colour of Cl07 400-10-Q/NQ solutions before and after oxidation by H<sub>2</sub>O<sub>2</sub>  
 b) colour of residue following the evaporation of extraction solutions from 400-10 combustion residues cooled under different conditions before extraction (Originally in colour)**

<sup>1</sup>H NMR of the solutions formed from the dissolution of the solid residues from the evaporation of Cl07 400-10-Q and NQ solutions (Figure 2.30b) in D<sub>2</sub>O further highlights a significant difference in the concentration of organic components extracted from the NQ ashes (Figure 2.31). In general, the peaks and their relative intensities are similar for both <sup>1</sup>H NMR spectra, however, all are more intense for the NQ solution (Figure 2.31b), except in the aromatic region. Although, specific compounds cannot be identified from these spectra, the peaks at 1.8 – 2.2 ppm indicate that a greater proportion of molecules containing weak electron withdrawing groups such as esters, carboxylic acids, ketones, aldehydes or alkenes are present in the NQ sample. The presence of alkenes is further supported by the peak at 5.0 ppm. The lack of any peaks between 10 – 12 ppm, in the carboxylic acid region, may be due to rapid exchange between <sup>2</sup>H and <sup>1</sup>H atoms. Unfortunately, the concentrations of the solutions were too low to gain any meaningful data via <sup>13</sup>C NMR. Nevertheless, the bulk of the evidence points towards oxidation continuing during air cooling, resulting in the increased solubility of organic components, potentially including acidic compounds, reducing the alkalinity of the solutions and therefore the silica solubility. As combustion temperatures and times increase these more reactive or volatile organic compounds are no longer formed, reducing their impact on the solution chemistry.

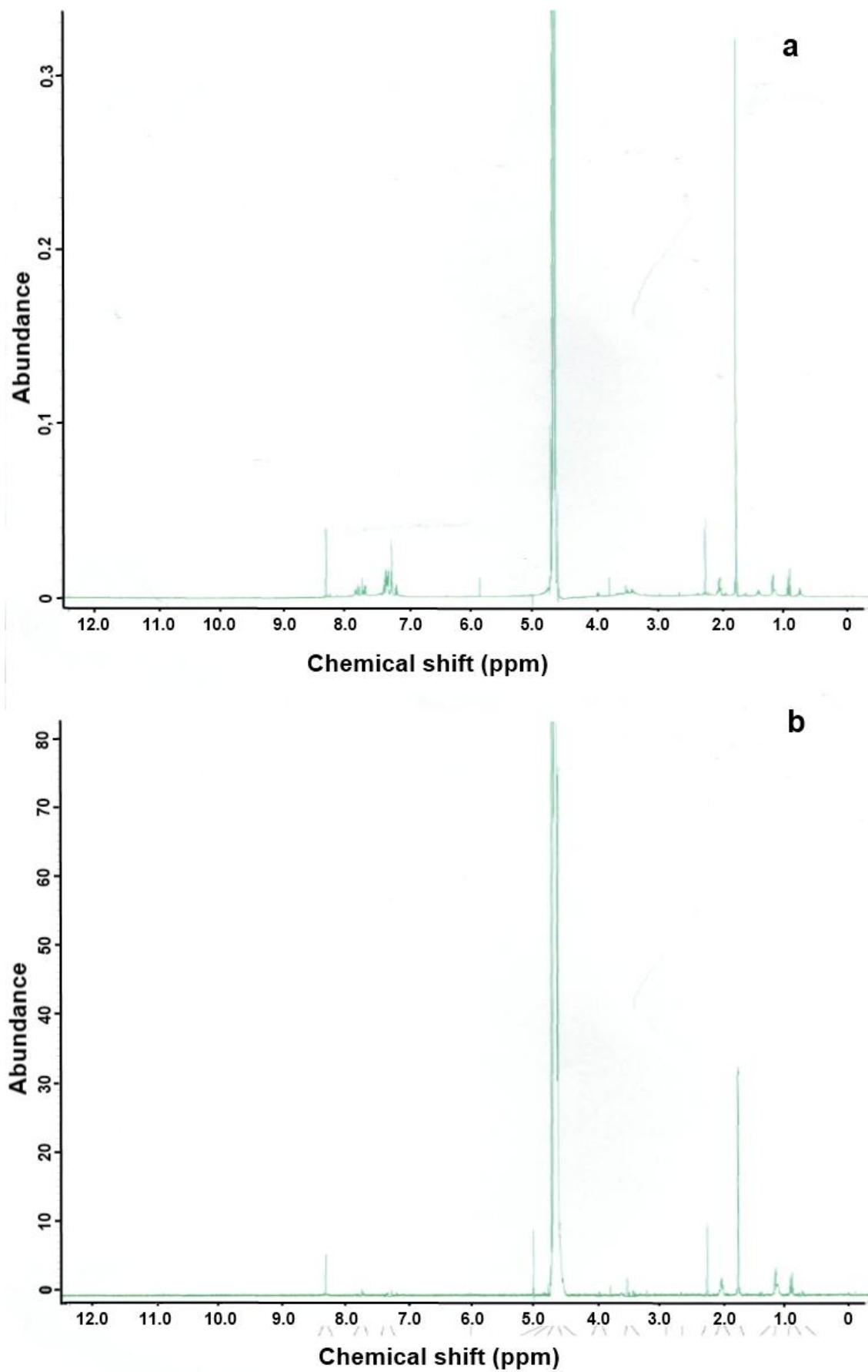


Figure 2.31:  $^1\text{H}$  NMR spectra of CI07 400-10 a) Q and b) NQ solution residues dissolved in  $\text{D}_2\text{O}$  (Originally in colour)

## 2.9 Textural properties

To further understand the changes occurring in the ashes during combustion and following extraction the textural properties of Cl07 ashes were examined. Nitrogen porosimetry was used to study the surface area, pore volume and pore diameters of the ashes. This technique analyses the relationship between the adsorption of  $N_2$  gas molecules on a solid surface with changing pressure at constant temperature to give an adsorption isotherm. Adsorption is the condensation of a gas on to a free surface due to physical interactions similar in nature to the Van der Waals forces that cause the condensation of a vapour into a liquid.<sup>41</sup> Six different general classifications of adsorption isotherms have been identified, which are often characteristic of different pore sizes or geometries (Figure 2.32). Pore sizes are conventionally classified into three categories according to their diameter: micropores, less than  $\sim 20 \text{ \AA}$  diameter (2 nm); mesopores, between  $\sim 20 - 500 \text{ \AA}$  diameter (2- 50 nm) and macropores, greater than  $\sim 500 \text{ \AA}$  diameter (50 nm).<sup>41</sup> The hysteresis loop observed in type IV adsorption isotherms is ascribed to the effect of capillary condensation in mesopores. Type I isotherms are typical of microporous materials, where the interaction potential is increased due to the narrower pore diameters, thereby enhancing the gas uptake at a particular pressure.

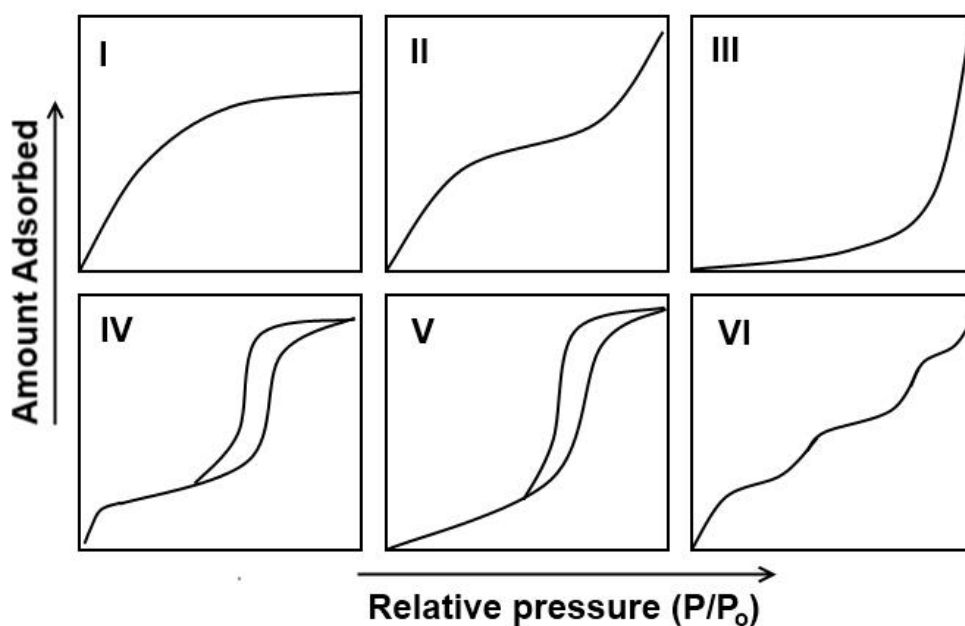


Figure 2.32: Classification of adsorption isotherms according to IUPAC classifications

The specific surface areas of the materials formed under different heat treatment processes were obtained using the Branauer, Emmett and Teller (BET) model, as the most commonly used method for calculating and reporting the porosity of solids. This model takes into account the potential for multilayer adsorption and is calculated using the following equation:

$$\frac{P}{V(P_o - P)} = \frac{1}{V_m C} + \frac{(C - 1)P}{V_m C P_o}$$

### Equation 2.1

Where  $V$  is the volume of adsorbate adsorbed at a given pressure,  $P$ ;  $V_m$  is the volume corresponding to monolayer coverage;  $P_o$  is the saturation pressure and  $C$  is a constant which is a function of the heat of adsorption. By plotting the expression on the left-hand side against  $\frac{P}{P_o}$ , a straight line should be formed.  $\frac{1}{V_m C}$  can be found from the intercept at  $\frac{P}{P_o} = 0$  and  $\frac{(C-1)}{V_m C}$  can be obtained from the gradient of the plot.  $V_m$  and  $C$  can then be determined and the surface area  $S_{BET}$  in  $m^2 g^{-1}$  can be calculated from:

$$S_{BET} = \frac{V_m A_m N_A \cdot 10^{-20}}{M_v}$$

### Equation 2.2

Where  $N_A$  is Avogadro's number ( $6.02 \times 10^{23}$  molecules per mole);  $M_v$  is the gram molecular volume (22,414 ml), and  $A_m$  is the cross-sectional surface of the adsorbate, in this case  $N_2$  ( $0.162 \text{ nm}^2$ ).

However,  $S_{BET}$  may not be applicable in highly microporous materials where the size of the pores inhibits the formation of a monolayer-multilayer system.<sup>42</sup> Several of the ashes formed after combustion for 10 min and leaching gave negative  $c$ -values. This suggests that the surface areas of these samples cannot be accurately analysed via the BET method. Therefore the surface area was also determined using the Dubinin-Astakhov model. This is a generalised version of the more widely used Dubinin-Radushkevich model based on the mechanism of micropore volume filling rather than layered adsorption on the pore walls.<sup>41</sup> This model has been shown to demonstrate linearity over a wider range

of materials and applies to solids with a non-uniform microporous structure.<sup>43</sup> However, the validity of this model does rely on the assumption that the surface is homogenous in nature.<sup>43</sup>

Bulk pore size distribution and pore volume are frequently characterised by the Barrett, Joyner and Helenda (BJH) model, particularly for mesoporous materials.<sup>44</sup> In this model the total volume of adsorbate adsorbed at a particular partial pressure is dependent on (1) the degree of adsorption of adsorbate on pore walls and (2) capillary condensation in the inner capillary volume. The model is generally based on the assumption that the pores are rigid and have a regular shape, generally either cylindrical or slits. The pore size distribution can be shown by plotting  $dV/dD$  against pore diameter where  $dV/dD$  represents the change in the volume adsorbed with the change in diameter. However, this method is not suitable for determining the micropore volume and micropore size distribution. The micropore (MP) method was used in this study to analyse the micropore volume and the micropore size distribution. This assumes a micropore filling mechanism, a parallel plate pore model and that, as the partial pressure increases, multilayer adsorption is retarded due to pore filling.<sup>45</sup> The latter assumption was observed to hold true for the combustion residues used in this study based on adsorbate thickness (in Å) vs adsorption volume ( $\text{cm}^3 \text{g}^{-1}$ ) plots. To check the accuracy of the MP method to determine the micropore volume, the results were also compared to the Dubinin-Astakhov model. The latter model was also be used to determine the surface energy of the samples.

The results of all of these analyses for CI07 combustion residues formed and treated over a range of conditions are shown in Table 2.6.

**Table 2.6: Porosimetry data of Cl07 combustion residues before (I) and after leaching (Q/NQ)**

Sample		Surface Area (m <sup>2</sup> g <sup>-1</sup> )		Pore volume (cm <sup>3</sup> g <sup>-1</sup> )			Pore size (Å)		Surface Energy (kJ mol <sup>-1</sup> ) <sup>b</sup> E <sub>DA</sub>
		<sup>a</sup> S <sub>BET</sub>	<sup>b</sup> S <sub>DA</sub>	<sup>c</sup> V <sub>total</sub> <sup>BJH</sup>	<sup>d</sup> V <sub>micro</sub> <sup>MP</sup>	<sup>b</sup> V <sub>micro</sub> <sup>DA</sup>	<sup>c</sup> APD <sub>BJH</sub>	<sup>d</sup> APR <sub>MP</sub>	
400-10	I	8.28	6.2	0.012	0.0005	0.004	45	5.1	5.1
	Q	106	128	0.078	0.058	0.052	5.4	3.4	20.4
	NQ	20.1	27.2	0.03	0.008	0.01	34	3.1	28.2
500-10	I	5.03	-	-	-	-	-	-	-
	Q	200	256	0.13	0.11	0.10	3.9	3.2	21.6
	NQ	198	236	0.14	0.11	0.09	4.6	3.2	20.4
600-10	I	28.2	16.3	0.035	0.014	0.01	40	9.4	2.4
	Q	273	428	0.25	0.16	0.14	11	3.1	43.0
	NQ	200	242	0.13	0.12	0.10	4.6	3.6	20.5
700-10	I	61.1	-	0.032	0.03	-	4.1	2.9	-
	Q	258	308	0.16	0.16	0.12	3.7	3.6	21.5
	NQ	222	268	0.15	0.12	0.10	3.8	3.2	23.1
800-10	I	200	201	0.14	0.11	0.08	5.1	4.0	21.4
	Q	346	437	0.21	0.19	0.16	3.0	3.0	24.7
	NQ	351	444	0.22	0.19	0.17	3.3	3.3	25.9
900-10	I	327	338	0.21	0.18	0.13	4.1	3.7	23.2
400-120	I	17.7	18.9	0.038	-	0.016	58	8.6	4.2
	Q	46.0	42.7	0.17	-	0.021	86	-	12.2
	NQ	56.3	46.3	0.16	-	0.024	81	-	10.3
500-120	I	1.8	1.6	0.009	0.001	0.001	117	3.5	7.6
	Q	60.2	65.8	0.098	0.038	0.029	21	7.2	17.7
	NQ	49.4	53.3	0.083	0.031	0.024	26	7.7	15.3
600-120	I	18.9	21.2	0.027	0.010	0.017	42	9.5	2.8
	Q	36.9	32.9	0.062	0.025	0.017	51	8.4	8.1
	NQ	40.9	33.2	0.072	0.019	0.019	53	8.7	11.9
800-120	I	35.6	33.7	0.035	0.026	0.028	32	10.3	2.9
	Q	10.7	10.9	0.010	0.020	0.010	31	9.7	3.8
	NQ	30.2	26.2	0.034	0.020	0.020	34	9.7	3.6

<sup>a</sup> BET surface area; <sup>b</sup> Surface area, micropore volume and surface energy from the Dubinin-Astakhov model;

<sup>c</sup> Total pore volume and average pore diameter (APD) from the BJH model; <sup>d</sup> Micropore volume and average pore radius (APR) from the MP model.

### 2.9.1 10 min combustion

The adsorption isotherms of the residues formed after 10 min combustion are typical of type I isotherms (Figure 2.33), with an almost horizontal plateau, particularly following leaching, indicative of microporous materials.<sup>41</sup> The initial sharp rise, corresponds to micropore filling, with the slope at higher pressures due to multilayer adsorption in the non-microporous region.<sup>46</sup> The open loop hysteresis can be observed in ultra-

microporous carbons such as charcoals or molecular sieves. It indicates that adsorption is irreversible at all pressures, contrasting with mesoporous materials, suggested to be due to the high activation energy associated with a constricted pore opening.<sup>47</sup> Overall, the shape, and total volume adsorbed in the case of the higher temperature materials, are highly comparable to those of the carbon molecular sieves Takada 4A and 5A.<sup>48</sup>

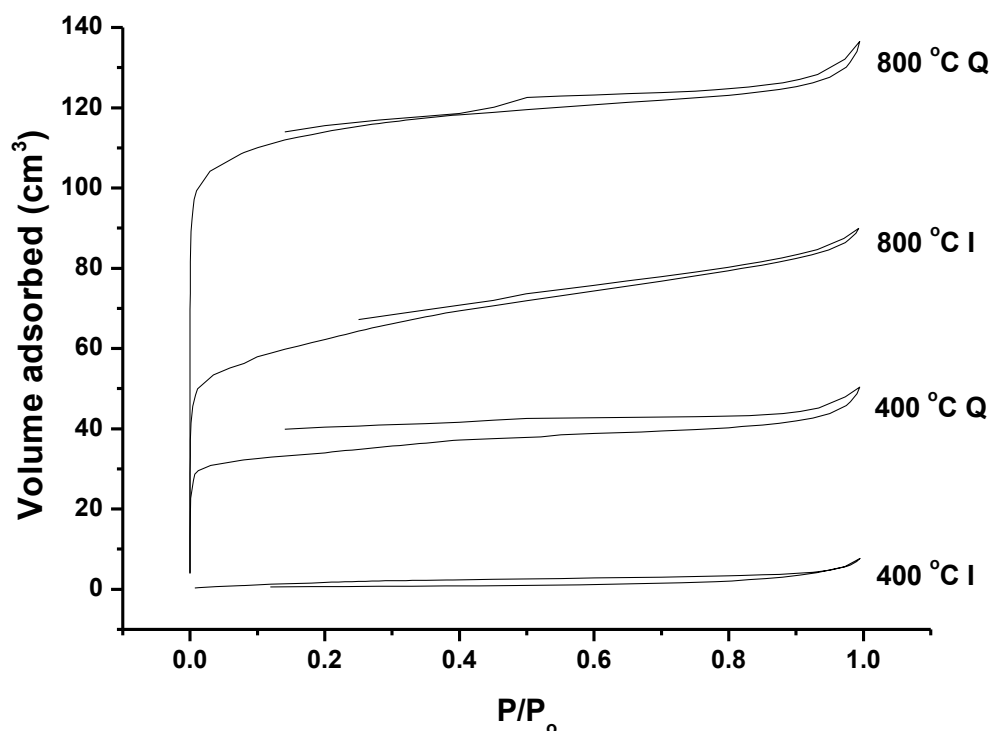


**Figure 2.33: Adsorption isotherms of CI07 residues following 10 min combustion at different temperatures before (I) and after (Q) leaching**

After 10 minutes combustion without extraction the surface area of the ashes rises dramatically with increasing temperature of combustion (Figure 2.34). For these samples the surface area found by both the BET and Dubinin-Astakhov models are very similar. Pore volume and pore size analyses demonstrate the formation of an increasingly microporous material developing above 700 °C. This coincides with the melting point and liberation to the gas phase of KCl and the softening of silica and formation of alkali silicate species. This could therefore be related to the movement of molten or gaseous salts through the carbon structure creating pores. This is supported by elemental analysis of melted wheat straw ash particles showing increased levels of K and Cl on the external surfaces due to evaporation at these temperatures, although these had been heat treated for 2 h.<sup>49</sup> TEM images of the ashes at 400 °C and 800 °C appear to show structural

changes in the inorganic species from discrete particles to fractured platelets, although EDX analysis would be required to confirm this (Figure 2.35). In addition, as the surface area of the materials increases, the surface energy correspondingly increases, to levels generally observed in graphite-like materials.<sup>50</sup> This either suggests a decrease in the O/C surface ratio and a greater degree of aromaticity, or the greater availability of the carbon surface for interaction.

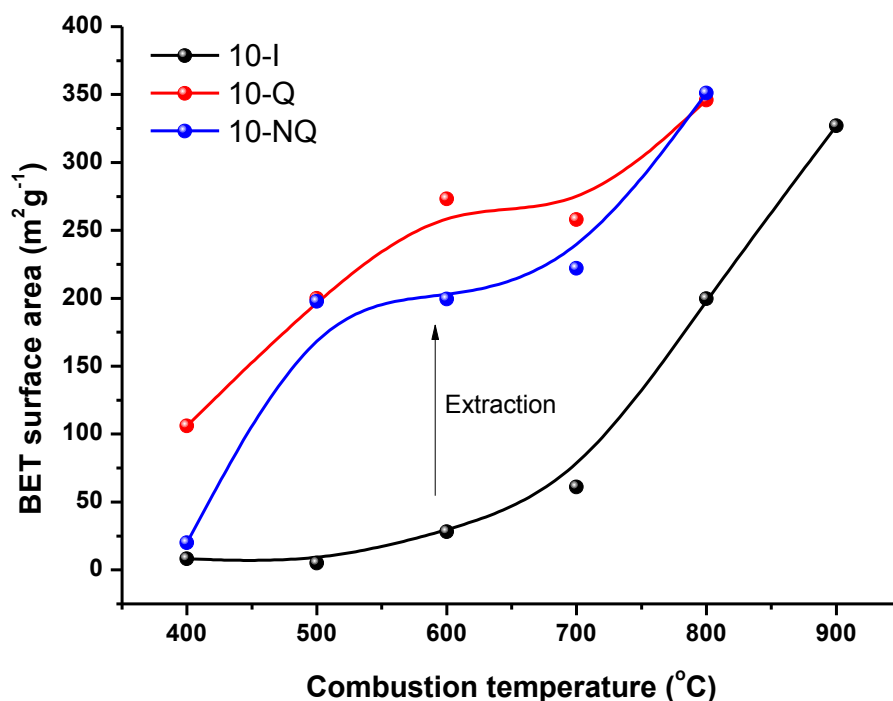


Figure 2.34: BET surface area of Cl07 ashes after 10 minutes combustion before leaching (black), and following extraction with water quenching (red) or air cooling (blue) (Originally in colour)

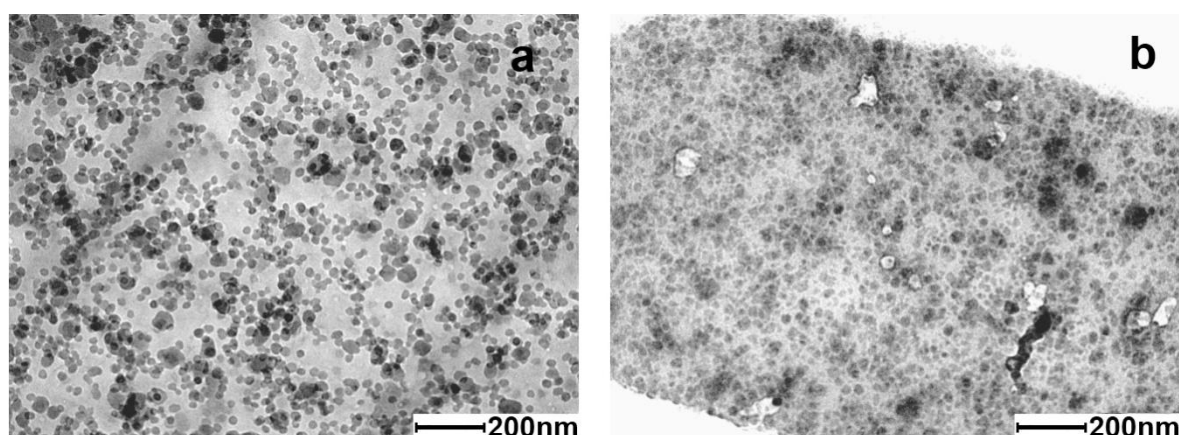


Figure 2.35: TEM images of Cl07 ashes after 10 minutes combustion at (a) 400 °C and (b) 800 °C

The surface area ( $S_{\text{BET}}$ ) and pore volume ( $V_{\text{total}}^{\text{BJH}}$ ) at 800 and 900 °C are similar to the lower to mid- end of those found during the physical activation of pyrolysis chars for the formation of activated carbons (AC) from agricultural residues,<sup>51</sup> whilst the micropore volume proportion is particularly high, when compared, for instance, with those formed from coconut shells.<sup>46</sup> The surface area and pore volume of residues formed at higher temperature are also comparable to those of commercial carbon molecular sieves.<sup>48</sup> Almost 1 million tonnes of ACs are produced per annum via pyrolysis and physical activation, mainly for water cleaning and decolouration.<sup>52</sup> During this process steam, air or CO<sub>2</sub> are added to char, formed from pyrolysis at up to 1000 °C, at temperatures of 800 °C or greater for between 30 minutes to 12 hours causing partial burn-off and the development of micropores.<sup>53, 54</sup> Many studies have shown an increase in  $S_{\text{BET}}$  with increasing temperature of physical activation, particularly between 700 – 900 °C.<sup>51</sup> However, some of these studies have reported  $S_{\text{BET}}$  of around 3000 cm<sup>3</sup> g<sup>-1</sup>,<sup>55</sup> which is slightly greater than the surface area that would be achieved by 1g of carbon present as layers of graphite one atom thick.<sup>41</sup> Chemical activation is also frequently employed utilising either ZnCl<sub>2</sub>, KOH, K<sub>2</sub>CO<sub>3</sub> or H<sub>3</sub>PO<sub>4</sub> with carbonisation and activation occurring in a one step process,<sup>54</sup> although the fundamental chemical processes occurring during these steps still do not seem to be well understood. Nevertheless, after 10 minutes combustion similar processes could be occurring as those suggested to occur during carbon activation, with both partial oxidation of the char surface or chemical activation through the presence of in situ KOH or K<sub>2</sub>CO<sub>3</sub> causing the development of pores and therefore the high surface areas of these materials with increased temperature.

Following water leaching, the 10 min combustion residues display an increased surface area (Figure 2.34), pore volume and surface energy relative to the initial ashes (Table 2.6), which correlates with the total inorganic content extracted. The  $S_{\text{DA}}$  for these samples are generally 20% higher than those found by the BET model, however, the trend is identical. The  $S_{\text{BET}}$  is used in this discussion as this can be more easily compared to the results of other researchers. Raveendran *et al* found that the surface area of chars formed from biomass pyrolysed at 500 °C increased with ash extraction.<sup>56</sup> However, the removal of inorganic species occurred before pyrolysis and the utilisation of concentrated acid may also have modified the organic structure. Within their study, the observed increase in  $S_{\text{BET}}$  was associated with an increased volatile yield. In addition, a higher gasification rate was

suggested to lead to a reduced micro:macro pore size ratio.<sup>56</sup> However, within this study, when a higher combustion temperature was used, which would be expected to result in a higher decomposition rate, the resulting  $S_{\text{BET}}$  is higher whilst the micropore radius remains constant. The surface area (Figure 2.34) and the pore size distribution (Figure 2.36) present after 10 minutes combustion from 500 – 700 °C are almost identical to that present at 800 °C before extraction. Particularly noticeable is the very narrow pore size distribution within the ultramicropore region (< 0.7 nm diameter) at all temperatures and particularly following leaching. This is much smaller and narrower than those of activated carbons from biomass materials in the literature,<sup>53, 57</sup> but similar to commercial activated carbons.<sup>48</sup> Carrying out  $\text{CO}_2$  adsorption at 273 K would be valuable in providing further information about the nature of the pores in this region, since the radius suggested for these pores is close to the radius of  $\text{N}_2$  generally used for porosimetry analysis of 2.0 Å (0.2 nm). Following extraction the surface energy changes dramatically, increasing from values similar to those of high O/C ratio materials to those close to graphite-like samples.<sup>50</sup>

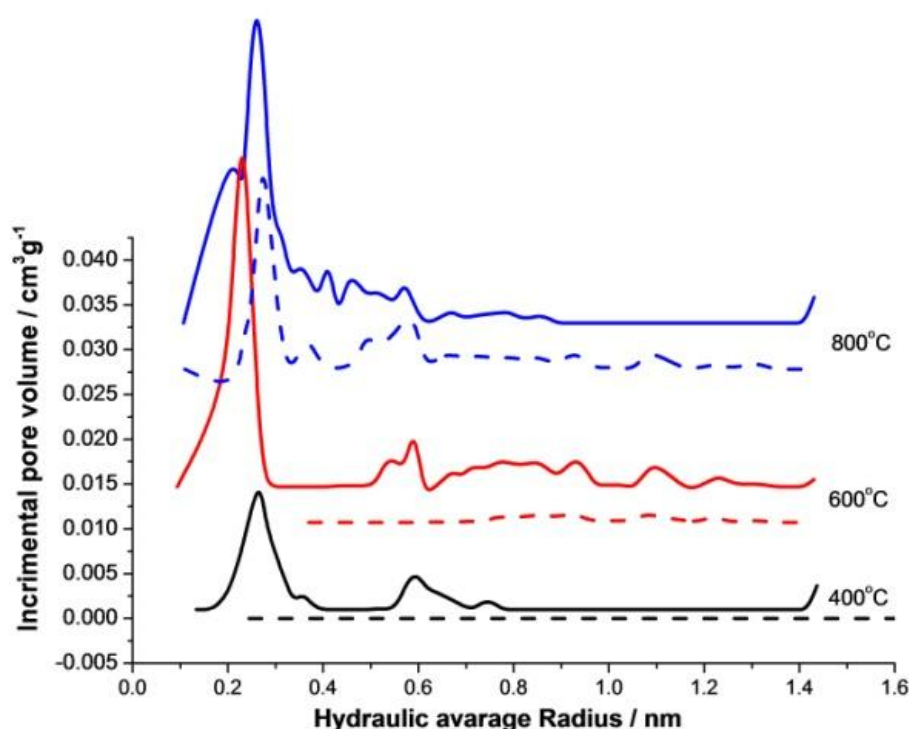
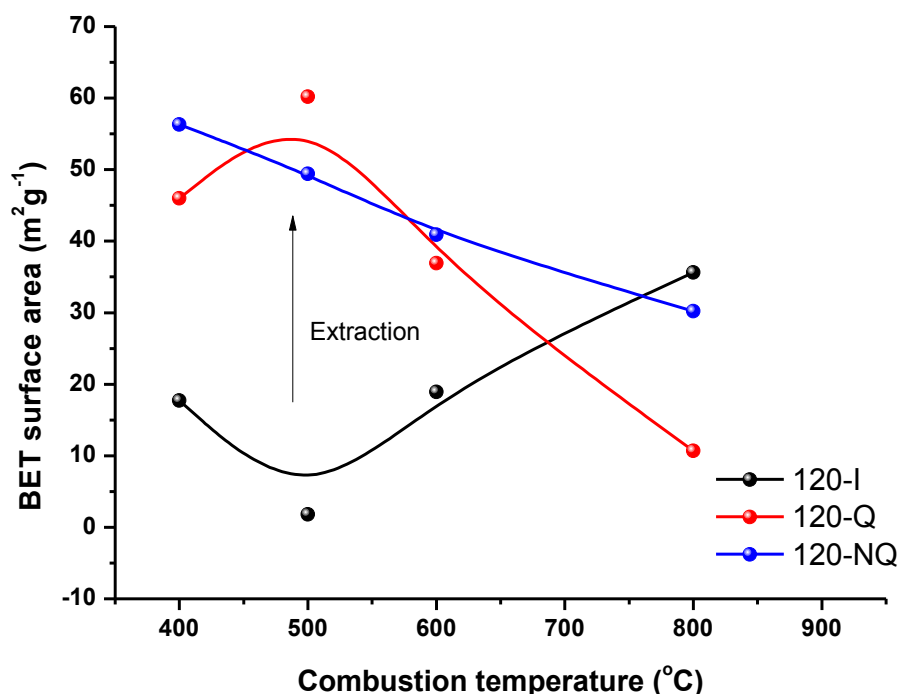


Figure 2.36: Pore size distribution of CI07 ashes after 10 min combustion before (dashed line) and after (solid line) extraction (Originally in colour)

Overall, this data appears to support the proposition that the mechanism causing the increase in surface area within the combustion residues is different to that generally put forward for the formation of activated carbon. Instead, soluble inorganic species appear to be causing the increase in pore volume and surface area in the initial ash as they become mobile at higher combustion temperatures. This suggests that the inorganics are distributed initially as a nano-network throughout the wheat straw material. The removal of this network by leaching after partial combustion produces high surface area, narrowly distributed, ultramicroporous carbonaceous materials at lower temperatures than traditionally used for activated carbon production. This outcome could potentially open up a less energy intensive route to the formation of molecular sieve materials.

### 2.9.2 2 h combustion

Following complete combustion the internal surface area is considerably reduced as the organic content burns out and the inorganic species begin to melt (Table 2.6). However, following extraction, particularly at lower temperatures where a greater level of inorganic material is removed, the surface area increases upon leaching (Figure 2.37).



**Figure 2.37: BET surface area of CI07 ashes after 2 h combustion before leaching (black), and following extraction with water quenching (red) or air cooling (blue) (Originally in colour)**

The shape of the adsorption isotherms differ significantly from those observed for the partially combusted materials (Figure 2.38). The isotherm for 500-120-Q can be assigned to a type IV according to the IUPAC classifications. This signifies some mesoporous character, particularly identifiable from the closed hysteresis loop.  $V^{BJH}$  demonstrates a significant increase in pore volume for this sample following leaching, with some contribution from the formation of micropores ( $V_{\text{micro}}^{\text{MP}}$  and  $V_{\text{micro}}^{\text{DA}}$ ), although in a smaller proportion than observed in the 10 min combustion residue. In contrast, the 800 °C samples demonstrate isotherms of classification type II, indicating that they are non-porous or macroporous adsorbents.<sup>41</sup> The pore size distribution of all of these samples is broad, (Figure 2.38 inset), however, the higher temperature samples have a smaller average pore diameter ( $APD_{\text{BJG}}$ ). This could be due to the formation of minute air pockets during the melting and release to the gas phase of inorganic components.

The generally larger pore sizes formed following extraction of the 2 h ashes indicates perhaps both an agglomeration of the inorganic particles and a shift to the hollowing out of the inorganic framework.

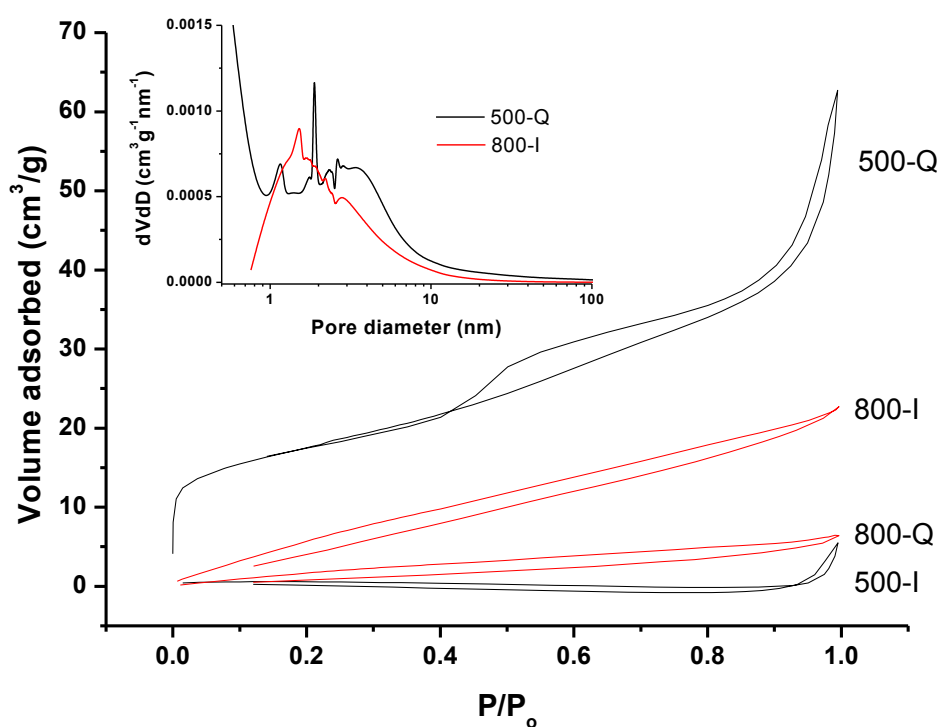


**Figure 2.38: Adsorption isotherms of ClO7 residues following 120 min combustion before (I) and after leaching (Q) (Originally in colour)**

The data shows the formation of substantially different materials during combustion. The leaching process increases the porosity of the materials, however, as combustion progresses this alters from a carbon-rich to an inorganic-rich material, altering porous distribution and the surface characteristics of the samples formed.

## **2.10 Conclusions and Further Work**

This work has studied the complete impact of combustion conditions on the major inorganic species within several wheat straw varieties and the mineralogical, chemical and textural changes that occur. Mineralogical and chemical changes occur above combustion temperatures of 500 °C causing reductions in the solubility of potassium, chloride, silica and sulfate. This can be correlated to evaporation of KCl, dissociation of  $K_2SO_4$ , softening of silica and formation of alkali silicates. Calcium extraction increased above combustion temperatures of 700 °C following the decomposition of  $CaCO_3$ .

This work has shown, for the first time, that the inherent alkali in unleached wheat straw is sufficient to solubilise up to 25% of the silica in the ash at room temperature. Combustion of wheat straw at temperatures below 600 °C gave the highest silica extraction by producing the most alkaline solutions, preventing calcium solubility and maintaining silica in a less crystalline form. Silica extraction can be significantly increased by leaching under reflux. Optimised silica extraction using the inherent alkalinity occurred at combustion conditions of 500 °C for 2 h with leaching under reflux.

Different wheat straw varieties varied in their initial inorganic composition, mainly dependent on their year of growth and specifically the level of rainfall causing the *in situ* leaching of soluble species. This initial composition influenced their combustion and pyrolysis decomposition, mineralogical ash composition, leaching of inorganic components, silica structure and alkalinity, which further affected silica extraction. Making the assumption that the available potassium was present as counter-ions to anionic species enabled the calculation of the additional alkali required for similar percentage levels of silica extraction for all wheat straw varieties. This data overall provides a better understanding of the correlation between the initial inorganic composition in wheat straw and the impacts on the mineralogical and chemical changes occurring within the ashes.

The textural properties show the development of porous materials following the extraction of inorganics for both incomplete and complete combustion. Partial combustion of biomass materials at low temperatures followed by leaching produces high surface area, narrowly distributed, ultramicroporous carbonaceous materials. This could be a viable route to lower cost nano-structured porous templates or adsorbents, combined with recovery of the inorganic species for recycling. The data indicates an alternative pore development mechanism to that traditionally observed for activated carbons, with the movement of mobile inorganic species at higher temperatures creating this fine structure within the carbon network. It would be interesting to take this work forward to study how it applies to other biomass materials of different inorganic compositions and the applications to which these materials could be put.

## 2.11 References for Chapter 2

1. HGCA, <http://www.hgca.com/content.output/4819/4819/Varieties/HGCA%20Recommended%20Lists/Winter%20wheat.msp>, Accessed 03/04/10.
2. P. A. Jensen, B. Sander and K. Dam-Johansen, *Biomass Bioenerg.*, 2001, **20**, 447-457.
3. T. R. Miles, T. R. Miles, L. L. Baxter, R. W. Bryers, B. M. Jenkins and L. L. Oden, *Biomass Bioenerg.*, 1996, **10**, 125-138.
4. D. C. Dayton, B. M. Jenkins, S. Q. Turn, R. R. Bakker, R. B. Williams, D. Belle-Oudry and L. M. Hill, *Energ. Fuel.*, 1999, **13**, 860-870.
5. S. Arvelakis, P. A. Jensen and M. Dam-Johansen, *Energ. Fuel.*, 2004, **18**, 1066-1076.
6. D. Nutalapati, R. Gupta, B. Moghtaderi and T. F. Wall, *Fuel Process. Technol.*, 2007, **88**, 1044-1052.
7. A. Demirbas, *Prog. Energy Combust. Sci.*, 2004, **30**, 219-230.
8. B. M. Jenkins, R. R. Bakker and J. B. Wei, *Biomass Bioenerg.*, 1996, **10**, 177-200.
9. V. Elliott, *Farmers count the cost as rain ruins wheat harvest*, <http://www.timesonline.co.uk/tol/news/environment/article4622264.ece>, Accessed 03/04/10.
10. C. Parker, *Pers. Comm.*, Editon edn., 17/09/08.
11. L. V. Alexander and P. D. Jones, *Atmos. Sci. Lett.*, 2001, **1**, 142-150.
12. J. M. Jones, L. I. Darvell, T. G. Bridgeman, M. Pourkashanian and A. Williams, *P. Combust. Inst.*, 2007, **31**, 1955-1963.
13. G. R. Ponder and G. N. Richards, *Carbohydr. Res.*, 1993, **244**, 27-47.
14. R. J. Evans and T. A. Milne, *Energ. Fuel.*, 1987, **1**, 123-137.
15. F. Shafizadeh, *J. Anal. Appl. Pyrol.*, 1982, **3**, 283-305.
16. A. Jensen, K. Dam-Johansen, M. A. Wojtowicz and M. A. Serio, *Energ. Fuel.*, 1998, **12**, 929-938.
17. R. Fahmi, A. V. Bridgwater, L. I. Darvell, J. M. Jones, N. Yates, S. Thain and I. S. Donnison, *Fuel*, 2007, **86**, 1560-1569.
18. P. Thy, B. M. Jenkins, S. Grundvig, R. Shiraki and C. E. Leshner, *Fuel*, 2006, **85**, 783-795.
19. Y. Huang, X. Yin, C. Wu, C. Wang, J. Xie, Z. Zhou, L. Ma and H. Li, *Biotechnol. Adv.*, 2009, **27**, 568-572.

20. B. Olanders and B.-M. Steenari, *Biomass Bioenerg.*, 1995, **8**, 105-115.
21. A. Proctor, *J. Am. Oil Chem. Soc.*, 1990, **67**, 576-584.
22. U. Kalapathy, A. Proctor and J. Shultz, *Bioresource Technol.*, 2000, **72**, 99-106.
23. U. Kalapathy, A. Proctor and J. Shultz, *Ind. Eng. Chem. Res.*, 2003, **42**, 46-49.
24. L. J. Bellamy, *The Infra-red Spectra of Complex Molecules*, Third edn., Chapman and Hall, London, 1975.
25. E. Greiner-Wronowa, C. Paluszkiwicz and L. Stoch, *J. Mol. Struct.*, 1999, **512**, 199-204.
26. F. A. Miller and C. H. Wilkins, *Analyt. Chem.*, 1952, **24**, 1253-1294.
27. B. Stewart, *Modern Infrared Spectroscopy*, John Wiley & Sons, Chichester, 1996.
28. J. R. Martinez, F. Ruiz, Y. V. Vorobiev, F. Perez-Robles and J. Gonzalez-Hernandez, *J. Chem. Phys.*, 1998, **109**, 7511-7514.
29. J. Osswald and K. T. Fehr, *J. Mater. Sci.*, 2006, **41**, 1335-1339.
30. F. Gervais, A. Blin, D. Massiot and J. P. Coutures, *J. Non-Cryst. Solids*, 1987, **89**, 384-401.
31. G. Engelhardt and D. Michel, *High-Resolution Solid-State NMR of Silicates and Zeolites*, John Wiley, New York, 1987.
32. P. Mellbo, S. Sarenbo, O. Stålnacke and T. Claesson, *Waste Manage.*, 2008, **28**, 2235-2244.
33. J. G. Olsson, U. Jaglid, J. B. C. Pettersson and P. Hald, *Energ. Fuel.*, 1997, **11**, 779-784.
34. D. C. Dayton, R. J. French and T. A. Milne, *Energ. Fuel.*, 1995, **9**, 855-865.
35. J. N. Knudsen, P. A. Jensen, W. G. Lin, F. J. Frandsen and K. Dam-Johansen, *Energ. Fuel.*, 2004, **18**, 810-819.
36. G. R. Rao, A. R. K. Sastry and P. K. Rohatgi, *Bull. Mat. Sci.*, 1989, **12**, 469-479.
37. R. K. Iler, *The Chemistry of Silica*, Wiley & Sons, New York, 1979.
38. D. G. Nair, A. Fraaij, A. A. K. Klaassen and A. P. M. Kentgens, *Cement Concrete Res.*, 2008, **38**, 861-869.
39. H. W. Nesbitt, G. M. Bancroft, G. S. Henderson, R. Ho, K. N. Dalby, Y. Huang and Z. Yan, *J. Non-Cryst. Solids*, 2011, **357**, 170-180.
40. I. D. Brown and R. D. Shannon, *Acta Crystallogr. A*, 1973, **29**, 266-282.
41. S. J. Gregg and K. S. W. Sing, *Adsorption, surface area and porosity*, 2nd edn., Academic Press Ltd, London, 1982.
42. A. Galarneau, H. I. n. Cambon, F. Di Renzo and F. o. Fajula, *Langmuir*, 2001, **17**, 8328-8335.
43. A. Gil and P. Grange, *Colloids and Surfaces A: Physicochemical and Engineering Aspects*, 1996, **113**, 39-50.
44. E. P. Barrett, L. G. Joyner and P. P. Halenda, *J. Am. Chem. Soc.*, 1951, **73**, 373-380.
45. J.-m. Yan and Q.-y. Zhang, *Particle & Particle Systems Characterization*, 1986, **3**, 81-88.
46. W. Li, K. Yang, J. Peng, L. Zhang, S. Guo and H. Xia, *Industrial Crops and Products*, 2008, **28**, 190-198.
47. S. Kaskel, P. Llewellyn, F. Rodriguez-Reinoso and N. A. Seaton, in *Characterisation of Porous Solids VIII: Proceedings of the 8th International Symposium on the Characterisation of Porous Solids*, The Royal Society of Chemistry, Editon edn., 2009, pp. 1-8.
48. S. Kaskel, P. Llewellyn, F. Rodriguez-Reinoso and N. A. Seaton, in *Characterisation of Porous Solids VIII: Proceedings of the 8th International Symposium on the Characterisation of Porous Solids*, The Royal Society of Chemistry, Editon edn., 2009, pp. 9-16.
49. Y. Q. Wu, S. Y. Wu, Y. Li and J. S. Gao, *Energ. Fuel.*, 2009, **23**, 5144-5150.
50. V. Budarin, J. H. Clark, J. J. E. Hardy, R. Luque, K. Milkowski, S. J. Tavener and A. J. Wilson, *Ange. Chem. Int. Ed.*, 2006, **45**, 3782-3786.

51. P. Paraskeva, D. Kalderis and E. Diamadopoulos, *J. Chem. Technol. Biotechnol.*, 2008, **83**, 581-592.
52. R. J. White, V. Budarin, R. Luque, J. H. Clark and D. J. MacQuarrie, *Chem. Soc. Rev.*, 2009, **38**, 3401-3418.
53. T. Zhang, W. P. Walawender, L. T. Fan, M. Fan, D. Daugaard and R. C. Brown, *Chem. Eng. J.*, 2004, **105**, 53-59.
54. O. Ioannidou and A. Zabaniotou, *Renew. Sust. Energ. Rev.*, 2007, **11**, 1966-2005.
55. G. G. Stavropoulos and A. A. Zabaniotou, *Microporous and Mesoporous Materials*, 2005, **82**, 79-85.
56. K. Raveendran and A. Ganesh, *Fuel*, 1998, **77**, 769-781.
57. K. Sun and J. c. Jiang, *Biomass Bioenerg.*, 2010, **34**, 539-544.



## **Chapter 3:**

# **The impact of pretreatment processes on inorganic species during the combustion and extraction of wheat straw**



### **3.1 Chapter 3 – Summary**

Cl07 wheat straw was pretreated by water and acid washing, using supercritical CO<sub>2</sub> (scCO<sub>2</sub>) and by ethanol and hexane Soxhlet extraction. The effects of these processes on the removal of inorganic species and higher value lipids, the thermochemical conversion of the pretreated straw and the formation of alkali silicates from the residual ashes are examined.

### **3.2 Pretreatment options**

A number of studies into the leaching of wheat straw and other agricultural residues to remove ash components and improve combustion have been carried out.<sup>1-10</sup> As discussed in Chapter 1, significant amounts of troublesome elements, including potassium, chlorine and sulfur can be removed either by rain leaching in the field or water submersion akin to an industrial process, although the studies show some variation in the quantities removed. Acid washing can reduce the potassium and chlorine content further.<sup>10</sup> During combustion leached wheat straw has been found to have a higher fusion temperature,<sup>1</sup> show reduced emissions of HCl and KCl vapours,<sup>5</sup> a slight increase in calorific value and a higher initial temperature of decomposition.<sup>2</sup> However, the impact of these pretreatment processes on the ash composition, particularly of silica, and therefore its utilisation, has not been studied.

In addition, researchers have aimed to valorise wheat straw by extracting the secondary metabolites, primarily a mixture of long chain fatty acids and fatty alcohols, sterols and alkanes, on the surface of the straw with potential uses in cosmetics, personal care products, polishes and coatings.<sup>11</sup> However, the impact of wax extraction on the use of the remaining straw in combustion processes has not been studied. Soxhlet extraction is a classical efficient method of solvent extraction. Supercritical CO<sub>2</sub> extraction is considered a greener and more selective extraction process.<sup>12</sup> Therefore, both of these techniques were studied to optimise the wax extraction process.

The combined study of these different pretreatment processes enables comparisons to be made of their impact on combustion and ash formation.

### 3.3 Wax extraction optimisation

#### 3.3.1 Soxhlet extraction

Soxhlet extraction is one of the oldest solid extraction techniques.<sup>13</sup> Conventionally, the sample to be extracted is placed within a thimble in a reservoir (Figure 3.1). Fresh solvent condenses into the reservoir; once it reaches a certain level a siphon returns the solvent containing extractives to the distillation flask. Thus, hot fresh solvent is continuously brought into contact with the sample, displacing the extraction equilibrium and thereby enabling the maximum yield of extractives to be obtained. However, method drawbacks include long processing times, possible thermal decomposition of products, large solvent volume requirements, non-automated processes and evaporation/concentration needed to yield products.<sup>13</sup>

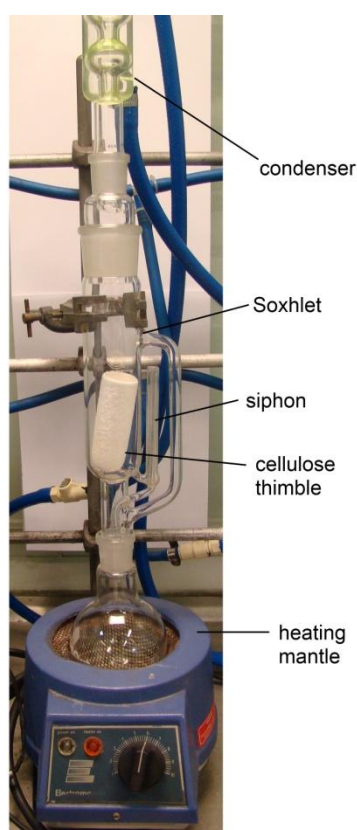


**Figure 3.1: Soxhlet extractor set-up (Originally in colour)**

Soxhlet extraction was undertaken using two solvents, ethanol and hexane. Of the traditional solvents hexane has previously been shown to be the most selective to lipid extraction, whilst ethanol usually demonstrates the highest total extract yield.<sup>12</sup>

The total Soxhlet extraction yield exhibited significant differences between the two solvents used (Figure 3.2). The lowest yields were for hexane, at 1.5 wt% yield (based on dry weight), with no dependence on the length of extraction time. The extractives level was much higher using ethanol with 4.4 wt% after 2 h and 5.4 wt% after 5 h. In general, hexane is observed to be a more selective solvent, removing mainly wax compounds, whilst ethanol co-extracts a large number of polar components such as pigments, polar lipids and free sugars.<sup>12</sup> These results demonstrate a good correlation with those of previously published work on wheat straw,<sup>12</sup> although the yield of extractives using ethanol in this study is nearly twice as high. Variation in the extraction level for different wheat straw varieties has been observed previously.<sup>11</sup>

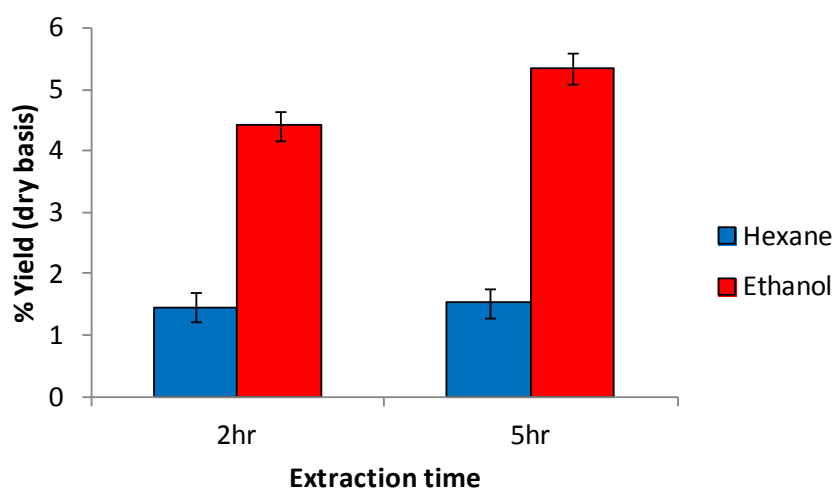


**Figure 3.2: Yield of crude extracts from Soxhlet extraction of Cl07 straw using hexane and ethanol with different extraction times (Originally in colour)**

### 3.3.2 Supercritical CO<sub>2</sub> extraction

A supercritical fluid (SCF) is one that is above its critical temperature ( $T_c$ ) and pressure ( $T_p$ ). This critical point is the highest temperature and pressure at which the solvent can exist as both a liquid and a vapour in equilibrium.<sup>14</sup> For carbon dioxide this critical point is at 31.1 °C and 73.8 bar.<sup>14</sup> Carbon dioxide is the most widely used SCF in food applications. It is viewed as a green solvent due to its low toxicity, low critical point, availability as a by-product from industry and the ease of isolation of extracts by pressure release.<sup>15</sup> It's solvent properties can be described as:<sup>15</sup>

- (i) Dissolves non-polar and slightly polar compounds

- (ii) Solvent power increases the lower the molecular weight of the compound
- (iii) High affinity for oxygenated organic compounds of medium molecular weight
- (iv) Low solubility of water at < 100 °C
- (v) Proteins, polysaccharides, sugars and mineral salts are insoluble
- (vi) As the pressure increases, more polar, higher molecular weight or less volatile compounds can be separated
- (vii) Low viscosity and high diffusivity

These properties make it ideal for the extraction of the secondary metabolites on the surface of straw.<sup>12, 16</sup> Several researchers have found similar extraction yields using both supercritical carbon dioxide (scCO<sub>2</sub>) and hot hexane.<sup>15</sup>

The solvation power of supercritical carbon dioxide (scCO<sub>2</sub>) can be tuned by varying its temperature and pressure (and therefore density) due to the high compressibility of the solvent (Figure 3.3). In order to optimise an extraction it is therefore necessary to study how both of these factors affect the extract yield and composition.

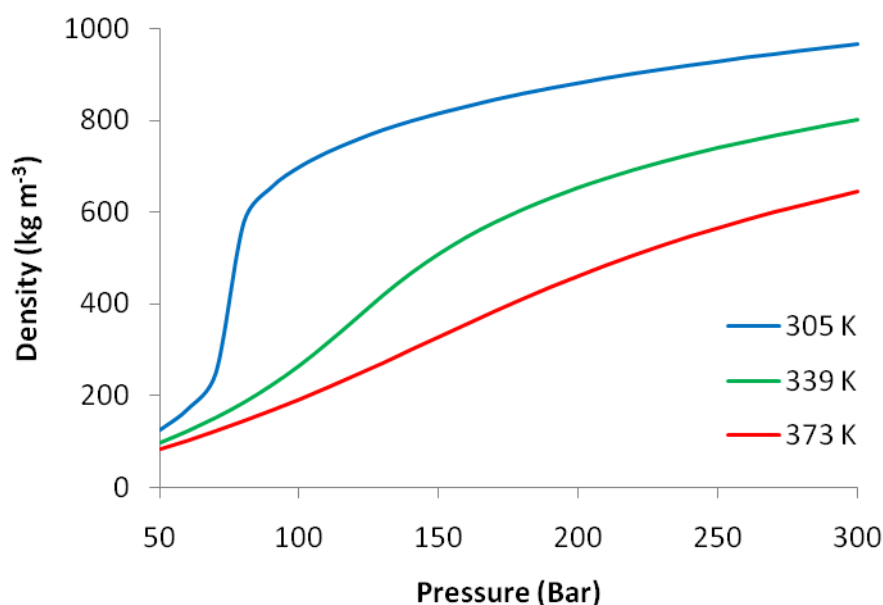


**Figure 3.3: Variation of density with pressure along different isotherms for supercritical carbon dioxide (based on calculated data from Ref 17) (Originally in colour)**

### 3.3.2.1 Statistical design

The extraction of secondary metabolites using scCO<sub>2</sub> was carried out using a factorial experimental design. This enables the optimisation of the experimental variables (the independent factors) in relation to the interested output (in this case the extraction yield) in as efficient a method as possible.<sup>18</sup> An understanding of the relationship between different variables that might synergistically affect the output is also enabled. A factorial design is denoted by:

$$N = n^f$$

#### Equation 3.1

where N is the number of experiments run, n is the number of levels and f is the number of factors or variables controlled. In the case of scCO<sub>2</sub> extraction several independent factors can influence the yield and product composition including temperature (T), pressure (P), flow rate, extraction time, particle size and mass of material. For this study T and P were selected as the independent factors to control with all other variables kept constant, since T and P are the main parameters affecting the solvation power of scCO<sub>2</sub>.<sup>15</sup> A full 2<sup>2</sup> factorial experimental design was used (Table 3.1). The two levels were assigned as +1, for the quantitative maximum, and -1 for the minimum. An additional centre point between the maximum and minimum was applied to minimize the risk of missing a non-linear relationship. Each experiment was repeated twice and the origin point was repeated in triplicate. The experiments were carried out in a random order to reduce systematic errors.

**Table 3.1: 2<sup>2</sup> factorial design - experimental and coded values**

	Temperature	Pressure	Coded value	
	(° C)	(bar)	T (X1)	P (X2)
<b>1</b>	32	100	-1	-1
<b>2</b>	32	300	-1	+1
<b>3</b>	100	100	+1	-1
<b>4</b>	100	300	+1	+1
<b>5</b>	66	200	0	0

Using the data obtained from the experimental design it should be possible to model the response using the following equation:

$$\text{Yield} = b_0 + b_1X_1 + b_2X_2 + b_{12}X_1X_2$$

### Equation 3.2

$X_1$  and  $X_2$  are the independent variables (T and P), the coefficients  $b_1$  and  $b_2$  account for the main effects of each factor and  $b_{12}$  measures the interaction between the factors. The coefficient  $b_0$  indicates the response of all the independent variables at the centre of the design, or point 0,0. It corresponds to a theoretical yield and therefore can be used to estimate the error in the system if an experimental value is obtained at this point and to check for non-linearity.

The values of the factors that were not varied were based on previous extraction experience within the group. Previously, a temperature range of 40-70 °C had been used to study wheat straw.<sup>12</sup> In this study the temperature range was extended to 32-100 °C, from just above the critical temperature of 31.1 °C,<sup>15</sup> to observe the effect on the yield and extraction model. These experimental conditions cover a wider range of carbon dioxide densities under supercritical conditions than studied previously from liquid-like densities (32 °C, 300 bar) to more vapour-like densities (100 °C, 100 bar) (Figure 3.4).<sup>14</sup>

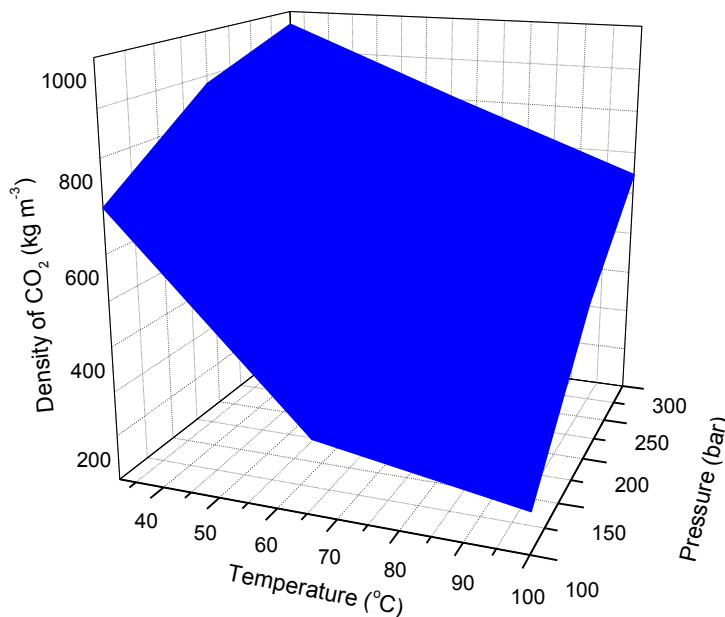


**Figure 3.4: Carbon dioxide densities over experimental range (based on calculated data from Ref 17) (Originally in colour)**

### 3.3.2.2 Extraction yields and modelling

The polarity of scCO<sub>2</sub> at its critical point is similar to hexane and so a similar yield was expected to that observed by Soxhlet extraction using hexane. In general, the solubility of compounds in CO<sub>2</sub> increase with density,<sup>14</sup> and therefore a trend that correlated with density was expected.

The maximum yield obtained was slightly lower than the Soxhlet hexane yield (Figure 3.5). This was also observed by Athukorala *et al* for flax straw extracts and was attributed to the more selective nature of supercritical carbon dioxide resulting in lower levels of co-extractants.<sup>19</sup> However, the extraction trend did not correlate directly with density. Although at the lowest densities (32 °C and 100 °C, 100 bar) the lowest yields were observed, at 100 °C and 300 bar the extraction yield increased dramatically despite the solvent density being lower than at 32 °C and 300 bar. This is in contrast to the findings of Deswarte *et al* who found that wax extraction from Sabre wheat straw fitted a linear model with the maximum yield at the highest CO<sub>2</sub> density (40 °C, 300 bar).<sup>12</sup>

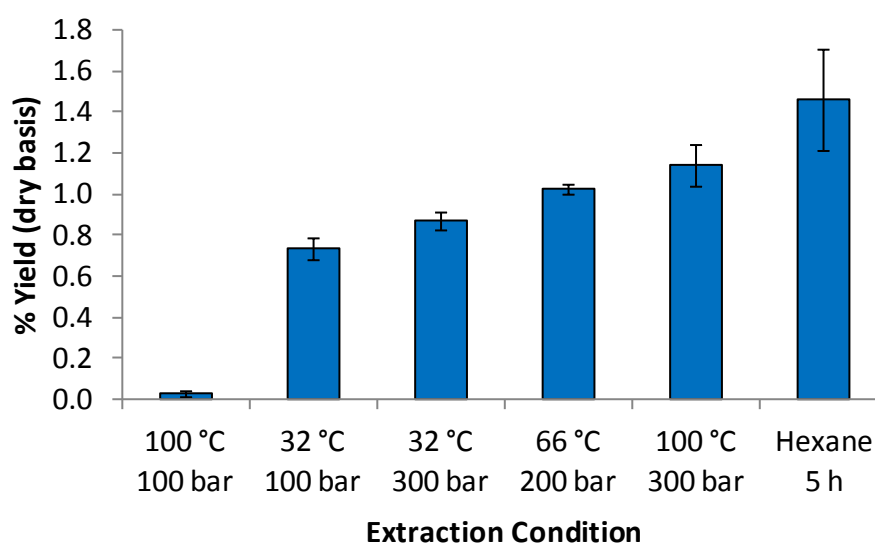
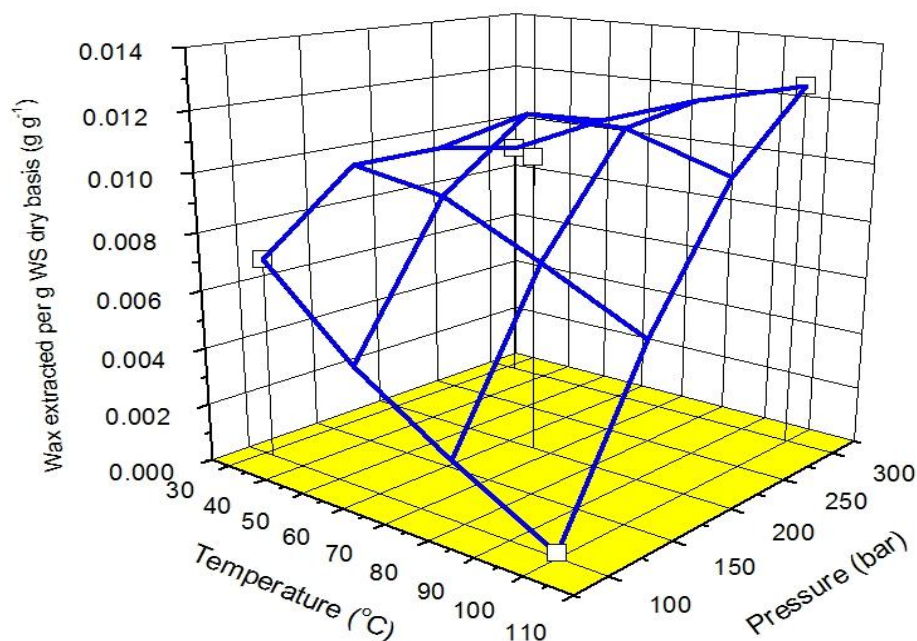


Figure 3.5: Extraction yield from Cl07 wheat straw using scCO<sub>2</sub> over factorial design conditions compared to hexane Soxhlet extraction (Originally in colour)



**Figure 3.6: Wax extraction by scCO<sub>2</sub>, yield and trend (Originally in colour)**

Attempts to model the data indicated a non-linear relationship (Figure 3.6). Regression analysis indicated that pressure was strongly positively correlated with wax yield, temperature was slightly negatively correlated, and there was a positive correlation for the combined effects of both parameters. However, substantially more data would be required to gain a more statistically accurate result on the magnitude of the effects of the two parameters.

A similar trend to the one found in this study on wheat straw was observed during the extraction of lipids from heather over a similar extraction range with the highest yield at 100 °C and 400 bar.<sup>20</sup> The higher wax extraction at these conditions was ascribed to the melting of surface waxes at higher temperatures. High pressure CO<sub>2</sub> is also known to decrease the melting point of some solids and could therefore affect the vapour phase composition.<sup>21</sup> Work by Lucas suggested that, in addition, the increased volatility and solubility of lipids at higher temperatures was more important than the reduction in scCO<sub>2</sub> density on the yields of extracted lipids.<sup>22</sup>

### 3.3.3 Extract composition and properties

In order to understand the differences in the extraction trends between Soxhlet and scCO<sub>2</sub> techniques and in comparison to the study by Deswarte *et al*, the composition and properties of the extracts were examined in more detail.

The colour and texture of the scCO<sub>2</sub> extracts in this study changed from a soft pale yellow wax (32 °C, 100 bar) to a harder light green extract at higher temperatures and pressures (100 °C, 300 bar) (Figure 3.7). The ethanol Soxhlet extract was sticky and brown whilst the hexane extract was honey-coloured and hard. These variations all imply changes in the composition of the extracts with varying extraction conditions.

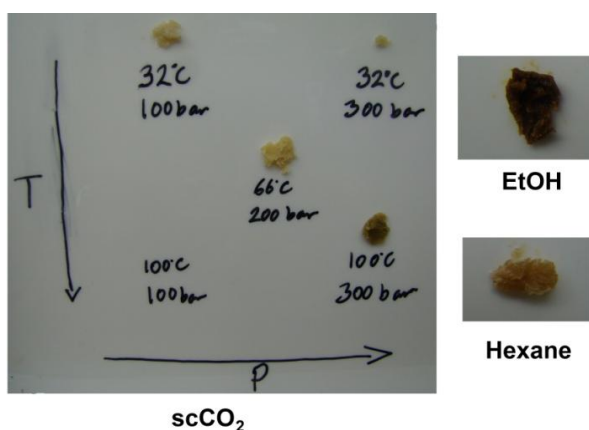


**Figure 3.7: Colour of waxes extracted from Cl07 under different conditions (Originally in colour)**

Differential scanning calorimetry (DSC) is a useful method for observing material properties such as phase transitions (e.g. melting) which are dependent on the compounds present. Phase transitions are usually endothermic and therefore show a decreased or negative heat flow. Thermal analysis of the crude extracts obtained by both Soxhlet and supercritical carbon dioxide extraction were undertaken without further purification (Figure 3.8). The analysis was carried out following an initial heating and cooling cycle to remove any prior thermal character.

The ethanol and hexane extracts (Figure 3.8a) both exhibit an early onset of melting and a characteristically broad melting range, with the slightly more well defined thermogram for hexane suggesting that a smaller range of compounds were extracted. The thermograms correlate with the lower extraction yield observed for hexane and the

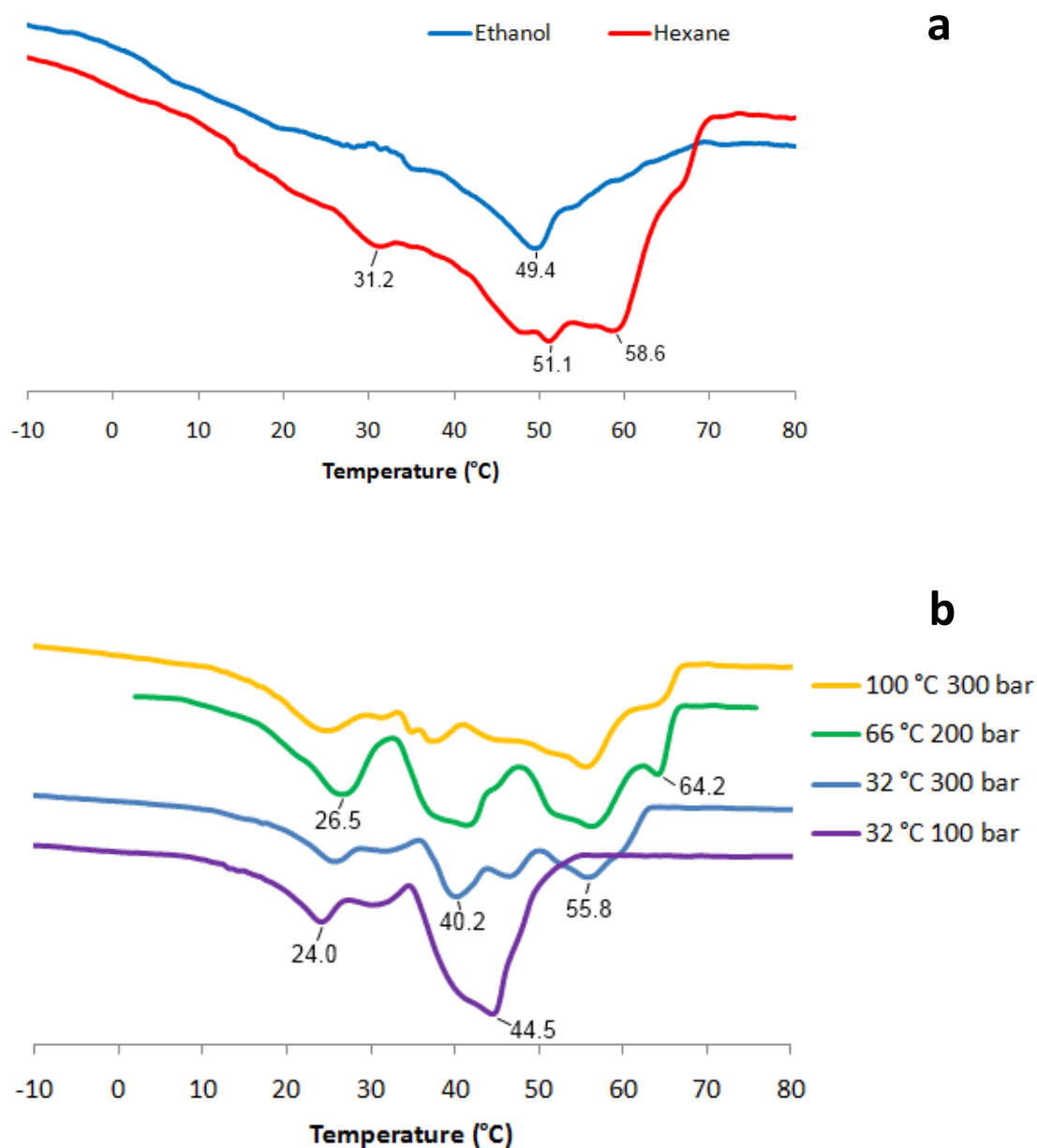


**Figure 3.8: DSC plots of extracts from (a) Soxhlet extraction and (b) supercritical carbon dioxide extraction (Originally in colour)**

larger amounts of co-extractives observed for ethanol by previous researchers.<sup>12</sup> Both of these extracts exhibit several minor endothermic events prior to melting. These could be due to the transformation between different crystalline polymorphs.<sup>20</sup> The energy content of the ethanol extract was much lower than that of the hexane extract at  $16.7 \text{ mJ mg}^{-1}$  compared to  $72.3 \text{ mJ mg}^{-1}$ , suggesting that the ethanol extract contains species with either a lower calorific value or that melt at higher temperatures.

The thermograms of the scCO<sub>2</sub> extracts (Figure 3.8b) vary considerably over the experimental range. In general, they are more defined and narrower than the Soxhlet extracts. The sample obtained at 32 °C and 100 bar notably displays a well-defined, albeit broad, melting range with the majority of the material melting between 35 – 50 °C. Similar melting point ranges were observed for scCO<sub>2</sub> and Soxhlet extracts of flax straw and triticale straw.<sup>16, 19</sup> As the pressure is increased to 300 bar an additional melting band between 50 – 60 °C appears, much higher than the extraction temperature. Deswarte *et al* also observed the presence of higher temperature peaks with increased pressure for wheat straw extracts, although the main melting point was at 71.1 °C, much higher than that observed in these extracts.<sup>12</sup> This either suggests the increased solubility of higher molecular weight components due to changes in the density, or the depression of the melting point at increased pressures.<sup>21</sup> Under extraction conditions of 66 °C 200 bar and 100 °C 300 bar a further peak is observed at 64 °C. This indicates that the melting and solubility of compounds at higher temperatures in sc CO<sub>2</sub> contributes to the additional extraction yield despite the decrease in solvent density.

The melting point depends on chain length, branching, functional group and degree of unsaturation. The lower melting ranges may be due to a higher proportion of unsaturated fatty acids or alkanes.<sup>12, 20</sup> Deswarte *et al* observed that higher temperature melting point extracts contained higher proportions of fatty alcohols.<sup>12</sup> Natural waxes are used in the cosmetics industry for lipsticks, creams and soaps.<sup>16</sup> The application depends partially on the melting point. Lanolin, used for body care uses, has a melting point of 40 °C, close to that of the scCO<sub>2</sub> 32 °C and 100 bar extract.<sup>20</sup> The higher temperature melting points are similar to those of beeswax and candillila wax.<sup>23</sup>

Infrared analysis of the samples was undertaken to observe whether there were any major compositional differences between the extracts (Figure 3.9). All of the scCO<sub>2</sub> extracts were virtually indistinguishable. The intense narrow peaks at 2916 and 2850 cm<sup>-1</sup> can be assigned to the asymmetric and symmetric stretching bands of CH<sub>2</sub> respectively, with the higher frequency shoulder at 2955 cm<sup>-1</sup> due to stretching of CH<sub>3</sub> groups.<sup>24</sup> The intensity of these peaks highlights the major aliphatic nature of the extracts, although their relative intensities are lower in the EtOH extract. These peaks are also apparent on the surface of the initial wheat straw and reduce in intensity following wax extraction.<sup>25</sup>

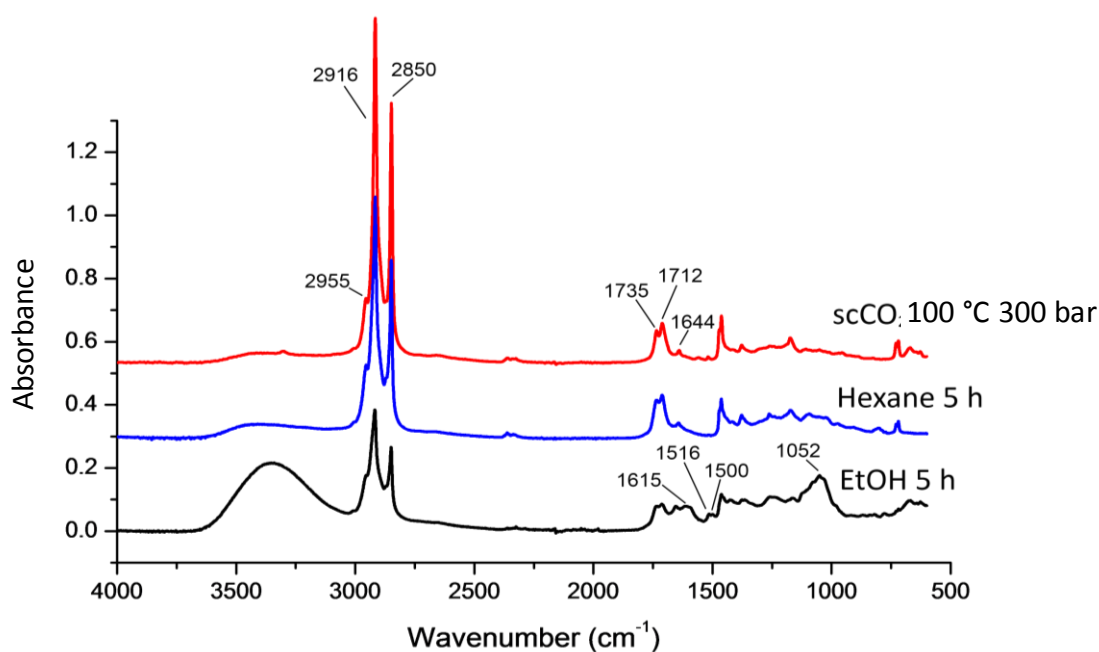


**Figure 3.9: Infrared spectra of extracts by ethanol and hexane Soxhlet extraction and  $\text{scCO}_2$  extraction at 100 °C and 300 bar (Originally in colour)**

The presence of aliphatic esters is indicated by the carbonyl stretch at  $1735\text{ cm}^{-1}$ , whilst carboxylic acid functionalities are highlighted by the broad OH stretch (weakly present in the hexane and  $\text{scCO}_2$  spectra) at  $3100\text{--}3500\text{ cm}^{-1}$  and the carbonyl stretch at  $1712\text{ cm}^{-1}$ .<sup>24, 26</sup> These bands could arise from extracted free fatty acid and wax ester or triglyceride compounds.<sup>26</sup> The peaks at  $1644\text{ cm}^{-1}$  are probably due to the *cis* C=C double bond in unsaturated fatty acids such as linoleic acid.<sup>26</sup> The  $\text{scCO}_2$  and hexane spectra are almost identical indicating the extraction of related compounds due to their similar polarity and are comparable to extracts of flax and triticle.<sup>16, 19</sup> The ethanol extract, in comparison, shows a much more intense broad OH band centred at  $3350\text{ cm}^{-1}$  and additional peaks at  $1615\text{ cm}^{-1}$  and between  $1100\text{--}1000\text{ cm}^{-1}$ . These peaks were observed in all of the ethanol extracts and in the infrared spectra of the initial wheat straw. They are also observed in cellulose and monoglycerides and are associated with stretches of the glycopyranose ring.<sup>27</sup> The maximum peak at  $1052\text{ cm}^{-1}$  can be assigned to symmetrical stretching of the C-O-C bond within the pyranose ring.<sup>28</sup> Two small peaks at  $1516\text{ cm}^{-1}$  and  $1500\text{ cm}^{-1}$  could be due to phenolic compounds.<sup>29</sup> This indicates the possible co-extraction of polar mono- and diglycerides or polysaccharides and other polar molecules in the ethanol extracts that are not observed in the hexane or  $\text{scCO}_2$  extracts. Similar FTIR spectra have been observed for extracts of straw using toluene-ethanol-methanol, toluene-ethanol and

chloroform-methanol solvent mixtures and explained by the removal of polysaccharides.<sup>29</sup>

These results indicate that hexane Soxhlet and scCO<sub>2</sub> give very similar extraction yields and extract compositions. Ethanol Soxhlet extraction with a 5 h extraction time and scCO<sub>2</sub> extraction at 100 °C and 300 bar gave the highest extract yields and different extraction compositions and were therefore chosen as the conditions to study the impacts of the pretreatment process on the combustion of wheat straw.

### **3.4 Inorganic leaching optimisation**

The aim of the leaching tests was to maximise the removal of troublesome elements, particularly potassium, sulfur and chlorine, from the wheat straw and thereby study the impact on the mineralogical changes during combustion, particularly of silica. The leaching tests were carried out by fully submerging the samples in the leaching solution as previous studies had shown this to be the most effective method for removing the unwanted inorganic components.<sup>1</sup> The washing procedure followed that of Thompson *et al* and studied the effect of time and temperature using both water and acid.<sup>10</sup> Following extraction, the acid leached straw was washed with water until a neutral filtrate was observed. This was to ensure that any remaining acid wouldn't affect decomposition and combustion studies. Freshly distilled water was used for all extractions to prevent minerals present in tap water from influencing the results. The process was optimized by analysing the degree of potassium removal. This species was selected due to its high concentration in the initial straw, ease of analysis, use as an indicator of fouling and slagging problems during combustion and its prevalence as a counter-ion to the problematic anionic species, Cl and S. The level of potassium extraction was based on the concentration of potassium observed in the leachate by Atomic Absorption Spectroscopy (AAS).

The level of potassium extracted was slightly higher at 50 °C than 25 °C, although no significant effect of time (1h or 6h) was observed on the extraction of potassium (Figure 3.10). This indicates that the equilibrium level has been reached after 1 h extraction for potassium. A similarly small impact of increasing temperature was seen previously up to

50 °C,<sup>10</sup> whilst during char washing increasing the leaching temperature to 80 °C reduced the residual K from 40 to 15%.<sup>30</sup>

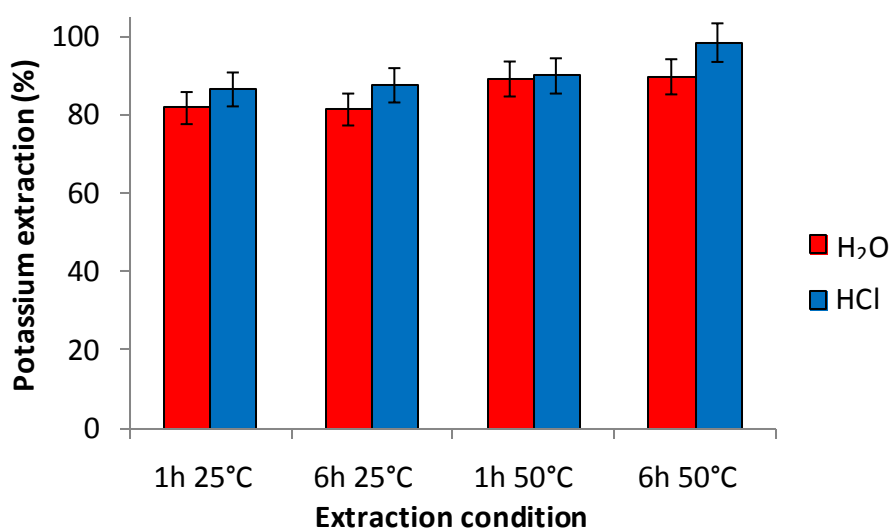


**Figure 3.10: Percentage potassium leached from Cl07 wheat straw with varying temperature, time and leaching solution. Based on AAS analysis of extract (Originally in colour)**

The leaching solution used did not have a significant impact, with the level of potassium extracted using distilled water similar to that of the acid leached solutions. The leaching of potassium in distilled water is similar to the 80-90% found by previous researchers.<sup>1, 5</sup> However, most of those experiments analysed the inorganic content in the residual wheat straw rather than the leachate, suggesting that analysis of the leachate and wheat straw give similar results.

Both citric acid and acetic acid were also tested for the removal of potassium (1 h, 50 °C) due to the possible addition of chlorine to the straw with the use of HCl, which could affect the combustion process. In addition, both of these organic acids can be produced from renewable resources.<sup>31</sup> Citric acid and acetic acid both gave similar potassium extraction yields compared to each other and to HCl (Figure 3.11). Acetic acid as a more mild and benign reagent was chosen for further acid extraction tests. Triplicate analysis using this reagent gave a highly reproducible potassium removal of  $90.4 \pm 2.9\%$  for acetic acid extraction and  $89.3 \pm 1.5\%$  for water extraction at 50 °C for 1 h.

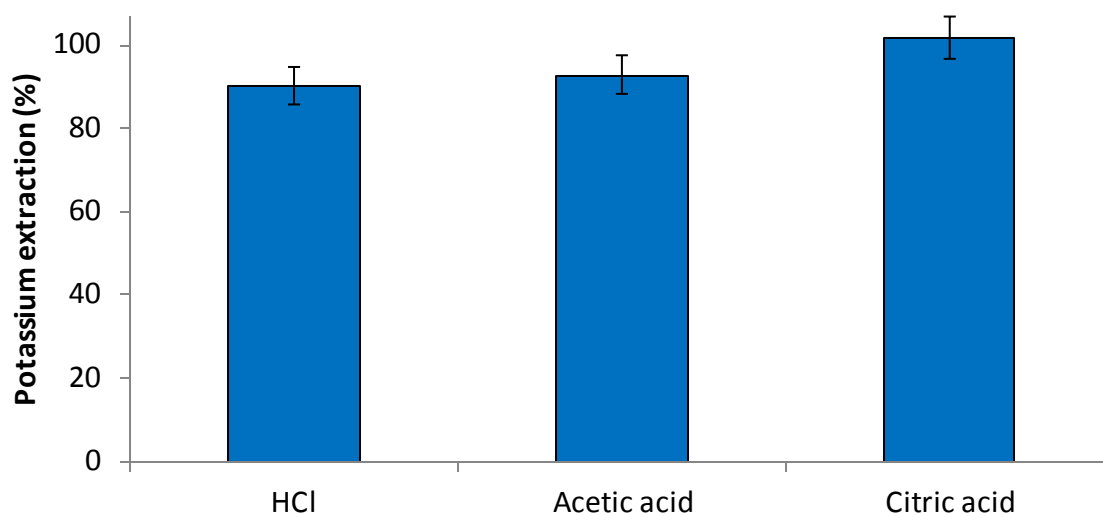


**Figure 3.11: Percentage potassium leached from CI07 wheat straw using different acids after extraction for 1 h at 50 °C. Based on AAS analysis of extract (Originally in colour)**

Analysis of the main anionic species extracted by the optimized leaching techniques, water and acetic acid at 50 °C for 1 h, was carried out by ion chromatography (IC) (Figure 3.12). Comparable levels of anions were found in both water and acid leachates. The level of chloride removed is 70% higher than the maximum expected based on XRF analysis of the initial straw (Figure 3.13). Jenkins *et al* assumed that excess concentrations for some species in the leachate of wheat straw were due to errors, however, most studies have followed the concentration of elements in the residue following leaching rather than the leachate.<sup>1</sup> The chlorine content detected by XRF in the ash (Table 2.1) could be lower than the content in the initial straw due to loss as HCl during the ashing process to 550 °C,<sup>5</sup> however, analysis of the initial straw indicated a similar chlorine content. The extraction data does, however, highlight the ease of solubilisation of chlorine. The ease of leaching is in agreement with the fact that most chlorine is taken up and remains in its ionic form within the plant.<sup>32</sup> Plants take up to 10-100 times more chloride than they require and it plays a key role in cell division, the oxidation of H<sub>2</sub>O during photosynthesis and as a regulator of osmotic pressure.<sup>32</sup>

50% of the sulfur and nearly 65% of the phosphorous present in the wheat straw are leached by both methods. Sulfur is absorbed from soils as divalent sulfate anions (SO<sub>4</sub><sup>2-</sup>). Some of this sulfur is metabolised to form proteins, vitamins and coenzyme A.<sup>32</sup> However, much of it remains in the ionic form and is translocated in the xylem. It is this sulfur that is

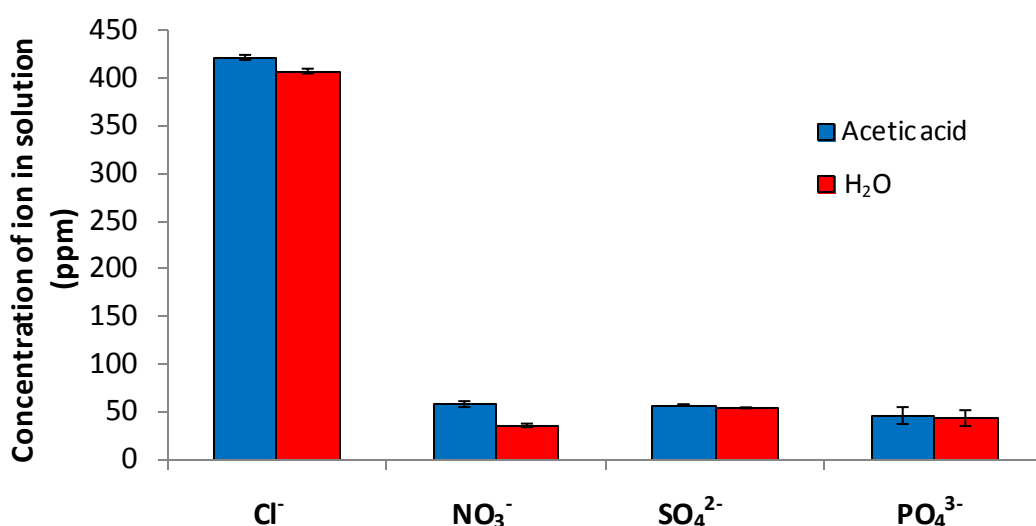


**Figure 3.12: Concentration of various anionic species in wheat straw leachates after extraction for 1 h at 50 °C using acetic acid or water (Originally in colour)**

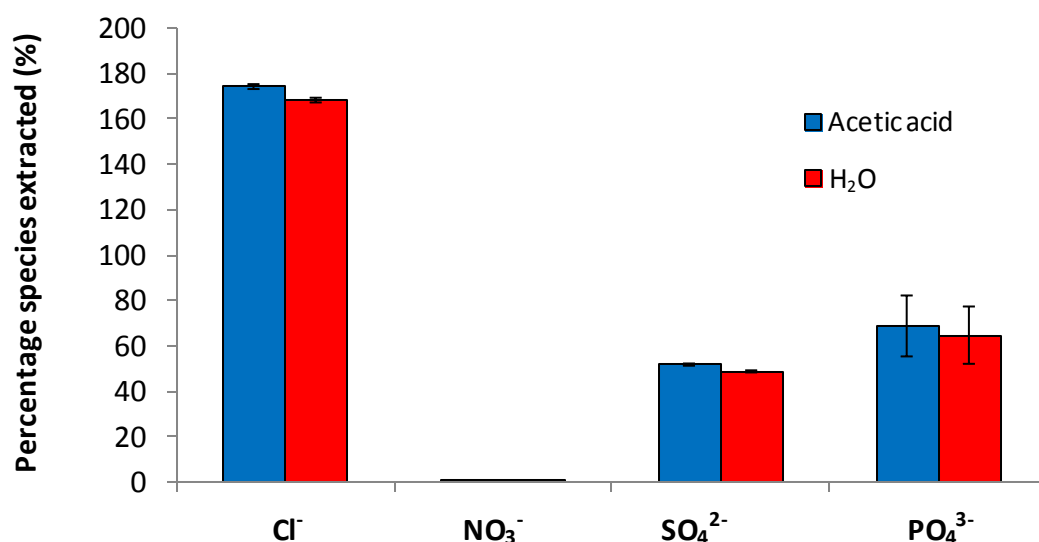


**Figure 3.13: Percentage of various anionic species extracted by leaching Cl07 wheat straw in acetic acid and water for 1 h at 50 °C (Originally in colour)**

predicted to be leached during acid and water washing. Knudsen *et al* previously found that 40 – 50% of the initial sulfur could be extracted from wheat straw either by water or acid leaching.<sup>33</sup> They assumed that the rest of the sulfur was organically associated. Phosphorous is absorbed primarily as the monovalent anion (H<sub>2</sub>PO<sub>4</sub><sup>-</sup>). It remains as phosphate in the plant either free or bound to organic components.<sup>32</sup> Nitrogen levels are only marginally reduced during leaching. Most nitrogen in the plant is incorporated into organic protein structures and is therefore inaccessible to leaching.<sup>32</sup> The same leaching

trends for sulfur and nitrogen have been observed for wheat straw,<sup>5</sup> and for phosphorous and sulfur from switchgrass by water washing.<sup>34</sup> Calculations of the relative moles of each species extracted are shown in Table 3.2 for the water leachate. The charge balance is almost neutral; the remaining charge could be due to the presence of small amounts of  $\text{Na}^+$ .

**Table 3.2: Concentrations of ions in water leached solution**

	$\text{K}^+$	$\text{Cl}^-$	$\text{NO}_3^-$	$\text{SO}_4^{2-}$	$\text{PO}_4^{3-}$
Moles ( $\times 10^{-3}$ )	14.2	11.9	0.44	0.67	0.45

This data indicates that both water and acid leaching result in the removal of similar levels of the inorganic species that cause the most challenges during combustion. However, water leaching may be most beneficial for the recovery and reutilisation of the inorganic species.

### **3.5 Impact of pretreatment on mineralogical changes during combustion**

#### **3.5.1 Fuel analysis**

The impact of the optimised pretreatment processes on the ultimate and proximate analyses and slagging indices were initially observed to predict their impact on the combustion processes (Table 3.3).

The moisture content of the  $\text{scCO}_2$  extracted wheat straw is significantly lower than both the initial straw and the other pretreated straws, with the water content observed to increase with time following extraction. The temperature used for this extraction is at the boiling point of water under atmospheric conditions, yet at the extraction pressure, 300 bar, the boiling point of water will be higher. Water has a low solubility in  $\text{scCO}_2$ , measured as  $4.92 \times 10^{-3} \text{ mol mol}^{-1}$  at 40 °C and 150 bar.<sup>35</sup> However, supercritical carbon dioxide has previously been shown to be effective at drying lignite coals from 30 wt% to 1.6 wt% moisture content at 40 °C and 147 bar over 30 h.<sup>36</sup> The addition of methanol as an entrainer (co-solvent) can increase the rate of drying by increasing the solvent

Table 3.3: Fuel analysis of pretreated CI07 wheat straw

	Pretreatment method				
	Initial	scCO <sub>2</sub>	EtOH	H <sub>2</sub> O	CH <sub>3</sub> COOH
<b>Moisture (%)</b>	7.10 ± 0.10	3.56 ± 1.7	6.74 ± 0.15	7.42 ± 0.36	7.10 ± 0.06
<b>Volatile content (%)<sup>dab</sup></b>	70.0	68.7	70.5	70.8	75.5
<b>Fixed carbon (%)<sup>dab</sup></b>	23.9	25.4	25.3	23.5	21.7
<b>Ash (%)<sup>db</sup></b>	6.03 ± 0.04	5.89 ± 0.51	5.66 ± 0.16	4.18 ± 0.78	2.74 ± 0.64
<b>C (%)<sup>db</sup></b>	45.5	46.0	47.2	47.5	47.4
<b>H (%)<sup>db</sup></b>	5.19	5.34	5.10	5.12	5.14
<b>N (%)<sup>db</sup></b>	0.39	0.32	0.29	0.25	0.15
<b>O (%)<sup>db</sup></b>	42.5	42.4	41.8	42.9	44.6
<b>HHV (MJ kg<sup>-1</sup>)<sup>db</sup></b>	18.4	17.6	18.3	17.8	18.1
<b>HHV (MJ kg<sup>-1</sup>)<sub>1</sub><sup>dab</sup></b>	19.5	18.7	19.3	18.5	18.6
<b>Elements (% ash)</b>					
<b>Na<sub>2</sub>O</b>	0.11	0.36	0.32	0.38	0.04
<b>MgO</b>	1.37	1.30	1.64	1.24	0.13
<b>Al<sub>2</sub>O<sub>3</sub></b>	0.19	0.14	0.26	0.20	0.10
<b>SiO<sub>2</sub></b>	44.3	40.8	53.4	60.8	78.5
<b>P<sub>2</sub>O<sub>5</sub></b>	1.54	1.82	2.26	1.22	1.18
<b>K<sub>2</sub>O</b>	28.3	26.0	17.4	14.1	0.6
<b>CaO</b>	12.6	9.08	11.4	11.7	5.14
<b>Mn<sub>3</sub>O<sub>4</sub></b>	0.14	0.14	0.16	0.14	0.02
<b>Fe<sub>2</sub>O<sub>3</sub></b>	0.07	0.22	0.38	0.34	0.28
<b>SO<sub>3</sub></b>	2.84	0.24	7.30	4.63	3.75
<b>Cl</b>	8.19	14.1	3.14	1.83	0.01
<b>Alkali index (kg M<sub>2</sub>O GJ<sup>-1</sup>)<sup>db</sup></b>	1.30	1.18	0.89	0.60	0.08

db – dry basis

dab – dry ash-free basis

polarity.<sup>14</sup> Co-extraction of water with lipid extraction has also been observed for other biomass materials.<sup>37</sup> Between 14 – 17% of the original water content of canola flakes was removed during scCO<sub>2</sub> extraction, with increasing removal of water at higher temperatures and pressures.<sup>37</sup> This was ascribed to increasing water solubility with increasing vapour pressure.<sup>37</sup> This data suggests a potential added benefit of using scCO<sub>2</sub> for the pretreatment of wet wheat straw by lowering the moisture content of the

material and thereby improving the combustion properties alongside the extraction of lipids. However, generally a high moisture content is unfavourable when using scCO<sub>2</sub> due to competition between water and the solute, potential ice blockages in the extractor and hydrolysis of extracts.<sup>38</sup> Increased solubility of palmitic acid, caffeine and essential oils have been found with water saturated scCO<sub>2</sub>.<sup>35, 39, 40</sup> These studies indicate that the moisture content can also affect the extract composition, particularly of more polar compounds.<sup>35</sup> The water-CO<sub>2</sub> interaction is therefore an important, but poorly researched, area to study for the industrial application of the extraction of valuable wax compounds by scCO<sub>2</sub>.<sup>41</sup>

The acetic acid pretreated straw displays an increased volatile yield and decreased fixed carbon content under pyrolysis conditions. Decreased char yields and increased volatile yields have been observed for many biomass materials following acid demineralization.<sup>42-</sup><sup>44</sup> Other researchers have also detected the same effect with water washing,<sup>34, 45, 46</sup> however, in this case none of the other pretreatment processes affected the volatile or fixed carbon levels. These observations are discussed in more detail in section 3.5.3. The percentage of carbon in the EtOH, water and CH<sub>3</sub>COOH pretreated straw increased marginally compared to the initial straw. The calorific value remained relatively constant, particularly on a dry, ash free basis.

The ash content of the biomass decreases dependent on the pretreatment process in the order: initial straw ~ scCO<sub>2</sub> > EtOH > H<sub>2</sub>O > CH<sub>3</sub>COOH. The inorganic composition of the ash also varies significantly between the pretreated straws. To enable a better comparison of the removal of ash components with different pretreatments the individual oxides were normalised to the silica content of the initial straw (Table 3.4). This method assumes that silica is not leached during the pretreatment processes, which is supported by evidence of the low solubility of silica in acidic to neutral pH solutions.<sup>47</sup>

Little to no inorganic removal occurs during extraction with scCO<sub>2</sub>, in particular, the level of potassium remains constant. This is unsurprising as the transfer of ionic species into an organic phase is energetically unfavourable.<sup>48</sup> The extraction of various metal ions, including for K<sup>+</sup> and Na<sup>+</sup>, in scCO<sub>2</sub> from aqueous solutions has only been achieved previously by utilising complexing agents such as crown ethers or

**Table 3.4: Normalised oxide content of ash following pretreatment processes (all wt%)**

	Initial	scCO <sub>2</sub>	EtOH	H <sub>2</sub> O	CH <sub>3</sub> COOH
Na <sub>2</sub> O	0.11	0.39	0.27	0.28	0.02
MgO	1.37	1.41	1.36	0.90	0.07
Al <sub>2</sub> O <sub>3</sub>	0.19	0.15	0.22	0.15	0.06
SiO <sub>2</sub>	44.3	44.3	44.3	44.3	44.3
P <sub>2</sub> O <sub>5</sub>	1.54	1.97	1.87	0.89	0.67
K <sub>2</sub> O	28.3	28.2	14.4	10.2	0.32
CaO	12.6	9.84	9.46	8.53	2.90
Mn <sub>3</sub> O <sub>4</sub>	0.14	0.15	0.13	0.10	0.01
Fe <sub>2</sub> O <sub>3</sub>	0.07	0.24	0.31	0.25	0.16
SO <sub>3</sub>	2.84	0.26	6.05	3.37	2.11
Cl	8.19	15.3	2.60	1.33	0.00
<b>Total</b>	<b>99.7</b>	<b>102.1</b>	<b>80.9</b>	<b>70.3</b>	<b>50.6</b>

pentadecafluorooctanoic acid.<sup>49</sup> The high chloride content identified in the ash of this sample compared to the initial straw might be due to variations during ash formation.

Water washing reduced the potassium (64%), phosphorous (42%) and chloride content (84%) of the straw. These levels are all lower than those measured by analysis of the leachate (section 3.4 above), probably due to residual salts remaining on the straw following filtering. The removal of potassium (99%), phosphorous (56%) and chloride (100%) is observed to be greater with acid washing, despite similar concentrations of species in the leachate. The disparity may be attributed to the repeated water washing of the acid leached straw to remove the residual acid. In addition, acid demineralisation removed the majority of the calcium (77%), sodium, magnesium and manganese. The presence of iron and aluminium in ashes has been accredited to soil contamination,<sup>5</sup> however, the levels of these elements are consistent and low between samples and don't decrease on water washing of the straw, supporting the visual observation that soil contamination was low. The percentages and species removed by water and acid leaching are comparable to those observed by previous researchers for wheat straw and other biomass samples,<sup>2, 5, 10, 50</sup> although less information is available in the literature on the complete inorganic species distribution in ashes following acid demineralisation.

The inorganic content of ethanol extracted straw ash was surprising, showing a large reduction in potassium (49%) and chloride (68%) content. This level was similar to that achieved by water washing, whilst the other species present were unaffected. Previous studies on ethanol extraction of wheat straw have focused on lipid removal and have not reported this observation.

The alkali index reduced along the same trend as the ash reduction (Table 3.3): Initial  $\sim$   $\text{scCO}_2 > \text{EtOH} > \text{H}_2\text{O} > \text{CH}_3\text{COOH}$ , due to the removal of problematic alkali species by the latter pretreatment methods. However, only the acid wash process reduced the material to a low slagging risk ( $< 0.17 \text{ kg GJ}^{-1}$ ).<sup>51</sup>

### 3.5.2 Mineralogical changes

In order to understand and explain the extraction of individual inorganic elements during the pretreatment processes the mineral phases within the samples combusted at 500 °C for 2 h were identified by XRD (Figure 3.14).

The diffractograms of the ash from the initial straw and that following extraction by  $\text{scCO}_2$  are almost identical in both the position and intensities of the peaks, further confirming that  $\text{scCO}_2$  extraction does not affect the inorganic composition of the materials. The XRD spectra of the water leached and ethanol extracted straws clearly show a reduction in potassium chloride content, with a corresponding relative increase in the calcite content of the ashes compared to the initial straw. The rest of the spectra remain relatively unchanged. Dayton *et al* previously reported a lack of HCl and KCl vapours during the combustion of water leached wheat straw.<sup>5</sup> This correlates with both the XRF data of the elemental content of the ashes and the analysis of the ion content of the leachate, confirming that K and Cl are leached as KCl. However, the reduction in KCl content of the ethanol extracted ashes was unexpected. Repeated ethanol extraction of wheat straw demonstrated the same reduction in KCl content by XRD. In addition, water leaching of the wax extract gave a potassium recovery of 40 – 45% of the initial content in the wheat straw. Solubility data demonstrates that KCl is essentially insoluble in ethanol, with an experimental value of only  $0.0063 \text{ mol kg}^{-1}$  at 20 °C reducing to  $0.0044 \text{ mol kg}^{-1}$  at 60 °C.<sup>52</sup> The addition of water improves the solubility dramatically; with 10 wt%  $\text{H}_2\text{O}$  the KCl solubility rises to  $0.0295 \text{ mol kg}^{-1}$  and increases exponentially with further  $\text{H}_2\text{O}$

thereafter.<sup>52</sup> This implies that the KCl is either solubilised due to the inherent moisture content of the wheat straw and/or due to the water content of the ethanol solvent. Drying the initial ethanol solvent using molecular sieves, or drying the wheat straw prior to use, did not result in a reduction in KCl removal as analysed by XRD suggesting that extraction by both routes is possible.

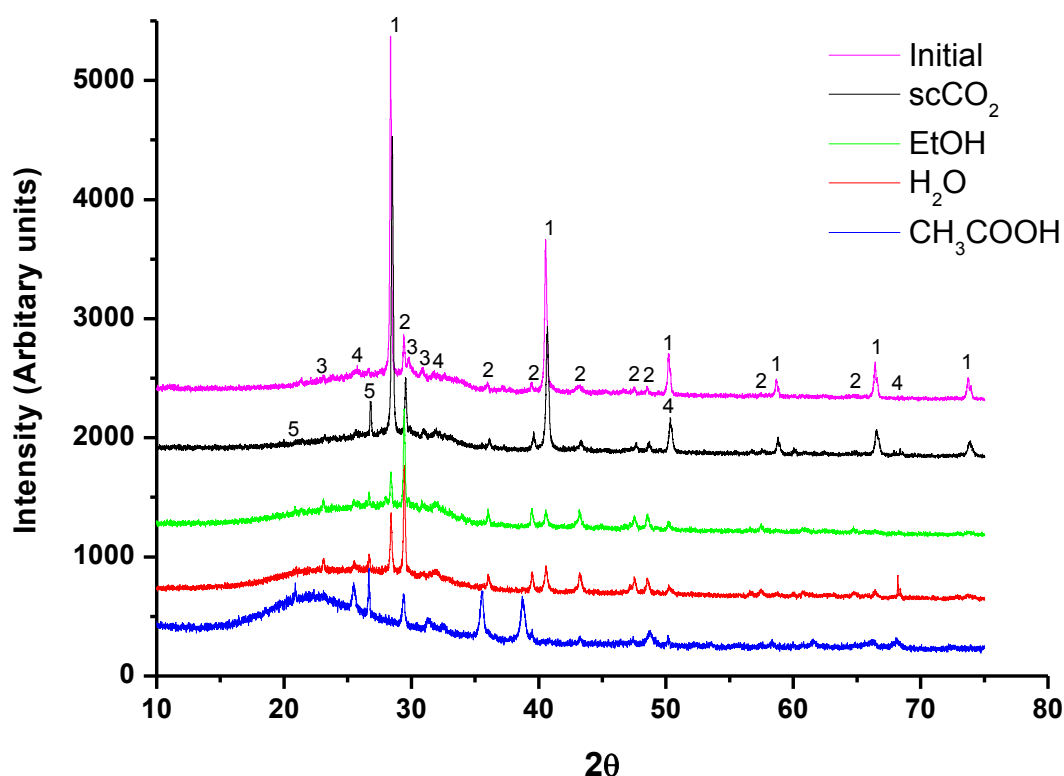


**Figure 3.14: X-ray diffraction of wheat straw ash following different pretreatment methods. All combusted at 500 °C for 2 h. 1 = Sylvite (KCl); 2 = Calcite (CaCO<sub>3</sub>); 3 = Arcanite (K<sub>2</sub>SO<sub>4</sub>); 4 = Anhydrite (CaSO<sub>4</sub>); 5 = Quartz (SiO<sub>2</sub>) (Originally in colour)**

The XRD pattern of the acid washed straw confirms the complete removal of KCl. Calcium was virtually entirely removed as calcite. The partial removal of carbonates with CH<sub>3</sub>COOH from cotton residue and waste wood was previously demonstrated by Vamvuka *et al.*<sup>43</sup> The spectrum contains a broad background peak between 15 – 30 2θ. This is reminiscent of the diffraction patterns of rice hull ashes (RHA) combusted at 600 °C due to the presence of disordered silica and the diffractogram of Cl08 ashes (Chapter 2).<sup>53</sup> The centre of the broad peak at 20.9 2θ is characteristic of α-cristobalite.<sup>54</sup> A slight increase in the background halo in this region can also be discerned for the H<sub>2</sub>O and EtOH extracted ashes, with H<sub>2</sub>O > EtOH, whilst it is absent for the initial and scCO<sub>2</sub> ashes. This corresponds to the degree of removal of potassium and calcium cations from the straw.

Thermodynamic calculations on the distribution of species within straw indicate that where there is a high Si/K ratio, up to 60% of the potassium present may be incorporated into silicates networks at 500 °C,<sup>55</sup> although it is found to preferentially form KCl where chlorides are present.<sup>56</sup> Phase diagrams show a ternary eutectic as low as 540 °C with 69% SiO<sub>2</sub>, 23% K<sub>2</sub>O and 8% Na<sub>2</sub>O.<sup>57</sup> Three eutectics in the SiO<sub>2</sub>-K<sub>2</sub>O system are also observed around 770 °C where there is a SiO<sub>2</sub> wt% of just over 55% and just under 80%.<sup>58</sup> In contrast a rise in CaO content generally increases the melting temperature in the K<sub>2</sub>O-CaO-SiO<sub>2</sub> ternary system.<sup>1</sup> The XRD data consequently suggests the formation of amorphous glasses rather than amorphous silica unless the potassium level is reduced to an insignificant level, which only acid leaching achieves.

### 3.5.3 Thermochemical changes

The pyrolysis and combustion decomposition profiles for all of the pretreated straws are shown in Figures 3.15 and 3.16 respectively. The ignition temperature, corresponding to a weight loss of 0.5 wt% min<sup>-1</sup>,<sup>59</sup> and the peak temperature, the maximum rate of weight loss, are important parameters indicating the reactivity of the sample. These are shown in Table 3.5.

**Table 3.5: Peak and ignition temperatures for pretreated straw samples under pyrolysis and combustion conditions**

		Initial	scCO <sub>2</sub>	EtOH	H <sub>2</sub> O	CH <sub>3</sub> COOH
Pyrolysis	Onset temperature (°C)	213	215	228	233	239
	Peak temperature (°C)	324	323	333	338	348
	Maximum rate of weight loss (mg min <sup>-1</sup> )	-7.8	-8.2	-7.8	-8.8	-9.4
Combustion	Ignition temperature (°C)	215	215	223	226	231
	Peak temperature (°C)	269	268	270	270	310
	Maximum rate of weight loss (mg min <sup>-1</sup> )	-8.0	-8.8	-8.7	-8.8	-10.9

The pyrolysis profiles (Figure 3.15) exhibit an increase in decomposition onset temperature, peak temperature and maximum rate of decomposition with increasing demineralisation, particularly with respect to potassium removal, of the samples: initial ~ scCO<sub>2</sub> > EtOH > H<sub>2</sub>O > CH<sub>3</sub>COOH. In addition, the acid leached sample has a higher volatile content and lower fixed carbon content in comparison to the other samples (Table 3.3).

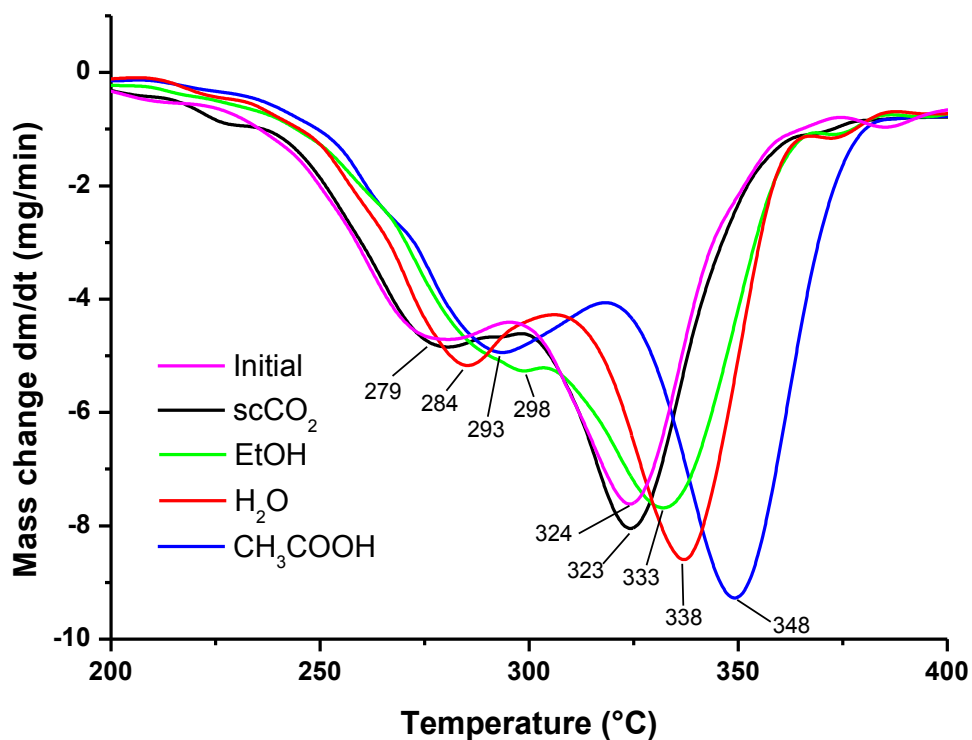


Figure 3.15: Pyrolysis profiles of pretreated Cl07 wheat straw (Originally in colour)

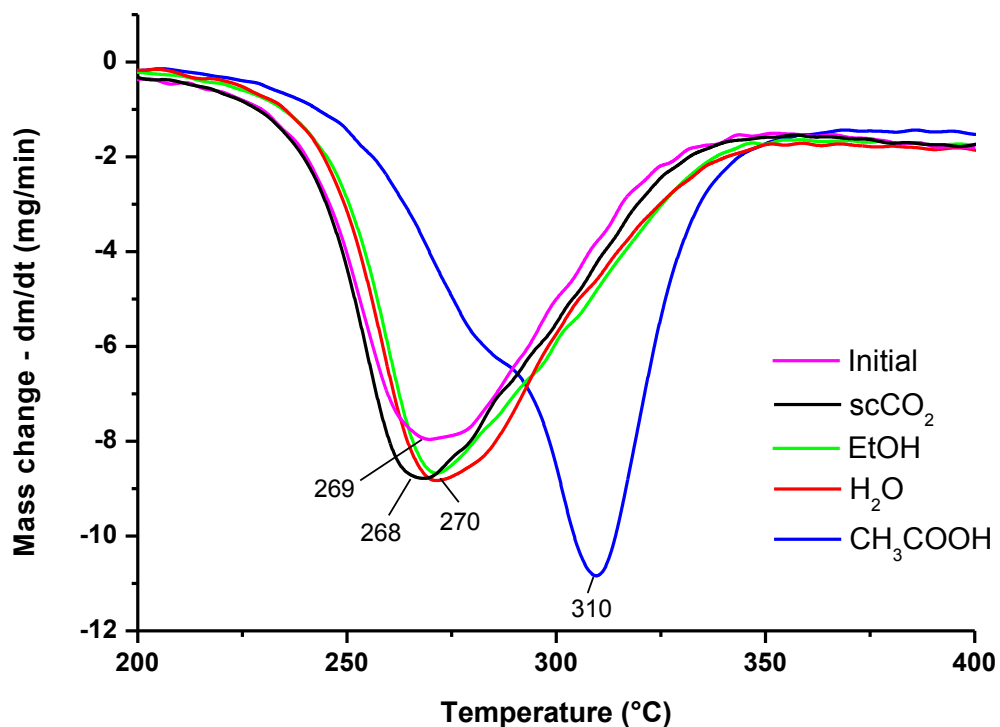


Figure 3.16: Combustion profiles of pretreated Cl07 wheat straw (Originally in colour)

Raveendran *et al* observed decreased char yields, increased volatile yields, increased onset temperatures (+ 20-30 °C), increased maximum devolatilisation rates and increased peak temperatures (+ 5-10 °C) following acid leaching of herbaceous and woody biomass including straw.<sup>42</sup> This has also been observed for water washed straw.<sup>59</sup> These changes are generally attributed to the impact of minerals present in the ash, particularly potassium, and its catalytic impact on decomposition processes, principally on cellulose. The exact mechanism of this process is still not fully understood with some authors suggesting an 'ionic force' interaction between the metal ions and the pyranose ring,<sup>50</sup> whilst others indicate a base catalysed process.<sup>31</sup> However, these observations support the demineralisation trend observed in this study for the different pretreatment processes. Frequently, a single decomposition peak is observed to split into two peaks on demineralisation,<sup>42, 59</sup> the lower temperature shoulder due to hemicellulose and the higher temperature peak caused by cellulose volatilisation (peak max ~ 350 °C), with lignin decomposing over a broad temperature range from 200 – 700 °C.<sup>60</sup> Two decomposition peaks are always observed in this study, however, following pretreatment the shift of the lower temperature peak is smaller than the higher temperature peak, except for the EtOH extracted straw. This may be due to the impacts of the hot water and hot acid treatments modifying the hemicellulose component of the wheat straw. Hemicellulose is the most thermo-chemically sensitive of the lignocellulosic components and under acidic conditions is hydrolysed to soluble compounds.<sup>61</sup> Hot water soluble extracts from wheat straw have been found to contain up to 27 wt% carbon,<sup>62</sup> with oxalic, citric, acetic, propionic, succinic, formic and fumaric acids identified in the leachate.<sup>8</sup> The water extracts in this study were observed to be mildly acidic with an average pH of  $6.7 \pm 0.04$  after 1 h at 50 °C. The pH was slightly lower at longer extraction times. In addition, drying of the leachate gave a solids content of 0.39 wt% for the water solution and 0.64 wt% for the acid solution. Analysis of the inorganic components gave a mass balance of 0.1 – 0.13 wt% in the leachate, therefore indicating some co-extraction of organic components. Infrared analysis of the solids indicated the presence of sugars. The hemicellulose component may therefore be chemically modified during water and acid treatments making it more reactive during pyrolysis relative to cellulose following demineralisation.

The devolatilisation stage during combustion demonstrates much less dependence on the mineral content of the straw, except for the acid washed straw, which has a very different burning profile to the other samples (Figure 3.16). The temperature range of decomposition is similar for all of the samples, however, the ignition temperature is shifted to higher temperatures with increasing demineralisation, indicating reduced reactivity. In addition, the char oxidation stage is completed at a higher temperature for the CH<sub>3</sub>COOH extracted straw, as observed in other studies.<sup>43</sup> This suggests that only a severe treatment, such as acid leaching, will significantly influence the combustion process.

### 3.5.4 Melting and decomposition characteristics of pretreated straw ash

#### 3.5.4.1 Simultaneous Thermal Analysis (STA)

Understanding the thermal characteristics and fusion points of the ashes formed following the pretreatment steps is vital for estimating the slagging and fouling potential during combustion and for gaining insight into the extraction and solubilisation of the elements during extraction. Ash fusion quantification by means of thermal analysis has previously been described by Hansen *et al* as a more reliable, quantifiable and detailed method than the traditional ash fusion tests.<sup>63</sup> Arvelakis *et al* used STA methods to study the melting and gas-phase release behaviour of various herbaceous biomass ashes in comparison to pure salts.<sup>64</sup> Only one study has previously examined the effect of pretreatments on the STA of ashes, studying the water leaching of peach, grape and cotton gin residues.<sup>65</sup> The ashes tested in this study were first combusted to 550 °C at a low heating rate to prevent volatilisation of inorganic species. The measurements were carried out by Phil Davies of TA Instruments. The results are shown (Figure 3.17 – 3.23).

The general mass loss curve (Figure 3.17) shows loss of water occurring between 0 – 175 °C, a small mass loss around 470 °C, a larger mass loss at 674 °C and variable mass losses of inorganic species at higher temperatures. The mass changes in the water region vary significantly for the various ashes (Figure 3.18). The acid washed sample exhibits a greater total mass loss at a lower temperature than the other samples. This suggests loss of free water due to a more hydrophobic material with a higher surface area. This is consistent with highly cross-linked amorphous silica as indicated by the XRD data (Figure 3.14). Rice hull ashes with high silica contents (~ 95%) have been shown to form high surface area

materials of 54–235 m<sup>2</sup> g<sup>-1</sup> following combustion.<sup>66-68</sup> <sup>29</sup>Si NMR of rice hull ashes combusted at 500 °C show a single peak at -113 ppm due to cross-linked Q<sup>4</sup> silica structures.<sup>69, 70</sup> Unfortunately, neither porosimetry measurements nor <sup>29</sup>Si NMR were carried out on the CH<sub>3</sub>COOH ashes.

The TG profiles of the initial, scCO<sub>2</sub> and EtOH pretreated straws all contain two water mass loss peaks at around 80 and 150 °C suggesting two processes of water desorption from the ash surface. The temperature ranges intimate the removal of water of hydration of the inorganic salts.<sup>71</sup> Potassium chloride, identified in the ashes by XRD, is known to be highly hygroscopic.<sup>72</sup> Therefore, the differences in the water content of the ashes may be due to the relative content of hygroscopic salts in the ashes following the different pretreatment processes.

The mass loss and heat release behaviour across the rest of the temperature range are similar for the initial and scCO<sub>2</sub> pretreated straw samples and the EtOH and H<sub>2</sub>O treated straw samples. The main decomposition peaks and their identification are shown in Table 3.6. The initial and scCO<sub>2</sub> samples display greater total mass losses overall of around 25% (Figure 3.17), the EtOH and H<sub>2</sub>O samples show mass losses at temperatures beyond 200 °C of 6 – 8%, whilst the loss from the CH<sub>3</sub>COOH sample is ~6% above 200 °C with half of this released below 600 °C. The mass losses in the temperature range above 200 °C but below the ash formation temperature (550 °C) are probably due to the devolatilisation of residual organic compounds, perhaps released due to grinding of the samples enabling trapped particles to decompose.

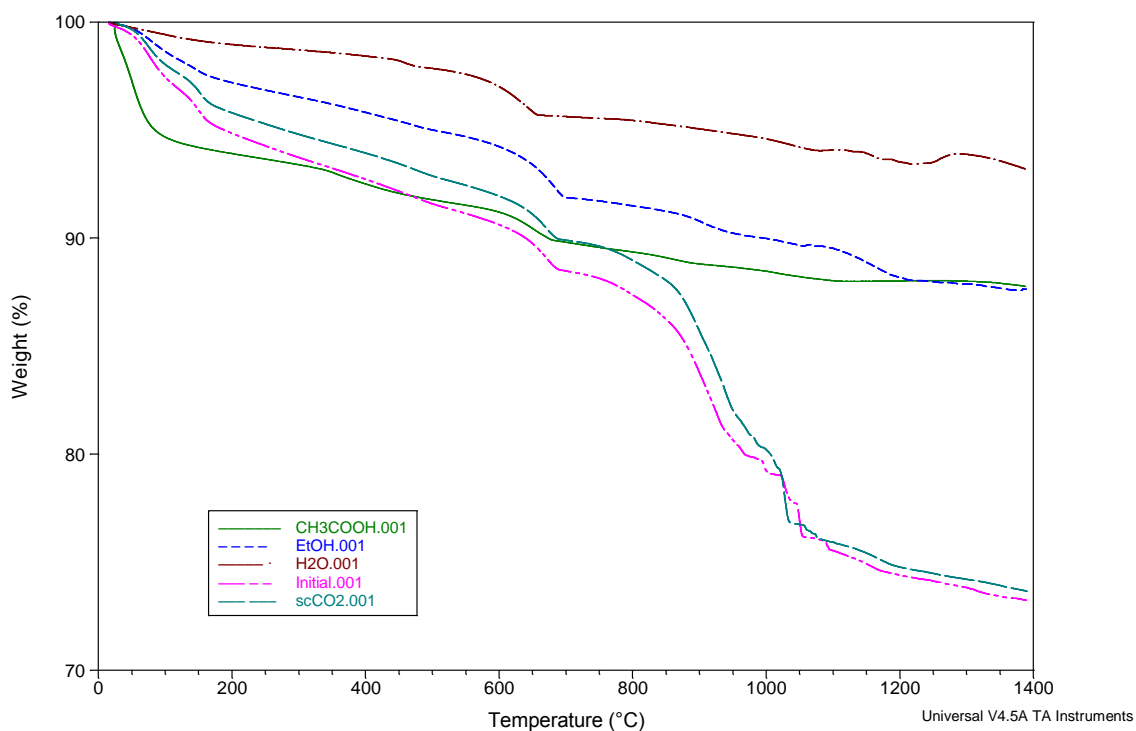


**Figure 3.17: Comparison of mass loss of ashes from pretreated wheat straw previously combusted at 550 °C (Originally in colour)**

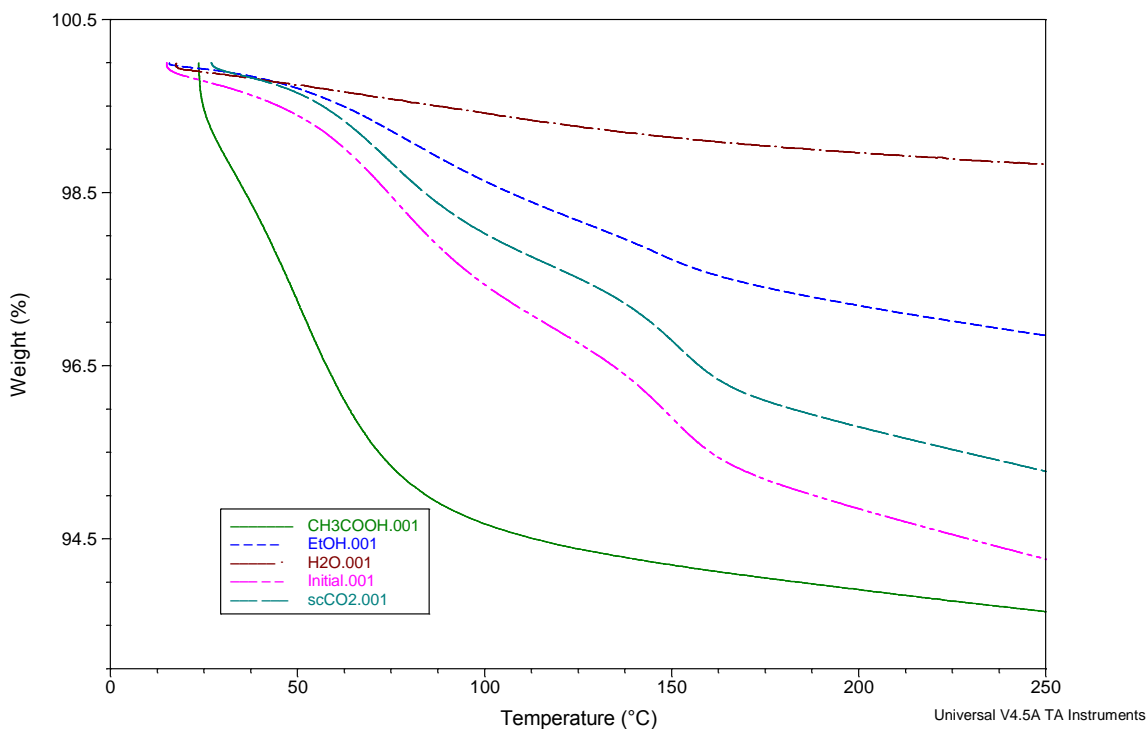


**Figure 3.18: Mass loss from ashes between 0 – 250 °C (Originally in colour)**

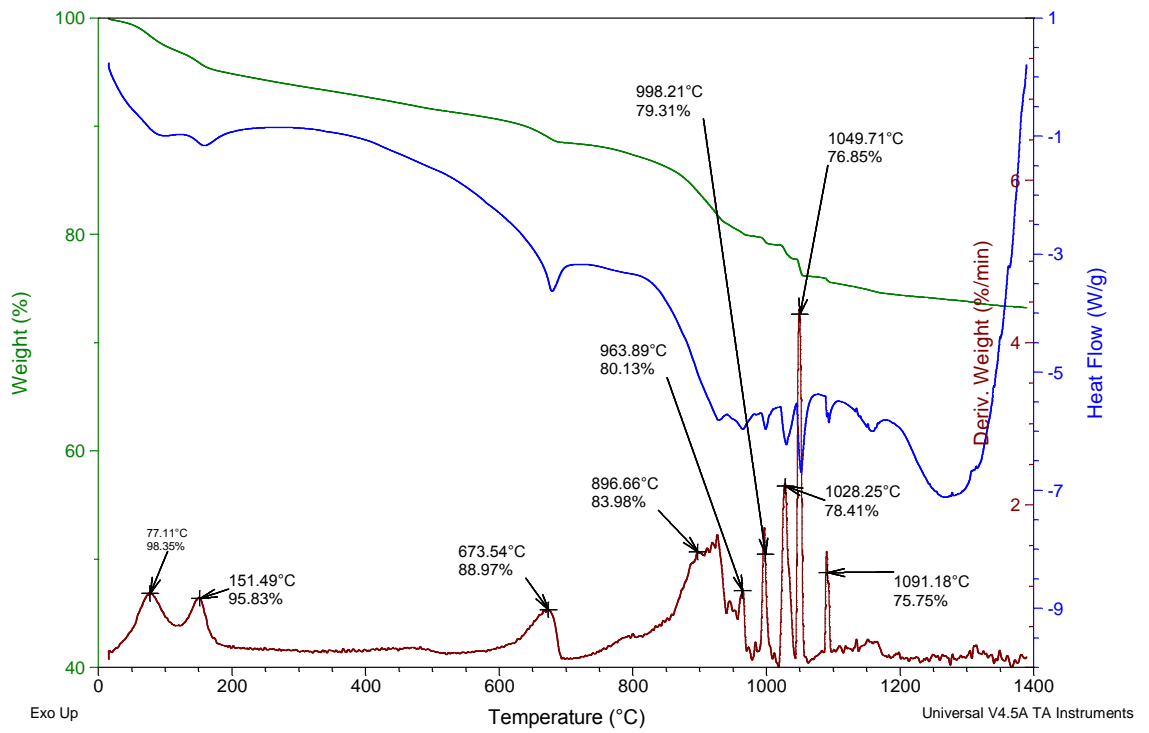


Figure 3.19: TG, DTG and DSC of ash of initial wheat straw (Originally in colour)

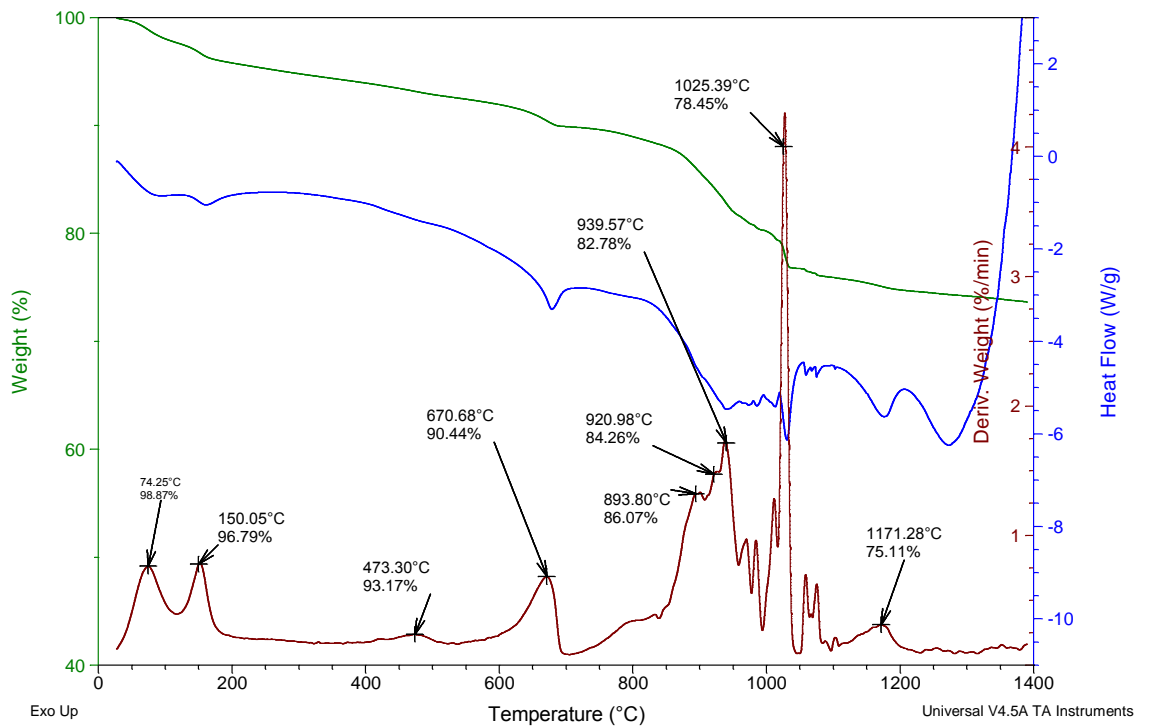
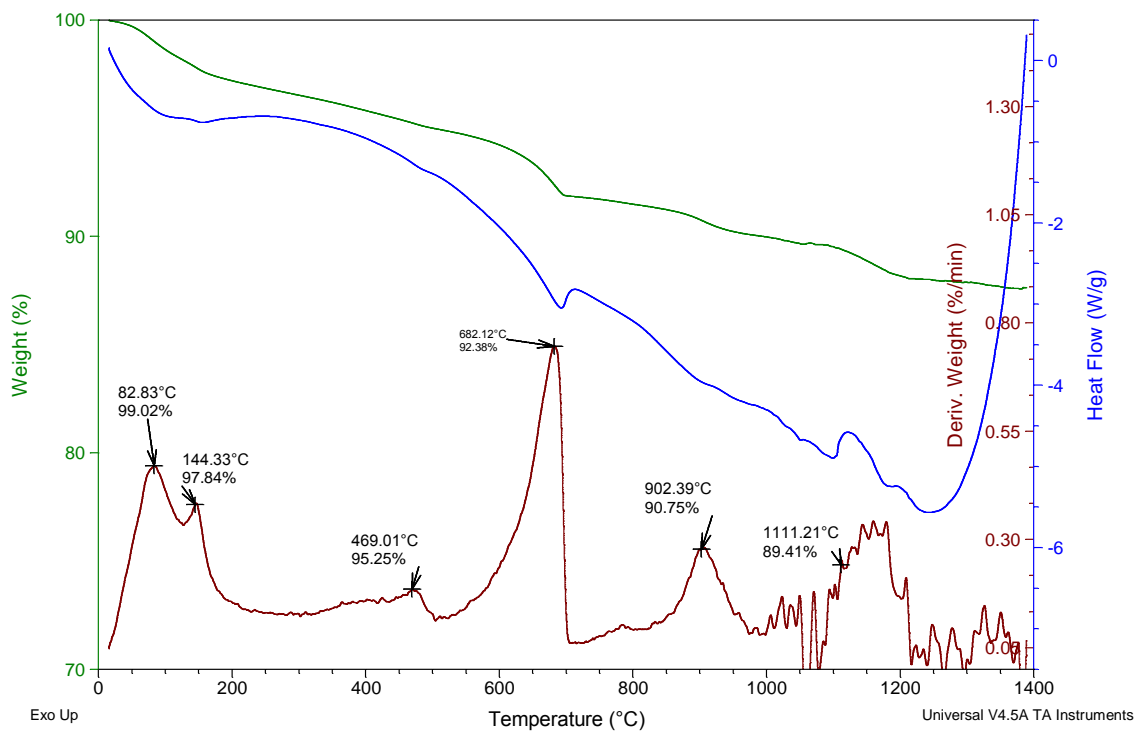
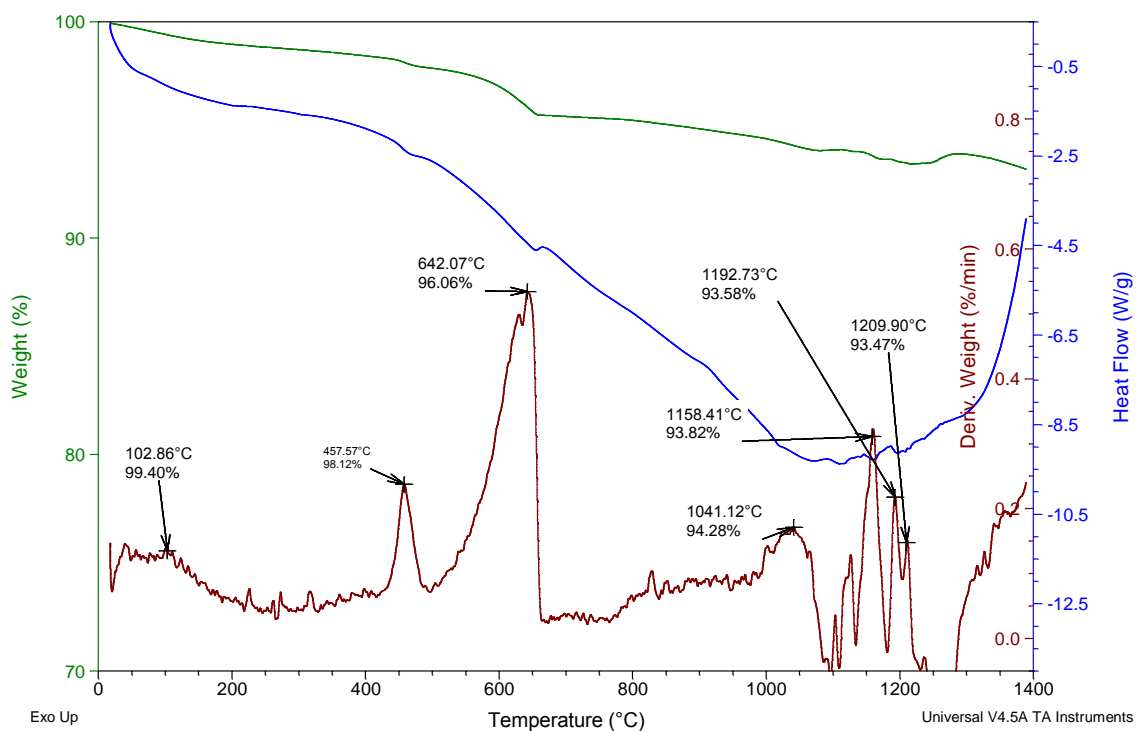


Figure 3.20: TG, DTG and DSC of ash of scCO<sub>2</sub> extracted wheat straw (Originally in colour)



**Figure 3.21: TG, DTG and DSC of ash of EtOH extracted wheat straw (Originally in colour)**



**Figure 3.22: TG, DTG and DSC of ash of H<sub>2</sub>O leached wheat straw (Originally in colour)**

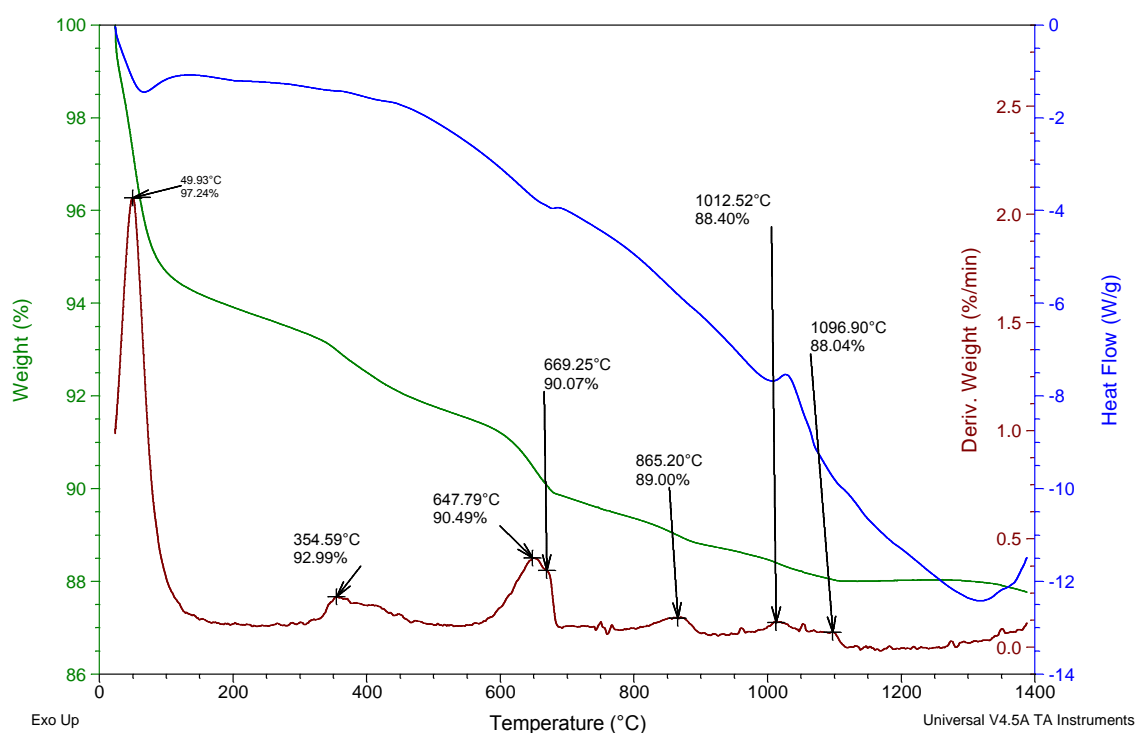


Figure 3.23: TG, DTG and DSC of ash of  $\text{CH}_3\text{COOH}$  leached wheat straw (Originally in colour)

Table 3.6: Mass losses from straw ashes pretreated by different methods showing the rate of mass loss in various temperature ranges and identification of the inorganic species associated with the mass loss

Temperature (°C)	Initial	scCO <sub>2</sub>	EtOH	H <sub>2</sub> O	CH <sub>3</sub> COOH	Identification
350 - 500	*	*	*	*	*	Residual organics
600 - 700	**	**	**	**	*	CaCO <sub>3</sub> decomposition
800 - 950	***	***	*	*	*	K <sub>2</sub> CO <sub>3</sub>
950 - 1100	***	***	*	*	*	KCl
1100 - 1250		*	*	*		K <sub>2</sub> SO <sub>4</sub> and CaSO <sub>4</sub>

\* 0 – 0.5 wt% /min

\*\* 0.5 – 1 wt% min

\*\*\* > 1 wt% min

All of the samples display a distinct mass loss between 600 – 700 °C, although the percentage lost is lower for the  $\text{CH}_3\text{COOH}$  treated sample. This can be attributed to the decomposition of  $\text{CaCO}_3$ . Calcite was observed in the XRD spectra of all of the samples, but at a lower intensity for the acid washed straw ash (Figure 3.14). Literature values indicate that decomposition of  $\text{CaCO}_3$  occurs at 898 °C.<sup>73</sup> However, STA analysis of the

decomposition of pure calcite shows the onset at 600 °C with the maximum release around 800 °C,<sup>64</sup> whilst Novokavic *et al* found that mixtures of  $K_2CO_3$ - $CaCO_3$ - $Ca_3(PO_3)_2$  and  $KCl$ - $CaCO_3$ - $Ca_3(PO_3)_2$  released  $CO_2$  from calcite between 600 – 730 °C.<sup>74</sup> The melting point of  $KCl$  is 772 °C, however, a peak in the DSC signal is not observed at this temperature in any of the ashes known to contain a large proportion of  $KCl$  based on XRD analysis. However,  $KCl$  is known to form eutectic mixtures with melting points of 690 °C with a minor amount of  $K_2SO_4$ ,<sup>75</sup> with  $CaSO_4$  at 688 °C,<sup>64</sup> or with 38%  $K_2CO_3$  at 631 °C. The analysis of salt extracts from the fly ashes of municipal solid waste displayed several melting peaks between 540 – 650 °C attributed to the presence of mixed alkali and alkali-calcium chloride and sulfates.<sup>76</sup> The sharper endothermic peak for the initial,  $scCO_2$ , and  $H_2O$  samples in this region may therefore be due to the co-current melting of mixed alkali salts along with the broader DSC signal from  $CaCO_3$  decomposition.

The large mass losses occurring in the initial and  $scCO_2$  ash between 800 – 950 °C and 950 – 1100 °C are not present to the same extent in the other samples. The former is suggested to be due to  $K_2CO_3$ , although this species could not be identified within the wheat straw ashes by XRD.<sup>64</sup>  $K_2CO_3$  has been found to decompose between 800 – 900 °C in the presence of  $SiO_2$ , with an ongoing mass loss above those temperatures, due to the formation of potassium silicates.<sup>64, 74</sup> Within mixtures of  $K_2CO_3$ - $CaCO_3$ - $Ca(PO_3)_2$  the decomposition or loss of  $CO_2$  from  $K_2CO_3$  appeared to occur between 800 – 900 °C with evaporation of potassium species at higher temperatures depending on the concentration of P.<sup>74</sup> These differ from the pure carbonate which decomposes to  $K_2O$  and  $CO_2$  between 1150 - 1400 °C.<sup>64</sup> The mass loss between 950 – 1100 °C and endothermic peak at 1025 – 1050 °C are predicted to be associated with the volatilisation of  $KCl$ . The reaction of  $KCl$  with  $SiO_2$  may be facilitated at lower temperatures by the presence of water vapour,<sup>77</sup> however the measurements shown above were undertaken in a nitrogen atmosphere. The decomposition profiles in this region highlight that the materials are not mixtures of just one of two pure components, with several mass loss and endothermic peaks occurring in quick succession. These are greatly reduced in the EtOH and  $H_2O$  samples indicating that they are mainly due to water soluble species and are probably mixtures of alkali chlorides, carbonates and sulfates.<sup>76</sup> The smaller mass loss between 1100 – 1250 °C is suggested to be due to the release of  $SO_3$  from the decomposition of  $K_2SO_4$  or  $CaSO_4$ .

The onset of decomposition of these species was found to decrease in the presence of KCl.<sup>64</sup>

Unfortunately, the complexity of the TG and DSC profiles makes it difficult to discern the onset of melting in the samples. Visual observation of the samples following heating to 1300 °C showed a brown glassy deposit from the initial and scCO<sub>2</sub> ashes, a clear glassy deposit from the EtOH and H<sub>2</sub>O samples and a pale brown powder from the CH<sub>3</sub>COOH sample. Arvelakis *et al* observed a dark glassy material during the heating of pure K<sub>2</sub>CO<sub>3</sub> and SiO<sub>2</sub>,<sup>64</sup> with Jenkins *et al* observing that unleached rice hull ashes contained dark inclusions whilst leached ashes were white.<sup>1</sup> This suggests that the dark colour of the initial and scCO<sub>2</sub> ashes may be due to potassium carbonates being captured in the melt.

### **3.5.4.2 Visual observation**

To further study the fusion of the different ashes following the pretreatment of the wheat straw, the same ashes that were used for the STA study were compressed into pellets and heated at 5 °C min<sup>-1</sup> to 1000 °C in a furnace. This is similar to the standard ash fusion test in which cubes of ash are heated and the temperatures corresponding to the rounding of the corners, the initial deformation temperature, the temperature of formation of a hemisphere and the flowing of the ash (fluid temperature) are noted.<sup>78</sup> Photographs of the pellets were taken at 25 °C intervals between 500 – 1000 °C (Figure 3.24). No changes were observed in the ashes below 700 °C. Unfortunately the furnace that was used could not be heated beyond 1000 °C and therefore the fluid temperature for the samples are not observed. The method used can only give a general indication of changes occurring within the ashes, however, clear differences are observed between the ashes formed from straw pretreated using different methods.

The CH<sub>3</sub>COOH sample was unchanged at all temperatures, whilst all of the other samples display some degree of melting or deformation at 1000 °C. This supports the previous evidence for this sample with little mass loss and no obvious melting points observed during thermal analysis (Figure 3.23). It also supports the elemental analysis which indicated a low slagging risk due to the low alkalinity and high silica purity. SiO<sub>2</sub>-CaO phase diagrams indicate that with the ratio of these species that are found in the CH<sub>3</sub>COOH ash, melting will not begin until the sample is above 1400 °C.<sup>79</sup> For both the

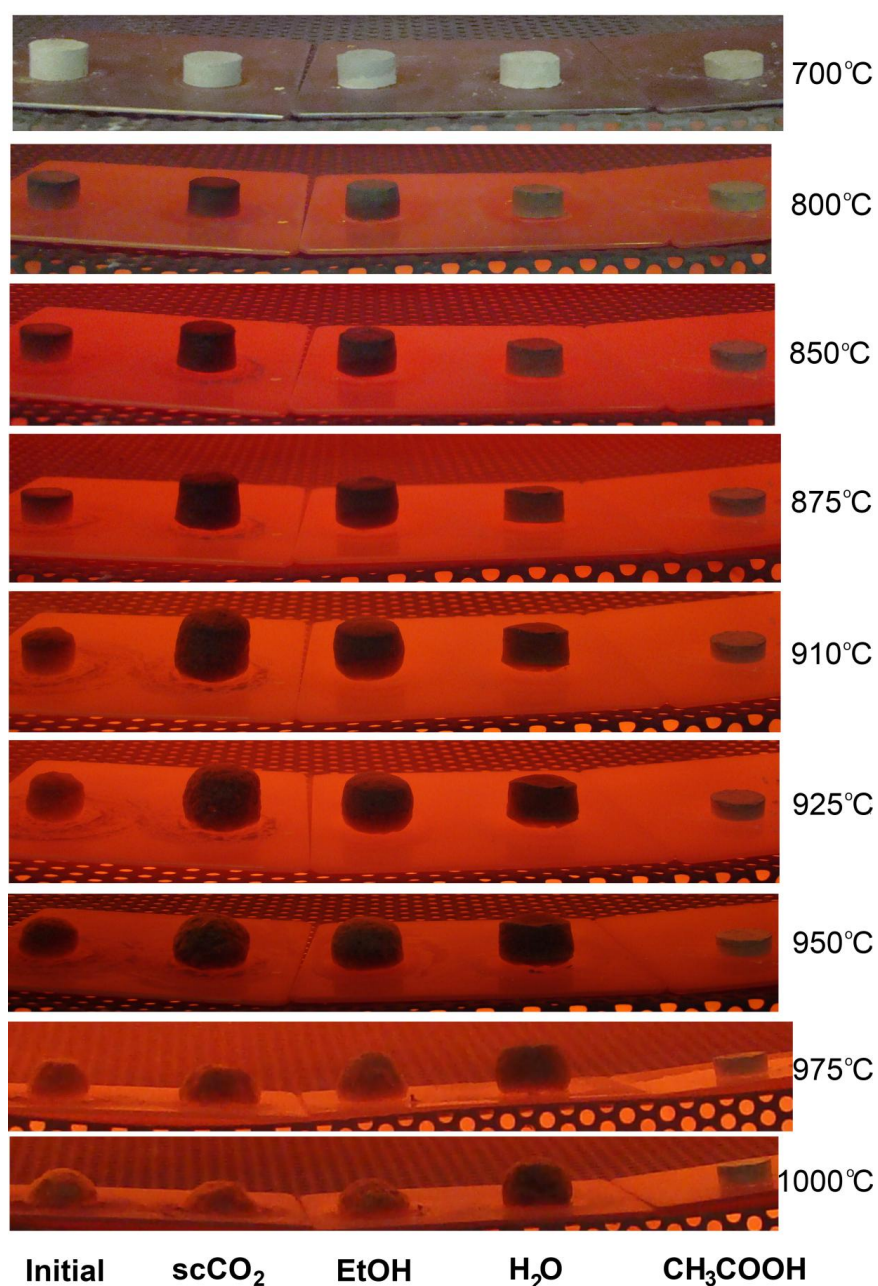


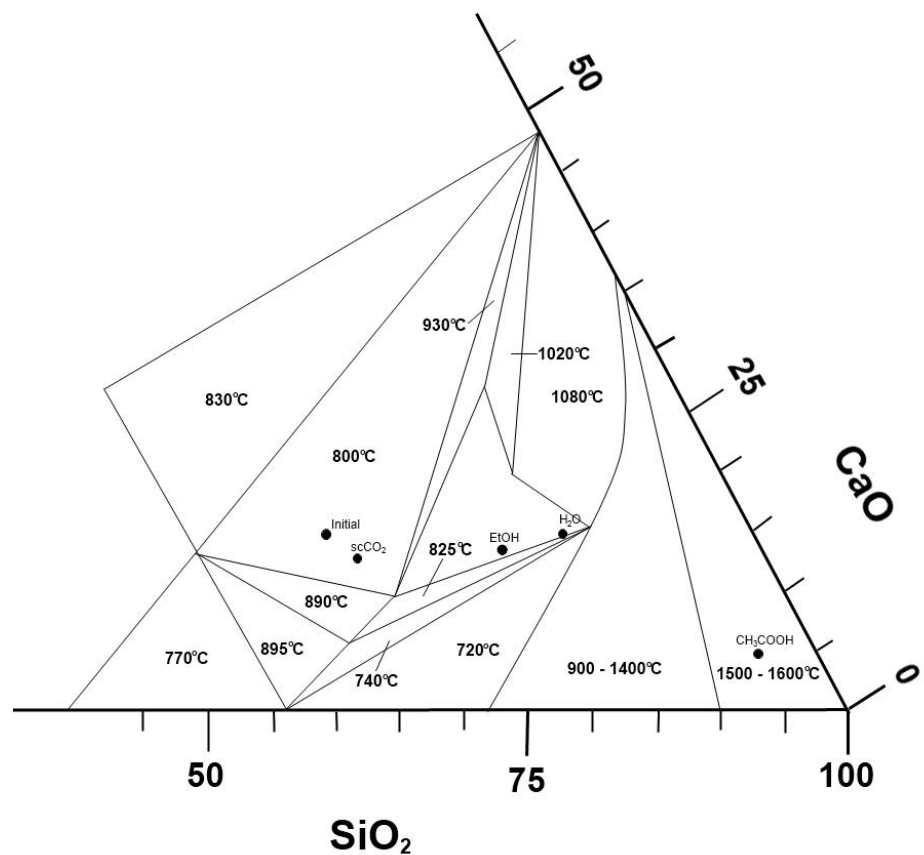
Figure 3.24: Changes in the shape of pellets of ash formed from pretreated Cl07 wheat straw previously combusted to 550 °C and heated to 1000 °C at 5 °C min<sup>-1</sup> (Originally in colour)

Table 3.7: Normalised content (wt%) of SiO<sub>2</sub>, K<sub>2</sub>O and CaO in ashes of pretreated straw

	Initial	$\text{scCO}_2$	EtOH	$\text{H}_2\text{O}$	$\text{CH}_3\text{COOH}$
SiO <sub>2</sub>	52	54	65	70	93
K <sub>2</sub> O	33	34	21	16	0.7
CaO	15	13	14	14	6

initial and scCO<sub>2</sub> samples initial deformation and rounding of the pellet occurs between 700 – 800 °C. As the temperature increases the pellet made from the initial straw decreases both in height and width whilst the scCO<sub>2</sub> pellet expands in size. This coincides with the temperature of release of CO<sub>2</sub> from CaCO<sub>3</sub>, suggesting that release of the gas can either cause collapse or expansion of the structure, and the initial melting of mixed alkali salts as observed by STA. Formation of a hemisphere shape occurs between 910 °C – 925 °C with the fluid temperature reached at 1000 °C. The EtOH sample behaves similarly to the scCO<sub>2</sub> pellet with the initial deformation occurring at a slightly higher temperature, however, melting occurs at 1000 °C. Deformation in the H<sub>2</sub>O sample is delayed until around 910 °C and the fluid temperature is not reached at 1000 °C.

The normalised content of SiO<sub>2</sub>, K<sub>2</sub>O and CaO for each of the ashes based on the XRF analyses (Table 3.3) are shown above in Table 3.7. The continued low melting points of the EtOH and H<sub>2</sub>O ashes despite the removal of potassium and increased relative ratio of SiO<sub>2</sub> can be explained by the phase diagram of the interrelation of these three species



**Figure 3.25: K<sub>2</sub>O-SiO<sub>2</sub>-CaO phase diagram displaying some of the solidus temperatures and the position of the pretreated wheat straw samples (Based on Ref 80)**

(Figure 3.25). The  $\text{SiO}_2\text{-K}_2\text{O}$  system contains three eutectic points, with 56.6%  $\text{SiO}_2$  at 781 °C, with 77.3%  $\text{SiO}_2$  at 743 °C and with 81%  $\text{SiO}_2$  at 770 °C.<sup>58</sup> These are comparable to the initial and scCO<sub>2</sub> samples, EtOH sample and H<sub>2</sub>O sample respectively. The presence of 10 – 15% CaO increases the melting points to between 800 – 850 °C. Therefore, to substantially increase the fusion point of the ashes the  $\text{SiO}_2$  content must be increased beyond 70% of the combined content of  $\text{K}_2\text{O}$ ,  $\text{SiO}_2$  and CaO. This was not achieved using EtOH or H<sub>2</sub>O within this study but was achieved by acid washing. However, the removal of some of the troublesome elements may still have a beneficial impact on the combustion process by reducing the presence of volatile species and corrosion of the boiler. Visual observation of the steel plates used for the fusion test showed much less corrosion by the EtOH and H<sub>2</sub>O samples compared to the Initial and scCO<sub>2</sub> samples.

### 3.5.5 Aqueous extraction of ash

The various pretreated wheat straws were combusted and extracted at the optimised conditions developed as described in Chapter 2; combusted at 500 °C 2h and extracted in water under reflux for 24 h. The results for the extraction of the major species are shown in Figure 3.26.

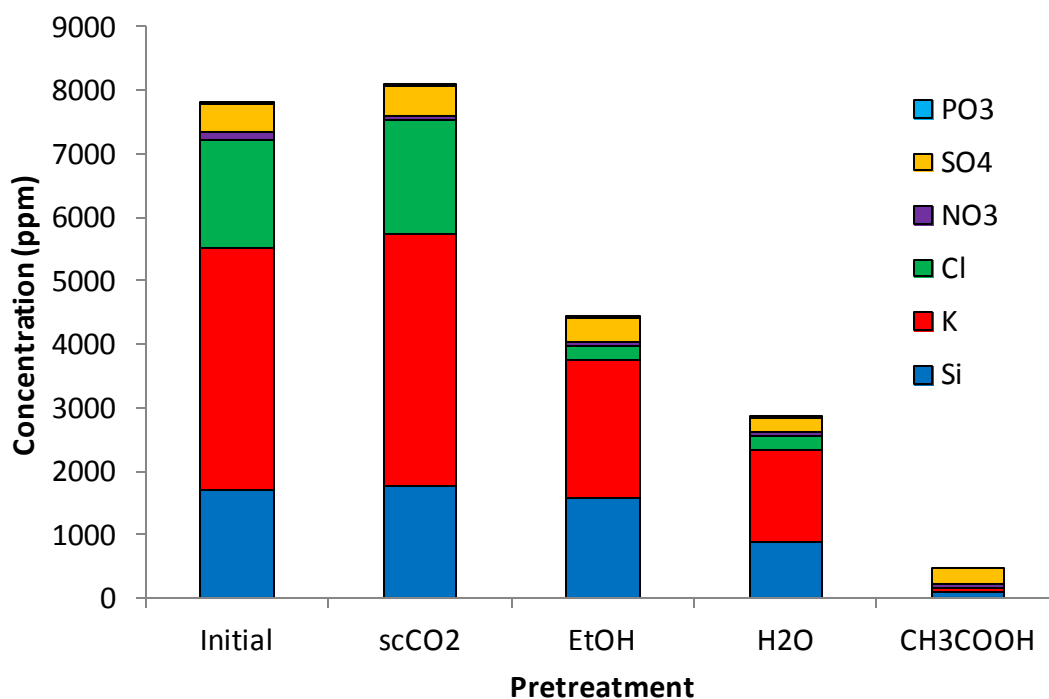


**Figure 3.26: Cumulative concentration of inorganic species in the aqueous extracts of pretreated Cl07 straw ash (Originally in colour)**

The initial and scCO<sub>2</sub> extracted straw ash demonstrate similar levels of extraction of all species, consistent with the mineralogical and thermochemical evidence that scCO<sub>2</sub> extraction does not affect the inorganic content of the straw. The ethanol extracted straw exhibits similar levels of silica (1580 ppm) extraction and lower levels of potassium (2170 ppm) and chloride (205 ppm) extraction. The water leached straw displays reduced extraction of all species, whilst only minor levels of all species are removed from the acetic acid treated straw ash. The nitrate extraction levels are similar for all of the ashes ranging from between 56 – 133 ppm, supporting the CHN analysis of the straw which indicated that nitrogen levels were unaffected by the pretreatment method (Table 3.3). The sulfate extraction decreases in the same order as the demineralisation trend, with the concentrations for the H<sub>2</sub>O and CH<sub>3</sub>COOH ashes (210 – 250 ppm) half that of the initial straw ash. The lowering of the sulfur dissolution is not surprising as leachate analysis of the H<sub>2</sub>O and CH<sub>3</sub>COOH extracts indicated that 40-50% of the sulfur present in the initial straw was removed (Figure 3.13). However, this also indicates that more sulfur becomes available for dissolution following combustion. The additional sulfur dissolved from the ash could come from organic sulfur. During char burnout, Knudesen *et al*, observed that 20 – 30% of the organic sulfur was captured as inorganic sulfur where there was an excess of potassium or calcium.<sup>33</sup> Based on XRF analysis of the initial wheat straw 68 – 70% of the sulfur content was extracted from the initial and scCO<sub>2</sub> straw ash following combustion indicating that around 20% of the initial organic-bound sulfur was captured in the ash during combustion.

The reduction in K and Cl concentrations for the EtOH, H<sub>2</sub>O and CH<sub>3</sub>COOH treated straw ash solutions further confirms the removal of KCl and other soluble potassium species from these samples. The total potassium removal remains consistently at around 70% of the predicted level in the different samples, but decreases in absolute terms with the potassium content of the pretreated samples. This suggests that a consistent proportion is either released to the gas phase or captured as silicate in all of the samples. There is, however, a varying impact on the silica extraction. The water leached sample displays much lower levels of silica extraction than the ethanol extracted sample. During ash extraction the pH of the H<sub>2</sub>O extract falls to 10.78, at which pH the solubility of silica declines dramatically, due to a reduction in the number of anionic species. This implies the removal during water leaching of alkaline potassium species, such as potassium

carbonate, that are not removed by ethanol extraction. The pH of the  $\text{CH}_3\text{COOH}$  ash extract was 9.2, explaining the low solubility of  $\text{SiO}_2$  from this sample, indicating the almost complete removal of alkaline compounds during acid leaching. The  $\text{SiO}_2$  concentration of 197 ppm is similar to that found during silica equilibrium experiments at a pH of 9.5 of 180 ppm.<sup>47</sup>

To test the maximum extractability of silica, each sample was extracted under reflux using a KOH solution, the concentration of which was determined as described in Chapter 2 section 2.7 for several varieties of wheat straw (Figure 3.27). Once again this demonstrates that similar silica extraction levels of between 60–70% can be achieved using a alkaline solution with a concentration calculated based on knowledge of the Si, K, Cl and S content of the ashes. Furthermore, the acetic acid treated straw does not demonstrate a significantly higher silica solubility despite its low potassium and calcium content and the more pronounced presence of amorphous silica identified in the XRD spectra.

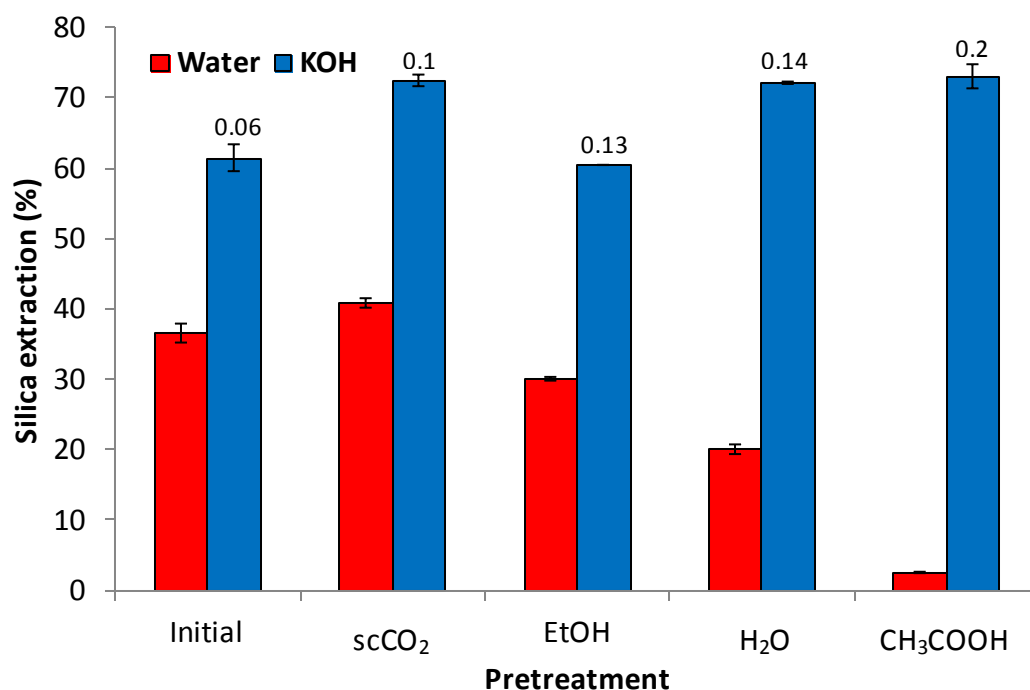


**Figure 3.27: Silica extraction from pretreated Cl07 straw ash using water and KOH solutions, showing the molar concentration of the KOH solutions used (Originally in colour)**

### **3.6 Conclusions and further work**

Wax extraction by Soxhlet and scCO<sub>2</sub>, water washing and acid washing were successfully applied as pretreatment methods to study the impact on the thermochemical, mineralogical and ash extraction analysis of one variety of wheat straw, Claire 07. As observed by previous researchers, a greater yield of secondary metabolites was extracted using ethanol rather than hexane as a solvent. The scCO<sub>2</sub> extraction conditions of wheat straw were extended beyond the previously studied temperature range to 32 – 100 °C. The extraction of lipids under these conditions did not follow the normal, and previously observed pattern, of increasing yield with increasing carbon dioxide density. Rather the highest yield was obtained at the highest temperature and pressure; 100 °C, 300 bar. The increasing volatility of the extracts under these conditions was proposed to be more important than the decrease in CO<sub>2</sub> density. DSC profiles of the high temperature scCO<sub>2</sub> extracts contained a higher melting point component (64 °C), supporting this hypothesis.

The effect of time and temperature were negligible on the extraction of potassium by water and acid, with similar extraction yields for both solutions (80 - 90%). Anions, including Cl<sup>-</sup> (171%), SO<sub>4</sub><sup>2-</sup> (50%), NO<sub>3</sub><sup>-</sup> (0.58%) and PO<sub>4</sub><sup>3-</sup> (89%), displayed similar solubility's by both water and acid treatment, the latter gave marginally higher extraction levels in all cases.

Under the most extreme scCO<sub>2</sub> conditions tested, the inorganic composition, decomposition profile, burning profile and mineralogical speciation within the ash formed were unaffected. This confirms scCO<sub>2</sub> as a highly selective solvent for the extraction of non-polar lipids. However, the moisture content of the straw was lowered. This could be beneficial for combustion if the normally high moisture content biomass taken from the fields is first pretreated using scCO<sub>2</sub> to recover valuable wax extracts. However, previous research indicates that this could also affect the nature of the extract composition. Further research is necessary to understand the interaction between these effects.

The ethanol extracted straw showed a reduction in K and Cl content similar to that achieved by water washing. This is believed to be the first reported observation of this effect. XRD analysis demonstrated that this was due to the removal of KCl either with the inherent moisture in the wheat straw or moisture content of the ethanol solvent.

Potassium could be recovered from the wax extract using water. The slagging index of the ethanol treated straw was reduced, although not to a level associated with limited slagging impact. This high removal of chlorine is predicted to improve the retention of potassium in the combustion bed. This was supported by STA analysis of the ashes which showed a low total mass loss to 1300 °C, the bulk of which is due to moisture loss and  $\text{CaCO}_3$  decomposition. However, visual fusion analysis suggested that the melting point of the ash was not significantly increased. The removal of salts did not affect the extraction of silica from the EtOH ashes, therefore implying that alkaline species were not removed during Soxhlet extraction. This suggests a highly beneficial interaction between ethanol extraction and combustion, enabling the recovery of valuable lipids and potassium salts as a fertiliser to return to the land whilst reducing the damaging impacts of volatile salts during combustion. In addition, a higher quality potassium silicate solution can be formed by reducing contaminating species. As it is more volatile, less energy would be required to remove the ethanol from the straw in comparison to water washing. A proposed scheme for combining these benefits is shown in Figure 3.28. Further research into the effect of ethanol extraction on the inorganic composition of different straws under varying extraction conditions is vital, along with a study of the feasibility of incorporating the different processes shown in Figure 3.28.

Acid washing reduces the straw to a low slagging risk by removing all of the potassium and chlorine species and reducing the calcium content by removing  $\text{CaCO}_3$ . The main component remaining is silica. The removal of the alkaline species results in the presence of amorphous silica (in a modified cristobalite form) at 500 °C. STA analysis indicates that this is a highly hydrophobic material suggesting a high content of cross-linked siloxane bridges similar to the silica formed from combustion of rice hull ashes. Both acid and water leaching reduce the pH of the ash extract solutions resulting in reduced silica extraction by the inherent alkalinity of the ashes.

scCO<sub>2</sub> treatment has the smallest impact on the straw for thermochemical purposes, whilst ethanol extraction provides the optimal removal of salts and valuable lipids without reducing the extraction of silica utilising the inherent alkalinity of the ashes.

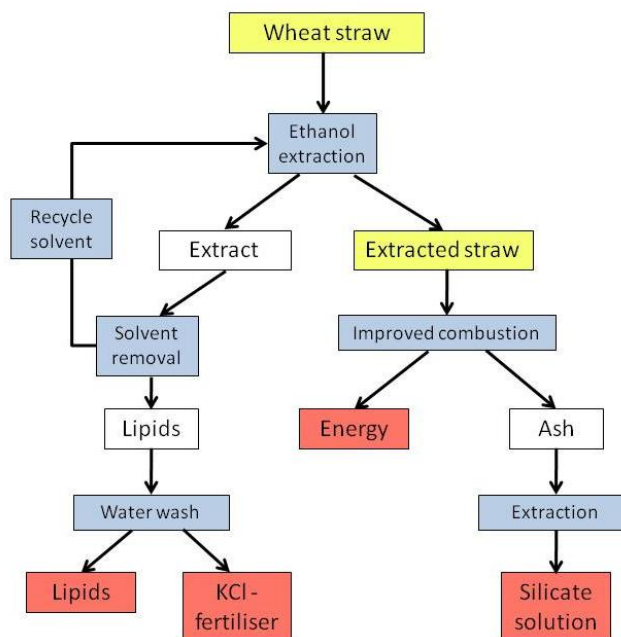


**Figure 3.28: Proposed scheme for the pretreatment of wheat straw by ethanol extraction prior to combustion**

### 3.7 References for Chapter 3

1. B. M. Jenkins, R. R. Bakker and J. B. Wei, *Biomass Bioenerg.*, 1996, **10**, 177-200.
2. S. Arvelakis and E. G. Koukios, *Biomass Bioenerg.*, 2002, **22**, 331-348.
3. S. Arvelakis, P. Vourliotis, E. Kakaras and E. G. Koukios, *Biomass Bioenerg.*, 2001, **20**, 459-470.
4. R. R. Bakker and B. M. Jenkins, *Biomass Bioenerg.*, 2003, **25**, 597-614.
5. D. C. Dayton, B. M. Jenkins, S. Q. Turn, R. R. Bakker, R. B. Williams, D. Belle-Oudry and L. M. Hill, *Energ. Fuel.*, 1999, **13**, 860-870.
6. A. Demirbas, *Energ. Source.*, 2003, **25**, 679-687.
7. C. Di Blasi and C. Branca, *Ind. Eng. Chem. Res.*, 2000, **39**, 2169-2174.
8. B. M. Jenkins, J. D. Mannapperuma and R. R. Bakker, *Fuel Process. Technol.*, 2003, **81**, 223-246.
9. N. O. Knudsen, P. A. Jensen, B. Sander and K. Dam-Johansen, in *Biomass for Energy and Industry*, eds. H. Kopetz, T. Weber, W. Palz, P. Chartier and G. L. Ferrero, Centrales Agrar Rohstoff Mkt & Entwicklung Netzwerk, Rimpf, Editon edn., 1998, pp. 224-228.
10. D. N. Thompson, P. G. Shaw and J. A. Lacey, *Appl. Biochem. Biotechnol.*, 2003, **105**, 205-218.
11. F. Deswarte, University of York, 2006.
12. F. E. I. Deswarte, J. H. Clark, J. J. E. Hardy and P. M. Rose, *Green Chem.*, 2006, **8**, 39-42.
13. M. D. Luque de Castro and L. E. García-Ayuso, *Anal. Chim. Acta*, 1998, **369**, 1-10.
14. R. S. Oakes, A. A. Clifford and C. M. Rayner, *J. Chem. Soc. Perk. T. 1.*, 2001, 917-941.
15. F. Sahena, I. S. M. Zaidul, S. Jinap, A. A. Karim, K. A. Abbas, N. A. N. Norulaini and A. K. M. Omar, *J. Food Eng.*, 2009, **95**, 240-253.
16. Y. Athukorala and G. Mazza, *Ind. Crop. Prod.*, 2010, **31**, 550-556.
17. C. Shen, W. Lin, S. H. Wu, X. B. Tong and W. L. Song, *Energ. Fuel.*, 2009, **23**, 5322-5330.
18. A. Gustavo González, *Anal. Chim. Acta*, 1998, **360**, 227-241.

19. Y. Athukorala, G. Mazza and B. D. Oomah, *Eur. J. Lipid Sci. Technol.*, 2009, **111**, 705-714.
20. A. J. Hunt, University of York, 2006.
21. F. P. Lucien and N. R. Foster, *J. Supercrit. Fluid.*, 2000, **17**, 111-134.
22. A. de Lucas, *Supercrit. Fluids*, 1992, **22**, 221-228.
23. B. Ritter, J. Schulte, E. Schulte and H.-P. Thier, *Eur. Food Res. Technol.*, 2001, **212**, 603-607.
24. J. H. van der Maas, *Basic Infrared Spectroscopy*, Heyden & Son Ltd, Bath, 1969.
25. H. Jiang, Y. Zhang and X. F. Wang, *Ind. Crop. Prod.*, 2009, **30**, 304-310.
26. R. C. Sun and J. Tomkinson, *J. Wood Sci.*, 2002, **48**, 222-226.
27. M. Kacuráková and M. Mathlouthi, *Carbohydr. Res.*, 1996, **284**, 145-157.
28. C. Pappas, P. A. Tarantilis, I. Daliani, T. Mavromoustakos and M. Polissiou, *Ultrason. Sonochem.*, 2002, **9**, 19-23.
29. R. C. Sun and X. F. Sun, *Ind. Crop. Prod.*, 2001, **14**, 51-64.
30. P. A. Jensen, B. Sander and K. Dam-Johansen, *Biomass Bioenerg.*, 2001, **20**, 447-457.
31. G. R. Ponder and G. N. Richards, *Carbohydr. Res.*, 1993, **244**, 27-47.
32. F. B. Salisbury and C. W. Ross, *Plant Physiology*, Fourth edn., Wadsworth, California, 1992.
33. J. N. Knudsen, P. A. Jensen, W. G. Lin, F. J. Frandsen and K. Dam-Johansen, *Energ. Fuel.*, 2004, **18**, 810-819.
34. R. Fahmi, A. V. Bridgwater, L. I. Darvell, J. M. Jones, N. Yates, S. Thain and I. S. Donnison, *Fuel*, 2007, **86**, 1560-1569.
35. Y. Iwai, M. Uno, H. Nagano and Y. Arai, *J. Supercrit. Fluid.*, 2004, **28**, 193-200.
36. Y. Iwai, Y. Koujina, Y. Arai, I. Watanabe, I. Mochida and K. Sakanishi, *J. Supercrit. Fluid.*, 2002, **23**, 251-255.
37. N. T. Dunford and F. Temelli, *J. Food Sci.*, 1997, **62**, 155-159.
38. C. Pereira and M. Meireles, *Food Bioprocess Tech.*, 2010, **3**, 340-372.
39. Y. Iwai, H. Nagano, G. S. Lee, M. Uno and Y. Arai, *J. Supercrit. Fluid.*, 2006, **38**, 312-318.
40. G. Leeke, F. Gaspar and R. Santos, *Ind. Eng. Chem. Res.*, 2002, **41**, 2033-2039.
41. V.-A. Glezakou, R. Rousseau, L. X. Dang and B. P. McGrail, *Phys. Chem. Chem. Phys.*, 2010, **12**, 8759-8771.
42. K. Raveendran, A. Ganesh and K. C. Khilar, *Fuel*, 1995, **74**, 1812-1822.
43. D. Vamvuka, S. Troulinos and E. Kastanaki, *Fuel*, 2006, **85**, 1763-1771.
44. D. J. Nowakowski, J. M. Jones, R. M. D. Brydson and A. B. Ross, *Fuel*, 2007, **86**, 2389-2402.
45. C. Di Blasi, C. Branca and G. D'Errico, *Thermochim. Acta*, 2000, **364**, 133-142.
46. A. Zolin, A. Jensen, P. A. Jensen, F. Frandsen and K. Dam-Johansen, *Energ. Fuel.*, 2001, **15**, 1110-1122.
47. R. K. Iler, *The Chemistry of Silica*, Wiley & Sons, New York, 1979.
48. C. Erkey, *J. Supercrit. Fluid.*, 2000, **17**, 259-287.
49. S. Mochizuki, N. Wada, R. L. Smith Jr and H. Inomata, *Analyst*, 1999, **124**, 1507-1511.
50. C. Y. Yang, X. S. Lu, W. G. Lin, X. M. Yang and J. Z. Yao, *Chem. Res. Chin. Univ.*, 2006, **22**, 524-532.
51. D. L. Klass, *Biomass for Renewable Energy, Fuels and Chemicals*, Academic Press, California, 1998.
52. M. Li, D. Constantinescu, L. Wang, A. Mohs and J. r. Gmehling, *Ind. Eng. Chem. Res.*, 2010, **49**, 4981-4988.
53. F. A. Rodrigues, *Cement Concrete Res.*, 2003, **33**, 1525-1529.
54. A. Proctor, *J. Am. Oil Chem. Soc.*, 1990, **67**, 576-584.

55. P. A. Jensen, F. J. Frandsen, K. Dam-Johansen and B. Sander, *Energ. Fuel.*, 2000, **14**, 1280-1285.
56. J. N. Knudsen, P. A. Jensen and K. Dam-Johansen, *Energ. Fuel.*, 2004, **18**, 1385-1399.
57. E. Yazhenskikh, K. Hack and M. Müller, *Calphad*, 2008, **32**, 506-513.
58. E. Yazhenskikh, K. Hack and M. Müller, *Calphad*, 2006, **30**, 270-276.
59. A. Jensen, K. Dam-Johansen, M. A. Wojtowicz and M. A. Serio, *Energ. Fuel.*, 1998, **12**, 929-938.
60. A. Barneto, J. Carmona, J. E. Alfonso and L. Alcaide, *Bioresour. Technol.*, 2009, **100**, 3963-3973.
61. A. T. W. M. Hendriks and G. Zeeman, *Bioresource Technol.*, 2009, **100**, 10-18.
62. S. Harper and J. Lynch, *Plant Soil*, 1982, **65**, 11-17.
63. L. A. Hansen, F. J. Fransen and K. Dam-Johansen, in *Impact of Mineral Impurities in Solid Fuel Combustion*, eds. R. Gupta, T. Wall and L. Baxter, Kluwer Academic / Plenum Publishers, New York, Editon edn., 1999, pp. 181-193.
64. S. Arvelakis, P. A. Jensen and M. Dam-Johansen, *Energ. Fuel.*, 2004, **18**, 1066-1076.
65. S. Arvelakis, H. Gehrman, M. Beckmann and E. G. Koukios, *J. Therm. Anal. Calorim.*, 2003, **72**, 1019-1030.
66. V. P. Della, I. Kuhn and D. Hotza, *Mater. Lett.*, 2002, **57**, 818-821.
67. M. Kim, S. H. Yoon, E. Choi and B. Gil, *LWT-Food Sci. Technol.*, 2008, **41**, 701-706.
68. T. H. Liou, *Mater. Sci. Eng. A-Struct. Mater. Prop. Microstruct. Process.*, 2004, **364**, 313-323.
69. D. Prasetyoko, Z. Ramli, S. Endud, H. Hamdan and B. Sulikowski, *Waste Manage.*, 2006, **26**, 1173-1179.
70. D. G. Nair, A. Fraaij, A. A. K. Klaassen and A. P. M. Kentgens, *Cement Concrete Res.*, 2008, **38**, 861-869.
71. P. J. Haines, *Thermal Methods of Analysis: Principles, applications and problems*, Blackie Academic and Professional, Glasgow, 1995.
72. T. D. Gonçalves, J. D. Rodrigues and M. M. Abreu, *J. Cult. Herit.*, 2006, **7**, 193-200.
73. R. C. Weast and M. J. Astle, *Handbook of Chemistry & Physics*, 63rd edn., CRC Press, Florida, 1982.
74. A. Novaković, S. C. van Lith, F. J. Frandsen, P. A. Jensen and L. B. Holgersen, *Energ. Fuel.*, 2009, **23**, 3423-3428.
75. M. Stenseng, A. Zolin, R. Cenni, F. Frandsen, A. Jensen and K. Dam-Johansen, *J. Therm. Anal. Calorim.*, 2001, **64**, 1325-1334.
76. S. Arvelakis and F. J. Frandsen, *Fuel*, 2005, **84**, 1725-1738.
77. E. Bjorkman and B. Stromberg, *Energ. Fuel.*, 1997, **11**, 1026-1032.
78. L. A. Hansen, F. J. Fransen, S. S. Henning, P. Rosenberg, K. Hjuler and K. Dam-Johansen, in *Impact of Mineral Impurities in Solid Fuel Combustion*, eds. R. Gupta, T. Wall and L. Baxter, Kluwer Academic / Plenum Publishers, New York, Editon edn., 1999, pp. 341-356.
79. Facility for the Analysis of Chemical Thermodynamics (FACT), *PhaseDiagram-Web*, <http://www.crct.polymtl.ca/fact/>, Accessed 27/07/11.
80. M. Ohman and A. Nordin, *Energ. Fuel.*, 2000, **14**, 169-178.



## Chapter 4:

# Lab-scale pyrolysis of wheat straw and extraction of chars

Some of the work described in this chapter is published in: V. L. Budarin, P. S. Shuttleworth, J. R. Dodson, A. J. Hunt, B. Lanigan, R. Marriott, K. J. Milkowski, A. J. Wilson, S. W. Breeden, J. Fan, E. H. K. Sin and J. H. Clark, *Energ. Environ. Sci.*, 2010, **4**, 471-479.



## **4.1 Chapter 4 – Summary**

The effect of temperature on the formation of wheat straw chars under pyrolysis conditions using microwave and conventional heating is studied. The aqueous leaching of inorganic species, particularly potassium and silica, are analysed and compared to the extraction of combustion ashes. The influence of leaching on the chemical composition, ash content, calorific value and combustion of the chars are examined with some suggestions about the underlying mechanisms put forward.

## **4.2 Pyrolysis**

The results described in Chapter 2 indicated that silica extraction was largely influenced by the temperature of combustion, with the maximum extraction utilising the inherent alkalinity of the ashes achieved up to a temperature of 500 °C. This temperature is lower than is commonly used in combustion systems; however, it is similar to the temperature used in conventional pyrolysis.<sup>1</sup> Pyrolysis is an alternative thermochemical process to combustion and could be utilised for the production of fuels, energy and chemicals. Less work has been carried out to understand the influence of the pyrolysis process on the inorganic species within biomass than for combustion. Therefore, a study was undertaken to determine how the pyrolysis temperature, in particular, affects the extraction of inorganic species and the subsequent utilisation of the char.

Pyrolysis is the thermal decomposition of organic components in the absence of air. A range of products are formed including a liquid fraction, char and gas. Several different technologies have been developed using different temperatures or different heating rates to influence the product composition.<sup>1</sup> Slow pyrolysis, at low heating rates and temperatures of 300 – 500 °C over several days, has traditionally been utilised for the production of charcoal. Conversely, flash pyrolysis at temperatures of 450 – 650 °C with a solid residence time of just 0.1 – 2 s and high heating rates can produce up to 70 wt% of liquid product.<sup>1</sup> Pyrolysis is a promising method for the conversion of biomass materials for the sustainable replacement of fossil fuels. The liquid component, or bio-oil, generally consists of an aqueous phase containing O-functionalised compounds of low molecular weight and a non-aqueous phase of organic molecules of higher molecular weight.<sup>2</sup> These are potential substitutes for petroleum-derived chemicals. However, there are currently

some limitations of the use of the oil due to its poor thermal stability and corrosiveness.<sup>3</sup> The maximum theoretical yield of solid carbonaceous materials from biomass using pyrolysis is 65 – 75% by dry weight.<sup>1</sup> The carbon rich solid has a higher heating value and increased density compared to the starting material, thereby reducing transportation costs and making it more suitable as a coal replacement for combustion. The incorporation of the biochar into soil for carbon sequestration as a means to reduce global CO<sub>2</sub> levels and improve organic soil content is also of current interest.<sup>4</sup> The pyrolysis operating conditions can therefore be modified dependent on the desired product. The most effective and sustainable method for the reduction of greenhouse gas emissions is still under discussion.<sup>5</sup> In this study the production of the chars was of most interest.

The detailed mechanism of biomass pyrolysis is still a current research priority. However, based on the study of cellulose a general mechanism involving two competing pathways has been described (Figure 4.1).<sup>6, 7</sup> 'Active cellulose' is proposed to form at low temperatures (150 – 250 °C) from a reduction in the degree of polymerisation of cellulose by dehydration and cleavage of the glycosidic bonds.<sup>6, 8</sup> The formation of the liquid products via transglycosylation increases with increasing temperature up to a maximum production at 500 – 600 °C.<sup>7</sup> At higher temperatures increasing levels of gas yields are observed.<sup>9</sup>

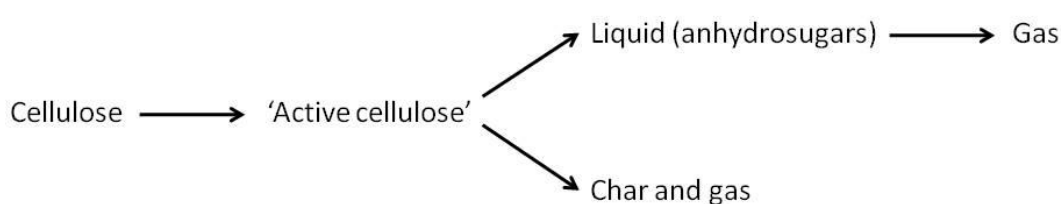


**Figure 4.1: Proposed general mechanism for cellulose pyrolysis**

The inorganic composition also impacts on the observed pyrolysis process, as mentioned in Chapter 2 and 3, with decreased char yields, increased liquid yields, increased onset temperatures (+ 20-30 °C), increased maximum devolatilisation rates and increased peak temperatures (+ 5-10 °C) observed following acid leaching of herbaceous and woody biomass and cell wall constituents.<sup>10, 11</sup> In particular, reduced yields of levoglucosan and higher yields of hydroxyacetaldehyde are found with increasing concentrations of alkali

metal salts.<sup>12</sup> The impacts of a variety of different metal salts have been studied including sodium, potassium, magnesium and calcium cations and hydroxide, sulfate, nitrate and carbonate anions on both pure cell wall constituents and biomass materials.<sup>11, 13-16</sup> The impacts appear to vary both dependent on the cation and the anion used. However, there does not appear to be a general understanding of the influence of the inorganic species on the underlying decomposition process with several different mechanisms proposed.

Understanding the effects of the pyrolysis conditions on the inorganic species is relevant both for the subsequent utilisation of the chars either for carbon sequestration, due to the release of minerals to soils, or for char combustion. The concentration of alkali ash within the char following pyrolysis could cause significant challenges during combustion. Jensen *et al* have previously proposed the leaching of char as a mechanism to reduce the ash content and to use less water and energy compared to water washing of the initial biomass.<sup>17</sup> Washing of wheat straw pyrolysed at 500 °C reduced the Cl and K contents by 95 – 100% and 90 – 95% in the char respectively.<sup>18</sup> An increased extraction temperature and a smaller particle size increased the absolute and rate of extraction. Lower ash extraction was observed than by water washing of the initial straw.<sup>19</sup> Nevertheless, the influence of pyrolysis temperature and the impact on all inorganic species, particularly silica, have not been studied. Furthermore, the effect on combustion of the char was not examined.

### **4.3 Low temperature microwave pyrolysis**

Research at the Green Chemistry Centre of Excellence at the University of York has demonstrated that microwave-assisted degradation of wheat straw can occur at much lower temperatures than previously reported.<sup>20</sup> This technology can offer advantages in terms of energy efficiency, greater flexibility, portability and ease of installation.<sup>21</sup> Five major types of products are produced during the microwave pyrolysis of lignocellulosic biomass:

1. A high quality char with properties superior to those achieved by most conventional methods and with an enhanced energy value, feedability and grindability, making it suitable for use as a coal replacement.
2. Bio-oil suitable for upgrading to liquid fuel.

3. An aqueous solution of organic acids and aldehydes.
4. An aqueous solution of sugars.
5. A gas fraction – containing combustable organic compounds, which could be used for energy production.

For untreated wheat straw, gas was the lowest yielding fraction (c.a. 14 wt%), with bio-oil and char yields of 20 and 30 wt% respectively, whilst the aqueous fraction gave the highest yield (c.a. 35 wt%).<sup>22</sup> Char is therefore one of the major products of microwave pyrolysis. A study on the extraction of microwave chars and the influence of the demineralisation on the char combustion properties, final ash structure and the nature of extracts formed had not previously been carried out. Aqueous leaching was performed on chars directly following the microwave pyrolysis of Claire 2007 wheat straw at elevated temperatures, using microwave heating. The microwave leaching of straw and the analysis of the decomposition profile of the residual chars was carried out in collaboration with Dr Vitaly Budarin.

Significant changes are observed in the total ash content and combustion profiles of the microwave pyrolysis chars before and after leaching (Figure 4.2). Demineralisation by aqueous extraction reduces the total ash residue by a third. In addition, both char oxidation peaks (> 350 °C) are shifted to higher temperatures in the char washed sample, which is generally associated with the removal of alkali metals in studies of washed straw.<sup>23</sup> Similar changes were observed for demineralised wheat straw in this study (section 3.5.3). The presence of two char oxidation peaks could imply some char heterogeneity and the changes in the relative contributions of the two char oxidation peaks to the combustion profiles might indicate different decomposition pathways dependent on the inorganic content of the char. The peak at 321 °C corresponds to the decomposition of the initial lignocellulosic material, signifying that there is incomplete carbonisation.

Analysis of the changing elemental nature of the chars confirms the predominant removal of potassium, along with chlorine and minor amounts of other elements, following aqueous extraction (Figure 4.3). The inorganic content of the chars was compared to the original straw by normalizing the element percentage relative to the ash content. Minor

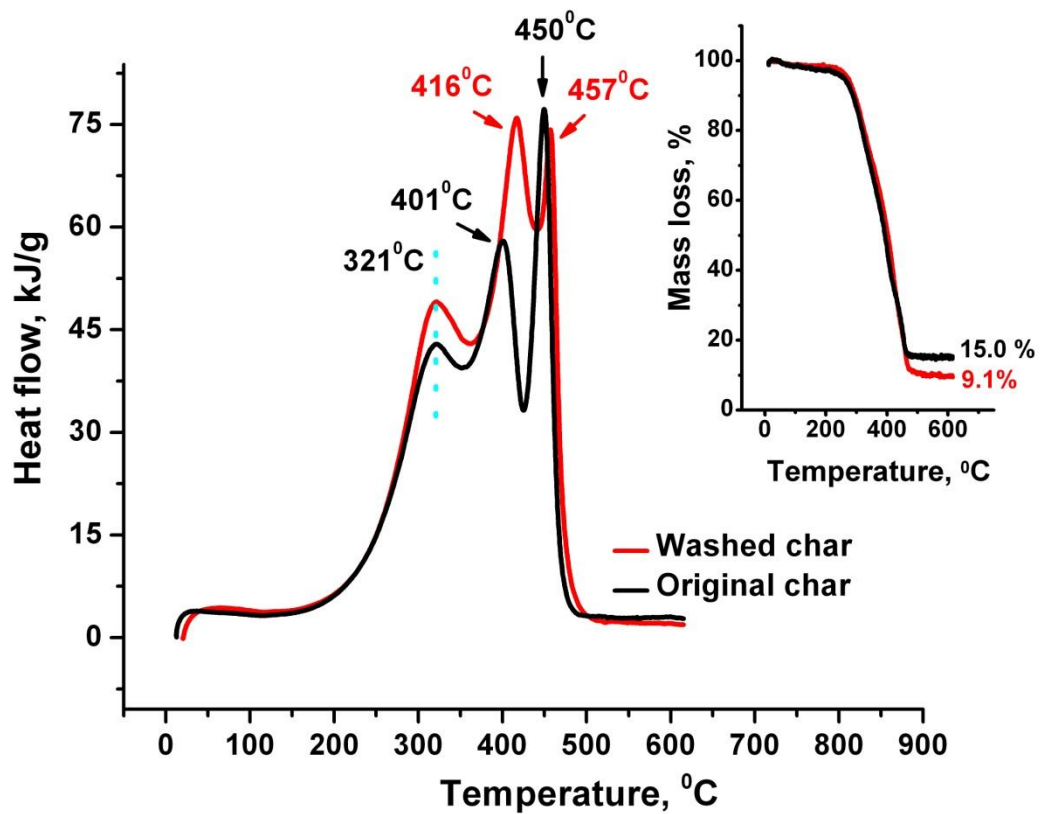


Figure 4.2: Combustion profiles of Cl07 char before and after washing showing the changes in heat flow and the mass loss profile (inset) This diagram was produced by Dr Vitaly Budarin (Originally in colour)

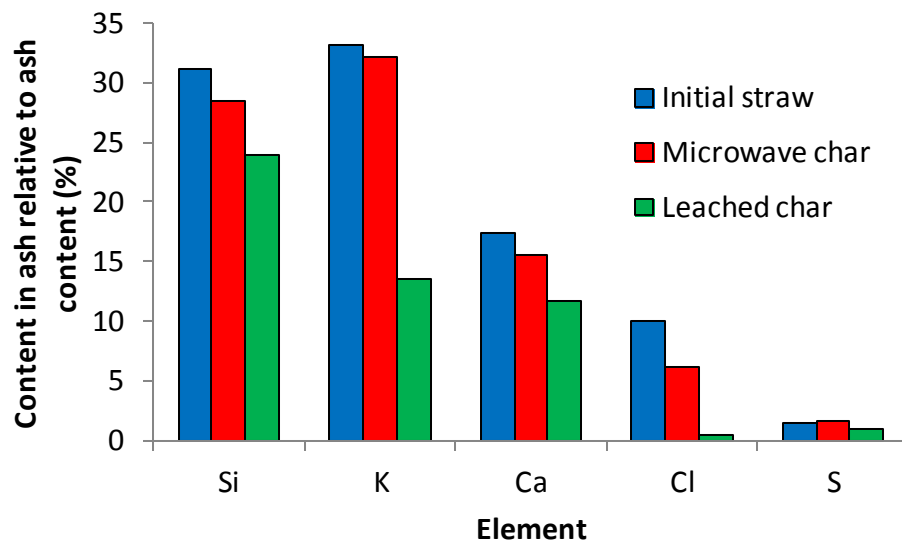
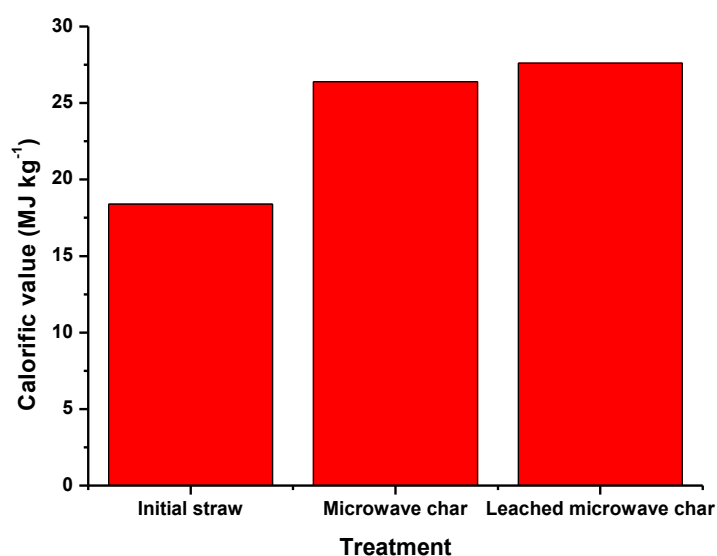


Figure 4.3: Elemental content of Cl07 straw and microwave chars before and after leaching. Based on XRF analysis of solid material (Originally in colour)

reductions in the total ash content following pyrolysis correspond mainly to a reduction in the chlorine content, either as HCl or in association with the organic phase.<sup>24</sup> Following the char wash, 60% of the potassium, 96% of the chlorine and 29% of the sulfur is extracted, whilst only minor amounts of calcium and silicon are removed, which was confirmed by ICP and AAS analysis. This indicates that the major elements indicative of problems during biomass combustion, potassium and chlorine, have been significantly reduced by microwave char demineralisation. Similar levels of potassium and chlorine removal were observed for wheat straw chars pyrolysed at 500 °C by Jensen *et al* and by water washing of Cl07 wheat straw based on XRF analysis of the pretreated straw (section 3.5.3).<sup>18</sup> The pH of the char extract was only 7.4, which explains the low levels of silica extracted. This is believed to be due to the incomplete carbonisation of the sample as exhibited by the decomposition profile. Attempts to carbonise the char further were unsuccessful. Similar pH levels have been observed for biochars produced from a variety of biomass, particularly at low temperatures (260 – 450 °C) by convective heating.<sup>4, 25</sup> Using pelletised straw may have improved the microwave pyrolysis process by preventing overheating. However, pelletised samples of the same wheat straw were unavailable.

Also of great importance is the effect of washing on the calorific value of the chars (Figure 4.4). Unsurprisingly, the chars show a much increased calorific value relative to the straws, whilst removal of inorganics also marginally improves the heating value by increasing the concentration of combustible organic material in the sample.



**Figure 4.4: Calorific values of straw and chars before and after washing (Originally in colour)**

## **4.4 Conventional pyrolysis**

### **4.4.1 Aqueous extraction**

The extraction of microwave pyrolysis chars yielded some interesting results, however, the extraction of silica was low due to the low pH of the solution formed. Therefore aqueous extractions of pyrolysis chars formed using convective heating at temperatures from 400 °C – 800 °C for 2 h were performed at room temperature under batch conditions to enable a direct comparison to the combustion residues previously studied (Chapter 2). To prevent oxidation occurring during conversion the quartz reaction vessel containing straw was filled with argon and the flow of nitrogen in the furnace started before the sample was added to the furnace. None of the chars formed showed any signs of oxidation. The chars were cooled under nitrogen before leaching at room temperature for 24 h. The extracts were analysed by AAS, IC and ICP to determine the concentrations of various inorganic species in the solutions (Table 4.1) and the pH of the solutions were examined. The ICP data showed the same trends as determined by AAS and IC.

**Table 4.1: Concentrations of inorganic species in aqueous extracts of pyrolysis chars formed at various temperatures**

		Pyrolysis temperature (°C)						
		400	450	500	600	650	700	800
	Initial pH	11.73	12.16	12.38	12.22	12.23	12.32	11.82
	Final pH	10.76	11.04	11.07	11.13	12.05	12.40	11.97
AAS (ppm)	K	3493	4085	3613	3520	3311	3526	3470
	Si	642	936	1330	1163	458	577	610
IC (ppm)	Cl	1535	1295	1500	1739	1475	1551	1183
	SO <sub>4</sub>	235	150	113	98	46	39	610
	NO <sub>3</sub>	134	126	109	117	35	109	122
	PO <sub>4</sub>	20.5	19.5	25.8	10.3	6.3	-	-
ICP (ppm)	Al	0.44	na	0.85	0.40	na	2.66	2.66
	Ba	7.76	na	5.89	6.31	na	6.32	6.32
	Bi	-	na	-	0.32	na	0.56	0.56
	Ca	16.7	na	20.0	10.6	na	11.1	11.1
	Cd	0.01	na	-	0.04	na	-	-
	Cr	-	na	-	-	na	-	-
	Cu	0.24	na	0.14	0.17	na	0.15	0.15
	Fe	0.09	na	0.56	0.34	na	0.01	0.01
	La	0.06	na	0.06	0.03	na	0.03	0.03
	Mg	6.17	na	6.18	4.78	na	2.02	2.02
	Mn	0.07	na	0.66	0.23	na	0.00	0.00
	Mo	-	na	-	-	na	-	-
	Na	332	na	263	393	na	325	325
	Pb	-	na	0.61	1.00	na	0.79	0.79
	Rb	1.14	na	1.29	1.45	na	1.28	1.28
	Sb	-	na	3.20	1.46	na	-	-
	Sc	0.00	na	0.00	0.00	na	0.00	0.00
	Se	-	na	4.27	-	na	-	-
	Sr	0.08	na	0.20	0.09	na	0.10	0.10
	Tl	-	na	-	1.54	na	-	-
V	-	na	-	0.01	na	0.01	0.01	
W	0.48	na	0.61	0.32	na	0.86	0.86	
Zn	0.07	na	0.16	0.11	na	0.15	0.15	
Total (ppm)		6425	6610	6998	7070	5331	6153	6348
Extraction (%)		44.11	45.30	47.57	48.25	36.53	42.37	39.38

na – not analysed

#### 4.4.1.1 Potassium and chloride

Neither the potassium nor chloride extraction levels were significantly affected by the pyrolysis temperature with consistent levels of potassium (average  $67 \pm 4.6\%$ ) and chloride (average  $80 \pm 9.1\%$ ) removed over the whole temperature range (Figure 4.5). A slight decrease may be occurring above 700 °C.

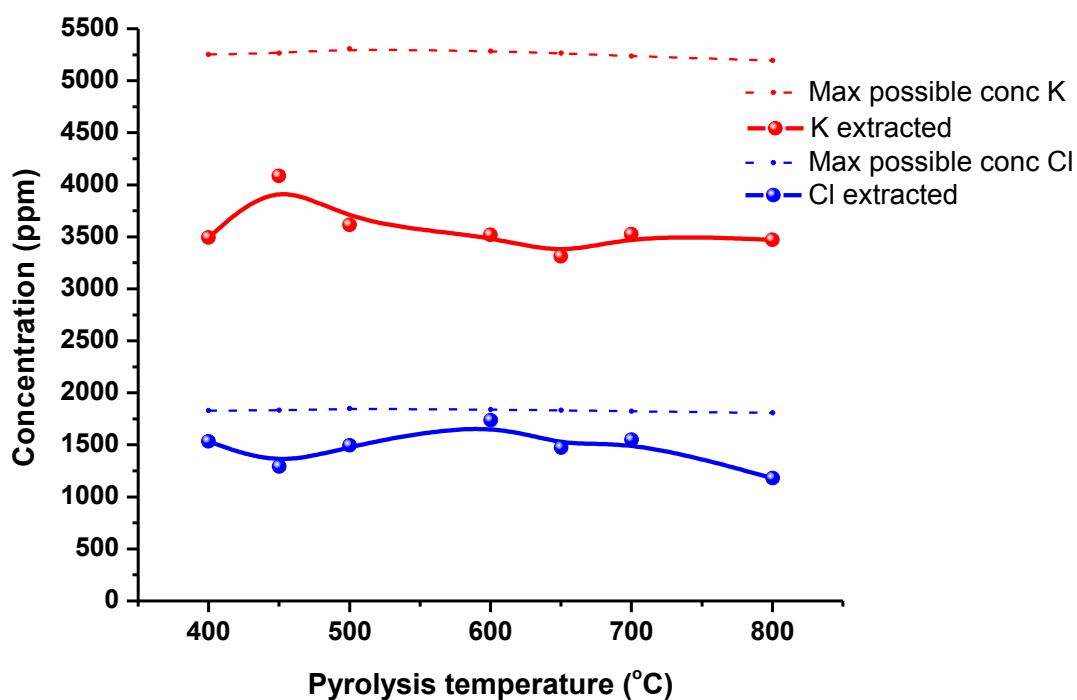


**Figure 4.5: Potassium and chloride concentrations in aqueous extracts of pyrolysis chars (Originally in colour)**

This contrasts with the extraction from combustion ashes, which saw vastly reduced levels of potassium and chloride extracted at temperatures above 600 °C (Chapter 2). The percentages removed are, however, similar to those from the combustion ashes formed at lower temperatures and also found by Jensen *et al* from leached wheat straw chars pyrolysed at 500 °C.<sup>18</sup> These levels are once again lower than those observed by the direct leaching of the initial wheat straw (Chapter 3). This indicates that similar processes are occurring in the biomass during the initial devolatilisation stage during both combustion and pyrolysis, however, at higher temperatures mineralogical reactions occur in the combustion ashes that do not in the pyrolysis chars. The consistency of the concentrations of K and Cl in the extracts in this temperature range is supported by analysis of their gas phase release during pyrolysis by previous researchers showing low levels of losses between 400 – 700 °C.<sup>26</sup> They found that approximately 70% of the Cl was

released from wheat straw during pyrolysis at < 400 °C and the majority of the residual chlorine was released between 700 – 900 °C. No significant potassium release was observed at temperatures below 700 °C. During the devolatilisation stage of biomass combustion the major inorganic species released was HCl.<sup>27</sup> Jensen *et al* also found that all potassium in the char was soluble up to a pyrolysis temperature of 700 °C using sulfuric acid.<sup>26</sup> An increased acid soluble but water insoluble potassium fraction following pyrolysis implies the formation of organically bound potassium species either as intercalation compounds or as counter-ions to oxygen-containing functional groups.<sup>26, 28</sup>

#### 4.4.1.2 Silica

Pyrolysis chars and combustion ashes demonstrate disparate silica extraction trends (Figure 4.6). In general, the levels of silica removed are higher from the pyrolysis chars, with the greatest extraction of 28.5% at 500 °C in comparison to a maximum of 17.2% from wheat straw ashes formed at 400 °C (with 2 h combustion). Both show a decrease in dissolution at elevated temperatures, although for the pyrolysis chars this starts at a higher heat treatment temperature (HTT) and the reduction is not so substantial. However, silica extraction is also lower at lower temperatures via pyrolysis. This can be explained by observing the pH of the extracts formed (Figure 4.7). The initial pH of the extracts increases with increasing pyrolysis temperature up to a maximum at 500 °C (pH 12.4), remains constant up to 700 °C, and decreases at 800 °C (pH 11.8). As with combustion, a decrease in the pH of the extracts occurs during leaching which correlates with the total silica removed. The pH decreases to 10.76 for the 400 °C sample. At pH's <10.7 silica solubility decreases dramatically due to an equilibrium between the silicate ion and monomer.<sup>29</sup>

From combustion studies, silica and potassium species in the biomass would be expected to react at the temperatures used in this pyrolysis study. The reaction of KCl and SiO<sub>2</sub> may be promoted at low temperatures by the presence of water vapour,<sup>30</sup> which will be released during pyrolysis.<sup>14</sup> Indeed, Bjorkmann *et al* explained the release of HCl during the pyrolysis of wood by the reaction of KCl with SiO<sub>2</sub> in the presence of water vapour released from the solid fuel.<sup>31</sup> However, both the potassium and silica extraction data intimate that there is little interaction between these two species during pyrolysis.

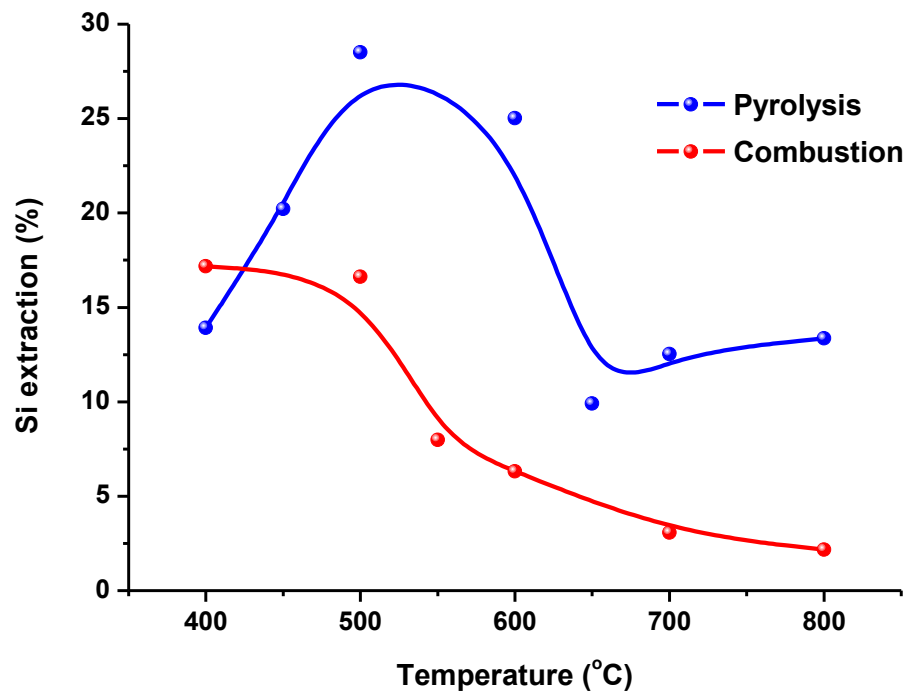


Figure 4.6: Si extraction trends for pyrolysis chars and combustion ashes following aqueous leaching at room temperature (Originally in colour)

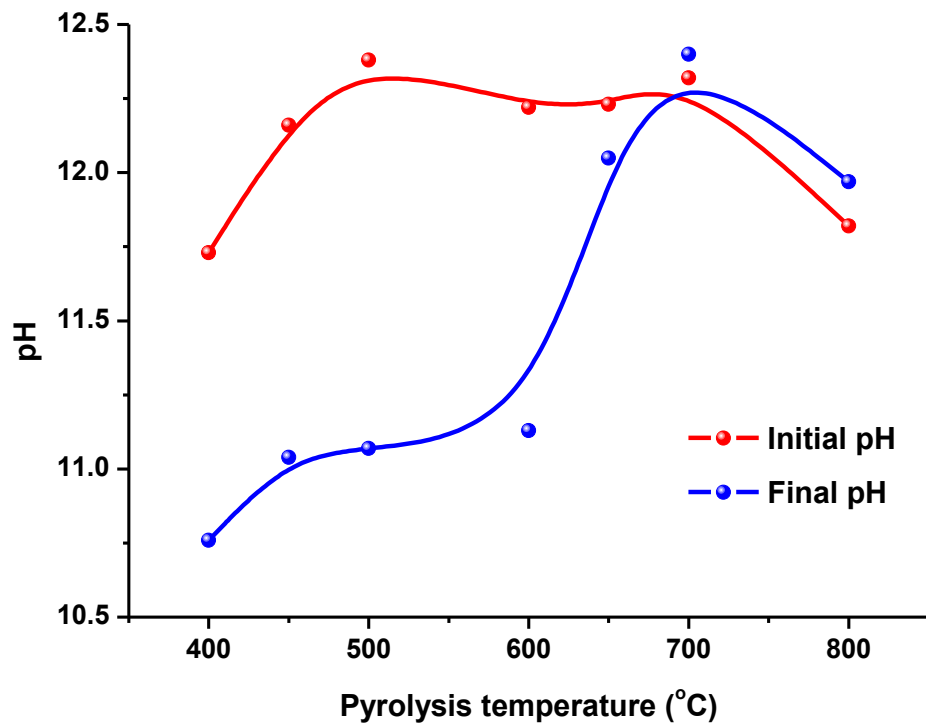
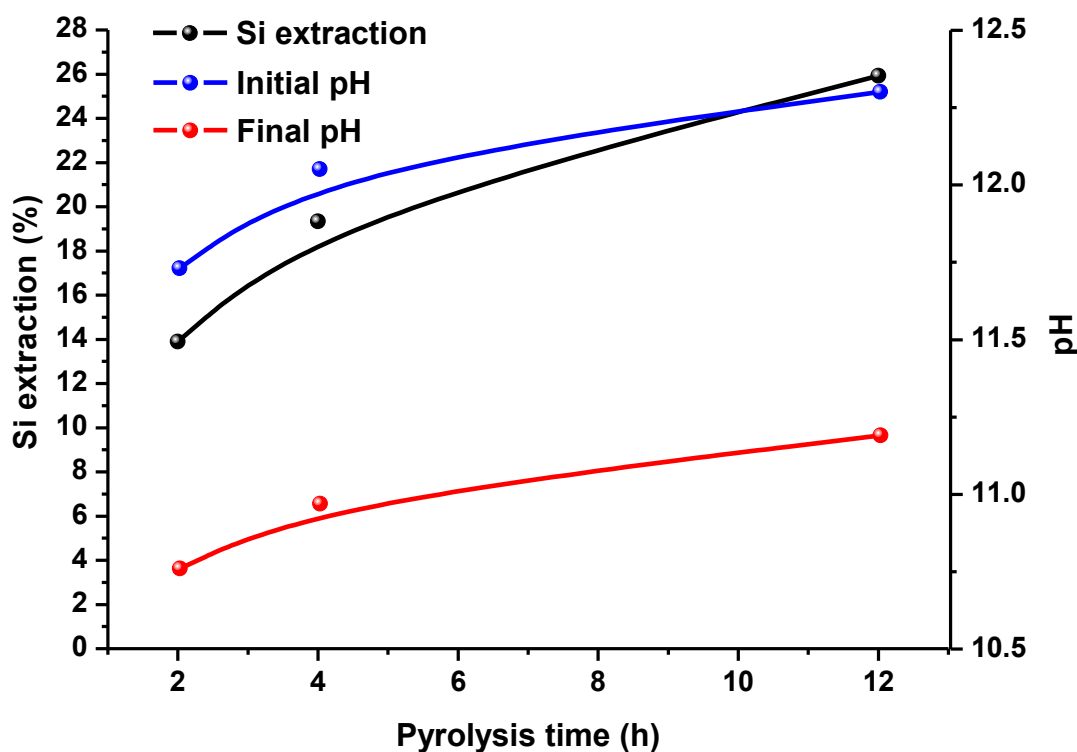


Figure 4.7: Initial pH and final pH after 24 h leaching of pyrolysis char extracts (Originally in colour)

SEM/EDX analyses of various biomass chars indicate that the morphology of the initial straw is retained during pyrolysis, although it shrinks slightly.<sup>18</sup> Identified mineral particles were found to consist of pure SiO<sub>2</sub>, K together with Cl, or C and O.<sup>26</sup> Potassium was dispersed throughout the char.<sup>32</sup> Overall, this suggests that SiO<sub>2</sub> and potassium species do not interact due to the presence of a carbonaceous barrier, preventing intimate mixing. This inhibits the formation of poorly soluble low temperature potassium silicate melts. This mechanism was also suggested by Knudsen *et al* studying potassium volatilisation from chars.<sup>33</sup> The decrease in silica solubility at higher pyrolysis temperatures may either be due to reaction with potassium due to increased cation mobility as the melting point of KCl is neared (770 °C, or lower amongst mixed alkali salts),<sup>34</sup> precipitation by Ca<sup>2+</sup> species following decomposition of CaCO<sub>3</sub> or increased sintering or crystallisation of silica. During the heating of pure amorphous silica, physically adsorbed water is initially lost, followed by the dehydroxylation of silanol groups above 190 °C initially via condensation of vicinal silanol groups and then isolated silanol groups, with the Si-OH surface coverage decreasing to approximately zero at 1000 °C.<sup>35</sup> This increases the siloxane linkages, sharply above 400 °C, reduces the ease of rehydroxylation in water and causes shrinkage and sintering of the silica structure, thereby decreasing the ease of dissolution.<sup>29, 35</sup> Devitrification occurs in pure silica at temperatures above 1000 °C, but is strongly catalysed by the presence of impurities, for instance the presence of minor amounts of potassium and sodium has been shown to lead to the formation of cristobalite and tridymite at 700 °C – 800 °C.<sup>36</sup> The decomposition temperature of CaCO<sub>3</sub> is normally 898 °C,<sup>34</sup> however, in the presence of carbon or potassium salts this has been observed to reduce to 700 °C or less.<sup>37-40</sup> XRD analysis of the chars and combustion residues in this study indicates the reduction in CaCO<sub>3</sub> content of the chars above 600 °C (Figure 4.14), whilst low Ca solubility remains at high temperatures which could be due to the formation of insoluble calcium silicate precipitates (Table 4.1). The explanations given above, individually or in combination, could therefore be equally responsible for the reduction in SiO<sub>2</sub> solubility at pyrolysis temperatures above 600 °C.

### 4.4.1.3 Effect of time



**Figure 4.8: Effect of pyrolysis time on silica extraction and the pH of the extract of wheat straw char pyrolysed at 400 °C (Originally in colour)**

An understanding of the low silica solubility at lower pyrolysis temperatures was developed by studying the effect of pyrolysis time on the extraction of Cl07 char formed at 400 °C (Figure 4.8). This demonstrates an increase in silica extraction, initial pH of the solution extract and final pH of the extract with increasing pyrolysis time. After 12 h pyrolysis at 400 °C the initial pH (12.3) and silica extraction (25.9%) of the extracts are similar to those formed from straw pyrolysed at 500 °C for 2 h (Figure 4.6, Figure 4.7). Hossain *et al* observed that the pH of a water solution made from sewage sludge chars increased with pyrolysis temperature, with a value of 4.87 found when the char was formed at 400 °C, rising to pH 12 when it was pyrolysed at 700 °C.<sup>41</sup> Mukherjee *et al* also observed the pH of biomass chars to increase with increasing pyrolysis temperature and between biomass types.<sup>42</sup> The pH of a biochar formed using a traditional charcoal method was 8.5, this decreased with ageing over 12 months when stored in a small amount of water.<sup>43</sup> This was explained as due to long term natural oxidation of the samples. Biochar produced at 500 °C in a fluidised bed from corn cob and corn stover gave water solutions

with a pH of 7.8 and 7.2 respectively after 72 h soaking. This emphasises the large variation in the alkalinity of pyrolysis chars, which will affect the solubility of different elements and therefore is important for understanding its utilisation.<sup>44</sup> Furthermore, one frequently raised benefit of the addition of biochar to agricultural soils is its liming effect, reducing the acidification of soils caused by nitrogen fertilisers.<sup>45</sup> However, the variation of pH with temperature of char preparation does not appear to be widely studied or understood. Two possible explanations seem to be available. Either the inorganic species within the chars need sufficient temperature and time to react and form highly alkaline species, such as KOH and K<sub>2</sub>CO<sub>3</sub>, or the presence of acidic functional groups in the char or acidic organic compounds on the char surface at low pyrolysis temperatures reduce the pH of the solution formed. It may also be a concerted process.

#### **4.4.1.4 Extraction model**

Both formic acid and acetic acid are products of biomass pyrolysis, with the formation of these products generally found to be favoured in higher potassium containing biomass.<sup>8</sup> The bio-oil produced from corn stover and corn cobs at 500 °C contained 6.3 - 6.4 wt% acetic acid,<sup>46</sup> whilst the majority of the bio-oil produced from wheat straw during heating to 1000 °C was composed of acetic acid.<sup>47</sup> Large amounts of acetic acid were also observed during the pyrolysis of willow.<sup>14</sup> The maximum release studied by FTIR was at ~370 °C, although release continued throughout the temperature range analysed (up to 800 °C). However, at higher pyrolysis temperatures a gas-forming pathway dominates, resulting in lower bio-oil production and consequently fewer acidic components.<sup>19</sup> In addition, the chars produced from corn stover and corn cobs at 500 °C had a low surface area suggesting condensation of compounds in the pores.<sup>46</sup> It is known that at low temperatures (< 500 °C) some of the tar and oil produced condenses on the char surface.<sup>48</sup> However, little work has been undertaken to study the bio-oil residues that remain on char surfaces. Therefore, the increased acidity of solutions at lower pyrolysis temperatures and times could be due to the dissolution of condensed acidic organic compounds from the char surface.

Analysis of biomass chars formed at lower temperatures and shorter times indicate a higher content of volatile and O-containing matter.<sup>47, 49-51</sup> The general trends in the ratios

of H/C and O/C indicate that increasing dehydration occurs with increasing pyrolysis temperature.<sup>51</sup> The recalcitrance of the char formed depends on the carbon structure. A

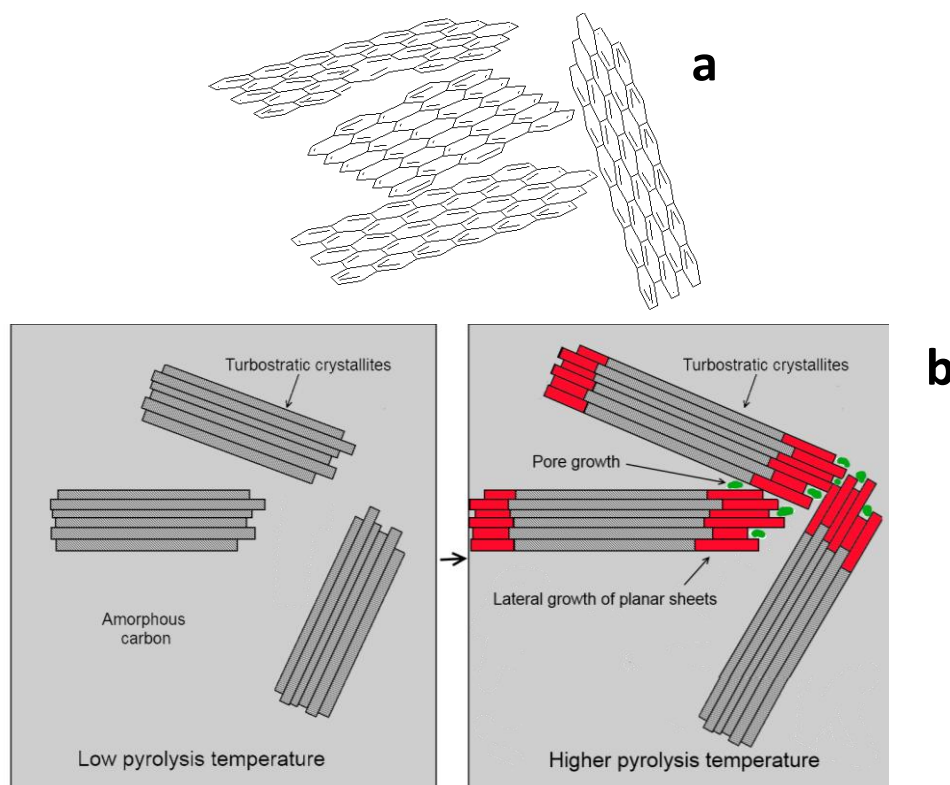


**Figure 4.9: a) Turbostratic carbon sheets showing the lack of 3-dimensional order. b) Growth of turbostratic sheets with increasing pyrolysis temperature. (Originally in colour)**

generally accepted mechanism is that as the carbonisation temperature increases plant biomass undergoes chemical transformations leading to the formation of aromatic ring structures which combine to form turbostratic graphene sheets (Figure 4.9).<sup>52</sup> This is supported by observations using XRD and  $^{13}\text{C}$  NMR of biomass chars.<sup>51, 53</sup> This suggests the presence of more labile carbon compounds at lower temperatures of preparation due to changes in the surface functionality.  $^{13}\text{C}$  NMR shows a relative increase in aryl C carbon and a reduction in alkyl, O-alkyl, O-aryl and carbonyl functionalities at higher pyrolysis temperatures.<sup>54</sup> An increased variety of O-containing functional groups have been observed in char compared to the starting material including a minor contribution of carboxylic carbon during the pyrolysis of switchgrass and corn stover at 500 °C.<sup>55</sup> Rutherford *et al* studied changes in surface acidic functional groups during the charring of cellulose, lignin, pinewood and bark at various temperatures.<sup>56</sup> They found that the total acidity of pure cellulose increased during pyrolysis with a maximum found at 250 °C with

longer pyrolysis times, which then decreased with increasing pyrolysis temperature. The acidity of lignin increased with increasing temperature to 400 °C, although not to the same level. Pine wood and bark followed the same trend as cellulose. Acidity was related to the concentration of phenols, lactones and carboxylic acid groups, with the latter contributing the most to the observed increase in acidity. Mukherjee *et al* also found by Boehm titration that total surface acidity decreased with pyrolysis production for oak, pine and grass at temperatures between 250 – 650 °C, with carboxyl functional groups the most abundant.<sup>42</sup>

Alkali cations such as potassium may act as counter-ions at these acidic sites. The cation exchange capacity (CEC) of biochars has been observed to decrease with increasing pyrolysis temperature.<sup>42</sup> This was found to directly correlate with the level of surface acidity and the remaining content of volatile organic matter.<sup>42</sup> The decomposition of the O-containing functionalities at higher temperatures or longer pyrolysis times will release the potassium ions where they may react with CO<sub>2</sub> or H<sub>2</sub>O to form K<sub>2</sub>CO<sub>3</sub> or KOH. In the presence of carbon these have been suggested to decompose to K<sub>2</sub>O between 500 – 600 °C.<sup>57</sup> The increasing content of any of these species in the chars, combined with the decomposition of the acidic functional groups, will increase the alkalinity of the solution formed on leaching. Alternatively, with further dehydration of the carbonaceous material KCl could react with the water released forming HCl and KOH. As mentioned earlier, HCl is the major inorganic species observed to be released at low temperatures during the pyrolysis of biomass and this release has been calculated to be thermodynamically more favourable in the presence of an acidic oxide such as SiO<sub>2</sub>.<sup>27,31</sup>

This suggests that all of these processes could be interacting to increase the alkalinity of chars formed at higher temperatures and for longer reaction times (Figure 4.10). Acidic bio-oil residues are more likely to condense on the surface at lower temperatures and will lower the pH as they dissolve into solution. Higher O/C ratio chars formed at lower temperatures have been shown to have a higher surface acidity in both pure cellulose and several biomass materials. Further decomposition of the char reducing the O/C ratio could release more K<sup>+</sup> ions to react with CO<sub>2</sub> or H<sub>2</sub>O forming alkaline species that will increase the alkalinity of the solutions formed.

Both a more alkaline char and a higher cation exchange capacity (CEC) are beneficial for the addition of biochar to soils to improve agronomic processes. The above discussion suggests that these two benefits are incompatible. Greater O-containing functional groups leads to greater CEC.<sup>58</sup> Greater O-containing functional groups also appear to contribute to a reduction in the alkalinity of the char. However, in acidic soil an additional liming effect will be present due to the content of calcium carbonate in the chars which will dissolve and neutralise any acid present.

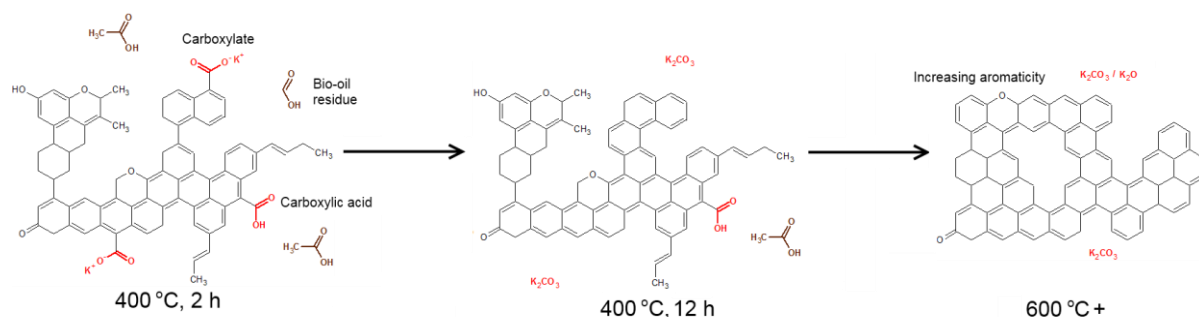


**Figure 4.10: Proposed mechanism for the increasing alkalinity of wheat straw char extracts with increasing combustion temperature and time (Originally in colour)**

#### 4.4.1.5 Other elements

Other species in the chars show varying dissolution trends with increasing pyrolysis temperature (Figure 4.11). The concentration of sodium is much lower than that of potassium in accordance with its lower content in the initial plant material. The concentration in the solution does appear to fluctuate, however, the overall trend is of a relatively constant extraction, decreasing at 800 °C. This is consistent with the release of NaCl or formation of sodium silicates at higher temperatures, analogous to potassium.

The nitrate concentration also remains constant with changing pyrolysis conditions. This level is nevertheless very small in comparison to the initial N content in the biomass and only around 3-5% of the N content of the char is extracted based on CHN analysis. CHN analysis shows that the samples lost 50% of their N content as volatiles at 400 °C increasing to 60% at 800 °C (Table 4.2). This is consistent with observations by other researchers during the pyrolysis of herbaceous biomass.<sup>59</sup> Yao *et al* also observed in a simulated geochemical weathering analysis of sewage sludge biochar that N was

relatively unavailable.<sup>60</sup> This has been attributed to the formation of N-containing heterocycles during pyrolysis.<sup>59</sup>

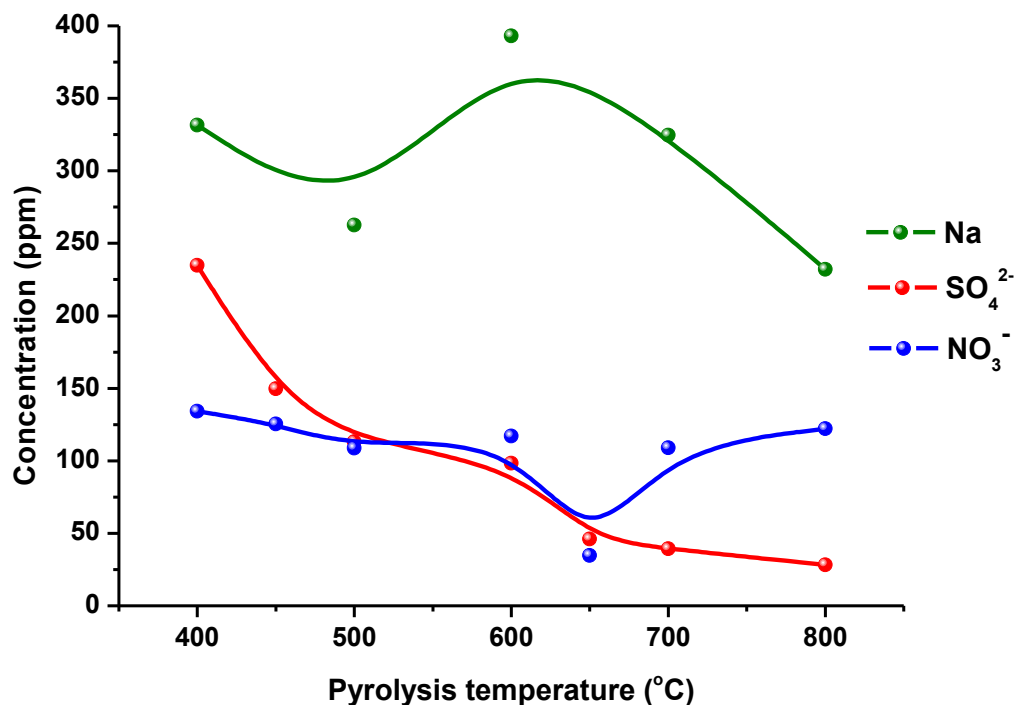


**Figure 4.11: Na, SO<sub>4</sub><sup>2-</sup> and NO<sub>3</sub><sup>-</sup> concentration in char extracts with pyrolysis temperature (Originally in colour)**

Sulfate, on the other hand, displays a continual reduction in solubility with increasing carbonisation temperature. Knudsen *et al* observed the same reduction in inorganic sulfate during the pyrolysis of wheat straw.<sup>33</sup> This was ascribed to the reductive decomposition of inorganic sulfate leading to both the formation of increasing levels of organic sulfur and inorganic sulfide at temperatures greater than 600 °C.<sup>33</sup>

Phosphate is another important nutrient for plant growth. Low levels of extraction are observed at all temperatures with decreasing extraction at increasing pyrolysis temperatures. The maximum extraction is 8.6% at 500 °C reducing to levels lower than the detection limit at 800 °C. Much higher levels of water solubility were observed for the initial wheat straw (Chapter 3), whilst similar levels were observed from wheat straw ashes (Chapter 2). This therefore indicates changes in the phosphate association occurring during pyrolysis. Equilibrium calculations suggest that phosphorous combines

with calcium to form  $\text{Ca}_3(\text{PO}_4)_2$  during combustion.<sup>61</sup> During Soxhlet leaching of biochar formed at 550 °C Yao *et al* found low levels of phosphate and calcium in solution but that higher levels had been leached from the chars suggesting reprecipitation.<sup>60</sup> The addition of humic acid increased the solubilisation of both species.<sup>60</sup> The formation of calcium phosphate salts may therefore be partially responsible for the low extraction of both of these elements. Mg displays similar dissolution levels as Ca suggesting similar structures in the char. Little data is available on the release of heavy metals from chars, however, this is vital for their utilisation.<sup>62</sup> More data is available on the uptake of heavy metals by activated carbons and biochar. No mercury was identified, cadmium was identified only in some samples at low levels, whilst concentrations of other metals were also low. This may be due to the high pH of the solution hindering dissolution.<sup>63</sup>

## 4.4.2 Char analysis

The char formed before and after extraction was analysed to determine the change in ash content by thermogravimetric analysis (TG), CHNO distribution by elemental analysis, mineral and char structure by XRD and ATR-IR and calorific value and char combustion characteristics by STA. Analyses of the char formed before and after extraction are shown in Table 4.2.

### 4.4.2.1 Char yield

The mass remaining following pyrolysis for 2 h decreases with increasing pyrolysis temperature, as observed by many other researchers (Figure 4.12). The char yields are similar to those found for palm shell,<sup>50</sup> pine shavings,<sup>51</sup> and Festuca grass,<sup>51</sup> amongst others. Generally the majority of the mass loss is observed to occur below 400 °C, with a decreasing mass loss rate at higher temperatures as fewer volatiles are released.<sup>49</sup> This is supported by the decomposition profile of the starting material (Claire 07 wheat straw) under nitrogen (Chapter 3, Figure 3.15), which showed that the major mass loss occurred below 400 °C with a continual mass loss observed up to 900 °C. In addition, an increased mass loss is observed with longer pyrolysis times at 400 °C indicating that carbonisation was not complete after 2 h at this temperature. The decrease in the char mass at higher temperatures may partly be due to carbonate decomposition and to further breakdown of the char matrix.

**Table 4.2: Moisture, ash and CHN analysis of the char formed before and after leaching. The sample numbers indicate the temperature of pyrolysis, and the second number the time of pyrolysis (e.g. 400-2 = 400 °C for 2 h)**

	Initial material	400-2	400-4	400-12	500-2	600-2	700-2	800-2
Char mass (% original straw)		30.5	27.6	26.9	30.5	26.3	24.0	23.3
Moisture (wt%)	7.10	3.63			3.24	4.14	5.75	5.06
Ash (wt%) <sup>db</sup>	6.03	17.6			20.4	20.6	21.6	24.0
C (wt%) <sup>db</sup>	45.3	68.7			71.0	72.5	72.5	71.5
H (wt%) <sup>db</sup>	5.1	2.8			1.9	1.2	0.5	1.0
N (wt%) <sup>db</sup>	0.4	0.6			0.6	0.5	0.5	0.6
O (wt%) <sup>db</sup>	39.5	10.4			6.1	5.3	4.8	2.9
H/C	1.34	0.48			0.32	0.19	0.09	0.16
O/C	0.66	0.11			0.07	0.06	0.05	0.03
Following extraction								
Moisture (wt%)		3.27	3.54	3.75	1.77	2.07	4.10	4.20
Ash (wt%) <sup>db</sup>		12.9	13.0	12.8	14.8	15.1	15.5	17.8
C (wt%) <sup>db</sup>		71.3	74.3	76.8	76.2	78.0	76.5	77.0
H (wt%) <sup>db</sup>		3.0	2.8	2.4	2.1	1.5	0.7	0.3
N (wt%) <sup>db</sup>		0.7	0.7	0.7	0.6	0.6	0.5	0.5
O (wt%) <sup>db</sup>		12.1	9.2	7.3	6.3	4.8	6.8	4.4
H/C		0.51	0.45	0.38	0.33	0.24	0.11	0.05
O/C		0.13	0.09	0.07	0.06	0.05	0.07	0.04
% extracted		27.1			28.4	28.1	29.5	26.7
Retention N (%)		43.3			38.1	30.1	29.2	36.5

db = Dry basis

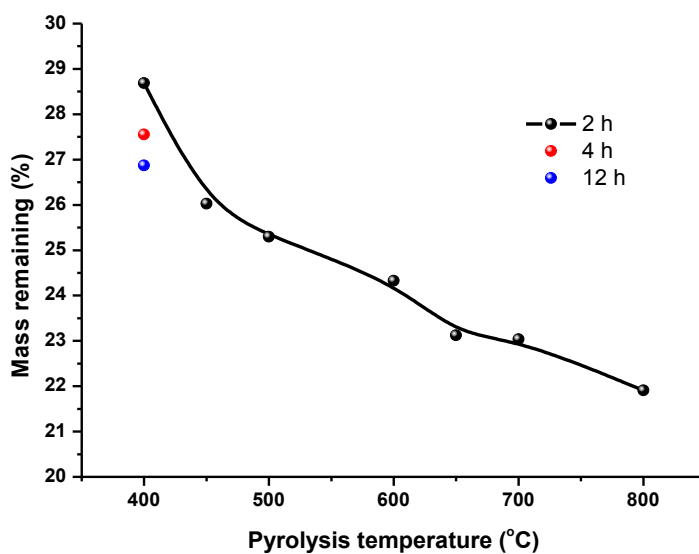


**Figure 4.12: Changing char yield with pyrolysis temperature and time (Originally in colour)**

#### 4.4.2.2 Elemental analysis

A van Krevelen diagram can be used to plot the change in elemental content. This is a useful tool, widely used for analysis of fuels to denote the degree of saturation (H/C atomic ratio) and oxygenation (O/C atomic ratio) (Figure 4.13).<sup>64</sup> The plot for the chars formed in this study show a decrease in both H/C and O/C ratio with increasing pyrolysis temperature corroborating the results of earlier researchers.<sup>54</sup> The changes in the atomic ratios initially show O/C decreasing faster than H/C indicating either decarbonylation or decarboxylation reactions occurring.<sup>12</sup> An increased loss of hydrogen appears to occur at 700 – 800 °C due to dehydrogenation.<sup>12</sup> This correlates with the proposed mechanism for char formation with some O-containing functionalities at lower temperatures of preparation which are decomposed at higher temperatures of pyrolysis with conversion of alkyl and O-alkyl C to aryl-C.<sup>54</sup> This also supports the hypothesis of increased acidity in solution occurring due to the presence of more O-functionalities, particularly carboxyl, at lower pyrolysis temperatures.

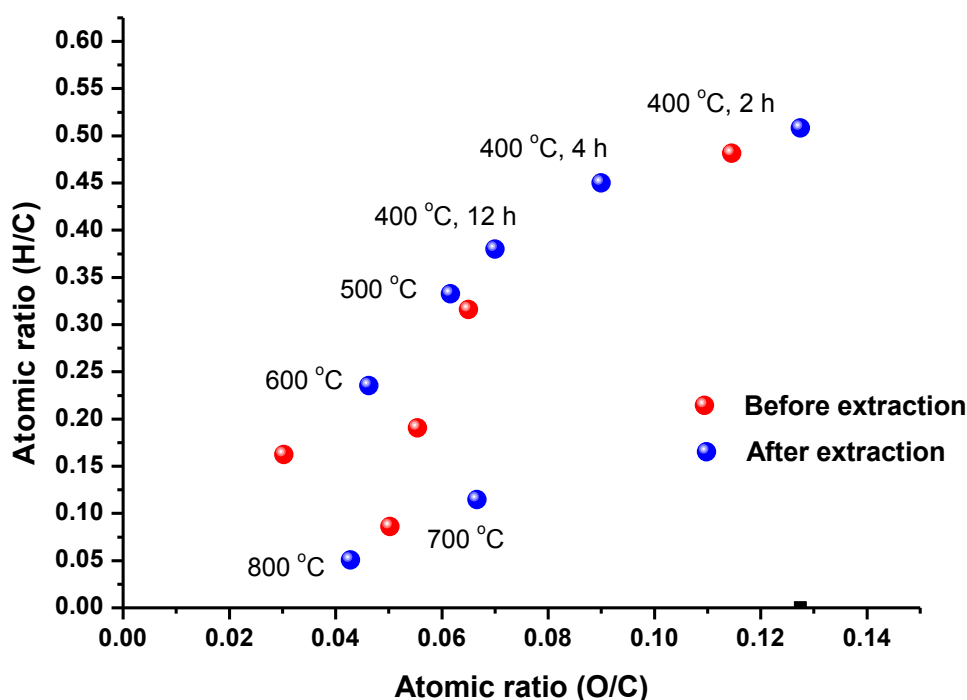


Figure 4.13: Van Krevelen diagram of changing atomic ratios of char on a H<sub>2</sub>O free basis (Originally in colour)

Following leaching for 24 h the elemental ratios of the 400 °C char appears to suggest a slight increase in oxygen content and hydrogen content, whilst the other samples remained relatively stable. Increased O/C ratios have been observed for biochar following artificial 'ageing'.<sup>58</sup> That study observed the O/C ratio to increase from 0.1 to 0.15 after incubation at 70 °C for six months. The data from this study suggests that oxidation of the chars may occur rapidly in an aqueous environment for chars containing a high level of O-containing species. This data should, however, be treated with caution as the oxygen content is determined by difference and is therefore subject to considerable error.

#### **4.4.2.3 X-Ray Diffraction**

X-Ray Diffraction (XRD) analysis of the chars indicates a similar amorphous structure throughout the temperature range studied (Figure 4.14). The broad halo centred at 23.1° 2θ was also observed for residues following 10 min combustion (Chapter 2) and attributed to the non-crystalline carbon structure.<sup>60</sup> This peak narrows at higher temperatures (inset) together with another broad peak around 43° 2θ, signifying developing atomic order during carbonisation, which is attributed to the lateral growth of graphene sheets within turbostratic crystallites.<sup>65</sup> Kercher *et al's* study on the carbonisation of thin MDF sheets indicated a 5% dimensional shrinkage at 400 °C rising to 20% at 800 °C with corresponding increases in bulk density.<sup>65</sup> This transformation of low density disordered carbon at low pyrolysis temperatures into high-density graphene sheets could be an explanation for the reduction in the intensity of the peaks observed at 38.2°, 44.6° and 65.0° 2θ. These peaks were also observed in the partially combusted residues and found to be due to the aluminium sample holder. Higher intensity peaks may correspond to a low density, randomly ordered sample, whilst a reduced intensity could indicate a higher density, more ordered sample with a greater number of crystalline planes reflecting the incoming x-rays.

The other peaks correspond to the crystalline inorganic species within the chars. The peaks are not as intense as those observed in the diffractograms of the ashes (Chapter 2 and 3) due to their dilution by the carbon present. The most intense peaks at 28.3°, 41.1° and 50.2° 2θ correspond to KCl. These reduce in intensity at pyrolysis temperatures of >500 °C although they do not disappear entirely in comparison to the changes observed

in the diffractograms of wheat straw ashes formed at 800 °C after 2 h combustion. The same melting and volatilisation process is therefore occurring as during combustion,

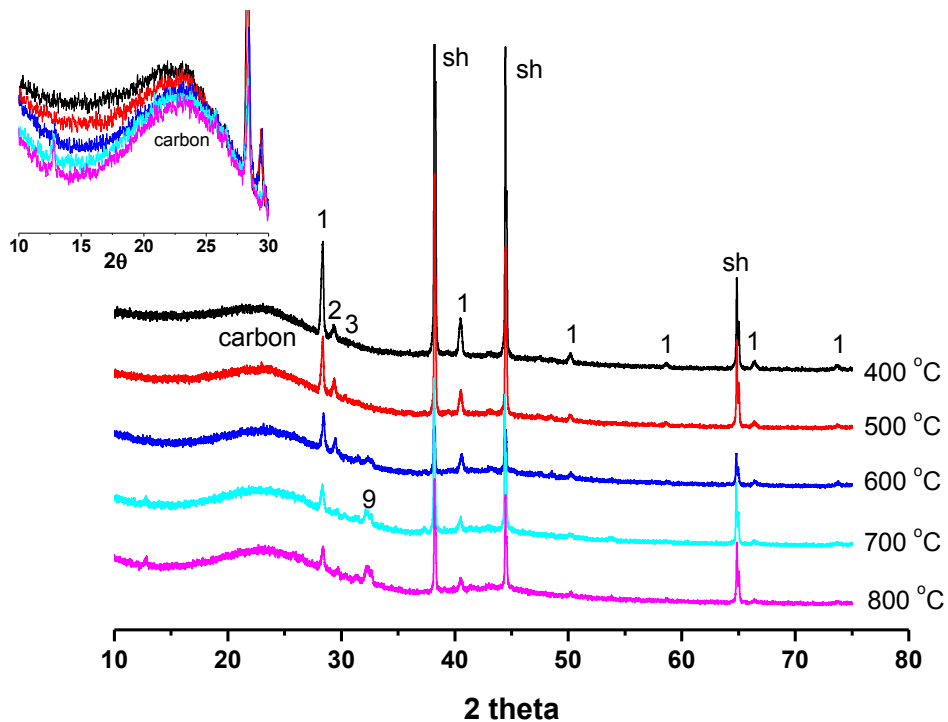


**Figure 4.14: X-ray diffractograms of chars formed at different temperatures after 2 h: 1 = Sylvite (KCl); 2 = Calcite ( $\text{CaCO}_3$ ); 3 = Arcanite ( $\text{K}_2\text{SO}_4$ ); 9 = Calcium silicate ( $\text{Ca}_2\text{SiO}_4$ ) or Potassium carbonate ( $\text{K}_2\text{CO}_3$ ); sh = sample holder (Originally in colour)**

although either higher temperatures are reached during oxidation causing complete volatilisation to occur or the carbonaceous barrier preventing potassium silicate formation is also preventing KCl decomposition.

A peak at  $29.3^\circ$   $2\theta$  correlates with  $\text{CaCO}_3$ . As observed for wheat straw ashes this is significantly reduced above 600 °C. As mentioned earlier this is lower than the literature decomposition temperature of 898 °C but this temperature has been observed to decrease in the presence of carbon.<sup>39</sup> Concurrently a series of minor peaks appear between  $32 - 33^\circ$   $2\theta$ . This can potentially be assigned to either  $\text{Ca}_2\text{SiO}_4$  or  $\text{K}_2\text{CO}_3$ . Both are plausible, with the release of  $\text{K}_2\text{CO}_3$  suggested in the pyrolysis model and the carbonaceous barrier suggesting that this species might be visible in these species in comparison to combustion ashes due to the inhibition of the reaction between  $\text{SiO}_2$  and  $\text{K}_2\text{CO}_3$ . Calcium silicate was visible in combustion ashes at 800 °C and the appearance of

these peaks coincides with the decrease in SiO<sub>2</sub> solubility at these temperatures without a corresponding rise in Ca solubility.

#### 4.4.2.4 Infrared

The ATR-IR spectra of the chars formed between 400 – 800 °C are shown in Figure 4.15. Similar spectra have been observed for chars by other researchers studying a whole host of different biomass materials and during the decomposition of the main structural components, particularly cellulose.<sup>66</sup> The spectra are substantially different from that observed for the initial material and there are also changes with increasing pyrolysis temperature and time. Difficulty in gaining detailed spectra can be observed at higher temperatures due to increasing absorption by the black material. Photoacoustic spectroscopy may enable more detailed analysis at higher char preparation temperature, however, it was not undertaken in this study. Assignments of the main peaks observed are shown in Table 4.3.

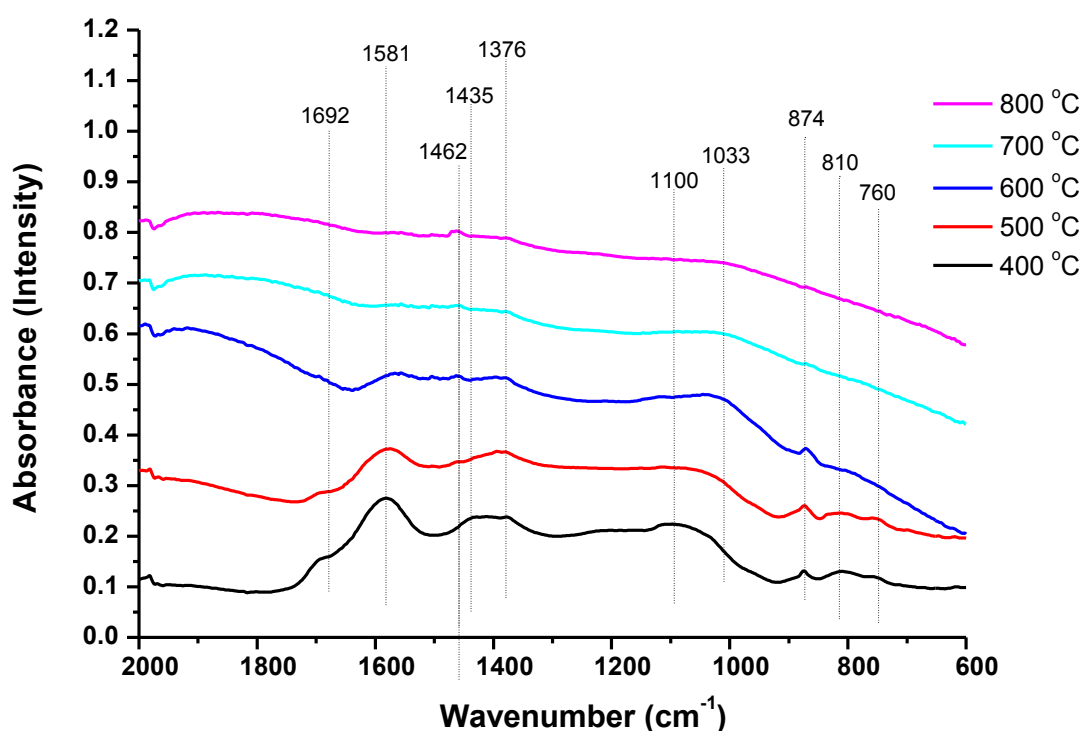


Figure 4.15: ATR spectra of pyrolysis chars formed at different temperatures before leaching (Originally in colour)

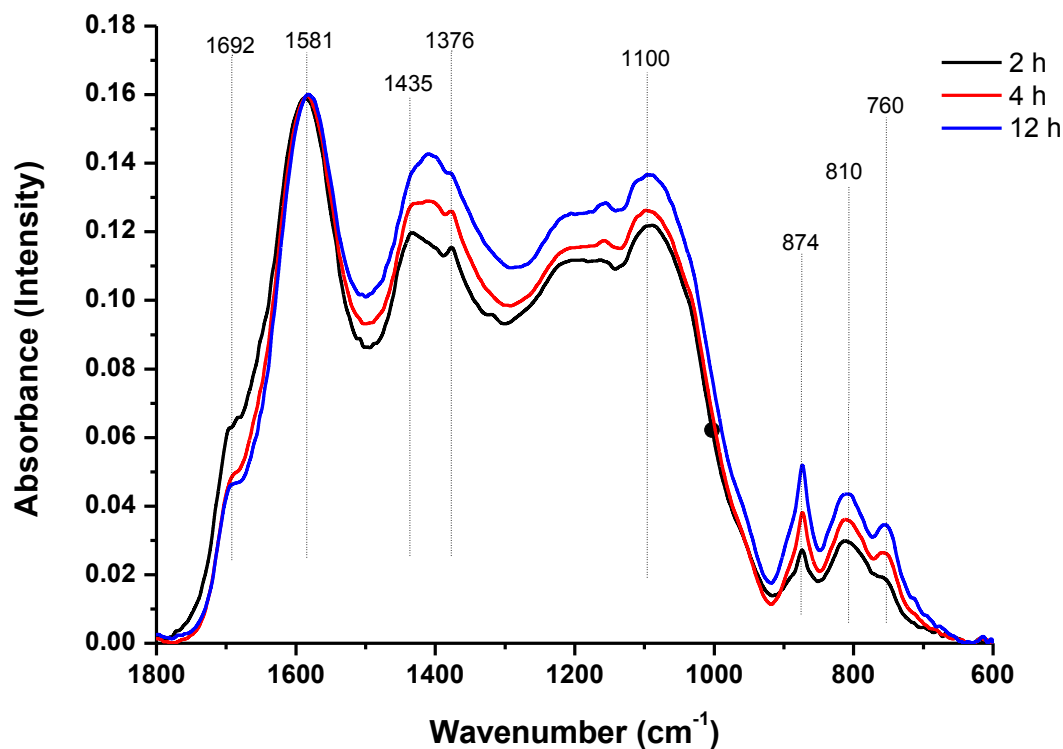


Figure 4.16: ATR-IR spectra of pyrolysis chars formed at 400 °C with different heating times following leaching (Originally in colour)

Table 4.3: Infrared band assignments for ATR-IR spectra of pyrolysis chars

Wavenumber (cm <sup>-1</sup> )	Assignment	Details	Reference
3351	O-H stretch	water, H-bonded hydroxyl (OH) groups	51
2919	asymmetric C-H stretch	aliphatic CH <sub>x</sub>	12, 49, 51
1692	C=O stretch	aldehydes, ketones, esters and carboxylic acids	51, 58, 66
1581	C=C stretch	aromatic carbon	49, 51, 66
1462	asymmetric C=O stretch	carboxylate	56, 67
1435	C=C stretch	aromatic carbon	49
1435	$\alpha$ -CH <sub>2</sub> bend	aliphatic -CH <sub>2</sub> deformations	49, 51
1376	O-H bend	in-plane bending of phenolic -OH	12
1376	$\alpha$ -CH <sub>3</sub> bend	aliphatic -CH <sub>3</sub> deformations	12, 49
1376	symmetric C=O stretch	carboxylate	51
1215	C-O or C-C stretch	aryl ethers; phenolic C-O, aliphatic C-C	56, 67
1100	C-O stretch	C-O-C stretch in cellulose or hemicelluloses; aliphatic -OH	12, 49
1200-1000	C-H deformation	substituted aromatics	51
874, 810, 760	C-H bend	aromatic CH out-of-plane	12, 49

The presence of an increasing aromatic structure is particularly highlighted by the peaks at 874, 810 and 760  $\text{cm}^{-1}$  characteristic of aromatic C-H out-of-plane bending.<sup>12, 66</sup> These are not observed in the starting material. At higher pyrolysis temperatures these bands reduce in intensity and disappear, presumably due to the increasing growth of graphene sheets. A peak due to carbonyl stretching is apparent at 1692  $\text{cm}^{-1}$ . This was observed to appear at between 250 – 350 °C during the degradation of cellulose and is probably mainly due to aryl-carboxyl or aryl-ketone functionalities.<sup>56, 66</sup> This peak reduces in intensity at higher temperatures, in agreement with the CHN analysis which showed a decrease in the O/C atomic ratio at increased degradation temperatures.

A broad peak is observed around 1581  $\text{cm}^{-1}$ . Peaks around 1600  $\text{cm}^{-1}$  are usually attributed to C=C stretching of aromatic components and therefore evinced as further proof of the development of aromaticity within the char during carbonisation.<sup>51, 66</sup> The most intense peak in the infrared spectra of graphite, following several hours of intensive grinding, was observed at 1587  $\text{cm}^{-1}$ .<sup>68</sup> However, peaks between 1610 – 1550  $\text{cm}^{-1}$  have also been identified as partially due to the asymmetric stretch of carboxylate species, with a peak between 1400 - 1300  $\text{cm}^{-1}$  due to the symmetric stretch.<sup>56</sup> Peaks at similar wavenumbers are observed in the pyrolysis chars formed in this study at 400 °C. These peaks, along with a C=O stretch at 1700  $\text{cm}^{-1}$ , were observed to increase during natural oxidation of wood charcoal over several months.<sup>58</sup> Carboxylate peaks were also identified in salts of carboxymethylcellulose with various cations, although the symmetric stretch was placed at 1417  $\text{cm}^{-1}$ .<sup>67</sup> Wright *et al* observed both the  $\text{COO}^-$  asymmetric and symmetric stretching peaks of various acids in water to shift with changing pKa.<sup>69</sup> This is also likely to occur with a carboxylate salt dependent on the counter-ion. Normalisation of the spectra to the 1581  $\text{cm}^{-1}$  peak for chars formed at 400 °C after quenching (Figure 4.16) shows that the carbonyl peak reduces in intensity relative to the 1581  $\text{cm}^{-1}$  peak with increasing pyrolysis time, whilst the aromatic C-H bending peaks and skeletal stretches in the region 1000 – 1500  $\text{cm}^{-1}$  all increase relative to this peak. If the peak at 1581  $\text{cm}^{-1}$  was only due to C=C stretching its intensity would be expected to increase along with the C-H bending peaks or even increase relative to them as greater aromaticity develops. This data therefore supports the hypothesis outlined in section 4.4.1.4 above,

suggesting that the increase in pH of the solution formed at increasing temperatures and times of pyrolysis is due both to a decrease in surface carboxylic acid groups and decomposition of carboxylate groups probably releasing potassium.

Further confirmation of this mechanism could be achieved by carrying out  $^{13}\text{C}$  NMR on the chars formed. Sharma *et al* observed a  $\text{COO}^-$  peak in the  $^{13}\text{C}$  NMR spectra of tobacco chars up to at 170 ppm which they attributed to calcium oxalate species.<sup>70</sup> The peak became more prominent up to 450 °C and then decreased in strength. This peak, however, could also have been due to other carboxylate salts.

Comparison of the spectra of char 400-2 before and after leaching normalised to the 1581  $\text{cm}^{-1}$  peak (Figure 4.17) shows a relative increase in the carboxyl peak (1692  $\text{cm}^{-1}$ ) intensity and the C-O and C-O-C stretching region (1200 – 1050  $\text{cm}^{-1}$ ) following leaching. Development of the peaks in these regions were also observed by Cheng *et al* during the oxidation of biochars over 12 months.<sup>43</sup> This supports the CHN analysis which indicated that oxidation of this char was occurring during leaching.

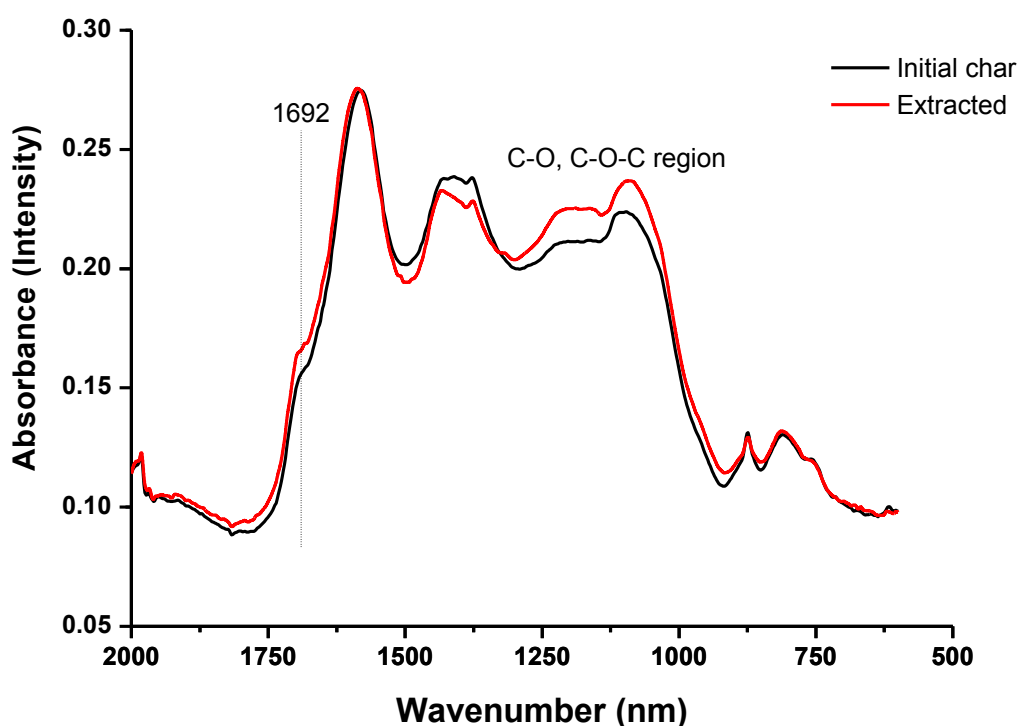
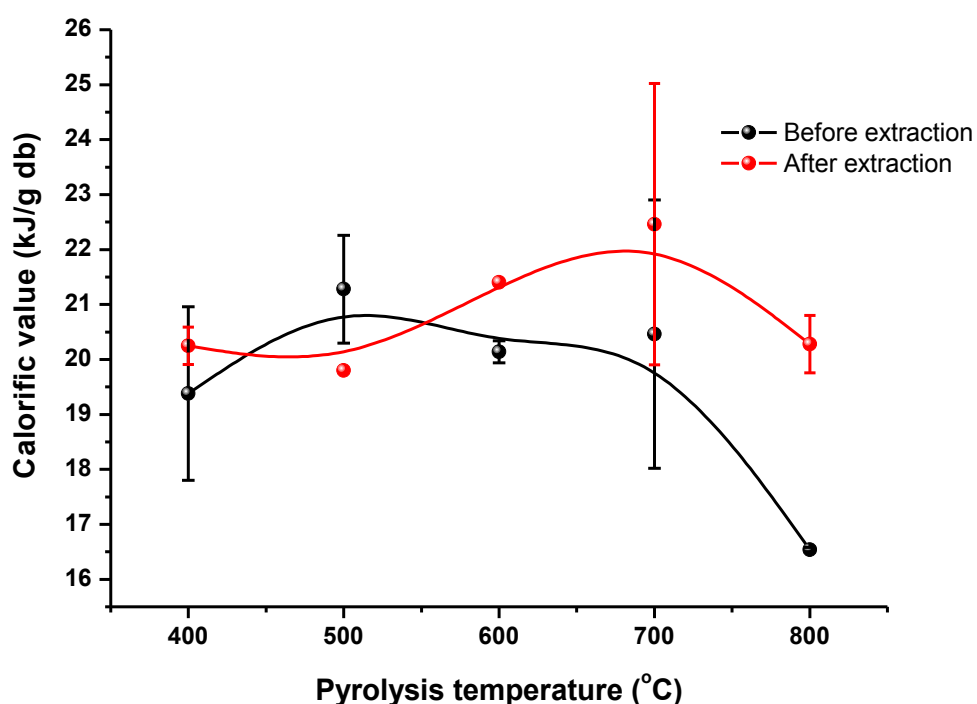


Figure 4.17: Comparison of infrared spectra before and after leaching of char for pyrolysis treatment of 400 °C for 2 h (Originally in colour)

#### 4.4.2.5 Thermal analysis

The chars were analysed by Simultaneous Thermal Analysis (STA) under oxidative conditions to determine the impact of leaching on the calorific value and combustion profile. Due to the small amount of sample available, the calorific values of the chars were determined using a technique developed by Dr. Vitaly Budarin and Dr. Peter Shuttleworth within the Green Chemistry Group. A layer of powdered palladium oxide was added to cover the char sample to ensure complete oxidation of the gases evolved from the sample, ensuring that the total energy of the sample was measured. Testing of the samples with and without added PdO indicated that it did not alter the decomposition profile. The calorific values of the chars before and after leaching are shown in Figure 4.18, mostly based on an average of duplicate measurements.



**Figure 4.18: Calorific value of chars before and after extraction based on STA analysis (Originally in colour)**

The calorific value remains relatively stable with heat treatment temperatures up to 700 °C. With a preparation temperature of 800 °C the calorific value decreases, which coincides with an increasing concentration of ash in the char (Figure 4.19). There may be a slight increase in the calorific value between 400 – 500 °C, which would be consistent

with the decline in the O/C ratio between these pyrolysis temperatures. Following leaching the calorific value of the chars generally appears to increase. This is unsurprising, as ash is removed which does not contribute to the calorific value of the material.

Based on thermogravimetric analysis of the chars (Table 4.2) the percentage of ash removed by aqueous leaching remained similar, between 25 – 29%, at all pyrolysis heat treatment temperatures (HTT) (Figure 4.19). This value is lower than that obtained by analysing the concentration of inorganic species in solution (Table 4.1). However, the analysis in Table 4.1 is based on an idealised recovery of all of the solution. Therefore, this difference can partially be explained by the presence of some inorganic species remaining on the char following filtration. It could also be explained by some co-extraction of organics. This isn't immediately obvious from the solutions, which were all clear except for treatment conditions of 400-2 and 400-4. Nevertheless, once again this confirms a significant reduction in ash content of the chars by aqueous extraction and a corresponding increase in calorific value following leaching, both of which should be beneficial for the utilisation of the chars in combustion facilities.

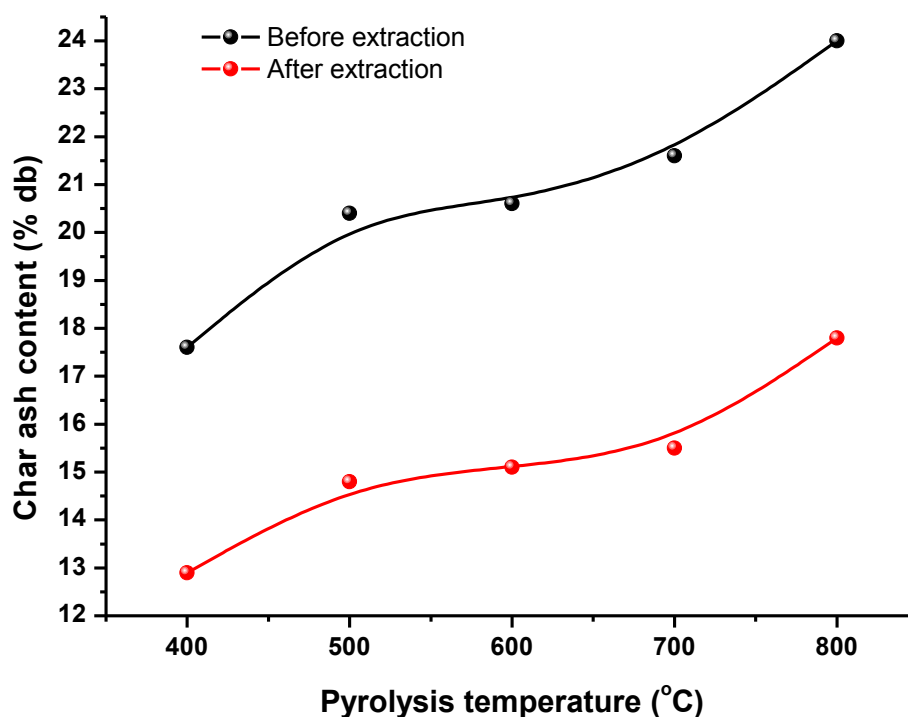
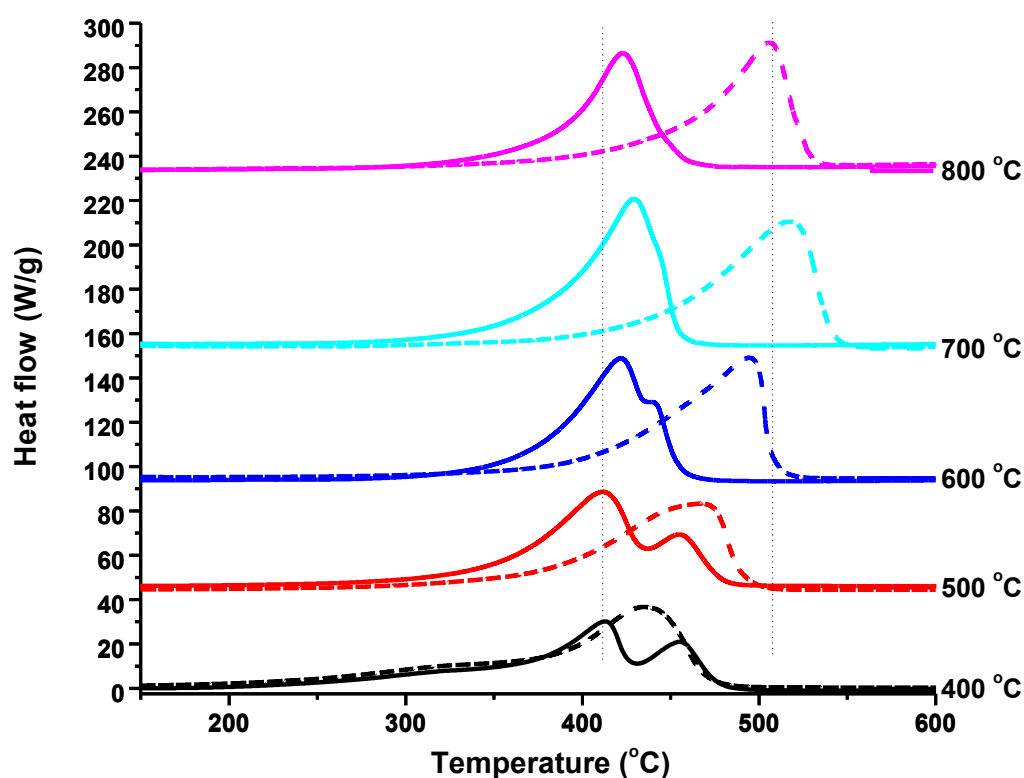


Figure 4.19: Change in ash content of chars before and after extraction based on thermogravimetric analysis (Originally in colour)

The chars demonstrate extremely different combustion behaviours before and after leaching, dependent on the HTT (Figure 4.20). The onset of decomposition for the chars formed at 400 °C occurs around 200 °C, much earlier than the other samples and this is unaffected by the leaching of the char. The onset of decomposition of raw biomass samples and their polysaccharide components usually occurs around this temperature.<sup>71</sup> The initial exotherm (~300 °C) is usually assigned to the breakdown of more labile aliphatic and carboxylic groups, whilst peaks at higher temperatures (~450 °C) are ascribed to more refractory aromatic structures.<sup>72</sup> This indicates the continued presence of labile species in the char formed at 400 °C for 2 h from the incomplete carbonisation of the initial starting material.



**Figure 4.20: DSC profiles of chars before (solid line) and after (dashed line) leaching (Originally in colour)**

Before leaching a general change in the oxidation process is apparent with increasing preparation temperature, as observed by following the temperature of maximum energy release ( $T_{\max}$ ) (Figure 4.21). With treatment temperatures of 400 °C and 500 °C two char oxidation peaks are present with  $T_{\max}$  at  $413 \pm 1.9$  °C and a smaller peak at  $453 \pm 3.5$  °C. Peaks at similar positions were also observed in the microwave char (Figure 4.2). The

positions of these peaks are highly reproducible and do not vary significantly between these two HTTs. At 600 °C the  $T_{\max}$  shifts to a higher temperature of  $423 \pm 0.6$  °C with a small shoulder at 440 °C. At HTTs of 700 °C and 800 °C this coalesces into one oxidation peak centred at  $438 \pm 6.4$  °C and  $425 \pm 3.7$  °C respectively.

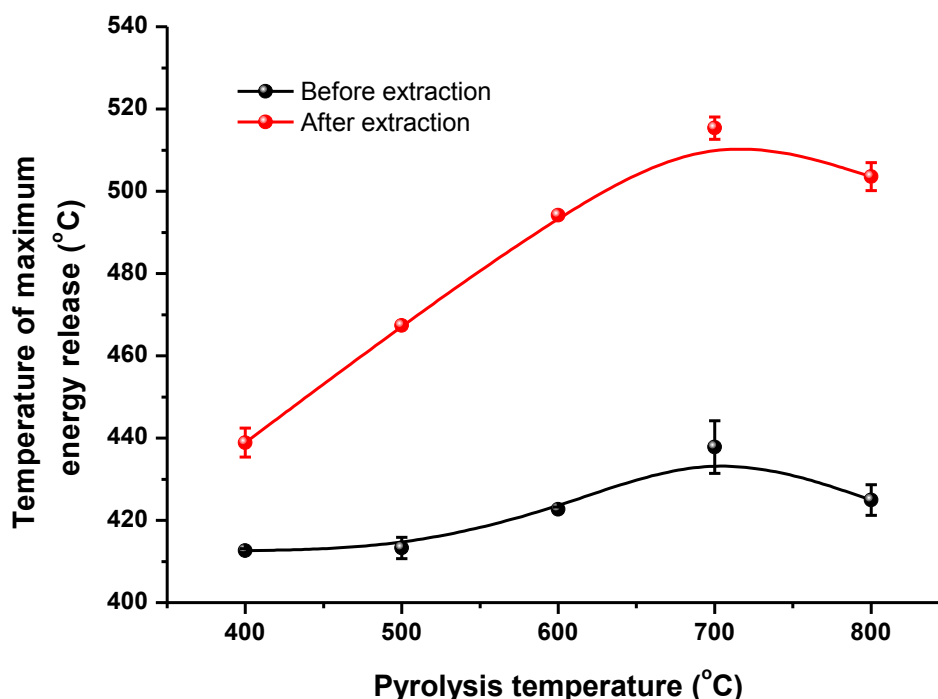


**Figure 4.21: Temperature of maximum energy release during combustion of chars with changing HTT before and after leaching (Originally in colour)**

Following leaching the  $T_{\max}$  increases, and by a greater amount for chars formed at higher HTTs. The chars formed at lower pyrolysis temperatures now contain only one broad oxidation peak, with that of 400-2-Q found at 439 °C, although, the peak covers the same range as that observed for the char prior to leaching. At 500 °C,  $T_{\max}$  is now at 467 °C, similar to the position of the previous higher temperature shoulder, whilst  $T_{\max}$  for 600-2 is at 494 °C. The chars formed at 700 °C and 800 °C show the greatest difference in  $T_{\max}$  before and after leaching. Following extraction they rise to  $515 \pm 2.7$  °C and  $504 \pm 3.4$  °C respectively.

The DSC profiles indicate that there is greater heterogeneity affecting combustion of chars with lower initial HTTs, however, overall the maximum temperature of oxidation of the char before leaching appears to be less dependent on the HTT. In comparison,

following leaching there is a decrease in the reactivity of the char, with the onset and maximum oxidation highly dependent on the pyrolysis temperature.

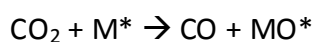
A wide range of researchers have observed a decrease in the reactivity of carbonaceous materials with increased heat treatment temperature. This is either explained by a decrease in the H/C ratio, and therefore an increase in the content of less reactive polyaromatic structures, or as due to the sintering of catalytic species.<sup>73</sup> However, the majority of the work has studied the effect on coal and particularly looking at gasification mechanisms.<sup>74</sup> A previous study looking at the effect of char leaching on the oxidative decomposition of biomass chars is unknown. Previous studies have looked at the effect of water or acid leaching of the initial biomass on the combustion of chars. Zolin *et al* studied the oxidation of char formed from leached and unleached wheat straw pyrolysed at temperatures between 700 – 1400 °C.<sup>32</sup> They observed an increase in reactivity of the unleached straw chars between 700 – 1000 °C, followed by a decrease at higher temperatures, whilst chars formed from leached straw showed a continuous decrease in reactivity with increasing HTT. However, the leaching process influences the formation of the char during pyrolysis and this could affect the combustion of the material.

Within this study, following leaching the nature of the underlying carbonaceous material appears to have the greatest influence on the oxidation process. As the initial pyrolysis temperature increases there is a decrease in the O/C and H/C ratios (Figure 4.13) with a suggested corresponding increase in the aromatic structure (Figure 4.15), increasing the oxidative activation energy and therefore  $T_{max}$ , supporting the process described by earlier researchers. However, prior to leaching a different process appears to be occurring. Catalytic oxidation appears to shift the maximum decomposition to lower and similar temperatures independent of the HTT. However, at lower HTTs two pathways of decomposition are apparent. As the pyrolysis temperatures is increased, specifically above 600 °C, char combustion is more homogeneous and decomposition appears to occur via a single route. This could either be due to increasing homogeneity of the carbon structure or to better dispersion of the catalytic species.

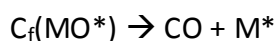
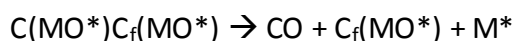
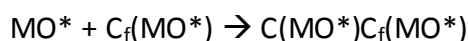
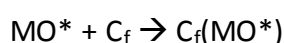
During char oxidation mechanisms in the literature suggest that an oxygen atom from a gaseous molecule is transferred to a free carbon site ( $C_f$ ) to form a carbon-oxygen complex, followed by release of a carbon-containing species from the surface ( $CO$ ,  $CO_2$ ).<sup>75</sup>

Catalysis of this process has been found to occur, with the most important catalysts for char and carbon oxidation suggested to be alkali and alkaline earth metals.<sup>75</sup> The catalytic effect of the alkali metals has been found to increase in the order  $\text{Li} < \text{Na} < \text{K} < \text{Rb} < \text{Cs}$  for both char gasification and combustion.<sup>76, 77</sup> This order is suggested to be due to the propensity of the smaller cations to form carbonate crystals, reducing their dispersion, or due to their varying influence on the weakening of carbon-carbon bonds.<sup>75, 76</sup> The anionic species also appears to have an impact, with lower catalytic activities observed for sulfate and chloride salts.<sup>75</sup>

The majority of mechanistic studies for the effect of alkali metal catalysts on chars have studied coal gasification. Many types of intermediates have been proposed as the catalytically active species and several mechanisms suggested. A generally postulated mechanism is that of a redox reaction.<sup>76</sup> An alkali-metal oxide transfers oxygen to  $\text{C}_f$  to form the C-O complex. This is released by the breaking of C-C bonds. Moulijn *et al* suggested that K-phenolate type structures forming at the zig-zag edges of aromatic laminar layers would increase the electron-density of the bridging carbon atom, increasing its probable oxidation and thereby weakening the neighbouring C-C bonds.<sup>75</sup> However, the increased reactivity at higher potassium loadings suggested a cluster model was more appropriate than individual phenolate groups.<sup>76</sup> Chen *et al* suggested the following reaction mechanism for gasification with  $\text{CO}_2$ :<sup>76</sup>



Diffusion of  $\text{MO}^*$



Where  $\text{M}^*$  is a metal oxide cluster and  $\text{C}_f(\text{MO}^*)$  and  $\text{C}(\text{MO}^*)\text{C}_f(\text{MO}^*)$  represent two different carbon-oxygen complexes as shown in Figure 4.22.

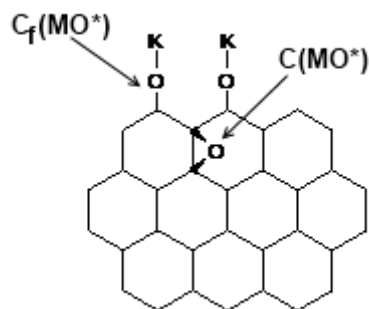


Figure 4.22: Carbon-oxygen complexes suggested to be formed during the catalytic decomposition of graphite (based on Ref 77)

For char oxidation a similar oxygen-transfer mechanism has been postulated.<sup>77</sup> All of these mechanisms require the decomposition of the alkali metal species to a metal oxide.  $K_2O$ ,  $KO_2$ ,  $K_2O_2$  and  $KOH$  have all been suggested as potential catalytic species.<sup>32, 78</sup> Neef *et al* added  $M_2CO_3$  ( $M = Li, Na, K, Cs$ ) to carbon black and studied the oxidation isothermally.<sup>77</sup> They found that catalytic oxidation occurred at temperatures as low as 280 °C with the reaction rate increasing with time, suggesting the slow formation of the catalytic species. Intimate contact between the carbon surface and alkali metal salt were vital for the observed catalytic effect at these temperatures. Where there was poor contact, higher temperatures were required for combustion of the material, and it was suggested that mobility of the catalyst was necessary to increase catalytic activity.<sup>77</sup> They concluded that the catalytic activity of  $K_2CO_3$  requires decomposition which can only occur when it is in close contact with the carbon surface.<sup>77</sup> However, the actual mechanism by which the catalytic species are formed within the char at low combustion temperatures does not appear to be completely understood.

In this study, the catalytic activity is therefore expected to be related to the high content of potassium in the initial chars, which is reduced upon leaching. At low HTT the chars may contain potassium carboxylate or phenolate species (as suggested from the IR spectra) which may catalyse the decomposition of the material under oxidative conditions. However, the lack of complete dispersion of the catalytic species is suggested to result in the uncatalysed decomposition of some of the char at higher temperatures. With higher HTTs, prior to leaching, the catalytic species is likely to be more uniformly distributed. At pyrolysis temperatures of between 600 – 800 °C the Tamman

temperatures (0.3 – 0.5 times the melting point) of KCl,  $K_2CO_3$  and  $K_2SO_4$  are all reached resulting in increased mobility of the species and therefore increased dispersion.<sup>57</sup> In addition, the carbon structure is more carbonaceous and uniform as indicated by the IR and CHN data. If  $K_2CO_3$  does decompose to  $K_2O$  during the pyrolysis process it may react with  $CO_2$  in the air to form  $K_2CO_3$  or with moisture to form KOH on cooling. The onset of decomposition of graphite covered in co-adsorbed atomic K and  $CO_2$  occurred around 375 °C when reacted with  $O_2$  or  $H_2O$ .<sup>78</sup> This reaction may occur at a lower temperature in the biomass chars due to incomplete graphitisation of the sample creating a higher number of surface defect sites. It may also be due to intimate contact between the biomass chars and the catalytic species. Therefore surface potassium oxide clusters may form catalysing the decomposition of the pyrolysis chars which cannot be formed following leaching of the chars. Much more research would be required to explore further the underlying mechanism occurring in the biomass chars with varying HTT before leaching; however, this is beyond the scope of this study. However, it suggests that by leaching the pyrolysis char formed at different temperatures the nature of the carbonaceous material can be tuned.

#### **4.5 Extraction at higher temperatures and with added alkali**

The optimum extraction of silica from chars using water under ambient conditions occurred after pyrolysis for 2 h at 500 °C. The extraction of chars formed at these conditions under reflux in water and using a KOH extractant were therefore also studied. A comparison of the extraction of silica from the pyrolysis chars and combustion ashes is shown in Figure 4.23. The pyrolysis chars continue to display a greater silica extraction compared to the ashes under reflux conditions. This can again be allied to the high alkalinity of the chars and separation of potassium and silica species in the chars preventing alkali silicate formation. However, using a hydroxide solution gave almost identical silica extraction for both the ashes and chars, possibly indicating that this is the maximum amount of silica that can be removed from the wheat straw under all conditions. There was no alteration in the removal of other elements, including Cl,  $NO_3^-$ ,  $SO_4^{2-}$  and  $PO_4^{3-}$ , with changing extraction conditions.

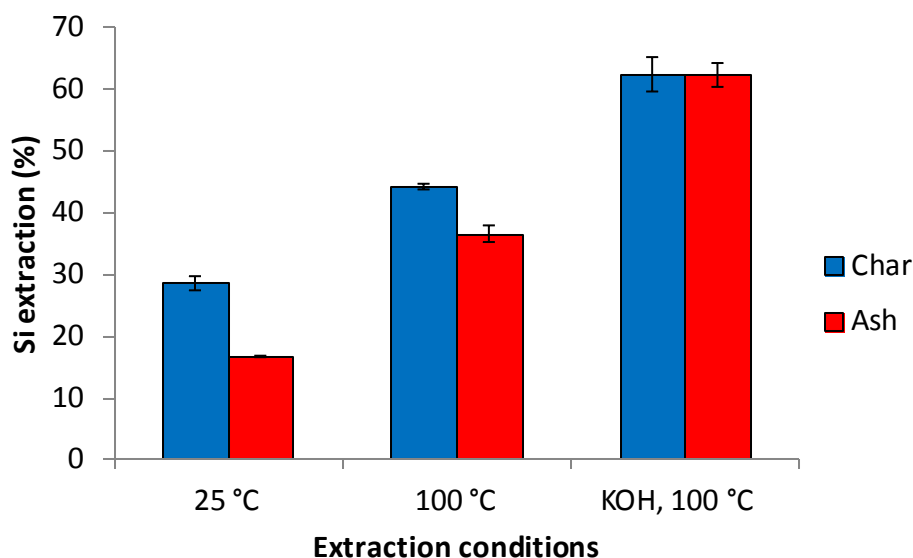


**Figure 4.23: Percentage Si removed from pyrolysis chars and combustion ashes formed at 500 °C after 2 h under different extraction conditions. Based on AAS analysis of extract (Originally in colour)**

#### **4.6 Conclusions and Further Work**

The pyrolysis chars demonstrated a very different relationship between the heat treatment temperature and the leaching of various inorganic elements in comparison to the combustion ashes formed. The extraction of potassium and chloride ions from pyrolysis char is constant at all pyrolysis temperatures between 400 – 800 °C, whilst the silica extraction varies extensively. This was related to the basicity of the char formed, with an increasingly alkaline char formed with increasing pyrolysis temperature and time up to 500 °C or 12 h at 400 °C. This was suggested to be due to a reduction in the O/C ratio reducing the number of acidic groups on the char surface, releasing basic potassium salts and decreasing the presence of acidic bio-oil residues within the char pores.

The maximum silica extraction utilising the inherent alkali was greater than from combustion ashes at both ambient and reflux conditions, indicating the possibility of using this method to form a potassium silicate solution from pyrolysis chars. Analysis of the solution indicated a total inorganic removal of 45 – 50%, whilst char analysis showed a reduction of 30%. The difference may be due to remaining inorganics on the surface of the char. The removal of inorganic species decreased the ash content (particularly the content of slag forming elements) thereby increasing the calorific value of the char, both beneficial for the combustion of the char.

The combustion characteristics were hugely altered by the removal of the inorganics from the char, despite the incomplete removal of alkali during leaching. The reactivity of all chars was relatively independent of the pyrolysis temperature prior to leaching. The decreasing reactivity of chars with higher HTT following leaching was related to the increasing aromaticity of the underlying char structure. Catalytic oxidation of the chars before leaching is potentially due to the formation of surface alkali oxide clusters which participate in an oxygen transfer decomposition mechanism. Chars formed at low HTT appear to display two different char oxidation mechanisms. Higher temperature HTT chars show only a single catalysed char oxidation mechanism, possibly due to the greater dispersion of alkali metal salts on the char surface. Further research is required to understand the mechanistic details and specifically the catalytic species involved in char oxidation.

These results indicate that wheat straw pyrolysis followed by char leaching is highly promising for the recycling of inorganic species and for the formation of an improved material for combustion. The chars demonstrate improved extractability of silica utilising the inherent alkalinity, making them more suitable for direct potassium silicate production than the combustion ashes. The leached chars have a lower ash content, lower potassium content, lower chloride content and higher calorific value making them more suitable for combustion, whilst chars produced at 500 °C do not show a significant drop in reactivity following leaching. Alternatively, the chars could be added to the soil for carbon sequestration. Bio-oil may also be produced as a beneficial side-product. Further work would be required to optimise the extraction for the required use and to demonstrate scalability.

#### **4.7 References for Chapter 4**

1. D. L. Klass, *Biomass for Renewable Energy, Fuels and Chemicals*, Academic Press, California, 1998.
2. A. Demirbas, *Energ. Source. Part A*, 2009, **31**, 1186 - 1193.
3. A. Demirbas, *Prog. Energy Combust. Sci.*, 2004, **30**, 219-230.
4. C. Atkinson, J. Fitzgerald and N. Hipps, *Plant Soil*, 2010, **337**, 1-18.
5. J. Lehmann, *Climatic Change*, 2009, **97**, 459-463.
6. F. Shafizadeh, *J. Anal. Appl. Pyrol.*, 1982, **3**, 283-305.
7. A. G. Liden, F. Berruti and D. S. Scott, *Chem. Eng. Commun.*, 1988, **65**, 207-221.

8. R. J. Evans and T. A. Milne, *Energ. Fuel.*, 1987, **1**, 123-137.
9. C. Di Blasi and C. Branca, *Ind. Eng. Chem. Res.*, 2000, **39**, 2169-2174.
10. K. Raveendran, A. Ganesh and K. C. Khilar, *Fuel*, 1995, **74**, 1812-1822.
11. D. J. Nowakowski and J. M. Jones, *J. Anal. Appl. Pyrol.*, 2008, **83**, 12-25.
12. S. Julien, E. Chornet, P. K. Tiwari and R. P. Overend, *J. Anal. Appl. Pyrol.*, 1991, **19**, 81-104.
13. P. R. Patwardhan, J. A. Satrio, R. C. Brown and B. H. Shanks, *Bioresour. Technol.*, 2010, **101**, 4646-4655.
14. D. J. Nowakowski, J. M. Jones, R. M. D. Brydson and A. B. Ross, *Fuel*, 2007, **86**, 2389-2402.
15. R. Fahmi, A. V. Bridgwater, L. I. Darvell, J. M. Jones, N. Yates, S. Thain and I. S. Donnison, *Fuel*, 2007, **86**, 1560-1569.
16. Q. Liu, S. R. Wang, Z. Y. Luo and K. F. Cen, *J. Chem. Eng. Jpn.*, 2008, **41**, 1133-1142.
17. P. A. Jensen, B. Sander and K. Dam-Johansen, *Biomass Bioenerg.*, 2001, **20**, 431-446.
18. P. A. Jensen, B. Sander and K. Dam-Johansen, *Biomass Bioenerg.*, 2001, **20**, 447-457.
19. C. Di Blasi, C. Branca and G. D'Errico, *Thermochim. Acta*, 2000, **364**, 133-142.
20. V. L. Budarin, J. H. Clark, B. A. Lanigan, P. Shuttleworth, S. W. Breeden, A. J. Wilson, D. J. Macquarrie, K. Milkowski, J. Jones, T. Bridgeman and A. Ross, *Bioresour. Technol.*, 2009, **100**, 6064-6068.
21. V. L. Budarin, J. H. Clark, B. A. Lanigan, P. Shuttleworth and D. J. Macquarrie, *Bioresour. Technol.*, 2010, **101**, 3776-3779.
22. V. L. Budarin, P. S. Shuttleworth, J. R. Dodson, A. J. Hunt, B. Lanigan, R. Marriott, K. J. Milkowski, A. J. Wilson, S. W. Breeden, J. Fan, E. H. K. Sin and J. H. Clark, *Energ. Environ. Sci.*, 2010, **4**, 471-479.
23. D. Vamvuka, S. Troulinos and E. Kastanaki, *Fuel*, 2006, **85**, 1763-1771.
24. J. N. Knudsen, P. A. Jensen and K. Dam-Johansen, *Energ. Fuel.*, 2004, **18**, 1385-1399.
25. M. Yamato, Y. Okimori, I. F. Wibowo, S. Anshori and M. Ogawa, *Soil Sci. Plant Nutr.*, 2006, **52**, 489-495.
26. P. A. Jensen, F. J. Frandsen, K. Dam-Johansen and B. Sander, *Energ. Fuel.*, 2000, **14**, 1280-1285.
27. D. C. Dayton, R. J. French and T. A. Milne, *Energ. Fuel.*, 1995, **9**, 855-865.
28. M. Zevenhoven-Onderwater, J. P. Blomquist, B. J. Skrifvars, R. Backman and M. Hupa, *Fuel*, 2000, **79**, 1353-1361.
29. R. K. Iler, *The Chemistry of Silica*, Wiley & Sons, New York, 1979.
30. S. Arvelakis, P. A. Jensen and M. Dam-Johansen, *Energ. Fuel.*, 2004, **18**, 1066-1076.
31. E. Bjorkman and B. Stromberg, *Energ. Fuel.*, 1997, **11**, 1026-1032.
32. A. Zolin, A. Jensen, P. A. Jensen, F. Frandsen and K. Dam-Johansen, *Energ. Fuel.*, 2001, **15**, 1110-1122.
33. J. N. Knudsen, P. A. Jensen, W. G. Lin, F. J. Frandsen and K. Dam-Johansen, *Energ. Fuel.*, 2004, **18**, 810-819.
34. R. C. Weast and M. J. Astle, *Handbook of Chemistry & Physics*, 63rd edn., CRC Press, Florida, 1982.
35. L. T. Zhuravlev, *Colloid. Surface. A*, 2000, **173**, 1-38.

36. A. M. Venezia, V. La Parola, A. Longo and A. Martorana, *J. Solid State Chem.*, 2001, **161**, 373-378.
37. D. W. McKee, *Fuel*, 1980, **59**, 308-314.
38. T. Ganga Devi and M. P. Kannan, *Fuel*, 1998, **77**, 1825-1830.
39. T. G. Devi and M. P. Kannan, *Energ. Fuel.*, 2007, **21**, 596-601.
40. A. Novaković, S. C. van Lith, F. J. Frandsen, P. A. Jensen and L. B. Holgersen, *Energ. Fuel.*, 2009, **23**, 3423-3428.
41. M. K. Hossain, V. Strezov, K. Y. Chan, A. Ziolkowski and P. F. Nelson, *J. Environ. Manage.*, 2011, **92**, 223-228.
42. A. Mukherjee, A. R. Zimmerman and W. Harris, *Geoderma*, **163**, 247-255.
43. C.-H. Cheng and J. Lehmann, *Chemosphere*, 2009, **75**, 1021-1027.
44. A. Silber, I. Levkovitch and E. R. Graber, *Environ. Sci. Technol.*, 2010, **44**, 9318-9323.
45. D. A. Laird, *Agron. J.*, 2008, **100**, 178-181.
46. C. A. Mullen, A. A. Boateng, N. M. Goldberg, I. M. Lima, D. A. Laird and K. B. Hicks, *Biomass Bioenerg.*, 2010, **34**, 67-74.
47. C. J. Mulligan, L. Strezov and V. Strezov, *Energ. Fuel.*, 2009, **24**, 46-52.
48. J. E. Amonette and S. Joseph, in *Biochar for Environmental Management*, eds. J. Lehmann and S. Joseph, Earthscan, London, Editon edn., 2009, pp. 33-52.
49. A. C. Lua and T. Yang, *J. Colloid Interf. Sci.*, 2004, **276**, 364-372.
50. W. M. A. W. Daud, W. S. W. Ali and M. Z. Sulaiman, *J. Chem. Technol. Biot.*, 2001, **76**, 1281-1285.
51. M. Keiluweit, P. S. Nico, M. G. Johnson and M. Kleber, *Environ. Sci. Technol.*, 2010, **44**, 1247-1253.
52. C. M. Preston and M. W. I. Schmidt, *Biogeosciences*, 2006, **3**, 397-420.
53. B. T. Nguyen and J. Lehmann, *Org. Geochem.*, 2009, **40**, 846-853.
54. E. S. Krull, J. A. Baldock, J. O. Skjemstad and R. J. Smernik, in *Biochar for Environmental Management*, eds. J. Lehmann and S. Joseph, Earthscan, London, Editon edn., 2009, pp. 53-65.
55. C. E. Brewer, K. Schmidt-Rohr, J. A. Satrio and R. C. Brown, *Environ. Prog. Sus. Energ.*, 2009, **28**, 386-396.
56. D. W. Rutherford, R. L. Wershaw and J. B. Reeves III, *Development of Acid Funtional Groups and Lactones During the Thermal Degradation of Wood and Wood Components*, US Geological Survey, Virginia, 2008.
57. T. G. Devi, M. P. Kannan and V. P. Abduraheem, *Fuel Process. Technol.*, 2010, **91**, 1826-1831.
58. C.-H. Cheng, J. Lehmann and M. H. Engelhard, *Geochim. Cosmochim. Ac.*, 2008, **72**, 1598-1610.
59. T. Lang, A. D. Jensen and P. A. Jensen, *Energ. Fuel.*, 2005, **19**, 1631-1643.
60. F. X. Yao, M. C. Arbestain, S. Virgel, F. Blanco, J. Arostegui, J. A. Maciá-Agulló and F. Macías, *Chemosphere*, 2010, **80**, 724-732.
61. A. Pettersson, L.-E. Åmand and B.-M. Steenari, *Biomass Bioenerg.*, 2008, **32**, 224-235.
62. K. Yin Chan and Z. Xu, in *Biochar for Environmental Management*, eds. J. Lehmann and S. Joseph, Earthscan, London, Editon edn., 2009, pp. 67-84.
63. P. Mellbo, S. Sarenbo, O. Stålnacke and T. Claesson, *Waste Manage.*, 2008, **28**, 2235-2244.

64. Z. Wu, R. P. Rodgers and A. G. Marshall, *Anal. Chem.*, 2004, **76**, 2511-2516.
65. A. K. Kercher and D. C. Nagle, *Carbon*, 2003, **41**, 15-27.
66. S. Soares, N. M. P. S. Ricardo, S. Jones and F. Heatley, *Eur. Polym. J.*, 2001, **37**, 737-745.
67. D. de Britto and O. B. G. Assis, *Thermochim. Acta*, 2009, **494**, 115-122.
68. R. A. Friedel and G. L. Carlson, *J. Phys. Chem.*, 1971, **75**, 1149-1151.
69. W. W. Wright, M. Laberge and J. M. Vanderkooi, *Biochemistry-US*, 1997, **36**, 14724-14732.
70. R. K. Sharma, J. B. Wooten, V. L. Baliga, P. A. Martoglio-Smith and M. R. Hajaligol, *J. Agr. Food Chem.*, 2002, **50**, 771-783.
71. A. Barneto, J. Carmona, J. E. Alfonso and L. Alcaide, *Bioresour. Technol.*, 2009, **100**, 3963-3973.
72. E. Lopez-Capel, S. P. Sohi, J. L. Gaunt and D. A. C. Manning, *Soil Sci. Soc. Am. J.*, 2005, **69**, 136-140.
73. T. G. Devi and M. P. Kannan, *Energ. Fuel.*, 1999, **14**, 127-130.
74. Y. Huang, X. Yin, C. Wu, C. Wang, J. Xie, Z. Zhou, L. Ma and H. Li, *Biotechnol. Adv.*, 2009, **27**, 568-572.
75. J. A. Moulijn and F. Kapteijn, *Carbon*, 1995, **33**, 1155-1165.
76. S. G. Chen and R. T. Yang, *Energ. Fuel.*, 1997, **11**, 421-427.
77. J. P. A. Neeft, M. Makkee and J. A. Moulijn, *Fuel*, 1998, **77**, 111-119.
78. P. Sjövall and B. Kasemo, *Surf. Sci.*, 1993, **290**, 55-68.

# **Chapter 5:**

## **Biosilicate formation and binder application using power station combustion residues**



## **5.1 Chapter 5 - Summary**

Ashes were collected from two commercial biomass combustion facilities burning miscanthus and wood chips. The starting materials from these facilities were analysed on a lab-scale to compare their combustion and extraction characteristics to those of the wheat straws analysed in Chapters 2-4. The combustion ashes were further characterised and the extraction of silica from the miscanthus bottom ash was studied using both potassium hydroxide and concentrated fly ash solutions. The alkali silicate solutions formed were tested as binders for wheat straw particleboards.

## **5.2 Power station ashes**

To scale-up the extraction and utilisation of inorganic species from combustion residues, and transfer knowledge gained at a lab-scale, several ashes were collected from two biomass power stations.

Ely Power Station, at 38 MW, is the largest straw burning power station in the world, with a total fuel demand of 200,000 tonnes per annum. The main fuel is wheat straw with additional utilisation of miscanthus and oil seed rape as required. At the time of collection Ely Power Station was burning miscanthus straw. Around 3000 tonnes pa of fly ash is produced and approximately 10,000 tonnes pa of bottom ash is formed. The materials collected were (Figure 5.1):

- a. Bottom ash, quenched in water (Ely-BA1)
- b. Fly ash (Ely-FA1)

Eccleshall is a 2 MW power station mainly using clean wood chip from forestry and arboriculture arisings along with an additional feed of miscanthus. 5 tonnes of bottom ash is produced a day and 300 kg of fly ash, with an annual production of 500-700 tonnes and 100 tonnes respectively. The materials collected were (Figure 5.1):

- a. Bottom ash, quenched in water (Ecc-BA1)
- b. Fly ash (Ecc-FA1)
- c. Starting materials of Wood Chip (WC) and Miscanthus (Mis)

The starting fuels were initially analysed to compare their extraction trends to those of the wheat straw previously studied. The ashes were then tested to study their suitability for the formation of biosilicate solutions as binders for inorganic composite boards.

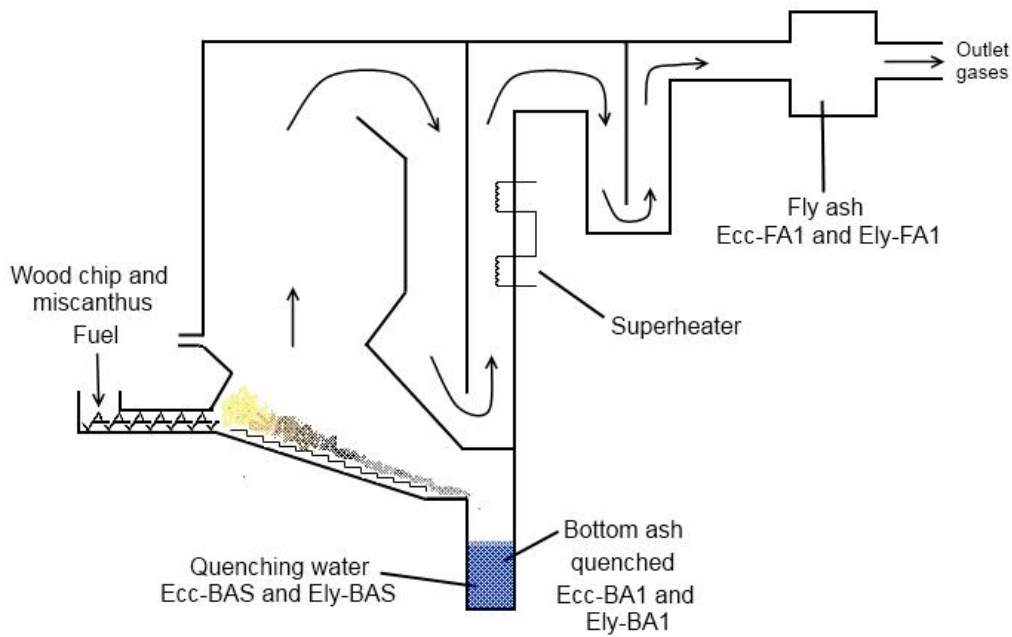


**Figure 5.1: Basic layout and collection points of material from power stations burning wood chip and miscanthus biomass (Originally in colour)**

### 5.3 Fuel analysis

The wood chip and miscanthus fuels that were collected from Eccleshall power station had a high moisture content and were therefore air dried before a full analysis was undertaken. The proximate and ultimate analyses of the fuels are shown in Table 5.1. Where the analysis was undertaken in duplicate or triplicate the average is shown, along with the standard deviation.

The ash (dry basis) content is similar for both fuels, and similar to those observed for wheat straw (Chapter 2). Generally, wood is observed to have a lower ash content than herbaceous biomass,<sup>1-3</sup> however, a large percentage of the woody material combusted at the Eccleshall plant consists of arboriculture arisings. These are the clippings from the management of municipal parks and verges and therefore contain a high content of fast growing biomass, particularly leaves, which generally have a higher concentration of nutrients.<sup>4,5-7</sup>

**Table 5.1: Fuel analysis of wood chip and miscanthus fuels**

	<b>Wood Chips</b>	<b>Miscanthus</b>
<b>Moisture (%)<sup>a</sup></b>	33.2 ± 0.9	22.6 ± 2.0
<b>Moisture (%)<sup>b</sup></b>	9.8 ± 0.2	7.4 ± 0.1
<b>Volatile matter (%)<sup>db</sup></b>	80.0	67.0
<b>Fixed carbon (%)<sup>db</sup></b>	15.3	28.5
<b>Ash (%)<sup>db</sup></b>	4.7 ± 0.1	4.5 ± 0.5
<b>C (%)<sup>db</sup></b>	50.0 ± 0.3	48.8 ± 0.2
<b>H (%)<sup>db</sup></b>	5.14 ± 0.1	5.28 ± 0.2
<b>N (%)<sup>db</sup></b>	0.26 ± 0.1	0.56 ± 0.1
<b>O (%)<sup>db</sup></b>	39.8 ± 0.7	40.9 ± 0.3
<b>HHV (MJ/kg)<sup>db</sup></b>	19.5 ± 0.2	17.1 ± 0.1
<b>Ash (%)</b>		
<b>Na<sub>2</sub>O</b>	1.22	0.98
<b>MgO</b>	2.79	3.14
<b>Al<sub>2</sub>O<sub>3</sub></b>	3.98	0.82
<b>SiO<sub>2</sub></b>	28.0	45.4
<b>P<sub>2</sub>O<sub>5</sub></b>	3.74	3.52
<b>SO<sub>3</sub></b>	0.42	0.50
<b>K<sub>2</sub>O</b>	9.61	24.9
<b>CaO</b>	31.4	8.28
<b>TiO<sub>2</sub></b>	0.24	0.06
<b>V<sub>2</sub>O<sub>5</sub></b>	0.01	0.00
<b>Cr<sub>2</sub>O<sub>3</sub></b>	0.02	0.08
<b>Mn<sub>3</sub>O<sub>4</sub></b>	0.16	0.28
<b>Fe<sub>2</sub>O<sub>3</sub></b>	4.25	1.44
<b>ZnO</b>	0.09	0.08
<b>SrO</b>	0.09	0.02
<b>Y<sub>2</sub>O<sub>3</sub></b>	0.00	0.00
<b>ZrO<sub>2</sub></b>	0.00	0.00
<b>BaO</b>	0.06	0.04
<b>Cl</b>	3.1	6.3
<b>Loss on Ignition</b>	10.8	4.2

a = as received

b = air dried

db = dry basis

The carbon content and calorific value of the wood chips are slightly higher than miscanthus, whilst the oxygen content is slightly lower. Generally woody biomass contains more lignin and less hemicellulose than grasses,<sup>8</sup> which could therefore account for the observed differences in the C and O content. A higher heating value is directly correlated to lower O/C ratios.<sup>9</sup>

The inorganic composition of the ash varies significantly between the two materials. The miscanthus ash has a similar distribution to that of wheat straw with higher K<sub>2</sub>O (24.9%),

SiO<sub>2</sub> (45.4%) and Cl (6.3%) contents and lower amounts of CaO (8.9%) and other elements, based on their oxide content. In contrast, the species with the highest concentration in the wood chip ash is CaO (31.4%), followed by SiO<sub>2</sub> (28.0%) and then K<sub>2</sub>O (9.6%). The chlorine content is low (3.1%), although not insignificant. The aluminium and iron content in the wood chip ash is also high. This may be due to contamination of the fuel during its collection from homes and businesses.<sup>10</sup> Indeed, a magnetic portion was found within the ashes. Similar variations of C, H, N content and ash composition have been noticed previously between wood pellets and straw.<sup>1, 2, 10</sup> The variation in the inorganic species between the fuels could significantly impact on the formation of ashes under combustion conditions and consequently their use.

#### 5.4 Combustion-extraction trends

The miscanthus (Mis) and wood chip (WC) fuels were combusted at temperatures between 400 – 800 °C for 2 h, as this had previously been observed to ensure complete combustion of wheat straw fuels (Chapter 2). The ashes were then quenched in water, leached for 24 h at room temperature and the filtrates were analysed for dissolved species (Table 5.1, Figure 5.2, Figure 5.3).

**Table 5.2: Levels of extraction of Si, K, Ca and Cl from miscanthus and wood chip ash**

Name	Combustion temperature (°C)	Initial pH	Final pH	Si (%)	K (%)	Ca (%)	Cl (%)
Mis-400-2	400	12.2	11.3	38.3 ± 1.3	72.5 ± 3.5	0.0	37.0
Mis-500-2	500	12.1	11.3	26.6 ± 1.7	63.5 ± 3.7		
Mis-600-2	600	12.2	12.3	10.4 ± 1.2	55.5 ± 3.4	0.0	40.9
Mis-700-2	700	12.0	12.2	0.3 ± 0.3	19.0 ± 1.3		
Mis-800-2	800	11.8	11.9	0.9 ± 0.1	10.2 ± 0.7	2.0 ± 0.1	40.7
WC-400-2	400	11.9	12.2	1.9 ± 0.03	96.3 ± 6.3	0.0	5.8
WC-500-2	500	11.5	11.9	1.4 ± 0.1	78.4 ± 4.0		
WC-600-2	600	12.7	12.8	0.5 ± 0.3	59.8 ± 3.9	13.2 ± 1.0	5.7
WC-700-2	700	12.4	12.5	0.2 ± 0.3	29.1 ± 2.7		
WC-800-2	800	12.7	12.7	0.5 ± 0.2	9.3 ± 1.1	15.7 ± 0.5	5.7

There is a stark contrast in the extraction trends for the main inorganic species from miscanthus (Figure 5.2) and wood chip (Figure 5.3) ashes. At 400 °C both ashes display initial high levels of dissolution of potassium (Table 5.2), with that of the wood chips nearing 100%. The potassium extraction of the wood chips decreases almost linearly with

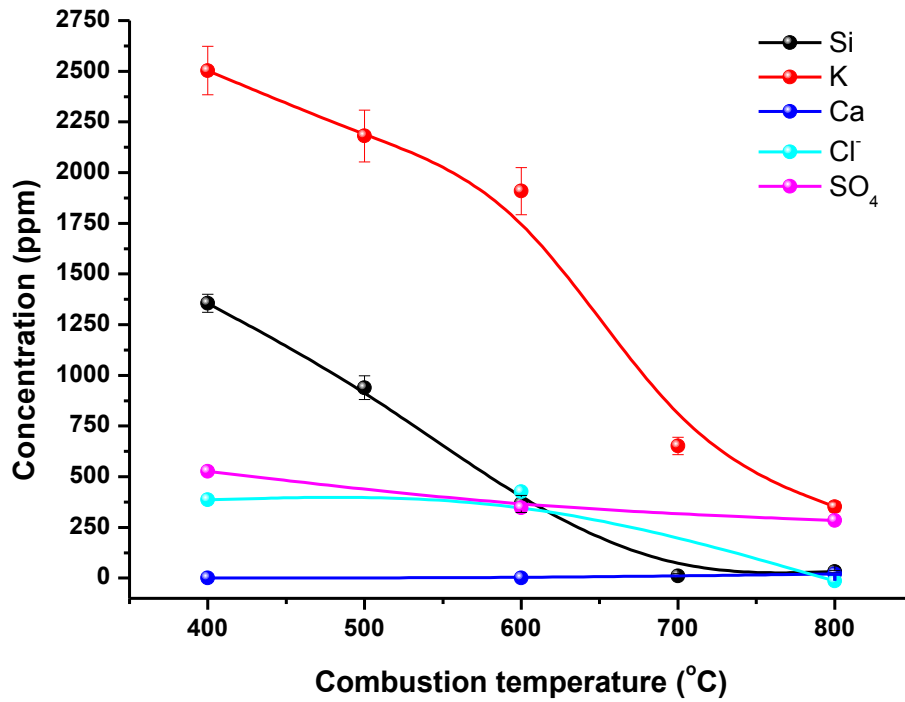


Figure 5.2: Concentration of various elements in extracts of miscanthus ash formed at different combustion temperatures (Originally in colour)

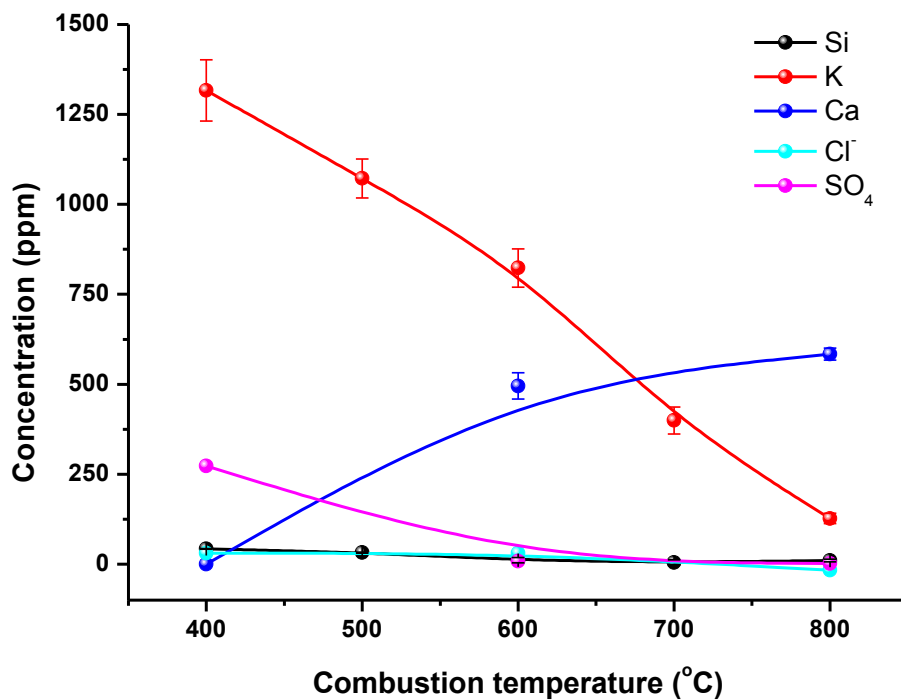


Figure 5.3: Concentration of various elements in extracts of wood chip ash formed at different combustion temperatures (Originally in colour)

increasing combustion temperature, whilst the potassium extraction only reduces significantly above 600 °C for the miscanthus ash. Chloride and sulfate extraction levels decrease at higher combustion temperatures from the miscanthus ash. Chloride extraction is very low from the wood chips, whilst sulfate extraction decreases above 400 °C. The silica and calcium extraction trends display the most obvious contrast between the two biomass materials. The maximum silica extraction from the miscanthus ashes is 38% at 400 °C and decreases with increasing combustion temperature, following the same trend observed for wheat straw ashes. Minor calcium concentrations in the filtrate only become apparent at a combustion temperature of 800 °C. In contrast, the maximum silica extraction from the wood chip ashes is only 1.9%, remaining low at all combustion temperatures, whilst the calcium concentration is significant at 600 °C (13.2%) and increases with increasing combustion temperature.

These extraction trends demonstrate that the inorganic material within miscanthus and wood chips behave very differently during combustion. Very low levels of silica are solubilised, even at low temperatures of combustion, from the wood chip ash despite a sufficiently high alkalinity within the solutions formed. This is highlighted by the difference in solution pH at the beginning and end of the extractions for the two materials at 400 °C (Table 5.2). The decrease in pH following extraction for miscanthus is compatible with the results obtained for wheat straw, where the dissolution of silica causes a lowering of the pH. In comparison, for wood chip ash, the pH increases during extraction and with higher combustion temperatures, which correlated with the increasing levels of calcium dissolved.

XRD analysis of the species present within the ashes further emphasises the differences between the materials (Figure 5.4 and 5.5). Miscanthus ashes have a similar speciation to wheat straw ashes. The main species present at 400 °C are KCl and CaCO<sub>3</sub>. A decrease in CaCO<sub>3</sub> content occurs at 600 °C coinciding with a reduction in silica extraction. The KCl content reduces at 800 °C suggesting that volatilisation is occurring, which is consistent with the reduced concentration detection in the solutions formed at these combustion temperatures. K<sub>2</sub>SO<sub>4</sub> is observed at all combustion temperatures. The wood chip ash formed at 400 °C contains a much lower level of KCl, a higher proportion of CaCO<sub>3</sub> and quartz and a high content of fairchildite (K<sub>2</sub>Ca(CO<sub>3</sub>)<sub>2</sub>). The high level of quartz observed in all of the ashes could be due to contamination of the fuel. As the combustion

temperature increases a decrease in the concentration of quartz and  $\text{CaCO}_3$  occurs, combined with the formation of calcium silicate and portlandite ( $\text{Ca}(\text{OH})_2$ ), which was not detected in either the wheat straw or miscanthus ashes. In addition, the diffractograms of the wood chip ashes have a much flatter baseline. The content of amorphous material in a sample can be semi-quantitatively calculated from the area of the amorphous halo in an XRD pattern.<sup>11</sup> This therefore indicates that the wood ash is much more crystalline than the miscanthus and wheat straw ashes. The low solubility of silica from wood chip ashes is therefore suggested to be due to the lack of amorphous silica and the formation of insoluble calcium silicate at higher combustion temperatures.

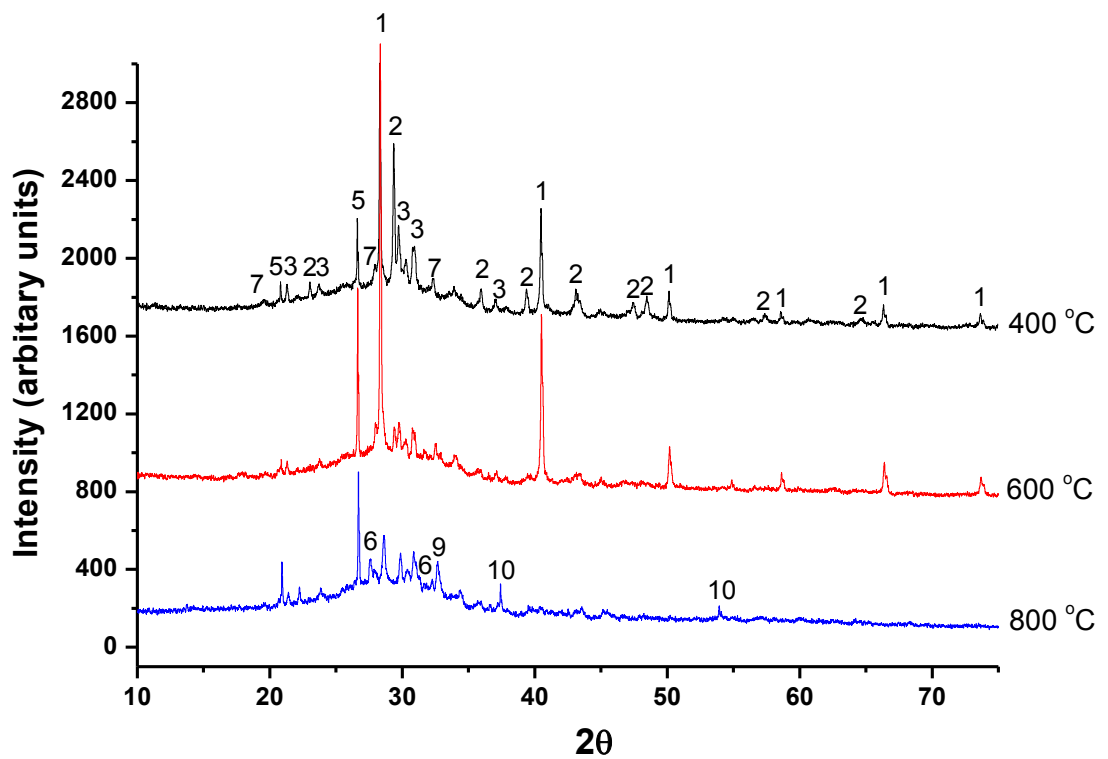


**Figure 5.4: Diffractograms of miscanthus ashes formed at different combustion temperatures: 1 = Sylvite ( $\text{KCl}$ ); 2 = Calcite ( $\text{CaCO}_3$ ); 3 = Arcanite ( $\text{K}_2\text{SO}_4$ ); 5 = Quartz ( $\text{SiO}_2$ ); 6 = Calcium silicate ( $\text{CaSiO}_3$ ); 7 = Fairchildite ( $\text{K}_2\text{Ca}(\text{CO}_3)_2$ ); 9 = Calcium silicate ( $\text{Ca}_2(\text{SiO}_4)$ ); 10 = Calcium oxide ( $\text{CaO}$ ) (Originally in colour)**

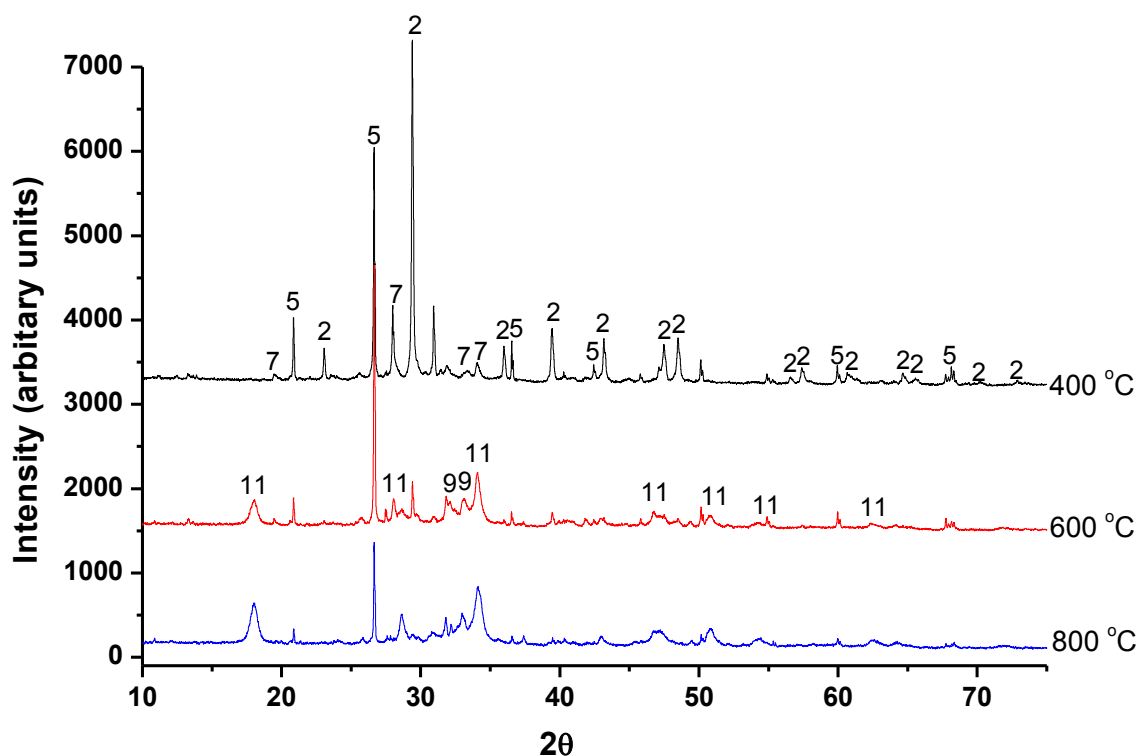


Figure 5.5: Diffractograms of wood chip ashes formed at different combustion temperatures: 2 = Calcite ( $\text{CaCO}_3$ ); 5 = Quartz ( $\text{SiO}_2$ ); 7 = Fairchildite ( $\text{K}_2\text{Ca}(\text{CO}_3)_2$ ); 9 = Calcium silicate ( $\text{Ca}_2(\text{SiO}_4)$ ); 11 = Portlandite ( $\text{Ca}(\text{OH})_2$ ) (Originally in colour)

## 5.5 Power station ashes

The data described above intimates that the bottom ashes collected from the two power stations will behave differently, particularly with respect to the extractability of the silica present within them. However, since the ashes obtained from both power stations had been formed under different conditions to those obtainable under laboratory conditions, and particularly since a separate fly ash fraction was acquired, all of the ashes collected were analysed further to gain information about their composition.

### 5.5.1 Mineral analysis of ashes

Both the fly ash and bottom ash from each power plant were analysed by XRF to determine their elemental composition (Table 5.3). As collected, the bottom ashes were wet from direct quenching in water. Visual observation of the bottom ashes showed the presence of mainly 1 – 2 cm pieces of fused aggregate. Before analysis the bottom ashes were dried and ground to  $<125 \mu\text{m}$  to ensure that a homogeneous sample was selected. The powder formed was dark grey in the case of Ely-BA1 and creamy-white for Ecc-BA1. The fly ashes were low in density, fine and dark.

**Table 5.3: Elemental composition of fly ash and bottom ashes from two biomass power plants analysed by XRF, all in wt%**

Compound	Ely-FA1	Ely-BA1	Ecc-FA1	Ecc-BA3
Na <sub>2</sub> O	2.45	0.16	2.24	1.18
MgO	1.02	2.82	2.55	2.69
Al <sub>2</sub> O <sub>3</sub>	0.19	0.76	3.13	6.54
SiO <sub>2</sub>	6.59	63.0	18.2	51.9
SO <sub>3</sub>	3.02	2.74	2.78	2.28
P <sub>2</sub> O <sub>5</sub>	18.3	4.37	7.80	1.45
K <sub>2</sub> O	32.0	14.6	23.3	8.70
CaO	16.8	8.28	17.7	18.7
TiO <sub>2</sub>	0.01	0.06	0.30	0.47
V <sub>2</sub> O <sub>5</sub>	0.00	0.00	0.01	0.01
Cr <sub>2</sub> O <sub>3</sub>	0.00	0.01	0.03	0.04
Mn <sub>3</sub> O <sub>4</sub>	0.05	0.14	0.26	0.30
Fe <sub>2</sub> O <sub>3</sub>	0.12	0.50	1.98	4.72
ZnO	0.08	0.02	1.17	0.04
SrO	0.03	0.02	0.06	0.13
Y <sub>2</sub> O <sub>3</sub>	0.00	0.00	0.00	0.00
ZrO <sub>2</sub>	0.00	0.00	0.01	0.01
BaO	0.02	0.06	0.08	0.34
CuO	0.01	0.02	0.05	0.15
SnO <sub>2</sub>		0.09	0.06	0.03
Cl	19.1	0.05	17.7	0.28
NiO	0.00			0.012
Br	0.53		0.12	
PbO	0.006		0.27	0.03
Rb <sub>2</sub> O	0.023		0.03	0.02
Nb <sub>2</sub> O <sub>5</sub>		0.038		
In <sub>2</sub> O <sub>3</sub>		0.031		
Sb <sub>2</sub> O <sub>3</sub>			0.03	
CdO			0.02	
Cr <sub>2</sub> O <sub>3</sub>			0.02	0.060
ZrO <sub>2</sub>			0.01	0.060
WO <sub>3</sub>				0.011
Co <sub>3</sub> O <sub>4</sub>				0.008
Sum	100.4	97.8	99.9	100.1

The main inorganic elements present in the power station ashes are silica, potassium, calcium and chlorine, as observed for the initial fuels. The data indicates that there is a fractionation of the elements between the fly ash and the bottom ash, dependent on the volatility of the elements. Potassium, chlorine, sulfur, sodium and phosphorous are enriched in the fly ash, whilst the majority of the silica is captured in the bottom ash.

Calcium is distributed between both ashes. A similar distribution of elements between fly ashes and bottom ashes has been detected in a power plant burning straw previously.<sup>10</sup>

XRD analyses of the mineral species present in each of the ashes show that both fly ashes are mainly composed of sylvite (KCl) (Figure 5.6 and 5.7). This has frequently been found to be the major phase in fly ashes from other power plants combusting both woody and herbaceous biofuels,<sup>1</sup> however, other researchers have also observed fly ashes to contain quartz.<sup>3</sup> Ely-BA1 (mainly miscanthus) (Figure 5.6) is primarily composed of cristobalite, whilst Ecc-BA1 (mainly wood chips) (Figure 5.7) is principally composed of quartz. The presence of these crystalline phases is consistent with the main elemental composition of each ash but is in contrast to the ashes formed from each starting material under lab-scale conditions up to 800 °C. In particular, purer silica phases are observed in each of the bottom ashes, similar to those observed for wheat straw ashes with low concentrations of alkali metals in the initial straw (Chapter 2). This suggests that both potassium and calcium are more easily volatilised and less likely to be captured in the bottom ashes under the power plant operating conditions. However, the highly crystalline silica content may affect its ease of solubilisation.<sup>12</sup>

Little data is available on the mineral composition of the bottom ashes of different biomass materials from commercial power plants, presumably due to commercially sensitive data, a lack of research into the utilisation of bottom ashes in comparison to the fly ashes and the current research focus on fluidised bed boilers. However, the data that is available indicates the main inorganic component to be SiO<sub>2</sub>, with minor quantities of K<sub>2</sub>O, CaO and Al<sub>2</sub>O<sub>3</sub>.<sup>13</sup>

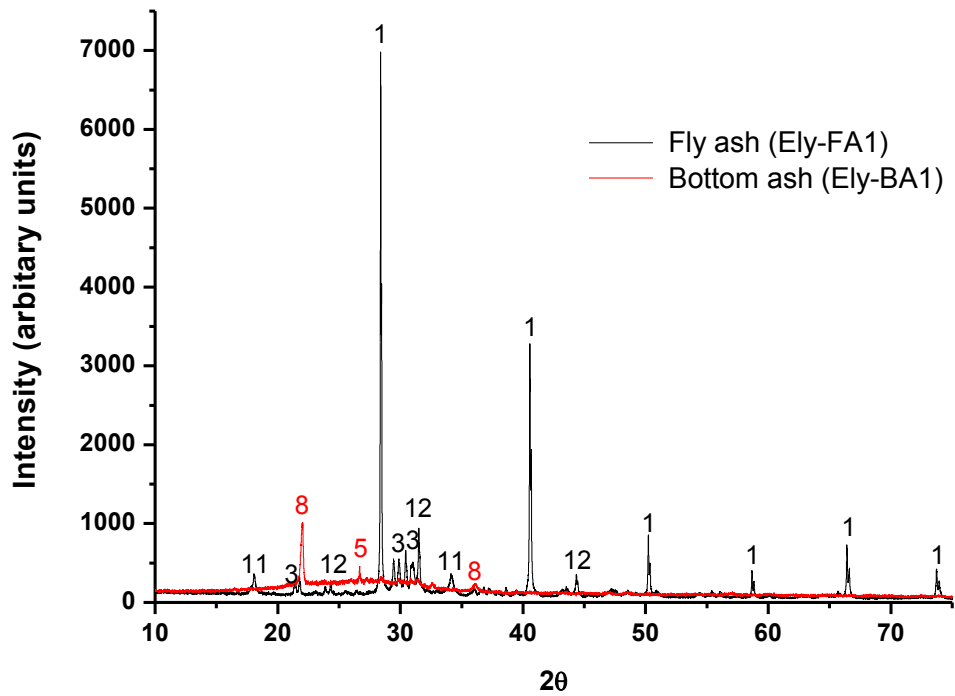


Figure 5.6: XRD of Ely-BA1 and Ely-FA1 - fly ash and bottom ash from a combustion facility primarily using miscanthus: 1 = Sylvite (KCl); 3 = Arcanite ( $K_2SO_4$ ); 8 = Cristobalite ( $SiO_2$ ); 11 = Portlandite ( $Ca(OH)_2$ ); 12 = Aphthitalite ( $K_3Na(SO_4)_2$ ) (Originally in colour)

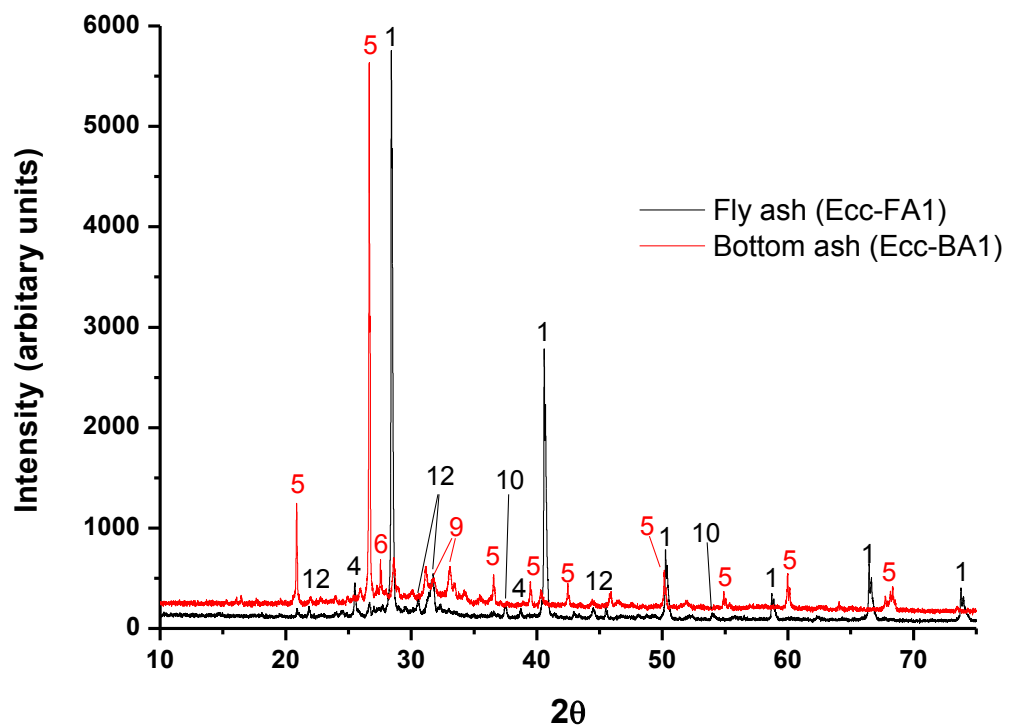
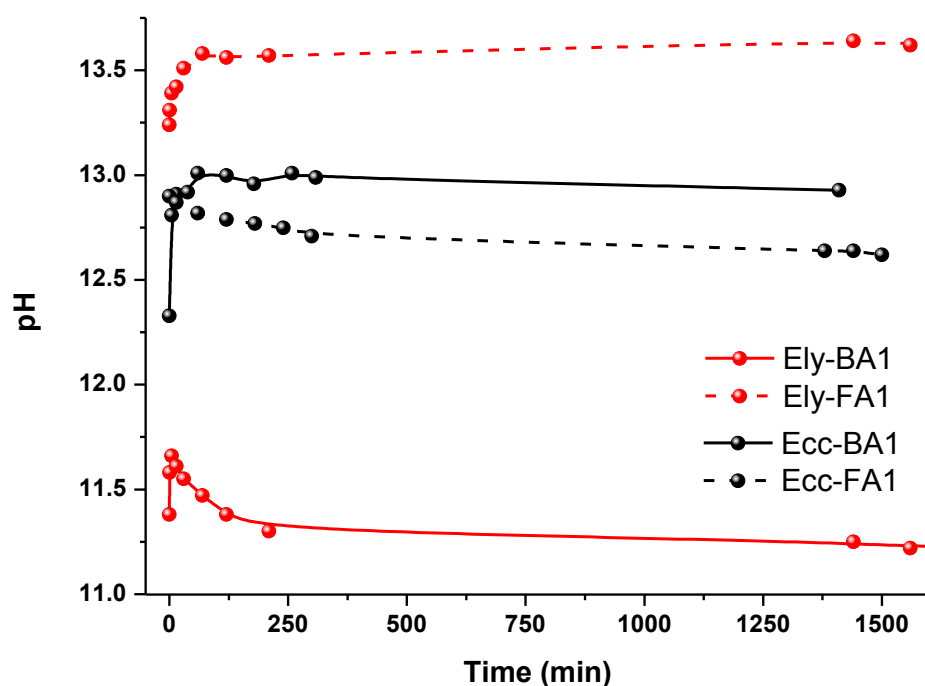


Figure 5.7: XRD of Ecc-BA1 and Ecc-FA1 - fly ash and bottom ash from a primarily wood chip combustion facility: 1 = Sylvite (KCl); 4 = Anhydrite ( $CaSO_4$ ); 5 = Quartz ( $SiO_2$ ); 9 = Calcium silicate ( $Ca_2(SiO_4)$ ); 10 = Calcium oxide (CaO); 12 = Aphthitalite ( $K_3Na(SO_4)_2$ ) (Originally in colour)

## 5.5.2 Chemical analysis of ashes

In order to study the potential alkalinity of the different ashes, the ashes were leached in water at a liquid:solid ratio of 3 over 24 h and the pH of the solution formed over time was measured (Figure 5.8). This illustrates a sizeable difference between both the fly ashes and bottom ashes from the two power stations burning different fuels. The elemental content of the solutions formed were also analysed by ICP-AES (Table 5.4). Analysis of potassium, silicon and sodium by AAS highlighted the same trends in concentrations, although gave slightly higher absolute values.



**Figure 5.8: pH of solutions during the leaching of power station bottom ashes and fly ashes with time (Originally in colour)**

All of the ashes display an instantaneously high pH upon addition of the ashes to water (13.2 for Ely-FA1 and 11.4 for Ely-BA1 within 30 s). Ely-FA1 has the highest initial pH which is followed by a slower increase up to a constant level of pH 13.6 after 70 min. This suggests an initial fast release of alkali species deposited on the surface of the ashes followed by a diffusion controlled release of species through the solid matrix as proposed for straw char.<sup>14</sup> The main element contributing to the alkalinity of the solution appears to be potassium with a minor input from sodium. Ely-BA1 has a much lower initial and final pH. It increases sharply within the first few minutes followed by a slow decrease indicating the neutralisation of some of the alkalinity. The presence of silica in the final

solution indicates that this may be causing the gradual reduction as observed for lab-scale ashes. However, this dissolution only represents 0.7% of the silica present within the ash.

In comparison the Ecc-BA1 shows a much slower increase in the pH of the solution with no decrease in the pH over time, whilst Ecc-FA1 reaches the maximum pH within the first minute followed by a slight decline over the following 24 h. Only a minute quantity of silica is dissolved from Ecc-BA1 in water. The minor amount of aluminium that is dissolved could be expected to neutralise some of the alkalinity, however, this does not appear to be the case. The reason for the slight decrease in alkalinity of the Ecc-FA1 with time is unknown. It could be due to some CO<sub>2</sub> from the atmosphere dissolving into the solution, however, this does not appear to have occurred for the other ashes studied under the same conditions.

The concentrations of the elements in the water solutions echo the concentrations in the starting ashes. Higher concentrations of potassium, chlorine, sulfur and sodium are found in the fly ash solutions compared to the bottom ash solutions. The low concentration of potassium in the bottom ash extracts suggests that it is more tightly bound within these ashes. Detectable levels of calcium are only found in the Ecc-FA1 solution indicating that the calcium species present in the ashes are also insoluble. The elemental analysis of the ashes indicated that the fly ashes were more suitable as fertilisers, having higher P and K levels. The water solubility analyses show that they do have a higher content of available potassium, however, the soluble phosphate levels are low. Chemical fractionation using ammonium acetate would show whether these are, however, available via ion exchange.<sup>1</sup>

Very low levels of other elements are observed in solution, many of them at or near the limit of detection. In particular, a major element of concern, cadmium is not detected in the solutions. Concentrations of other heavy metals including Cr, Zn, Ni, Pb and Cu are very low or were not detected.

This data indicates that the silica within the ashes is not solubilised directly using the inherent alkalinity of the ashes in water at room temperature. However, utilising the alkalinity of the fly ashes, particularly for the miscanthus ashes (Ely-FA1) could be a method to solubilise the greater content of silica in the bottom ashes.

**Table 5.4: Elemental composition of solutions formed from the water leaching of power station ashes. All concentrations in ppm.**

Element	Ely-FA1	Ely-BA1	Ecc-FA1	Ecc-BA3
Ag	nd	nd	nd	nd
Al	0.2	0.5	0.3	64.4
As	0.7	0.2	0.6	2.4
Au	nd	nd	nd	nd
B	2.9	0.2	1.7	1.0
Ba	0.0	0.0	0.1	nd
Be	nd	nd	nd	nd
Bi	nd	nd	nd	nd
Ca	6.4	1.8	52.9	5.2
Cd	nd	nd	nd	0.0
Co	0.0	nd	nd	nd
Cr	0.2	nd	0.1	0.1
Cu	0.1	nd	0.1	0.4
Fe	nd	nd	nd	nd
Hg	0.4	nd	0.0	1.3
K	12873	988	9922	560
La	0.0	nd	0.1	0.0
Li	0.2	nd	0.1	nd
Mg	0.1	1.0	nd	1.0
Mn	nd	nd	nd	nd
Mo	1.6	0.2	0.9	0.4
Na	1345	20.4	861	91.4
Ni	nd	nd	nd	0.2
P	0.5	6.8	0.1	0.8
Pb	nd	nd	0.1	nd
Pd	0.1	0.5	0.2	0.4
Pt	nd	nd	nd	nd
Rb	24.7	1.2	14.3	1.6
S	2757	248	2220	82
Sb	0.5	nd	nd	0.5
Sc	nd	nd	nd	nd
Se	nd	nd	nd	nd
Si	2.8	273.3	1.6	12.3
Si (AAS)	4.0	462.7	6.3	10.4
Sn	0.2	nd	0.2	2.4
Sr	0.1	0.0	0.2	0.1
Te	nd	nd	nd	nd
Ti	nd	nd	nd	nd
Tl	0.7	1.0	0.5	2.4
V	0.1	0.4	0.1	0.4
W	0.3	15.1	0.1	1.1
Zn	0.1	0.2	0.1	0.2
Cl	12038	80.8	7895	38.3
NO <sub>3</sub>	88.8	73.3	68.0	50.0

## 5.6 Silicate analysis development

Within this study there was a desire to produce a silicate solution similar in  $\text{SiO}_2$  and wt% to commercial silicate solutions from combustion residues, however, these are much more concentrated than the silicate solutions analysed in previous chapters from lab-scale ashes. The use of atomic absorption was therefore deemed unsuitable due to the high dilution errors inherent during the analysis. Commercial silicate solutions are normally analysed for solids content and  $\text{SiO}_2:\text{M}_2\text{O}$  content by measuring their density and alkali content by titration. However, this is also a time-consuming process and requires a large amount of solution. An alternative method was required that was quick and needed only a small quantity of solution to analyse the silica content.

It was noticed during some early work that the IR absorbance of the silicate bands ( $1250 - 650 \text{ cm}^{-1}$ ) increased in intensity with increasing concentration of the solution. This also gave further information about the nature of the silicate species within the solution and could be used with only a small drop on an ATR-IR, with analysis taking under a minute. It was therefore decided to test the hypothesis that the silica concentration could be analysed by studying the changing area of the silicate IR band. Several commercial silicate solutions were diluted to different concentrations (4, 8, 12, 16 and 32% of the original concentration) and analysed by ATR-IR. Solutions with both sodium and potassium counter-ions and of various molar ratios were chosen. Details of the solutions used based on the product information sheets are shown in Table 5.5.

Infrared spectra of the K120 solution at all dilutions, following subtraction of the water background, are shown in Figure 5.9, whilst IR spectra of all of the 32% silicate solutions are displayed in Figure 5.10. Figure 5.9 demonstrates that the general shape of the observed spectra remains constant at all of the dilutions used, whilst the overall intensity of the absorbance increases with increasing concentration of the solution. The peak maxima do shift slightly from  $1017$  to  $1009 \text{ cm}^{-1}$  as the concentration of the silicate solution increases. This was also observed by Bass and Turner and Halasz *et al* but ascribed to different causes.<sup>15, 16</sup>

**Table 5.5: Details of commercial silicate solutions used for silicate analysis development**

Name (Counter- ion)	Mean specific gravity (g cm <sup>-3</sup> @ 20 °C)	Mean wt ratio (SiO <sub>2</sub> : M <sub>2</sub> O)	Mean molar ratio (SiO <sub>2</sub> : M <sub>2</sub> O)	Mean M <sub>2</sub> O (wt%)	Mean SiO <sub>2</sub> (wt%)	Mean total solids (wt%)
C501 (Na)	1.6	1.6	1.65	18.0	28.8	46.7
C503 (Na)	1.5	2.5	2.58	12.5	31.1	43.6
C75 (Na)	1.38	3.2	3.3	8.6	27.6	36.2
K120 (K)	1.6	1.43	2.24	21.6	20.8	52.4
K78 (K)	1.39	2.09	3.27	13.0	27.1	40.1
K53 (K)	1.26	2.48	3.89	8.6	21.3	29.9

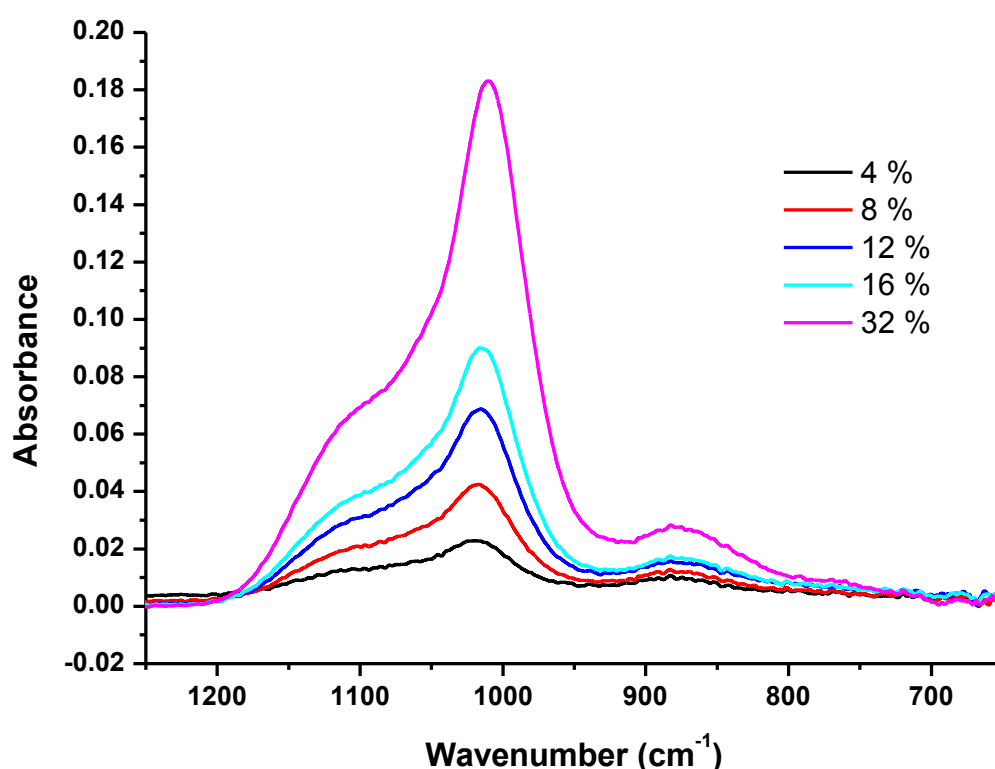
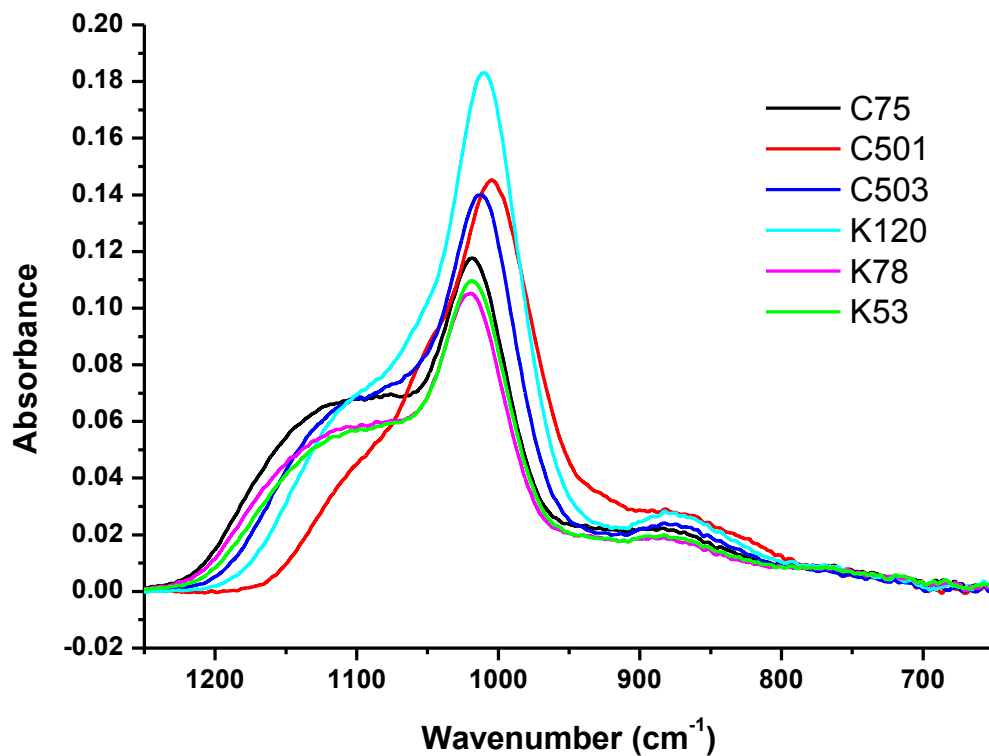
**Figure 5.9: Infrared spectra of K120 solution at various concentrations relative to the original solution (Originally in colour)**

Figure 5.10 exemplifies how the shape of the observed absorbance spectra alters with changing silicate speciation. The higher ratio silicate solutions (C75, K78 and K73) display a shift in the frequency of the main peak ( $1018\text{ cm}^{-1}$ ) to higher wavenumbers and greater development of a high frequency shoulder ( $1225\text{--}1064\text{ cm}^{-1}$ ). The lowest ratio silicate solution (C501) show the reverse behaviour.



**Figure 5.10: Infrared spectra of various commercial silicate solutions diluted to 32% of the original concentration (Originally in colour)**

The area of the silicate band between 1250 – 650 cm<sup>-1</sup> was correlated to the silicon concentration of the initial solution analysed by AAS. The concentration was not taken from the data sheets due to the variation in silica concentration between each batch. The correlations for the dilutions of each individual solution are shown in Figures 5.11 and 5.12 whilst the correlation for all of the solutions combined is shown in Figure 5.13. These reveal a very strong linear correlation between the Si concentration as measured by AAS and the area of the silicate peak, with  $R^2$  values for each of the silicate solutions of 0.99. The inset diagram in Figure 5.12 demonstrates that this correlation continues at concentrations up to those of the initial commercial silicate concentrations.

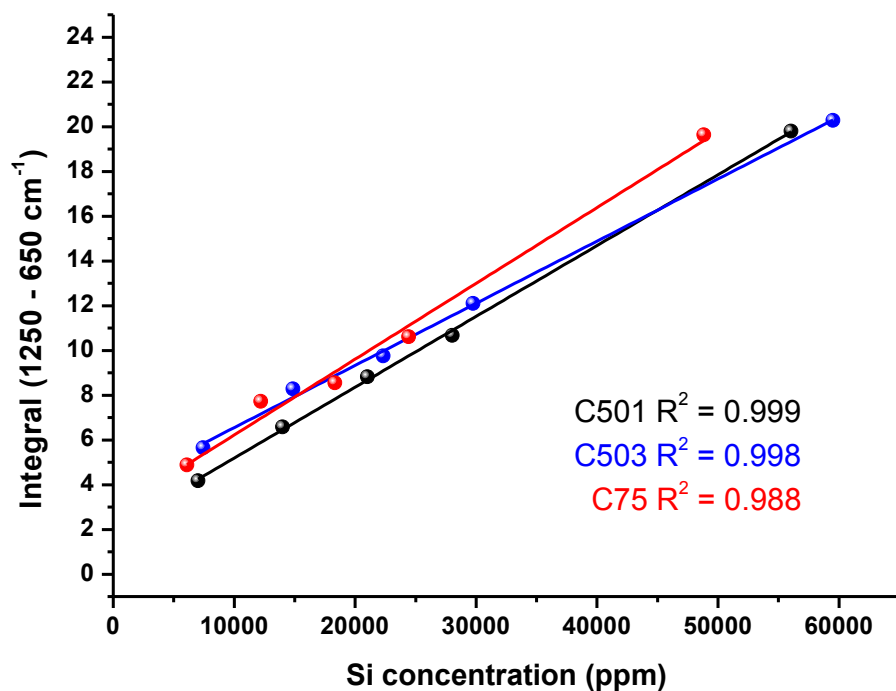


Figure 5.11: Correlation between the Si concentration of three sodium silicate solutions analysed by AAS and the area of the silicate band in their IR spectra (Originally in colour)

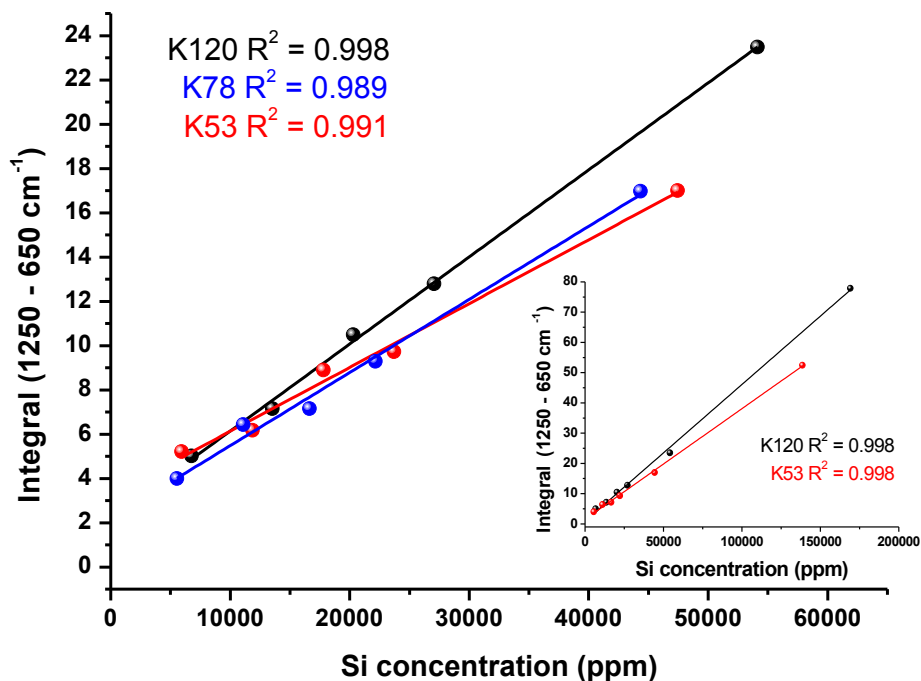


Figure 5.12: Correlation between the Si concentration of three potassium silicate solutions analysed by AAS and the area of the silicate band in their IR spectra (Originally in colour)

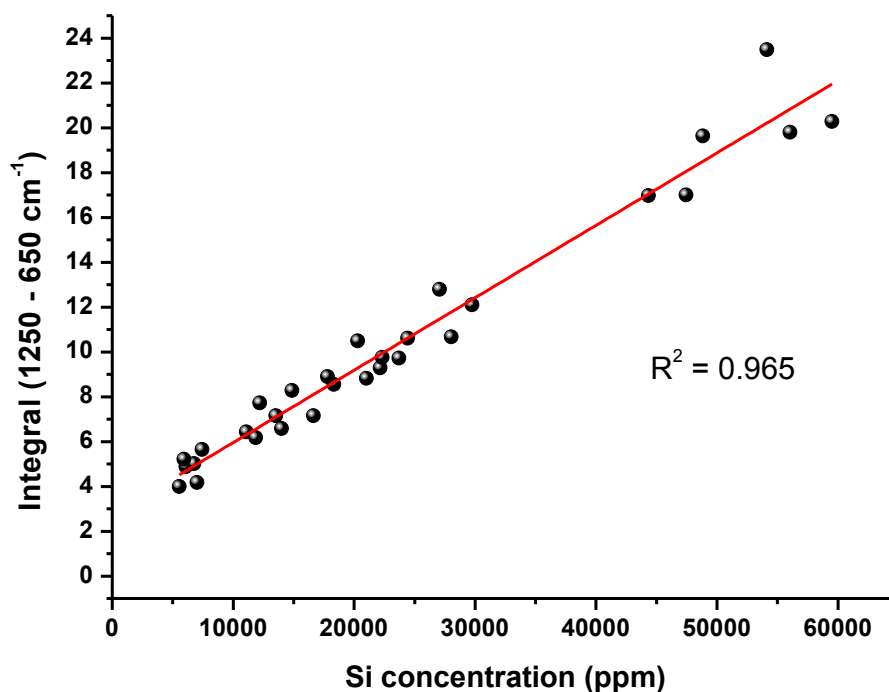


Figure 5.13: Correlation between the Si concentration of several potassium and sodium silicate solutions analysed by AAS and the area of the silicate band in their IR spectra (Originally in colour)

Table 5.6: Slope, intercept and  $R^2$  values for the correlation between Si concentration analysed by AAS and silicate IR band area for different silicate solutions

Name (Counter-ion)	Mean molar ratio (SiO <sub>2</sub> : M <sub>2</sub> O)	Slope ( $\times 10^{-4}$ )	Intercept	$R^2$
Crystal 501 (Na)	1.65	3.17	2.02	0.999
Crystal 503 (Na)	2.58	2.78	3.77	0.998
Crystal 75 (Na)	3.3	3.39	2.83	0.998
K120 (K)	2.24	3.93	2.21	0.998
K78 (K)	3.27	2.88	3.24	0.989
K53 (K)	3.89	3.30	2.18	0.991
<b>Combined</b>		<b>3.23</b>	<b>2.72</b>	<b>0.965</b>

When the data points for all of the solutions are combined (Figure 5.13) a strong linear correlation is still observed, although it is slightly weaker and appears to show greater disparity as the concentrations of the solutions increase. This appears to be due to variations in the slopes of the linear trends for each individual silicate solution (Table 5.6).

K120, in particular, seems to show a greater increase in peak area with increasing concentration than the other solutions. However, there doesn't appear to be any connection between the changing linear relationship on dilution and the molar ratio of the solution.

This data indicates that using the IR integral is a valid and valuable method for the analysis of the silica concentration of both sodium and potassium silicate solutions of different molar ratios. The method appears to be best utilised for dilutions of solutions of one molar ratio, however, the linear relationship still remains robust when samples with a wide range of solids concentrations and molar ratios are used, particularly at lower concentrations.

Shortly following the development of this method, Falcone *et al* published details of a method using the position of the maximum band ( $\sim 1000\text{ cm}^{-1}$ ) and the area of the silicate peak ( $1250 - 715\text{ cm}^{-1}$ ) to determine the concentration and ratio of a silicate solution.<sup>17</sup> However, these researchers only studied sodium silicate solutions and the correlation between the area of the band and the concentration of the solution was only demonstrated for a solution of a single molar ratio. This study, therefore, expands on this work and establishes the validity of this method for a wider range of solutions. Consequently, this method was utilised and tested further for the analysis of silicate solutions formed from the extraction of biomass ashes.

## **5.7 Biosilicate solution**

### **5.7.1 Effect of alkali concentration**

The extraction of Ely-BA1 was initially tested, since the data had indicated that silica was more easily solubilised from miscanthus ash during the lab-scale tests, and from the miscanthus bottom ash by water extraction. The effect of several concentrations of potassium hydroxide solution were tested on ash ground to  $<125\text{ }\mu\text{m}$ , under reflux for 24 h (Table 5.7 and Figure 5.14). This highlights that the majority of the silica present in the ash can be extracted under these conditions, forming solutions of varying molar ratios and with solids contents slightly lower or similar to those of commercial silicate solutions. The data from both the Si AAS analysis and IR integral analysis of the solution indicates the same extraction trend with increasing alkali concentration, although there is a discrepancy between the two methods of analysis for the 3 M concentration solution.

Overall, this implies a KOH concentration of 7.5 M or above is necessary to reach the maximum silica extraction of 80%. Studies of the formation of geopolymers from aluminosilicate mineral wastes have shown that the dissolution of Si and Al increases exponentially with increasing pH.<sup>18</sup>

**Table 5.7: Results of silica extraction from Ely-BA1 using KOH solutions of different concentrations (based on AAS analysis)**

Conc KOH (M)	Si conc (ppm)	Si extraction (%)	Density (g/cm <sup>3</sup> )	SiO <sub>2</sub> (wt%)	K <sub>2</sub> O (wt%)	Weight ratio (SiO <sub>2</sub> :K <sub>2</sub> O)	Solids content (%)
1	24771	42.1	1.09	4.8	4.3	1.13	9.14
3	48572	82.5	1.22	8.5	11.6	0.74	20.0
5	43112	73.5	1.27	7.2	18.5	0.39	25.7
7.5	48095	81.7	1.37	7.5	25.7	0.29	33.1
10	47631	80.9	1.46	7.0	32.3	0.22	39.3

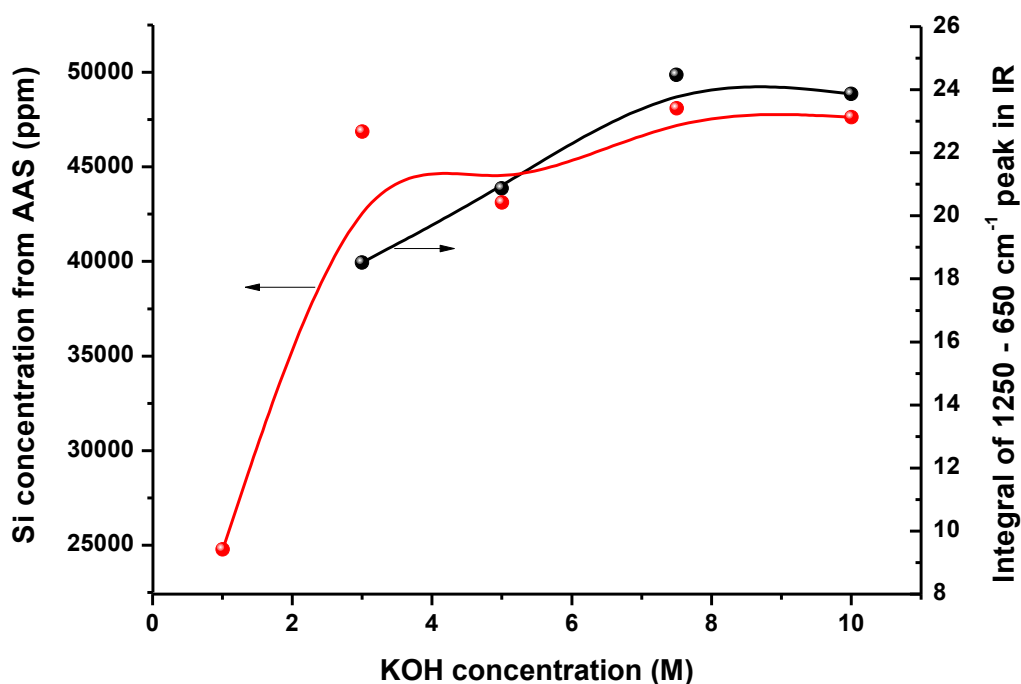


**Figure 5.14: Comparison of Si concentration analysed by AAS and using the IR integral for Ely-BA1 extraction solutions formed with different KOH solution concentrations (Originally in colour)**

Variations in the silicate solutions formed with different KOH concentrations can be observed by studying the IR spectra (Figure 5.15). These display a reduction in the high frequency shoulder, shift of the frequency of the main silicate peak to lower wavenumbers and development of peaks at lower frequencies with an increase in the KOH solution concentration and a reduction in the SiO<sub>2</sub>:K<sub>2</sub>O molar ratio. These changes

were also observed by Bass and Turner for commercial sodium silicate solutions on going from  $\text{SiO}_2:\text{Na}_2\text{O}$  ratios of 3.3 to 0.2 and by Halasz *et al* on the dilution of aqueous solutions of crystalline  $\text{Na}_2\text{SiO}_3$ .<sup>15, 16</sup>

The connection of IR peaks to specific silicate species or sites is still contentious, however, some conclusions can be drawn, with the starting point for most analyses of silicate solutions by FTIR being a comparison with solid silica glasses and gels, for which a much greater body of research exists. In solid silica three main bands are observed centred around 1070 (with a high frequency shoulder at  $1200\text{ cm}^{-1}$ ), 810 and  $457\text{ cm}^{-1}$ .<sup>19</sup> The latter is assigned to rocking or bending of the bridging O-atom,<sup>20, 21</sup> whilst the peak at  $810\text{ cm}^{-1}$  is characterised as symmetrical stretching or bending of the Si-O-Si bond.<sup>19, 21, 22, 23</sup> The most intense mode, centred at  $1076\text{ cm}^{-1}$ , is correlated to the asymmetrical stretching of the Si-O-Si bond,<sup>24</sup> with its high frequency shoulder potentially due to coupling of vibrational modes in the silica skeleton or when the stretching is  $180^\circ$  out of phase.<sup>19</sup> A band is also sometimes observed around  $960\text{ cm}^{-1}$ , which is frequently assigned to silanol (Si-OH) or  $\text{Si-O}^-$  stretching on the surface of the amorphous silica,<sup>21, 22</sup> or to the localised vibrations of cations against the silica framework in sodium and potassium silicate

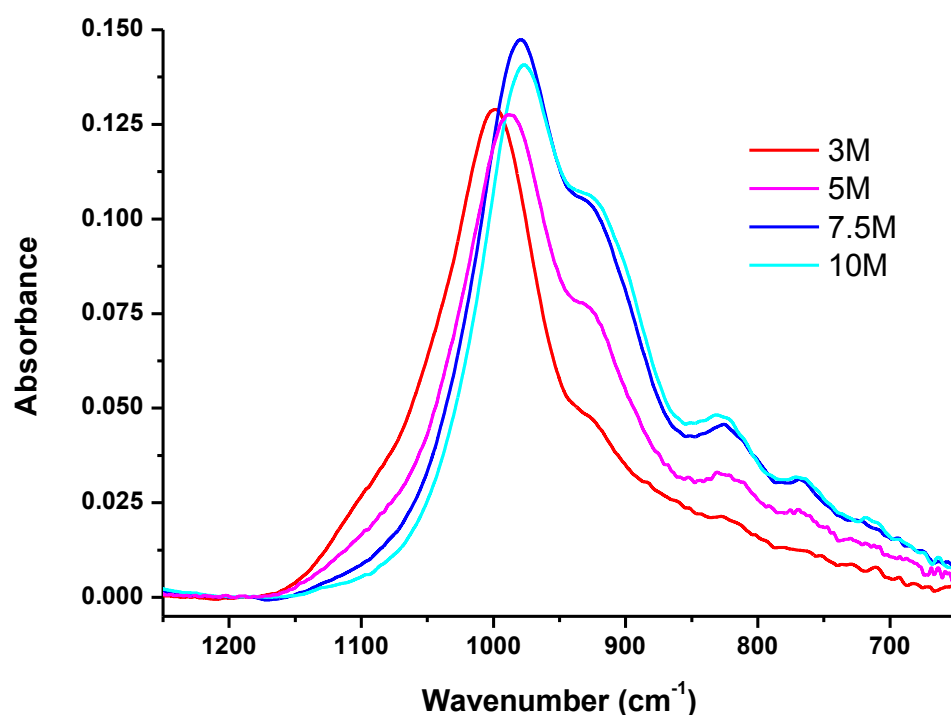


Figure 5.15: IR spectra of silicate solutions formed by the extraction of Ely-BA1 using different KOH concentrations (Originally in colour)

glasses.<sup>23</sup> This peak is observed to decrease on annealing of silica at high temperatures and to shift to lower frequency where the counter-ion is  $K^+$  as opposed to  $Na^+$ .<sup>22, 23</sup> In addition, when silica is heated to higher temperatures the most intense band shifts to a higher frequency ( $\sim 1120\text{ cm}^{-1}$ ) and the shoulder increases in relative intensity, suggested to be due to bond shortening and a reduction in the mean bond angle as densification of the silica structure occurs.<sup>21</sup>

In contrast to solid silica, the main peak present in the silicate solutions is found at lower wavenumbers, between  $1010 - 977\text{ cm}^{-1}$ , with several peaks present at even lower wavenumbers. Different authors have associated these peaks with different species (Table 5.8). Bass and Turner attributed the position and presence of different peaks in the IR spectra of silicate solutions to different  $Q^n$  species.<sup>15, 25</sup> In contrast Halasz *et al* connected them to a change in the degree of dissociation dependent on both the concentration and ratio of the silicate solution,<sup>16, 26</sup> whilst Osswald and Fehr identified changes due to the alteration in the ratio of surface silanol groups to internal siloxane groups as particle sizes decreased.<sup>27</sup> Water solvation was also found to be important for better fitting of calculated IR spectra to the experimental data.<sup>28</sup>

**Table 5.8: Peak frequencies and identification in the ATR-IR spectra of Ely-BA1 silicate solutions**

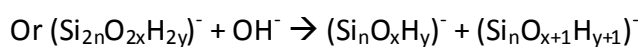
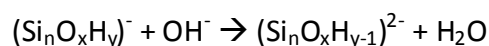
	Concentration of KOH extraction solution (M)				Identification of peaks			
	3	5	7.5	10	Bass and Turner <sup>15</sup>	Osswald and Fehr <sup>27</sup>	Halasz <i>et al</i> <sup>16, 26</sup>	
Peak positions observed ( $\text{cm}^{-1}$ )				714			$\delta_{as}(\text{H})\text{O-Si-O}(\text{Na})$	
		768	769	764			$\delta_{as}(\text{H})\text{O-Si-O}(\text{H})$	
		824	825	826	828		$\nu_s(\text{Na})\text{O-Si-O}(\text{Na})$	
					$\text{SiO}^-$ small anions	$\delta$ Si-OH	$\delta_{as} \text{O}^- \text{Si-O}^-$	
		923	926	924	921	Monomer and dimer	$\nu$ Si-OH	$\nu_s(\text{H})\text{O-Si-O}(\text{Na})$
		999	989	979	977	Linear Q1 and monomer	$\nu_{as}$ Si-O-Si (surface)	$\nu_{as}(\text{X})\text{O-Si-O}(\text{X})$ where X = Na, H in $\text{Na}_2\text{H}_2\text{SiO}_4$
		1097	1096			$Q^3$ and $Q^2$ species	$\nu_{as}$ Si-O-Si (internal)	

Overall, the literature data indicates that the shoulder at  $1080\text{-}1097\text{ cm}^{-1}$ , only observed in the solutions using the lower concentration KOH extraction solution, is due to

asymmetric Si-O-Si stretching ( $\nu_{as}$ ). Most data indicates that silicate anions adopt formations that are as condensed as possible such as cyclic- and cage-like- species.<sup>15, 29</sup> The reduction in this peak with decreasing SiO<sub>2</sub>:M<sub>2</sub>O ratio suggests a reduction in Si-O-Si bridging bonds and a shift to smaller anionic species. The absence of peaks at higher wavenumbers in this study ( $\sim 1200\text{ cm}^{-1}$ ) indicates a lack of colloidal silica (Q<sup>4</sup>).<sup>30</sup>

The main band shifts to lower wavenumber, from  $999 - 977\text{ cm}^{-1}$ , with increasing alkali content. Overall, all three authors correlate this peak to surface  $\nu_{as}$  (Y)O-Si-O(X) where Y = Si or H and X = - charge or H with the peak shifting as the attached functional groups vary.<sup>27</sup> Bass and Turner suggested that the position of the IR peak could be correlated to individual Q<sup>n</sup> species.<sup>15</sup> However, more recently Falcone *et al* have suggested that assignment of peaks to specific species is not supported and instead, that the large variation in the shift in the peak around  $980\text{ cm}^{-1}$  may be due to changes in hydrogen bonding affecting Si-O<sup>-</sup> stretching.<sup>30</sup> These suppositions are supported by computational studies of the changing molecular structure of silicate species.<sup>29, 31</sup> With a decreasing SiO<sub>2</sub>:M<sub>2</sub>O ratio NMR studies show the main species formed to be Q<sup>0</sup> monomer as an increasing number of repulsive anions are formed.<sup>15</sup> Where a silicon atom is bonded to a charged oxygen atom, computational studies indicate that the SiO<sup>-</sup> bond is shortened, whilst silanol and siloxane bonds on the same atom are lengthened. The longest bond in the latter is the one attaching the bridging oxygen to the Si-O<sup>-</sup> species and therefore makes it more susceptible to hydrolysis. Bond strength is negatively correlated to bond length and therefore if the bond length increases a shift in the IR spectra to lower wavenumbers would be expected.<sup>32</sup> The studies by Halasz *et al* on sodium silicate solutions indicated that the shift to lower wavenumbers for the main peak may also be associated to the increased surface adsorption or ion pairing of sodium metal cations at anionic sites at higher solution concentrations and higher alkali ratios as dissociation decreases.<sup>16, 26, 27</sup> Electrical conductivity measurements and sodium selective electrode measurements showed a decreasing proportion of free Na<sup>+</sup> in solution at higher concentrations and a decreasing number of totally dissociated anions with higher Na/Si ratios.<sup>16, 26</sup> This could decrease the frequency of absorption by decreasing the force constant. Silicate anion pairing with alkali metal cations has been identified by NMR and computational methods indicate that ion-pairing is energetically favourable for monomeric, dimeric and higher anionic species.<sup>33, 34</sup> <sup>29</sup>Si NMR measurements indicate that ion pairing is favoured by a rising OH<sup>-</sup>:Si ratio.<sup>35</sup> Upon the addition of base, the level of

negative charges on silicate anions will increase either by deprotonation or depolymerisation, such as:



This will eventually reach a maximum when all of the anions are depolymerised to monomer anions. At this point, the addition of further base results in the increasing formation of anion-cation pairs.<sup>33, 36</sup> This can stabilise silicate anions, reducing the likelihood of condensation reactions but can also reduce electrostatic repulsions thereby mediating silicate condensation.<sup>35</sup> Whichever is the dominating factor will depend on the strength of the cation-anion interaction, with evidence suggesting that this depends on the cation in the order  $\text{Li}^+ > \text{Na}^+ > \text{K}^+ > \text{Rb}^+ > \text{Cs}^+$  from  $^{29}\text{Si}$  NMR,<sup>35</sup> or in the order  $\text{Li}^+ < \text{Na}^+ < \text{Cs}^+ < \text{Rb}^+ < \text{K}^+$  based on the preferential formation of  $\text{M}^+ \dots \text{O-Si}$  pairs from NMR of the alkali metal.<sup>37</sup> The latter assignments were supported by theoretical calculations of the energy change associated with the replacement of a water molecule with a silicate anion within the hydration sphere of the alkali metal cation. Moreover, at high solids concentrations and low  $\text{SiO}_2:\text{K}_2\text{O}$  ratios, where insufficient water may be present for hydration of the alkali cation, the replacement of a water molecule of solvation by  $\text{Si-O}^-$  may be even more favourable.<sup>38</sup> All of this data, along with observations for the shift of IR frequencies due to the alkali metal cation in silicate glasses,<sup>23</sup> suggest that the assignments by Halasz *et al* may most accurately correlate with the results observed in this study.<sup>16, 26</sup> That is, that the shift of the main peak at  $1010 - 977 \text{ cm}^{-1}$  is due to  $\nu_{\text{as}}(\text{Y})\text{O-Si-O}(\text{X})$  where  $\text{Y} = \text{Si}$  or  $\text{H}$  and  $\text{X} = \text{H}$  or  $\text{K}^+$  and is dependent on the degree of anion-cation pairing in solution. The increasing relative intensity of the  $970\text{-}1010 \text{ cm}^{-1}$  peak can overall be associated with the increasing concentration of surface species with respect to siloxane bonds and therefore the formation of more  $\text{Q}^0$ ,  $\text{Q}^1$  and  $\text{Q}^2$  species with increasing alkali concentration as observed by NMR.

Bands at  $934 \text{ cm}^{-1}$  have been linked to  $\nu_s$  of  $(\text{Na})\text{O-Si-OH}$  species and those at  $830 \text{ cm}^{-1}$  with  $\nu_s$  of  $(\text{Na})\text{O-Si-O}(\text{Na})$ .<sup>26</sup> These would be expected to be observed at a lower frequency in the presence of a heavier potassium cation, which is indeed the case and so further supports these assignments. The peak at  $776 \text{ cm}^{-1}$  has been ascribed to the  $\text{HO-Si-OH}$  bending vibration ( $\delta_{\text{as}}$ ).<sup>28</sup> The decrease in all of these peaks with decreasing

concentration and increasing  $\text{SiO}_2:\text{K}_2\text{O}$  molar ratio supports the theory of the formation of more dissociated and condensed species.

### 5.7.2 Reproducibility

Using the data from the study above, the required ratio of Ely-BA1 and KOH was calculated for the formation of a solution with an equivalent ratio to the commercial K120 solution. K120 was chosen as the solution to simulate as initial testing had shown that this was a promising silicate binder for board formation. The extraction calculation was based on an assumption that 80% of the silica present in the bottom ash could be solubilised. The maximum total solids content of the solution formed was lower than that of the K120 solution due to the difficulty of efficient stirring of the solution at higher solid:liquid ratios. It was noticed that the ash was hydrated during the reaction with a large amount of solid black sludge formed as the reaction progressed. The results of the extraction are shown in Table 5.9.

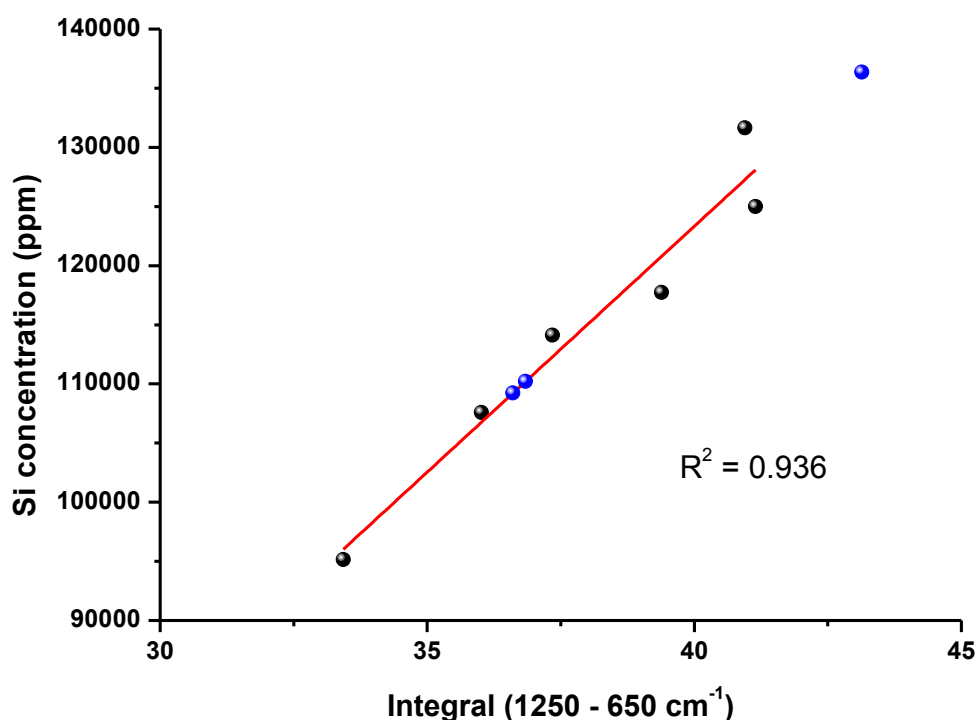
The results demonstrate quite a varied degree of reproducibility based on Si AAS analysis of the solutions formed ( $65.9 \pm 7.3\%$ ). The much lower Si concentration for expt 17 and the generally low extractions compared to those described in section 5.7.1 are probably caused by poor stirring, specifically due to the higher initial solid:liquid ratio used. Overall, analysis using the IR integral and the linear correlation equation found for the commercial solutions in section 5.6 above, reasonably accurately determines the silica concentration. The concentrations are always slightly lower than those found by Si AAS, for expt 9 and 15 significantly so. However, this may imply a greater degree of error in the dilutions of the highly concentrated solutions during AAS analysis than within the IR data.

The densities, weight ratios and solid contents are similar for all of the solutions. They are lower in all cases than the commercial K120 solution, due to the low solid:liquid ratio used and the lower than predicted extraction of silica.

The silica concentrations of the solutions from experiments 18 - 21 were calculated using the IR method based on the correlation between the Si AAS and IR integrals for experiments 9 – 17 (Figure 5.16). The linear relationship and fit are similar to that found for the combined commercial silicate solutions (Figure 5.13), despite the concentrations of the solutions being higher.

**Table 5.9: Analysis of biosilicate solutions from Ely-BA1 ash using constant KOH solution concentrations and ash:liquid ratios with extraction occurring under reflux over 24 h**

Expt No.	Si conc AAS (ppm)	Integral	Si conc IR (ppm)	Si extraction (%)	Density (gcm <sup>-3</sup> )	SiO <sub>2</sub> (wt%)	K <sub>2</sub> O (wt%)	Wt ratio (SiO <sub>2</sub> :K <sub>2</sub> O)	Solids content (%)
9	131630	40.9	115107	74.5					
12	114124	37.3	104335	64.6	1.35	18.0	18.6	1.0	36.6
13	107583	36.0	100346	60.9	1.34	17.2	18.8	0.9	36.1
14	117747	39.4	110436	66.7	1.35	18.7	18.6	1.0	37.3
15	124978	41.1	115694	70.8	1.36	19.6	18.4	1.1	38.1
17	95150	33.4	92614	53.9	1.32	15.4	19.1	0.8	34.5
18		43.1	135701	76.8	1.38	21.0	18.2	1.2	39.2
20		36.6	109247	61.8	1.35	17.4	18.7	0.9	36.0
21		36.8	110044	62.3	1.35	17.4	18.6	0.9	36.1

**Figure 5.16: Correlation between the IR integral and Si AAS analysis for several silicate solutions formed from the extraction of Ely-BA1. The points in blue indicate solutions calculated from the linear fitting. (Originally in colour)**

Two of the solutions formed from Ely-BA1 were analysed by ICP-AES to study their elemental content, the results of which are shown in Table 5.10. The elemental composition of the solutions is highly reproducible. The data illustrates the predominance of potassium and silicon. The levels of silicon detected are lower than those found by

AAS, however, previous measurements indicated that ICP-AES was not as accurate for analysing the amount of silicon and potassium present at very high concentrations. The other elements present are the same as those observed in the water extracted solutions (Table 5.4), but are generally found at a slightly higher concentration.

Sulfur and phosphorus both display a higher level of dissolution than by water extraction and both were also major components in the initial ash. This could indicate that they were either trapped in silica melts or forms that were more easily dissolved under the highly alkaline and hot conditions used for the extraction of silica. The low levels of magnesium and calcium suggests that any that has dissolved has co-precipitated some silica from solution, which may account for the incomplete dissolution of the silica present in the ash. Alumina is soluble in alkaline solutions which accounts for its increased concentration in comparison to the water extraction of Ely-BA1. Aluminium is known to flocculate colloidal silica, although this is unlikely to occur for the highly concentrated and charged silicate anions in the solution formed, although aluminosilicate species might form.<sup>12</sup> Very minor quantities of other elements are present, however, these should not pose challenges for the utilisation of the silicate solution for a variety of applications.

**Table 5.10: Elemental analysis of two potassium silicate solutions formed from Ely-BA1**

Element	BA1-12		BA1-13	
	Concentration (ppm)	Percentage (wt%)	Concentration (ppm)	Percentage (wt%)
Ag	nd		nd	
Al	198	0.09	179	0.08
As	1.2	0.00	nd	
Au	nd		nd	
B	15.0	0.01	14.0	0.01
Ba	16.0	0.01	1.2	0.00
Be	nd		nd	
Bi	nd		0.5	0.00
Ca	14.0	0.01	27.0	0.01
Cd	nd		nd	
Co	nd		0.3	0.00
Cr	0.1	0.00	0.2	0.00
Cu	nd		1.0	0.00
Fe	4.0	0.00	5.0	0.00
Hg	nd		nd	
K	140440	62.0	133780	62.4
La	0.1	0.00	0.1	0.00
Li	nd		nd	
Mg	13.0	0.01	14.0	0.01
Mn	2.0	0.00	2.0	0.00
Mo	5.0	0.00	5.0	0.00
Na	725	0.32	710	0.33
Ni	nd		nd	
P	5005	2.21	4651	2.17
Pb	1.1	0.00	1.3	0.00
Pd	2.0	0.00	1.9	0.00
Pt	nd		nd	
Rb	54.8	0.02	51.8	0.02
S	1578	0.70	1463	0.68
Sb	nd		nd	
Se	nd		nd	
Si	78471	34.6	73262	34.2
Sn	0.3	0.00	nd	
Sr	0.4	0.00	0.3	0.00
Te	nd		nd	
Ti	0.7	0.00	0.7	0.00
Tl	4.2	0.00	0.6	0.00
V	4.9	0.00	4.6	0.00
W	89.5	0.04	85.1	0.04
Zn	nd		2.0	0.00
Zr	1.4	0.00	1.2	0.00
<b>Sum</b>	<b>226646</b>		<b>214265</b>	

### 5.7.3 Effect of time

A kinetic study on the extraction of Ely-BA1 ash was carried out using the same experimental conditions as for experiments 9-21, to ensure that an equilibrium was reached over the reaction period and to obtain a greater understanding of the extraction process (Figure 5.17). The experimental work was carried out by an undergraduate student, Anna Schaub, in collaboration with and under the supervision of Ms Jennie Dodson. Due to the high temperature of extraction, large inaccuracies occurred if samples were taken from the reaction vessel and directly analysed by IR. Therefore, each measurement corresponds to a separate sample, rapidly cooled before analysis.

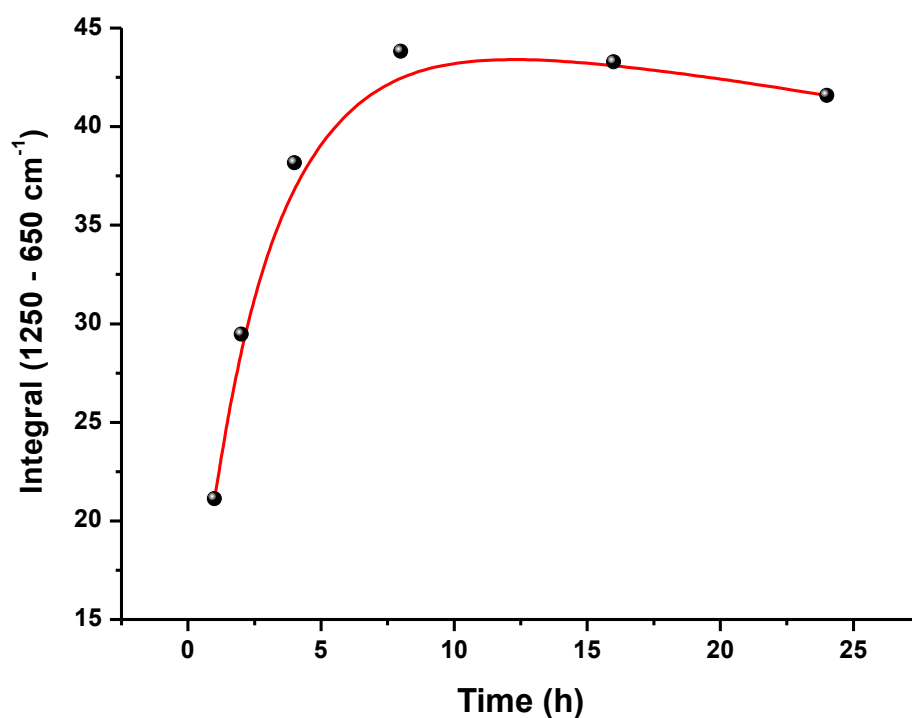


**Figure 5.17: Area of silicate peak vs time during the extraction of Ely-BA1 ash (Originally in colour)**

This data shows a rapid rise in silica dissolution over the first few hours, with a maximum extraction after 8 h. Following this there is a slight decrease in the area of the silicate peak, from the IR analysis, with increasing time. This could be due to variations in the extraction between different samples, as seen in Table 5.9, or some concentration of the solution before analysis, however, it could also indicate a re-precipitation or polymerisation of silica out of the solution beyond this point. The latter effect could be

caused by the large quantity of calcium present in the ash with this possibility discussed in more detail in relation to the residue remaining following extraction in section 5.9. Consequently, there could be an optimum extraction time. Further research is necessary to study this process in more detail.

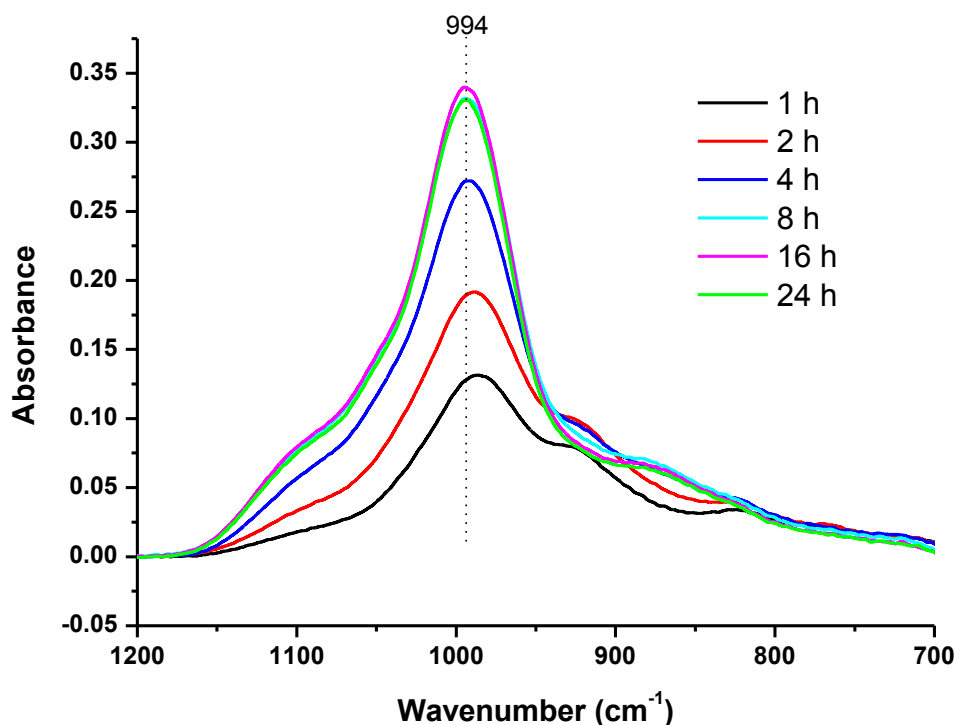


**Figure 5.18: IR spectra of silicate solutions formed during the extraction of Ely-BA1 for different lengths of time (Originally in colour)**

The changes occurring in the silicate IR band during extraction are shown in Figure 5.18. This clearly highlights differences in the silicate bands and silicate species present as dissolution progresses. These appear to be similar to those observed on extraction of Ely-BA1 with different concentrations of KOH. At the lowest  $\text{SiO}_2:\text{K}_2\text{O}$  ratio (1 h) the main bands in the IR spectra are found at 986, 927 and 822  $\text{cm}^{-1}$ , similar to those detected using a 5, 7.5 or 10 M KOH solution (Table 5.8). As the extraction progresses, and the  $\text{SiO}_2:\text{K}_2\text{O}$  ratio increases, the overall silicate band increases in intensity, a high frequency shoulder at 1100  $\text{cm}^{-1}$  develops, the main peak shifts to higher wavenumber (994  $\text{cm}^{-1}$ , 24 h), the bands at 927 and 822  $\text{cm}^{-1}$  reduce in intensity, whilst a new band at 880  $\text{cm}^{-1}$  appears. This process appears to be gradual with the spectra of the solution formed after 4 h displaying all of these peaks. Overall, according to the IR assignments from Table 5.8, initially monomeric anions with a low dissociation of the  $\text{K}^+$  counter-ion are extracted into

solution. As the extraction progresses increasing dissociation of the anion occurs as the ratio of  $\text{SiO}_2:\text{K}_2\text{O}$  increases, eventually leading to the formation of larger anionic species evidenced by the shoulder around  $1100\text{ cm}^{-1}$ .

#### 5.7.4 Using fly ash solution for extraction

The experiments above show that a concentrated potassium silicate solution can be controllably formed from biomass bottom ashes. However, a highly concentrated hydroxide solution was required. The overall aim of this study was utilise the inherent alkalinity of the combustion residues. Earlier tests had shown that following combustion in a large-scale system this mainly resided in the fly ashes. Therefore a test was undertaken to observe whether a sufficiently concentrated alkaline solution could be formed from the fly ashes to extract silica from the bottom ashes and form a potassium silicate solution similar to those achieved using synthetic potassium hydroxide. Ely-FA1 was leached with water at a liquid:solid ratio of 5:1. The filtered solution was reduced to a volume  $1/16^{\text{th}}$  of the original, at which point salt was beginning to crystallise out of solution. The alkalinity of this solution was tested by titrating against a 0.1M HCl solution. This gave a solution concentration of 1.4 M. Based on the analysis of the concentration of the alkaline solution the amount of bottom ash required to produce an approximately 1.2 weight ratio potassium silicate solution was calculated. The resultant mixture was extracted under reflux.

The IR spectra of the solution formed is shown in Figure 5.19. This is different in shape to the silicate solutions formed using potassium hydroxide solutions of higher concentrations, however, a solution formed using a 1M KOH solution and the same liquid:solid ratio displays a similar IR spectra, both of which more closely resemble the higher molar ratio commercial silicate solutions (Figure 5.10). The developed high frequency shoulder around  $1105\text{ cm}^{-1}$  is usually attributed to  $\nu_{\text{as}}\text{ Si-O-Si}$  and indicative of the presence of more highly polymerised silicate species and high  $\text{SiO}_2:\text{M}_2\text{O}$  ratio solutions.<sup>15, 30</sup> However, based on the IR peak areas, silica extraction from the bottom ash using the fly ash solution only reached 27%, producing a solution with a lower ratio than the majority of the Ely-BA1 solutions.

This demonstrates in principle that it is possible to form a sufficiently alkaline solution using the collected fly ashes to extract a proportion of the silica from the bottom ashes.

Unfortunately, it was not possible to form a solution of higher alkalinity due to the precipitation of salts from the fly ash solution on concentrating it. Further analysis of the salts precipitating might, however, provide information about further possible uses of the fly ashes.

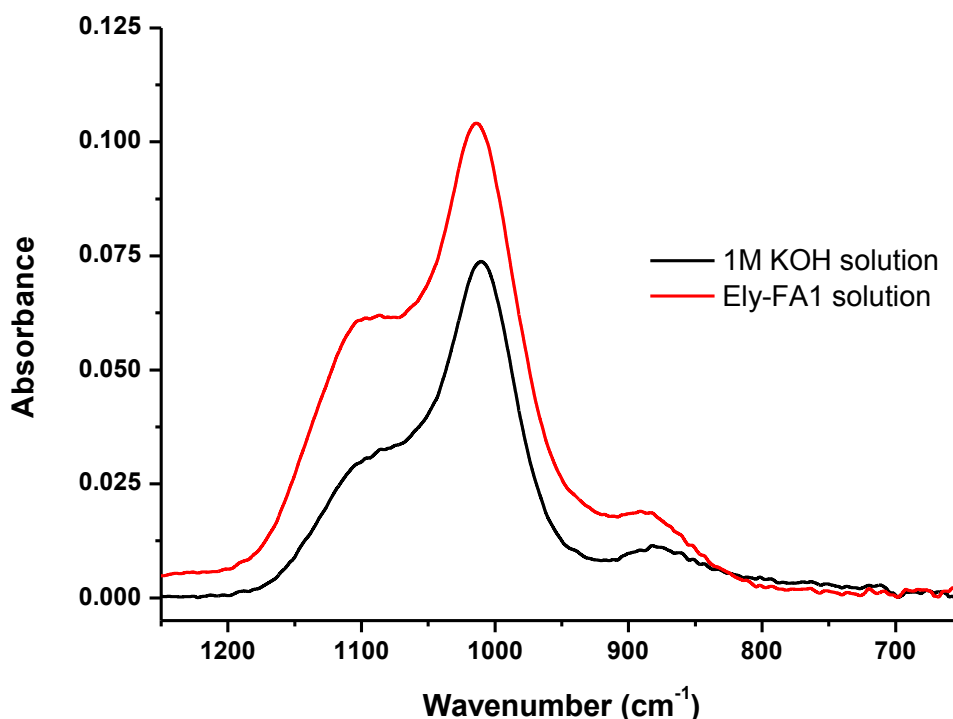


Figure 5.19: IR spectra of silicate solutions formed during the extraction of Ely-BA1 using a 1M KOH solution and a concentrated solution from the extraction of Ely-FA1 (Originally in colour)

## 5.8 Board formation

### 5.8.1 Biosilicate

The formation of a highly concentrated silicate solution from the extraction of Ely-BA1 ashes using a potassium hydroxide solution was demonstrated in section 5.7.1 – 5.7.3 above. The further aim of this study was to utilise this silicate solution as a novel binder in the production of composite boards, with wheat straw as the main substrate, as a replacement for formaldehyde-based binders in particle and MDF boards. The silicate solutions formed above had a lower silica content than K120. Therefore, in order to compare the results using both the bottom ash and commercial silicate solutions the biosilicate solutions were concentrated further. Two solutions were formed, one with a SiO<sub>2</sub> concentration similar to K120 and the other with a higher concentration, to observe if this improved the binder efficacy. Comparisons of the solutions are shown in Table 5.11. The differences in the weight ratios between K120 and the biosilicate solutions are

due to a lower than expected extraction of  $\text{SiO}_2$  from the Ely-BA1 ash, resulting in a higher total solids content for the same  $\text{SiO}_2$  wt% for Biosilicate 1 compared to K120, and therefore a higher density.

**Table 5.11: Characterisation of silicate solutions used for binder tests**

Name	Silicate peak area (IR)	$\text{SiO}_2$ (wt%)	$\text{K}_2\text{O}$ (wt%)	Solids content (wt%)	$\text{SiO}_2:\text{M}_2\text{O}$ wt ratio	Density ( $\text{gcm}^{-3}$ )
<b>K120</b>	77.9	31.8	21.6	53.4	1.47	1.52
<b>Biosilicate 1</b>	75.8	29.4	31.4	60.7	0.94	1.64
<b>Biosilicate 2</b>	103.8	36.7	39.2	75.9	0.94	1.85

The effect of these variations on the silicate anion speciation can be observed from the IR spectra of all three solutions (Figure 5.20). Although the area of the silicate peak is almost identical for K120 and Biosilicate 1, representing the slight difference in silica content, the K120 solution has a more developed high frequency shoulder and peak at  $880\text{ cm}^{-1}$  with the main peak shifted to slightly higher wavenumber. This follows the trend observed for increased  $\text{SiO}_2:\text{K}_2\text{O}$  ratio solutions as larger or more dissociated anions form. Biosilicate 2 generally has a similar shape, but with greater intensity, than that of Biosilicate 1. However, the main peak is shifted to even lower frequency ( $963\text{ cm}^{-1}$ ), with the band at  $884\text{ cm}^{-1}$  increasing in relative intensity. A similar effect was observed by Halasz *et al* as a monomeric solution was concentrated.<sup>16</sup>

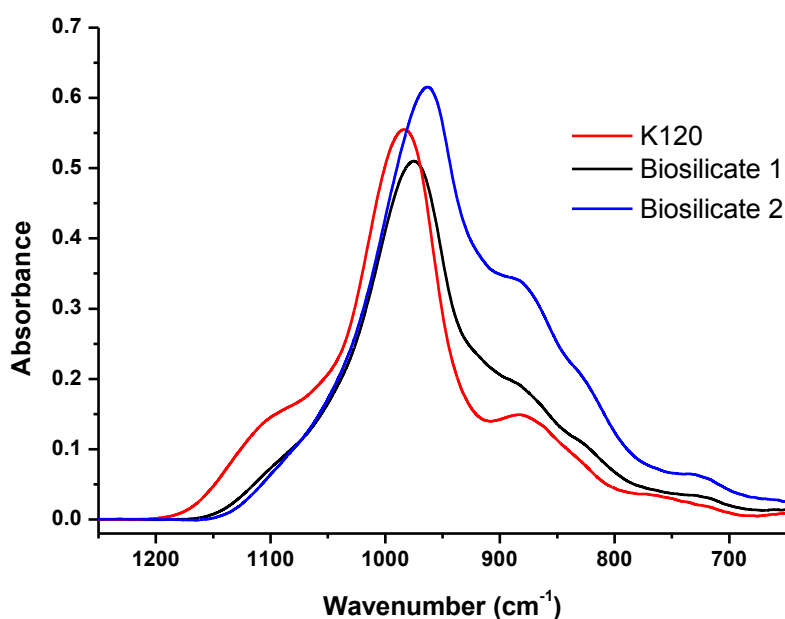


**Figure 5.20: IR spectra of K120 and Ely-BA1 biosilicate solutions used as binders for board formation testing (Originally in colour)**

## 5.8.2 Board making

5 x 5 cm boards were initially formed in order to test the effectiveness of the biosilicate solutions in comparison to the K120 solution. The making of these boards was carried out in collaboration with a co-worker on the same project, Dr Mario de Bruyn, using a procedure that he had previously developed (Figure 5.21). A single source of wheat straw, milled and sieved to the same size fractions, was used throughout, to prevent irregularities on a small scale due to particle size or wheat straw variety. The material was dewaxed by Soxhlet using EtOH before use. This had been shown to increase the hydrophilicity of the surface and therefore improve contact and adhesion between the water based binder and straw surface by removal of lipophilic secondary metabolites.<sup>39</sup> Some boards were formed with the addition of whey protein as early indications had shown that this improved the internal bond strength.

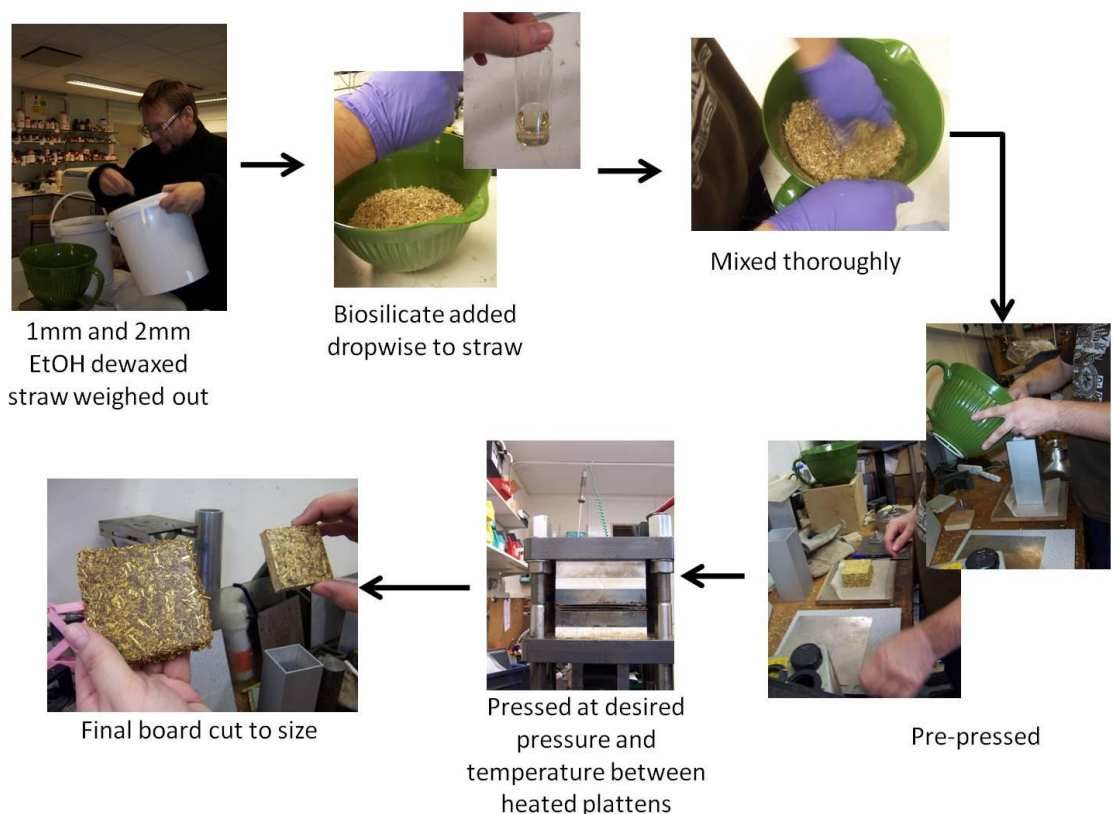


**Figure 5.21: Procedure for formation of test boards using a wheat straw substrate with different potassium silicate binders (Originally in colour)**

Visual observations during the board making process identified slightly more spring-back during pre-pressing, along with a darker colouration of the surface of the board following pressing when using the biosilicate solutions compared to K120.

The first set of boards formed were sent to Bangor University's Biocomposite Centre for internal bond strength testing (Table 5.12). Another set was tested at the University of York by Dr Mario de Bruyn following the acquisition of a larger load cell (Table 5.13). The boards tested at Bangor were subject to conditioning for a longer period of time, 2 weeks, whilst those tested at York were conditioned for only 1 day.

The minimum standards that were aimed for were an internal bond strength of 0.45 Nmm<sup>-2</sup> and swelling on immersion in water of 14%. The internal swelling tests were not measured using the appropriate standards as this requires the formation of larger boards. In addition, only general conclusions can be drawn from the data presented as the production of a much larger sample size would be necessary to produce a statistically significant data set.

**Table 5.12: Strawboard composite properties using different silicate binders (tested at Bangor University)**

Binder details		Width (mm)	Breadth (mm)	Density (gcm <sup>-3</sup> )	Maximum Load (N)	Internal bond strength (Nmm <sup>-2</sup> )
No protein	K120	50.5	50.3	0.660	185.7	0.07
		50.8	50.7	0.636	207.5	0.08
	Biosilicate 1	50.4	50.6	0.646	398.7	0.16
		50.2	50.1	0.698	479.0	0.19
	Biosilicate 2	50.0	50.1	0.647	388.5	0.16
	With protein	K120	50.6	50.2	0.692	517.7
50.6			50.8		662.7	0.26
Biosilicate 1		50.0	49.7	0.688	525.4	0.21
		49.9	50.2	0.693	690.7	0.28
Biosilicate 2		49.9	49.8	0.707	620.0	0.25
		49.8	49.7	0.696	828.4	0.33

From Table 5.12, without the addition of protein, the biosilicate solutions both show a substantially higher bonding strength than the K120 solution. This may be due to the higher total solids content, reducing the amount of water required to be removed to set the silicate bond via dehydration. On addition of protein, all of the binders display a

higher bonding strength. The biosilicate solutions still exhibit slightly higher tensile strength, especially where boards of equal density are compared, however, the disparity is reduced in comparison to the case where no protein is added. Biosilicate 2 demonstrates the highest strength. This may not be reproducible, however, it could indicate the benefit of an increased solids content. The additional strength imbued by the presence of whey protein is perhaps not surprising. It consists of soluble proteins including  $\beta$ -lactoglobulin and  $\alpha$ -Lactalbumin. Under the action of heat these proteins can be denatured causing them to coagulate. In addition, albumin is known to coalesce by the adsorption of polysilicic acid, which then polymerises, although this appears to be promoted at acidic to neutral pH.<sup>12</sup>

From the initial set of results it appeared that the biosilicate was showing improved strength in comparison to K120. Therefore, additional KOH was added to K120, based on the characterisation of Biosilicate 1, to produce a silicate of similar composition. The silicate peak shape of K120, analysed by IR, was altered by the addition of KOH, being almost identical to that of Biosilicate 1.

**Table 5.13: Strawboard composite properties using different silicate binders (tested at the University of York)**

Binder	Additives	Density (gcm <sup>-3</sup> )	Internal bond strength (Nmm <sup>-2</sup> )	Thickness swelling (%)
<b>K120</b>	Protein	0.712	0.49	51
<b>K120 + KOH</b>	Protein	0.721	0.36	48
<b>Biosilicate 1</b>	Protein	0.726	0.41	51

The second set of results analysed at the University of York (Table 5.13) illustrate an almost universal increase in the internal bond strength in comparison to the first set of boards. The probable cause of this is the difference in the conditioning methods. As can be observed by the thickness swelling, all of the boards are still relatively hydrophilic. Therefore, a longer conditioning time in a high humidity chamber may significantly reduce the internal bond strength. In addition, the densities are slightly higher, which may also be due to swelling occurring in the first set of boards upon conditioning. Within the second set, the boards set using K120 display a higher internal bond strength. Indeed, these are the first to meet the required strength for the particleboard standards. The

K120 solution with added base and the Biosilicate 1 boards both exhibit lower tensile strengths. It is impossible to say whether these differences are significant and further testing is required to understand the full impacts of the different variables on the board strength. The water swelling for all of the boards are similar, although greater than the required standard. Nevertheless, these boards do demonstrate promise in producing a novel inorganic composite material utilising low concentrations of alkali silicate binder from biomass combustion residues.

## 5.9 Residual solids

### 5.9.1 Analysis of residue

Following centrifugation and recovery of the silicate solution from the Ely-BA1 extracted ash mixture a residual black sludge remained. There was interest in looking for an application for this material to complete the holistic utilisation of all of the products from biomass combustion.

Initially, the elemental content of the residue following separation of the biosilicate solution was analysed. The extracted ash from Expt 15 (Table 5.9) was washed thoroughly, until the washing waters had a neutral pH, to remove any remaining silicate solution. The material was then dried and analysed by XRF, XRD and  $^{29}\text{Si}$  NMR.

**Table 5.14: Elemental composition of Ely-BA1-15 solid residue after extraction and the percentage of each element solubilised**

Oxide	Initial Ely-BA1	After extraction	Normalised	
			to CaO content	% extraction
Na <sub>2</sub> O	0.16	0.12	0.06	60.7
MgO	2.82	5.74	3.01	-6.6
Al <sub>2</sub> O <sub>3</sub>	0.76	1.28	0.67	11.5
SiO <sub>2</sub>	62.98	43.59	22.84	63.7
SO <sub>3</sub>	2.74	1.25	0.66	76.1
P <sub>2</sub> O <sub>5</sub>	4.37	0.00	0.00	100.0
K <sub>2</sub> O	14.64	2.65	1.39	90.5
CaO	8.28	15.80	8.28	0.0
TiO <sub>2</sub>	0.06	0.10	0.05	16.2
Cr <sub>2</sub> O <sub>3</sub>	0.01	0.02	0.01	-31.0
Mn <sub>3</sub> O <sub>4</sub>	0.14	0.31	0.16	-16.8
Fe <sub>2</sub> O <sub>3</sub>	0.50	0.87	0.46	8.6
<b>SUM</b>	<b>97.78</b>	<b>71.92</b>	<b>37.68</b>	<b>60.1</b>

In order to compare the elemental composition before and after extraction and calculate the percentage of each element that had been solubilised, the oxide contents in the extracted ash analysed by XRF were normalised to the CaO content in the initial ash (Table 5.14). This assumes that all of the CaO remains in the ash during the extraction procedure. This is a reasonable assumption based on the low level of Ca observed in the biosilicate solutions (Table 5.10). This data confirms that significant levels of silicon, potassium, sodium, phosphorus and sulfur are all removed from the bottom ash during extraction. These were also the main species identified in the solutions (Table 5.10). The calculated removal of silica based on the XRF data is similar to that based on Si AAS analysis of the solution. This also confirms the minor solubilisation of iron and aluminium. The lower total oxide sum for the extracted ash may be due to an enrichment of any unburnt carbon in the ash.

The  $^{29}\text{Si}$  MAS NMR spectra (Figure 5.22) of the ash before and after extraction emphasise the changes that have taken place within the silica in the ash during extraction. The broad shape of the NMR spectra of the initial ash indicates that the silicon atoms are in a large range of structural environments with various  $Q^n$  assignments, bond angles and bond lengths.<sup>40</sup> Rice hull ash, calcined at 1100 °C, contained two single narrow peaks, centred at -110 and -112 ppm, in its  $^{29}\text{Si}$  MAS NMR spectra.<sup>41</sup> These were identified as due mainly to cristobalite and partially to tridymite by comparison with XRD data. Cristobalite was identified as the main crystalline phase by XRD analysis of Ely-BA1 ash (Figure 5.6), however, although the presence of  $Q^4$  species is signified by the shoulder around 110 ppm, the contribution of a disordered structure such as amorphous  $\text{SiO}_2$  or glass-like structures is apparent by the resonances over a wide-range of chemical shifts. Within both solid and liquid silicates, to a first approximation, the isotropic chemical shift is determined by the polymerisation of the  $\text{SiO}_4$  structural units, with an increasing chemical shift as  $Q^n$  increases, i.e.  $Q^0 < Q^1 < Q^2 < Q^3 < Q^4$  due to increasing shielding of the nucleus.<sup>40</sup> This can be correlated with the bond length and bond strength of the substituent atoms connected to the tetrahedral Si atom of interest.<sup>42</sup> The bond strength for  $O_b$  (Si-O-Si) atoms is generally greater than for  $O_{nb}$  (Si-OH) and therefore the greater the  $Q^n$  value the greater the shielding of the Si nucleus and the greater the high field chemical shift.<sup>40</sup> Overall, the bond strength of the nearest neighbour cation-oxygen bond influences the chemical shift, with weaker bonds causing a greater low field shift.<sup>42</sup> These have been connected with the changing hybridisation and s-character of the bridging O-atom.<sup>43</sup> The

broad peak of the Ely-BA1 ash narrows following extraction with two maxima at -85.6 and -90.9 ppm; the former increasing in relative intensity during the extraction process. These are associated with  $Q^2$  and  $Q^3$  type species,<sup>40, 44</sup> and may also correspond to increasing interaction with alkali or alkaline earth metal cations as observed in silicate glasses.<sup>40</sup> Peaks at -85 and -79 ppm were observed to develop upon hydration of rice hull ash silica with CaO due to formation of calcium-silicate-hydrate and associated with  $Q^2$  and  $Q^1$  sites respectively.<sup>45</sup> A band at -90 ppm in the initial rice hull ash was attributed to amorphous  $Q^2$  sites.<sup>29</sup>  $^{29}\text{Si}$  NMR spectra with increasing addition of sodium in sodium silicate glasses demonstrated a reduction in  $Q^4$  bands and downfield shifts to less negative  $\delta$  as the number of non-bridging oxygen atoms increased.<sup>40, 44</sup> Overall, this suggests that the extraction process breaks down the most cross-linked species leaving a residue consisting of  $Q^2$  and  $Q^3$  structures. The end-groups may be either silanol or potentially alkaline earth metal counter ions; this could be plausible due to the high concentration of calcium in the remaining ash.

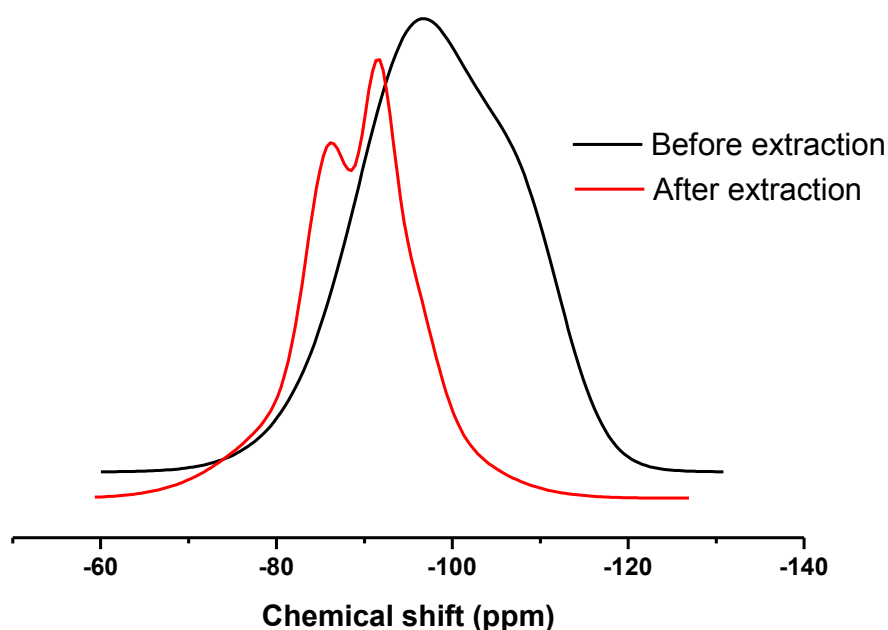


**Figure 5.22:**  $^{29}\text{Si}$  NMR of Ely-BA1 before and after extraction (Originally in colour)

XRD analysis, comparing the Ely-BA1 ash before and after extraction (Figure 5.23), indicates the continued presence of cristobalite, although the intensity is reduced relative to the background halo. This suggests an overall increase in amorphous or glassy material

following extraction relative to crystalline. In addition, a broad peak centred around  $29^\circ$  may be due to calcium carbonate or some form of calcium silicate hydrate.

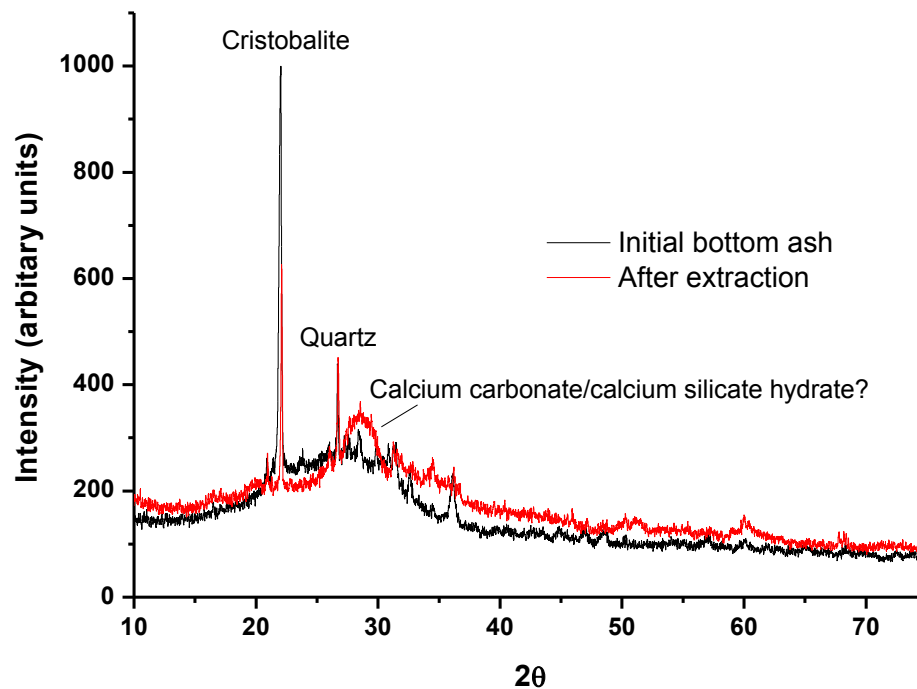


**Figure 5.23: XRD of initial Ely-BA1 and Ely-BA1-15 residue following silica extraction and washing to remove residual silicate (Originally in colour)**

### 5.9.2 Test hardened blocks

The analyses of the residual solid indicated that the major species remaining are silica and calcium along with some residual potassium silicate solution in the unwashed samples. Comparisons to the formation of alkali-activated cements and the chemical composition of cement suggest that this may be useful for the formation of a hardened binder, especially as alkali silicate solutions have been found to be the most effective alkaline activator for many cement systems.<sup>46</sup> Initial tests showed that on drying the black sludge following silicate recovery, without water washing, an extremely hard material formed. XRD analysis identified significant changes occurring during the drying process (Figure 5.24). In particular, the cristobalite vestiges disappear, alongside the development of calcium silicate hydrates, the main components of portland cement.<sup>46</sup> This further highlights the possible use of this remaining material for the production of concrete or cement blocks.

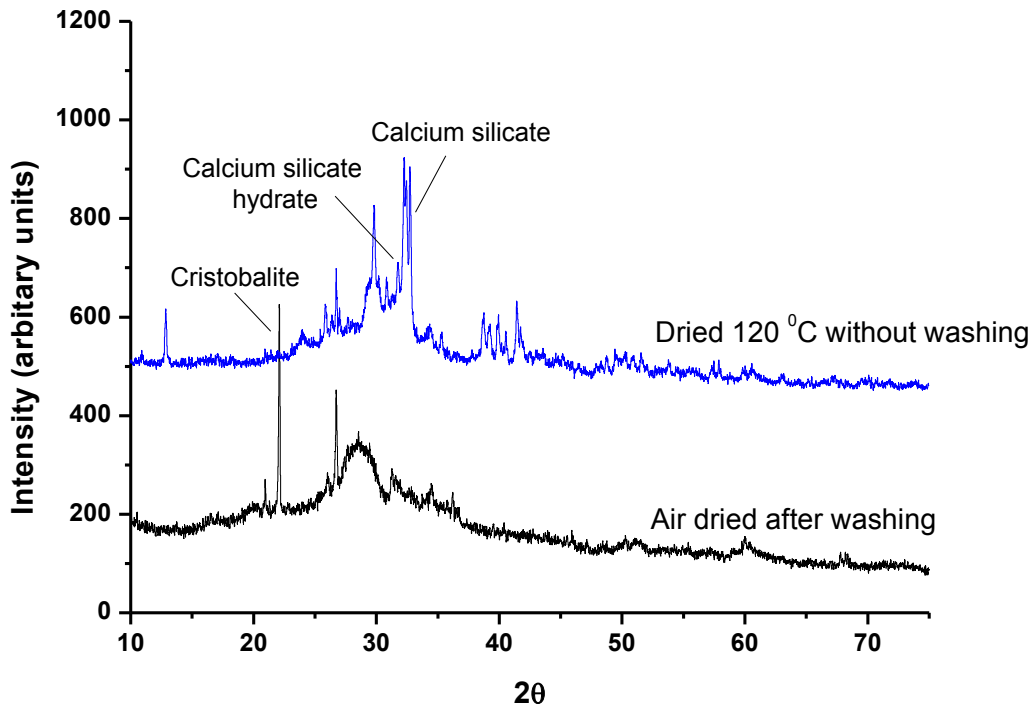


**Figure 5.24: XRD of residual Ely-BA1 material after silicate extraction and drying with or without washing**

To test this hypothesis several bricks composed of the residual black sludge were formed in a mould and left to dry for 3 days within the mould, followed by several days in air outside of the mould. As can be observed (Figure 5.25) cracks appeared in many of the blocks during the setting process. This appeared to be caused by shrinkage of the material during setting as condensation of the silicate species progressed. These blocks were subject to 3-point bending tests to test their strength (Figure 5.26, Table 5.15). These results show that the formation of cracks negates any bonding force in the material. Those blocks where cracks did not form showed a high flexural strength, around half that of various alkali-activated slag cements.<sup>46</sup> The compressive strengths of these materials were not tested due to the lack of the necessary testing equipment.

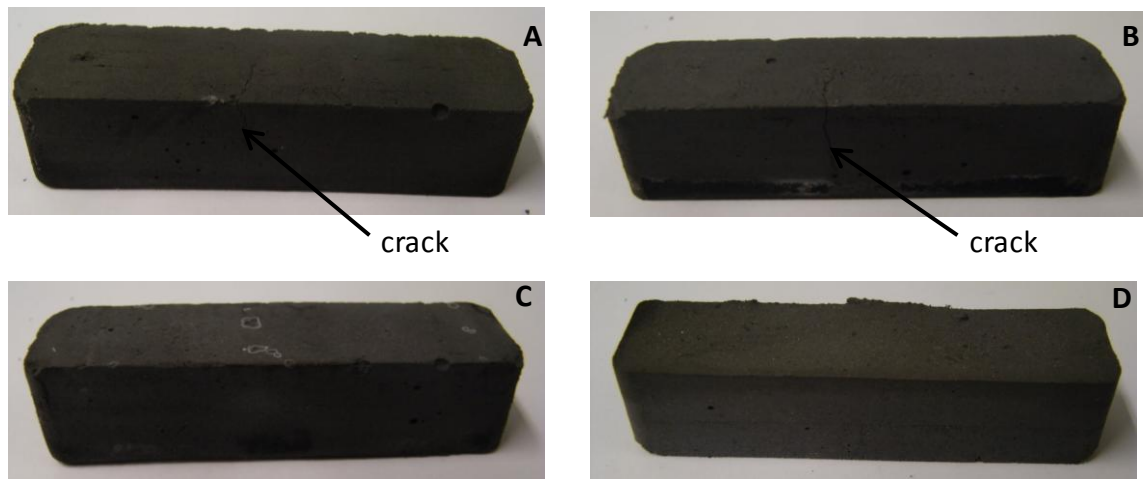


Figure 5.25: Blocks formed from biosilicate ash residue showing samples where cracks have formed on drying after A: 2 days; B and C: 7 days; D 9 days air drying

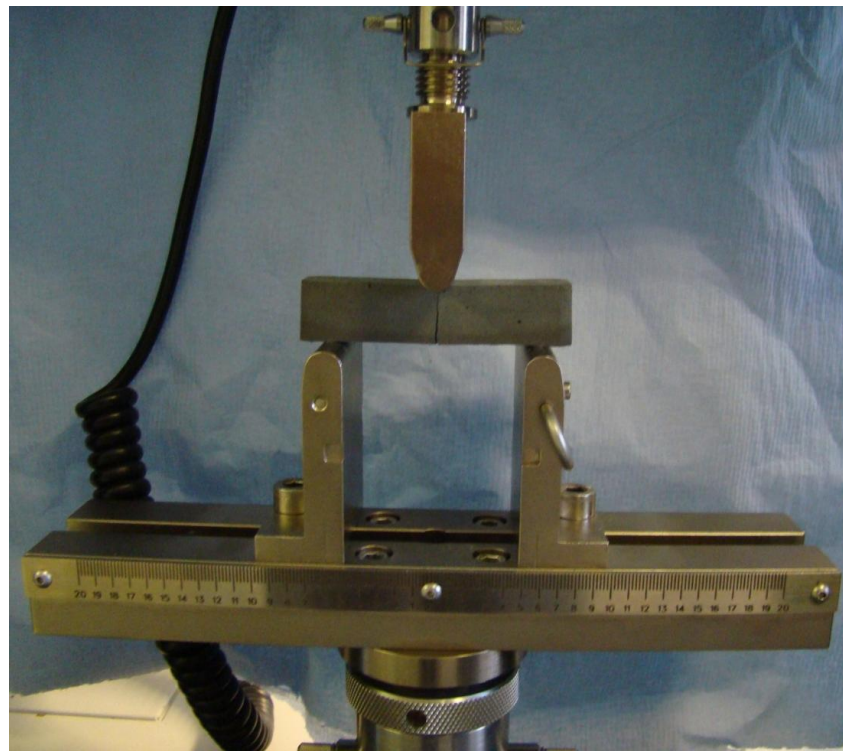


Figure 5.26: 3-point bending test set-up

Table 5.15: Initial 3-point bending test results

Name	Setting time (days)	Dimensions (mm)			Crack seen before analysis?	Maximum stress (MPa)	Maximum load (N)
		Length	Width	Height			
A	2	77.6	19.6	19.0	Yes	0.27	22.1
C	7	76.3	19.5	19.1	No	1.00	81.9
D	9	76.9	19.3	17.2	No	1.80	111
E	30	73.0	18.9	18.6	Yes	0.064	3.9

Researchers have also observed that alkali-activated cement pastes formed from blast furnace slag demonstrate greater drying shrinkage than Portland cements.<sup>46</sup> This was greatest as the lime content of the system decreased and under dry conditions. Setting of the material under humid conditions may reduce the shrinkage and therefore the formation of cracks. However, there was insufficient time to study this possibility further. Nevertheless, this demonstrates that the residue of miscanthus bottom ash following recovery of an alkali silicate solution may be suitable for utilisation in construction materials, as a binder or by forming solid blocks.

### **5.10 Conclusions and Further Work**

This work has shown that different biomass materials, specifically miscanthus and wood chips, show varying elemental solubility trends with combustion temperature, dependent on their initial inorganic composition. The low solubility of silica from wood chip ashes could be attributed to the formation of insoluble calcium silicate. The trends for miscanthus were comparable to wheat straw, highlighting their similarities as herbaceous grasses, with significant levels of silica extracted by the inherent alkali content but reducing at combustion temperatures above 500 °C.

The fly ashes and bottom ashes obtained from the large-scale combustion of miscanthus straw and wood chips displayed greater similarities with comparable partitioning of elements between the two ash deposits. Greater potassium, chlorine and sulfur levels were found in the fly ash, mainly as sylvite, whilst chiefly crystalline silica remained in the bottom ashes.

The extraction of silica from the miscanthus straw based bottom ashes was achieved utilising a highly alkaline potassium hydroxide solution. The extraction could be controlled to produce a solution of similar concentration and ratio to the commercially available silicate solutions. Initial tests also suggested that a concentrated alkaline solution could be formed from the fly ash. This could dissolve some of the silica within the bottom ash, however, it was not sufficiently alkaline to dissolve the majority.

The solutions produced using potassium hydroxide extractants were tested as binders for the formation of inorganic composite boards with a wheat straw substrate. The results for both the internal bond strength were promising, however, further work is necessary to study the production of solutions with varying concentrations and weight ratios and to

improve the water swelling of the boards. In addition, it would be interesting to study the use of CO<sub>2</sub> as a hardener to set the binder, which could be obtained from the combustion facility in an integrated system. Furthermore, this work suggests that using a substrate with a higher silica content, such as rice hulls, rice straw or sugarcane could potentially enable the production of boards directly using the *in situ* silica content within the biomass as part of the binder.

A new IR method for the analysis of the silica concentration in the solutions was developed enabling the fast, rapid and accurate assessment of the concentration of the solution formed. However, the data obtained indicated that the relationship between the peak area and silica concentration varied with the silicate solution molar ratio. Further exploration of this relationship and the association of spectral peaks with silicate solution structures are needed to extend the applicability of IR spectroscopy in the study of silicate solutions.

Initial tests demonstrated that the residue from the formation of potassium silicate solutions from the Ely-BA1 ashes is a potential structural material for the partial replacement of cement. This is especially valuable as cement production is a highly energy intensive process. Much further work would need to be applied to studying this process, especially to reduce the formation of cracks on shrinkage during drying and to study the properties of the material formed in more detail.

## **5.11 References for Chapter 5**

1. A. Pettersson, L. E. Amand and B. M. Steenari, *Fuel*, 2009, **88**, 1758-1772.
2. P. Thy, B. M. Jenkins, S. Grundvig, R. Shiraki and C. E. Lesher, *Fuel*, 2006, **85**, 783-795.
3. R. Rajamma, R. J. Ball, L. A. C. Tarelho, G. C. Allen, J. A. Labrincha and V. M. Ferreira, *J. Hazard. Mater.*, 2009, **172**, 1049-1060.
4. Biomass Energy Centre,  
[http://www.biomassenergycentre.org.uk/portal/page?\\_pageid=75,18521&\\_dad=portal&\\_schema=PORTAL](http://www.biomassenergycentre.org.uk/portal/page?_pageid=75,18521&_dad=portal&_schema=PORTAL), Accessed 15/03/11.
5. F. B. Salisbury and C. W. Ross, *Plant Physiology*, Fourth edn., Wadsworth, California, 1992.
6. R. W. Bryers, in *Impact of Mineral Impurities in Solid Fuel Combustion*, eds. R. Gupta, T. Wall and L. Baxter, Kluwer Academic / Plenum Publishers, New York, Editon edn., 1999, pp. 105-131.
7. A. Monti, N. Di Virgilio and G. Venturi, *Biomass Bioenerg.*, 2008, **32**, 216-223.
8. A. Barneto, J. Carmona, J. E. Alfonso and L. Alcaide, *Bioresour. Technol.*, 2009, **100**, 3963-3973.
9. J. M. Jones, M. Nawaz, L. I. Darvell, A. B. Ross, M. Pourashanian and A. Williams, in *Science in Thermal and Chemical Biomass Conversion*, ed. A. Bridgewater, Blackwell Science Ltd, Oxford, Editon edn., 2006, pp. 331-339.

10. T. R. Miles, T. R. Miles, L. L. Baxter, R. W. Bryers, B. M. Jenkins and L. L. Oden, *Biomass Bioenerg.*, 1996, **10**, 125-138.
11. M. S. Tianinen, J. S. Ryyanen, J. T. Rantala, H. Tapio Patrikainen and R. S. Laitinen, in *Impact of Mineral Impurities in Solid Fuel Combustion*, eds. R. Gupta, T. Wall and L. Baxter, Kluwer Academic / Plenum Publishers, New York, Editon edn., 1999, pp. 217-224.
12. R. K. Iler, *The Chemistry of Silica*, Wiley & Sons, New York, 1979.
13. L. L. Baxter, T. R. Miles, T. R. Miles, B. M. Jenkins, T. Milne, D. Dayton, R. W. Bryers and L. L. Oden, *Fuel Process. Technol.*, 1998, **54**, 47-78.
14. P. A. Jensen, B. Sander and K. Dam-Johansen, *Biomass Bioenerg.*, 2001, **20**, 447-457.
15. J. L. Bass and G. L. Turner, *J. Phys. Chem. B*, 1997, **101**, 10638-10644.
16. I. Halasz, M. Agarwal, R. Li and N. Miller, *Catal. Lett.*, 2007, **117**, 34-42.
17. J. S. Falcone, J. L. Bass, M. Angelella, E. R. Schenk and K. A. Brensinger, *Ind. Eng. Chem. Res.*, 2010, **49**, 6287-6290.
18. J. W. Phair and J. S. J. Van Deventer, *Int. J. Miner. Process.*, 2002, **66**, 121-143.
19. C. T. Kirk, *Phys. Rev. B*, 1988, **38**, 1255.
20. E. Greiner-Wronowa, C. Paluszkiwicz and L. Stoch, *J. Mol. Struct.*, 1999, **512**, 199-204.
21. C. C. Perry, X. Li and D. N. Waters, *Spectrochim. Acta A-M.*, 1991, **47**, 1487-1494.
22. J. R. Martinez, F. Ruiz, Y. V. Vorobiev, F. Perez-Robles and J. Gonzalez-Hernandez, *J. Chem. Phys.*, 1998, **109**, 7511-7514.
23. F. Gervais, A. Blin, D. Massiot and J. P. Coutures, *J. Non-Cryst. Solids*, 1987, **89**, 384-401.
24. F. L. Galeener, *Phys. Rev. B*, 1979, **19**, 4292.
25. J. L. Bass, G. L. Turner and M. D. Morris, *Macromol. Symp.*, 1999, **140**, 263-270.
26. I. Halasz, M. Agarwal, R. Li and N. Miller, *Micropor. Mesopor. Mat.*, 2010, **135**, 74-81.
27. J. Osswald and K. T. Fehr, *J. Mater. Sci.*, 2006, **41**, 1335-1339.
28. I. Halasz and A. Derecskei-Kovacs, *Mol. Simul.*, 2008, **34**, 937-942.
29. J. R. B. Gomes, M. Cordeiro and M. Jorge, *Geochim. Cosmochim. Ac.*, 2008, **72**, 4421-4439.
30. J. S. Falcone Jr, J. L. Bass, P. H. Krumrine, K. Brensinger and E. R. Schenk, *J. Phys. Chem. A*, 2010, **114**, 2438-2446.
31. G. V. Gibbs, M. B. Boisen, F. C. Hill, O. Tamada and R. T. Downs, *Phys. Chem. Miner.*, 1998, **25**, 574-584.
32. I. D. Brown and R. D. Shannon, *Acta Crystallogr. A*, 1973, **29**, 266-282.
33. A. V. McCormick, A. T. Bell and C. J. Radke, *J. Phys. Chem-US.*, 1989, **93**, 1733-1737.
34. M. J. Mora-Fonz, C. R. A. Catlow and D. W. Lewis, *J. Phys. Chem. C*, 2007, **111**, 18155-18158.
35. S. D. Kinrade and D. L. Pole, *Inorg. Chem.*, 1992, **31**, 4558-4563.
36. C. A. Rees, J. L. Provis, G. C. Lukey and J. S. J. van Deventer, *Langmuir*, 2007, **23**, 9076-9082.
37. J. Sanchez and A. McCormick, *Chem. Mater.*, 1991, **3**, 320-324.
38. J. L. Provis, P. Duxson, G. C. Lukey, F. Separovic, W. M. Kriven and J. S. J. van Deventer, *Ind. Eng. Chem. Res.*, 2005, **44**, 8899-8908.
39. H. Jiang, Y. Zhang and X. F. Wang, *Ind. Crop. Prod.*, 2009, **30**, 304-310.
40. G. Engelhardt and D. Michel, *High-Resolution Solid-State NMR of Silicates and Zeolites*, John Wiley, New York, 1987.
41. D. G. Nair, A. Fraaij, A. A. K. Klaassen and A. P. M. Kentgens, *Cement Concrete Res.*, 2008, **38**, 861-869.
42. K. A. Smith, R. J. Kirkpatrick, E. Oldfield and D. M. Henderson, *Am. Mineral.*, 1983, **68**, 1206-1215.

43. G. V. Gibbs, *Am. Mineral.*, 1982, **67**, 421-450.
44. H. W. Nesbitt, G. M. Bancroft, G. S. Henderson, R. Ho, K. N. Dalby, Y. Huang and Z. Yan, *J. Non-Cryst. Solids*, 2011, **357**, 170-180.
45. R. F. Abreu and J. S. M. A. Cincotto, *J. Am. Ceram. Soc.*, 2005, **88**, 1514-1520.
46. C. Shi, P. V. Krivenko and D. Roy, *Alkali activated cements and concretes*, Taylor & Francis, Abingdon, 2006.



# **Chapter 6:**

# **Materials and Experimental Methods**



## **6.1 Chemicals**

Chemicals were purchased from Aldrich, Sigma and Fisher and were used without purification. Potassium silicate and sodium silicate solutions of various concentrations and molar ratios were obtained from PQ Corporation. Supercritical grade carbon dioxide (99.99%) was purchased from BOC Ltd. and was used without purification. Analytical grade solvents including ethanol, acetone, hexane and dichloromethane were purchased from Fisher Scientific.

Si and K AAS standards (1000ppm) and palladium oxide (99.995%) were purchased from Aldrich. KOH (86.1%), KCl (99.6%), NaOH (99.1%), NaCl, glacial Acetic acid, HCl (36% w/w) and pH buffer solutions (pH 4, 7, 9.1, 10 and 12) were obtained from Fisher. Soxhlet cellulose extraction thimbles came from Fluka.

## **6.2 Experimental details and instrumentation for Chapters 2, 3 and 4**

### **6.2.1 Straw collection and processing**

*Triticum aestivum* (wheat) straw was collected over three years from G & H Cholmley, at either their Castle Howard or Wintringham farms, following harvesting. The varieties of straw collected were Claire (2007, 2008 and 2009), Robigus (2008 and 2009), Najinsky (2008) and Viscount (2009). In 2007 and 2009 the straw was collected from baled material a few weeks after harvesting. In 2008 the straw was collected directly from the field. Potassium, phosphate, nitrogen and sulphate fertilisers were applied during the year.

Fresh plant material was transported in paper sacks. Material from 2007 and 2009 was air dried for 3 weeks in the lab. Claire, Robigus and Nijinsky varieties from 2008 were dried at 105 °C for 3 h. This may have affected their surface properties so these straws were only used for combustion and ash extraction tests.

Following drying, the straw was chopped using a Glen Creston cutting mill (equipment number: 15190) with a passing screen of 2mm and stored in the laboratory in paper sacks at room temperature prior to use.

### **6.2.2 Thermogravimetric analysis of wheat straw**

The inorganic content and moisture content of the initial and pretreated milled wheat straws were obtained on a Netzsch 409 Simultaneous Thermal Analyser. Wheat straw

(~150 mg) was accurately weighed into a dry and clean porcelain cup, heated at  $10 \text{ K min}^{-1}$  from  $20 \text{ }^\circ\text{C}$  to  $550 \text{ }^\circ\text{C}$  under  $150 \text{ mL min}^{-1}$  air and  $50 \text{ mL min}^{-1}$   $\text{N}_2$  and held until no further mass loss was observed. The moisture content and inorganic content were calculated based on triplicate measurements. The moisture content was calculated as the percentage mass loss between  $0 - 120 \text{ }^\circ\text{C}$  (Equation 6.1). The inorganic content on a dry basis was calculated as shown in Equation 6.1.

$$\% \text{ inorganic (dry basis)} = [100 / (\% \text{ mass loss} - \% \text{ mass loss to } 120^\circ\text{C})] \times \% \text{ residual mass}$$

### Equation 6.1

The volatile and fixed carbon contents were analysed using the same procedure with a flow of  $100 \text{ mL min}^{-1}$  nitrogen. Air was removed by vacuuming down the system and backfilling with nitrogen two times. The fixed carbon content was calculated as the difference between the remaining mass at  $550 \text{ }^\circ\text{C}$  and the average ash content. The volatile carbon content was calculated as the mass loss between  $120 \text{ }^\circ\text{C}$  and  $550 \text{ }^\circ\text{C}$ .

### 6.2.3 Simultaneous Thermal Analysis of wheat straw and chars

Thermogravimetric analysis (TG) and differential scanning calorimetry (DSC) were carried out simultaneously on a PL Thermal Sciences STA 625. Milled wheat straw (1.5 mg) or chars (10 mg) were accurately weighed into an aluminium TGA pan and analysed against an empty aluminium reference pan from  $20^\circ\text{C}$  to  $625^\circ\text{C}$  at a heating rate of  $5 \text{ K min}^{-1}$  under a  $60 \text{ mL min}^{-1}$  flow of air. Where the calorific value of the char was to be analysed powdered palladium oxide (35 mg) was added to cover the surface of the char to ensure that complete oxidation of the gases occurred. Analyses were carried out in duplicate. The calorific content was calculated on a dry basis using the following equation:

$$\text{Joules gram}^{-1} = [(4.19 \times 100 \times \Delta Q) / (100 - \text{moisture } \%) ] / 1000$$

### Equation 6.2

### 6.2.4 Calorific value of wheat straw

The calorific value of milled wheat straw was measured using a Parr 6200 Calorimeter. Distilled water ( $2000 \pm 1 \text{ mL}$ ) was weighed into a bucket and heated to a constant temperature. Milled water straw ( $0.5 - 1 \text{ g}$ ) was weighed accurately into a cup, mixed with 10 drops of distilled water and left to soak for 30 min to produce a slow and

complete combustion. The cup was placed in the bomb with a fuse wire suspended over the sample, sealed, filled with pure oxygen at pressure and lowered into the water bucket. Ignition, measurement of the temperature rise within the bucket and calculation of the energy content of the sample was calculated automatically by the calorimeter. A benzoic acid standard was used to calibrate the calorimeter which gave an average of  $26.46 \pm 0.09 \text{ MJ kg}^{-1}$  over 10 runs.

### 6.2.5 CHN analysis

Elemental analysis based on carbon, hydrogen and nitrogen content was carried out using an Exeter Analytical (Warwick, UK) CE440 Elemental Analyser, calibrated against acetanilide with a S-benzyl-thiuronium chloride internal standard. Duplicate analyses of each sample were carried out and the average taken.

### 6.2.6 Typical combustion and extraction procedure

Milled wheat straw (10.0 g) was accurately weighed into a porcelain crucible and combusted in a Barnstead Thermolyne 6000 furnace. The furnace was heated to the desired temperature and equilibrated for 5 minutes before the crucible was added and combustion occurred for a set period of time. The crucibles were removed. Ash for analysis that required no further treatment was cooled in air and stored in plastic bags.

Typically on removal from the furnace the ash was either quenched directly or cooled in air before adding to the extraction solution (25 mL distilled water or KOH solution), sealed in a polypropylene bottle and stirred at 450 rpm for 24 h, or the specified time. Where heating was required the polypropylene bottles were added to oil baths heated to the desired temperature, or heated under reflux in Teflon round-bottomed flasks. Following extraction the ashes were filtered under vacuum. The solutions were further filtered through  $0.22 \mu\text{m}$  Millex membrane filters to remove fine particulates and the residual ashes were dried before analysis. Some extractions were repeated in triplicate to test the reproducibility. Polypropylene equipment was used for all extraction, storage and analytical processes to prevent silica contamination from glassware.

When cooling under controlled conditions, such as argon or carbon dioxide, was required, combustion was carried out in a long-necked quartz flask with a quartz tube placed into the flask. Before removal of the flask from the furnace the required gas was added for 3 minutes at  $0.2 \text{ L min}^{-1}$  via the glass tube and on removal a flow of  $0.2 \text{ L min}^{-1}$  continued to

be added until the ash was completely cooled. The ash was then added to distilled water and extracted as described above, or stored for analysis.

### 6.2.7 pH measurements

PH measurements of solutions were performed using a Jenway 3505 pH meter attached with a glass Thermo Scientific Russell Ultra high accuracy K-series polymer reference electrode. Calibrations using NIST buffer solutions of either pH 4 and 7 or pH 7 and 12 were carried out prior to analysis. PH's of solutions were recorded once no change  $\pm 0.01$  was observed.

### 6.2.8 Atomic Absorption Spectroscopy (AAS)

Potassium and silicon concentrations of the extracted solutions were analysed using a Hitachi Z5300 Polarised Zeeman Atomic Absorption Spectrometer (AAS).

Silicon concentrations were analysed using the 251.6 nm line by a hollow cathode Si lamp with a high temperature burner and a combined nitrous oxide-acetylene flame under stoichiometric conditions. Flow rates were generally  $5.6 \text{ L min}^{-1} \text{ C}_2\text{H}_2$ ,  $6.2 \text{ L min}^{-1} \text{ N}_2\text{O}$  with a 7.5mm burner height and 12mA lamp current. 0.2 % w/v KCl was added to all solutions to reduce ionisation. Prior to aspiration of the samples the burner was heated for 10 minutes with a  $5.0 \text{ L min}^{-1}$  flow of  $\text{C}_2\text{H}_2$  before increasing to the analysis flow rate.

Typically calibration solutions between 0 – 1000 ppm silicon were made up in polypropylene volumetric flasks using Purelite distilled water. Samples were diluted with Purelite distilled water, using calibrated automatic pipettes and polypropylene volumetric flasks, to the required concentration and analysed alternated with a standard of similar concentration. This was required due to graphite build-up on the burner altering the detected concentration. When the measurement of the standard varied by 10 % from the initial measurement (typically following 15 – 20 samples) the burner was cleaned. Concentrations of the samples were found by normalising the absorption against the expected absorption of the standard run prior and following it and using this to calculate the concentration from the calibration curve. Each sample was run in duplicate and the average obtained. Where the error between duplicate samples was greater than 5% further repeat measurements were run. Typically, errors were in the order of less than 3% or below the limit of detection.

Potassium concentrations were analysed from the 766.5 nm line using a hollow cathode potassium lamp and a low temperature burner with an air-acetylene flame. Flow rates were 2.4 L min<sup>-1</sup> acetylene and 15.0 L min<sup>-1</sup> air with a 7.5 mm burner height, 10 mA lamp current. 0.5% w/v NaCl was added to all solutions to reduce ionisation. Calibration standards containing 0, 1, 2, 5 and 7.5 ppm potassium were made up in polypropylene volumetric flasks with Purelite distilled water. All samples were analysed in duplicate. Errors were calculated as the variation from the average response. Typically errors were in the order of less than 5% or below the limit of detection.

### 6.2.9 Transmission Electron Microscopy (TEM)

TEM micrographs were recorded by Dr Meg Stark at the Department of Biology, University of York. A small sample (1 mg) was added to ethanol and shaken. Following settling, a drop was added to a carbon grid and allowed to dry before analysis.

### 6.2.10 Nitrogen adsorption studies

Nitrogen adsorption measurements were carried out at 77 K using a Micromeritics ASAP 2010 volumetric adsorption analyser. Prior to analysis, finely ground samples were outgassed at 120 °C for 1 h under vacuum. Specific surface areas ( $S_{\text{BET}}$ ) were analysed using the Brunauer, Emmett and Teller (BET) method based on the cross-sectional surface area of the nitrogen molecule in the relative pressure range from 0.06 to 0.15. A micropore analysis method (MP method) was used to evaluate the microporous volume of the samples and the pore size distribution of the materials.

### 6.2.11 X-Ray Fluorescence

Elemental analyses of solid samples were undertaken by Mr Robert Burton at Sheffield Hallam University. Quantitative analysis was carried out by fusing ground ashes with lithium tetraborate ( $\text{Li}_2\text{B}_4\text{O}_7$ ) in a 10:1 ratio in a platinum crucible at 1200 °C for 12 minutes. The flux was then cooled in a round container to produce a flat solid disc that was studied for all the major oxides.

Semi-quantitative elemental analysis of ashes before and after extraction under different combustion conditions was performed on a Horiba XGT 7000 X-ray analytical microscope. Ground samples of straw, ash or char (~1 g) were compressed into a holder and analysed using a standardless independent parameters method. Each measurement was repeated five times and the average was taken.

### 6.2.12 Powder X-Ray Diffraction

A Bruker-AXS D8 Advance diffractometer with a Kristalloflex 760 X-ray generator which produces monochromatic  $K\alpha$  X-rays from a copper source was employed. The sample to be studied was finely ground and the powdered material was placed and levelled within a small round hole bevelled out of an aluminium sample holder. Scans were taken across the range 5 - 80  $2\theta$  over 14 minutes with a 45 kV voltage and 20 mA current. The evaluation programme EVA and the Bruker CDS database were used to identify the phases present in the samples.

### 6.2.13 Infrared Spectroscopy

Infrared absorption spectra were obtained on a Bruker Vertex 70 FTIR spectrometer equipped with a MKII Golden Gate Single Reflection ATR System with a 45° diamond crystal. Solid samples were finely ground, placed on the crystal surface and then clamped tightly to the crystal using a sapphire anvil. Liquid samples were analysed without any preparation, a small drop was placed covering the crystal surface. Spectra were taken from 4000  $\text{cm}^{-1}$  to 600  $\text{cm}^{-1}$  at 64 scans with a spectral resolution of 4  $\text{cm}^{-1}$ . Spectra were recorded with either a water or blank window for the background. Analysis was carried out using Bruker OPUS software.

### 6.2.14 Ion Chromatography

A Dionex ICS2000 was used with an eluent generator and a Dionex IonPac AS18 column under the supervision of Rebecca Sutton in the Environment Department at the University of York. KOH was used as the eluent. Five standards containing varying concentrations of  $\text{Cl}^-$ ,  $\text{NO}_3^-$ ,  $\text{SO}_4^{2-}$  and  $\text{PO}_4^{3-}$  were made up using freshly deionised water. Samples were diluted to concentrations within the range of the standards.

### 6.2.15 Inductively Coupled Plasma Atomic Emission Spectroscopy (ICP-AES)

Inductively Coupled Plasma - Atomic Emission Spectroscopy (ICP-AES) data presented in this report were carried out by Yara Analytical Services, York and were analysed for 39 inorganic elements.

### 6.2.16 Solution Nuclear Magnetic Resonance

$^1\text{H}$  NMR were carried out using a JEOL JNM-ECS400 NMR operating at 400 MHz. A single pulse acquisition method was used with a relaxation delay of 4 s. 1024 scans were taken for each sample. The chemical shifts were recorded at 25 °C in  $\text{D}_2\text{O}$ .

### 6.2.17 Solid State Nuclear Magnetic Resonance

Solid state  $^{29}\text{Si}$  NMR was carried out by the Solid State NMR Research Service at the University of Durham using a Varian Unity Inova spectrometer operating at 59.56 MHz for  $^{29}\text{Si}$ . Spectral referencing was with respect to neat, external tetramethylsilane. The spectra were recorded with direct excitation and a 30 s recycle delay.

## 6.3 Experimental details and instrumentation for Chapter 3

### 6.3.1 Typical Soxhlet extraction of wheat straw

Air-dried milled wheat straw (variety Claire, harvested 2007, 10g) was weighed into a cellulose Soxhlet thimble and placed in a standard Soxhlet extraction apparatus. The straw was extracted with ethanol or hexane (300 mL) at reflux for 2 or 5 hours. The resulting solution was collected, concentrated to dryness on a rotary evaporator and the remaining extract was weighed. The pretreated wheat straw was air dried to constant weight.

### 6.3.2 Typical supercritical carbon dioxide extraction

Supercritical carbon dioxide ( $\text{scCO}_2$ ) wax extractions were carried out using a Thar Technologies  $\text{scCO}_2$  rig. Air-dried milled wheat straw (variety Claire, harvested 2007, 30g) was loaded into an extraction vessel and fitted into the extraction system. The reaction vessel and pre-heater were heated to the required temperature (40-100 °C) before supercritical carbon dioxide was allowed to pass into the extractor vessel. Once the required pressure (100-300 bar) had been reached,  $\text{scCO}_2$  containing extracted material entered into the collector vessel (maintained at 40 °C). The desired pressure was maintained by a Thar Technologies ABPR-200 automated back pressure regulator. Extractions were carried out for 2 hours at a constant flow rate of  $40 \text{ g min}^{-1}$ . Following completion of the extraction the system was depressurised at  $12 \text{ bar min}^{-1}$ . Extracts were collected by washing out the collector with DCM, evaporating the solvent to dryness at room temperature and recording the mass of lipids obtained. The extracted straw was stored as removed in plastic bags.

### 6.3.3 Acid and water leaching of wheat straw

Wheat straw (variety Claire, harvested 2007) was leached with distilled water and acid solutions (0.5 M HCl, 1 M Acetic acid, 1 M Citric acid). Air-dried milled wheat straw (10.0 g) was added to a 500 mL polypropylene flask containing the desired leachate (200 mL). Extractions were carried out in a shaking Julabo SW22 water bath previously heated to the required temperature (25 or 50 °C) for 1 or 6 hours at 150 rpm. The material was immediately filtered, initially through a Buchner filter, followed by filtering of the resultant solution through a 0.22 µm Millex membrane filter. The solutions were stored in sealed polypropylene bottles until analysis. The acid washed straw was further washed with distilled water until the washing water showed a neutral pH. All straw was oven dried at 40 °C to constant weight.

### 6.3.4 Differential Scanning Calorimetry of lipids

Differential Scanning Calorimetry (DSC) measurements of the lipids extracted from the wheat straw were carried out on a Seiko SII Exstar6000. Lipid extract (10 mg) was placed in the base of an aluminium sample pan and analysed under nitrogen using a four-stage heating profile to remove any prior thermal character. The sample was initially cooled to -50 °C then heated to 110 °C at 5 °C min<sup>-1</sup>, then cooled at the same rate back down to -50 °C. This was then repeated. The measurements were recorded against an empty aluminium sample pan.

### 6.3.5 Fusion tests

Pretreated straw (5 g) for melting and fusion tests was combusted in a porcelain crucible to 550 °C at 5 °C min<sup>-1</sup> (held at 250 °C for 60 min and 550 °C for 10 h). The samples were then finely ground and sent for analysis by Dr Phil Davies at Thermal Analysis Instruments. Samples were analysed under nitrogen and heated initially to 1400 °C at 20 °C min<sup>-1</sup>, cooled to 550 °C, then heated to 1400 °C at 20 °C min<sup>-1</sup> again before cooling to room temperature.

Fusions tests were carried out on the same ashes in a Barnstead Thermolyne 6000 furnace under a flow of nitrogen. Pellets (12.8 mm diameter) of the ashes were formed using a Parr pellet press and placed on a steel plate. The temperature was ramped at 5 °C min<sup>-1</sup> to 1000 °C. Photographs of the pellets were taken between 500 °C and 1000 °C.

## **6.4 Experimental details and instrumentation for Chapter 4**

### **6.4.1 Microwave pyrolysis procedure**

The microwave treatment of wheat straw was carried out using a Milestone ROTO SYNTH Rotative Solid Phase Microwave Reactor (Milestone Srl., Italy) fitted with a VAC 2000 vacuum module in series. The average sample mass was between 150 and 200 g. Samples were exposed to a maximum microwave power of 1200 W with an operating microwave frequency of 2.45 GHz (wavelength 12.2 cm) under fixed power conditions. The process temperature was maintained below 180 °C as measured by in-situ and infrared temperature probes. These measurements showed no significant difference in the temperature throughout the entire sample. The process pressure was monitored at all times.

### **6.4.2 Microwave char demineralisation**

Microwave pyrolysed wheat straw char (~20 g, variety Claire) was mixed with distilled water (150 mL) and heated in a Milestone RotoSYNTH microwave at 100 °C for 10 min. The resulting mixture was stirred overnight in a sealed bottle, filtered and stored. The leached char was dried at 40 °C.

### **6.4.3 Convection heating pyrolysis procedure**

Wheat straw (10 g) was weighed into a long-necked quartz flask and filled with argon for 2 min. The furnace was heated to the required temperature under a flow of nitrogen and the air vent from the furnace was almost completely sealed. When the desired temperature had been reached, the quartz vessel containing the sample was placed in the furnace with nitrogen flowing (200 mL min<sup>-1</sup>) into the flask from a long quartz tube. The furnace was sealed to reduce air entering the chamber. After 2 h the quartz flask was removed from the furnace and cooled under a flow of nitrogen. The extraction of the char then proceeded as for the combustion ashes (section 8.2.6).

## **6.5 Experimental details and instrumentation for Chapter 5**

### **6.5.1 Collection of residues from combustion boilers**

Samples (2 x 10 L of each) of bottom ash and fly ash were collected from Ely and Eccleshall Power Stations in May 2010. Samples of the miscanthus and wood chip starting materials were also collected from Eccleshall Power Station.

Before analysis and extraction bottom ash samples were dried at 105 °C and ground in a Retsch PM400 ball mill until the ash passed through a <125 µm sieve. Fly ash samples were used directly. Miscanthus and wood chip samples were air dried, chopped using a Glen Creston cutting mill (equipment number: 15190) with a passing screen of 2mm and stored in the laboratory in paper sacks at room temperature prior to use.

### **6.5.2 Water leaching of ashes**

Fly ash and ground bottom ash were mixed with distilled water with a liquid:solid ratio of 3:1 and stirred at room temperature for 24 h. The pH of the solutions was tested at regular intervals. Following extraction, the solutions were filtered and analysed by ICP-AES, IC and AAS.

### **6.5.3 Typical alkali extraction of bottom ashes**

Ground bottom ash (30 g) was added to a potassium hydroxide solution of the required concentration (1 – 10 M) made up in a volumetric flask using distilled water. The mixture was heated in a Teflon round-bottomed flask with stirring under reflux for 24 h and then separated by centrifuging for 30 min at 4000 rpm. The clear solution was decanted and stored in a sealed propylene bottle for further analysis. Some samples were concentrated on a rotary evaporator for use as a binder in board-making. The residual ash was directly air dried, or washed, until the washing waters were neutral, before drying.

### **6.5.4 Extraction of bottom ashes using fly ash extract**

Fly ash (400 g) was extracted with distilled water (2 L) with stirring for 1 h. The solution formed was filtered and concentrated to 100 mL and the alkalinity was tested by titrating with a 0.1 M HCl solution. The concentrated fly ash solution (15 mL) was mixed with ground bottom ash (4.4 g), with the extraction proceeding as described in section 6.5.3.

### **6.5.5 Typical board formation procedure**

5 x 5 cm boards were made in collaboration with and following a procedure developed by Dr Mario de Bruyn. Chopped straw was sieved to separate out the required 1 mm and 2 mm size fractions. These fractions were Soxhlet extracted using ethanol as described in section 6.3.1, air dried and combined in a 50:50 ratio (total 41 g). Silicate solution (12 – 13 g) was dropped over the straw in three aliquots and mixed thoroughly with the straw by hand. Where whey protein was used this was dissolved in water (0.9 g in 2.7 g water) and

added dropwise to the straw, half before and half after the silicate solution. The silicate-straw mixture was poured into a metal box on top of a metal platen and pre-pressed for 60 s. The metal box was removed, another metal platen was placed on top of the pre-pressed material, and the material was pressed for 8 min with a platen temperature of 210 °C and a distance between the plates of 11.7 mm. The boards were allowed to cool and the edges were removed to form a board of 5 x 5 cm.

The required amounts of straw, silicate solution and protein were calculated based on a square block with sides of 7.4 cm, thickness of 1.2 cm, density of 0.68 g cm<sup>-3</sup> and a final binder content of 15 wt%. These tests were carried out in collaboration with Dr Mario de Bruyn.

### **6.5.6 Internal bond strength test**

The majority of the internal bond strength tests were carried out at Bangor University by Dr Morwenna Spear. Prior to testing samples were conditioned for a week at 20 °C at a humidity of 65%. Tests were carried out on an Instron analyser at a pull rate of 10 mm min<sup>-1</sup>. Samples measured at York were carried out by Dr Mario de Bruyn using the same test profile. These samples were conditioned for only 1 day.

### **6.5.7 Water swelling test**

Water swelling tests were carried out by Dr Mario de Bruyn, these were not carried out according to British Standards due to insufficient material for testing the swelling of whole 5 x 5 cm boards. Instead, offcuts of the 5 x 5 cm boards were added to water for 24 h, followed by drying for 24 h. The water swelling was calculated from the difference in thickness before and after addition to water.

### **6.5.8 Block formation procedure for extraction residue**

Norms for testing hardened concrete (BS EN 12390) were used as a guideline to form hardened samples and to perform three point bend tests. Residual ash following alkali extraction (section 6.5.3) was spread into a Teflon mould (8 x 2 x 2 cm), shaken to remove air bubbles and cured for three days. The samples were then removed and dried at room temperature for a number of days. Three point bend tests (Instron 3367, preload: 2.5 mm min<sup>-1</sup> at a load of 0.2 MPa; test load rate: 2.4 MPa min<sup>-1</sup>) were run on several samples to examine their flexural strength.



# **Chapter 7:**

## **Concluding Remarks and Further Work**



## 7.1 Concluding remarks

The overall aim of this project was to study the reutilisation of the major ash components, predominantly silica and potassium, in wheat straw combustion residues to form alkali silicate binders for novel inorganic composite boards.

Initial tests on a laboratory scale were carried out on one variety of wheat straw. This work showed, for the first time, that the inherent alkali in unleached wheat straw was sufficient to solubilise up to 25% of the silica in the ash at room temperature. Combustion of wheat straw at temperatures below 600 °C gave the highest silica extraction by producing the most alkaline solutions, preventing calcium solubility and maintaining silica in a less crystalline form. Silica extraction was significantly increased by leaching under reflux. Optimised silica extraction, using only the inherent alkalinity, was achieved at combustion conditions of 500 °C for 2 h with leaching under reflux giving a silica extraction of 36%. Under these optimised conditions comparisons were made between different wheat straw varieties and straw collected in different years. This demonstrated that the straw varied in its initial inorganic composition, mainly dependent on their year of growth and specifically the level of rainfall causing the *in situ* leaching of soluble species. This initial composition influenced their combustion and pyrolysis decomposition, mineralogical ash composition, leaching of inorganic components, silica structure and alkalinity, which further affected silica extraction.

Studies were carried out on alternative routes to the recovery of inorganic species from wheat straw since the initial results had demonstrated that the greatest recovery of silica using the inherent alkalinity was achieved at lower temperatures than typically utilised in large-scale combustion facilities. Partial combustion of one wheat straw variety, Claire from 2007 was tested. Following leaching this produced a high surface area, narrowly distributed, ultramicroporous carbonaceous materials. This could potentially be a viable route to lower cost nano-structured porous templates or adsorbents, combined with recovery of the inorganics for recycling.

Wax extraction by Soxhlet and  $\text{scCO}_2$ , water washing and acid washing were successfully applied as pretreatment methods to study the impact on the thermochemical, mineralogical and ash extraction analysis of one variety of wheat straw, Claire 07. Water

washing and acid leaching demonstrated similar results to those found by previous researchers with substantial removal of inorganic species, however, acid leaching was required to significantly increase the ash fusion temperature.  $\text{scCO}_2$  treatment had the smallest impact on the straw for thermochemical purposes whilst ethanol extraction produced a reduction in K and Cl content similar to that achieved by water washing. This is believed to be the first reported observation of this effect. Pretreatment of straw by ethanol extraction prior to combustion therefore potentially provides an economic benefit by removing salts which could be recovered as fertilisers and valuable lipids without reducing the extraction of silica utilising the inherent alkalinity of the ashes. A biorefinery system by which these additional chemicals could be recovered was suggested.

Pyrolysis followed by char leaching of Claire 2007 wheat straw indicated highly promising results for the recycling of inorganic species and for the formation of an improved material for combustion. The chars demonstrated improved extractability of silica utilising the inherent alkalinity compared to ashes, with a maximum silica extraction of 44%, making them more suitable for direct potassium silicate production than combustion ashes. The leached chars had a lower ash content, lower potassium content, lower chloride content and higher calorific value making them more suitable for combustion.

Finally, the extraction of silica from the combustion residues from a commercial facility burning miscanthus straw was achieved utilising a highly alkaline potassium hydroxide solution. The extraction could be controlled to produce a solution of similar concentration and ratio to the commercially available potassium silicate solutions. Initial tests also suggested that a concentrated alkaline solution could be formed from the fly ash. This could dissolve some of the silica within the bottom ash, however, it was not sufficiently alkaline to dissolve the majority. The solutions produced using potassium hydroxide were tested as binders for the formation of inorganic composite boards with a wheat straw substrate. The results for the internal bond strength and water swelling were promising.

Overall, it has been demonstrated that alkali silicate solutions can be formed from biomass combustion residues and that these can be used as a binder for inorganic composite boards, however, there may be insufficient inherent alkalinity within the biomass to form entirely bioderived solutions. In addition, the evidence suggests that the

temperatures utilised in traditional combustion facilities will negatively affect the formation of alkali silicate solutions using the inherent inorganic species. Following an holistic and green chemistry approach to the utilisation of all valuable aspects of the material, alternative beneficial solutions appear to lie either with pretreatment by ethanol extraction with recovery of waxes and salts or pyrolysis followed by char leaching prior to combustion with recovery of bio-oils. Both of these approaches would enable additional valuable chemicals to be obtained alongside improving the combustion properties of the wheat straw by reducing its alkali and chloride content.

## **7.2 Further Work**

In order to assess the future potential for the ideas outlined above larger-scale tests of: ethanol extraction followed by combustion; pyrolysis and char washing followed by combustion; or silicate production from combustion residues would need to be carried out. From these both the economics and sustainability of the processes would need to be assessed in comparison with each other and in comparison with the traditional methods for the production of alkali silicates.

Work is also ongoing within the Green Chemistry Centre of Excellence and with collaborators to improve the formation of inorganic composite boards using both commercial and biomass derived alkali silicate solutions. It would also be of interest to study the end-of-life use of these boards and look at whether via pyrolysis or combustion it would be possible to reform the alkali silicate solutions for reuse as a binder.

It would also be of interest to study whether alternative uses could be found for the alkali silicate solutions formed from the combustion residues. Indeed, this work is being expanded upon by another PhD student, Emma Cooper, who is studying the use of combustion residues to form zeolites.

Finally, it would be of interest to undertake similar studies using other biomass materials individually and in combination to understand further how the initial inorganic composition can potentially be controlled to influence the flow and interaction of inorganic species during thermal processes and therefore their reutilisation.

## 7.3 Outcomes of the PhD

### 7.3.1 Published work

V. L. Budarin, P. S. Shuttleworth, **J. R. Dodson**, A. J. Hunt, B. Lanigan, R. Marriott, K. J. Milkowski, A. J. Wilson, S. W. Breeden, J. Fan, E. H. K. Sin and J. H. Clark, Use of Green Chemical Technologies in an Integrated Biorefinery, *Energy and Environmental Science*, 2010, **4**, 471-479.

**J. R. Dodson**, A. J. Hunt, A. S. Matharu, V. L. Budarin and J. H. Clark, The chemical value of wheat straw combustion residues, *RSC Advances*, DOI:10.1039/C1RA00271F.

**J. R. Dodson**, A. J. Hunt, H. L. Parker and J. H. Clark, Elemental Sustainability: Towards the total recovery of scarce metals, *Chemical Engineering and Processing: Process Intensification*, 2011. (Accepted for Special Edition)

**J. R. Dodson**, Green Communication: Getting the message across, *Chemistry & Industry*, 2009, **11**.

### 7.3.2 Patents

James H. Clark, Krzysztof J. Milkowski, **Jennifer R. Dodson**, Vitaly L. Budarin, *Biorefinery Products in Structural Materials*. Date of Publication 13/10/2010. Patent Number WO 2009/087360

### 7.3.3 Oral Presentations

- **Jennifer R. Dodson**, *The reutilisation of inorganic species from agricultural residues*, 1<sup>st</sup> Pan Africa Chemistry Network Green Chemistry Congress, Addis Ababa, Ethiopia, 15-17 November 2010.
- **Jennifer R. Dodson**, *The elemental value of ash*, BioTEN Conference, Birmingham, UK, 21 – 23 September 2010.
- **Jennifer R. Dodson**, *'Plants: Minerals and metals of the future?'*, Franco-British Collaboration Workshop, York, UK, 17 March 2010.
- **Jennifer R. Dodson**, *'Green Communication with Fabs the Frog'*, Creating Sustainable Laboratories Symposium, Bradford, UK, 30 April 2009.

### 7.3.4 Selected Poster Presentations

- **Jennifer R. Dodson**, *The reutilisation of inorganic species from agricultural residues*, Enhanced Landfill Mining Symposium, Molenheide, Belgium 4-6 October 2010.
- **Jennifer R. Dodson**, James H. Clark, Andrew J. Hunt, Avtar S. Matharu, *The elemental value of ash*, BioTEN Conference, Birmingham, 21 - 23 September 2010. Awarded 1<sup>st</sup> prize.
- **Jennifer R. Dodson**, Vitaly Budarin, Peter S. Shuttleworth, Andrew J. Hunt, Ray Marriott, Emily Sin, Kris Milkowski and James H. Clark, *An integrated wheat straw biorefinery*, 6th International Conference on Renewable Resources and Biorefineries, Dusseldorf, Germany, 7 - 9 June 2010.
- **Jennifer R. Dodson**, Kris Milkowski, James Clark Vitaly Budarin, Fabien Deswerte, Andrew Hunt and Peter Shuttleworth, *Green Office: environmental technologies for the construction and furniture industry*, 4th International Conference on Renewable Resources and Biorefineries, Rotterdam, Netherlands, 1 - 4 June 2008.



# Appendix A:

## XRD spectra



## XRD spectra from ICSD database

### 1. Sylvite (KCl)

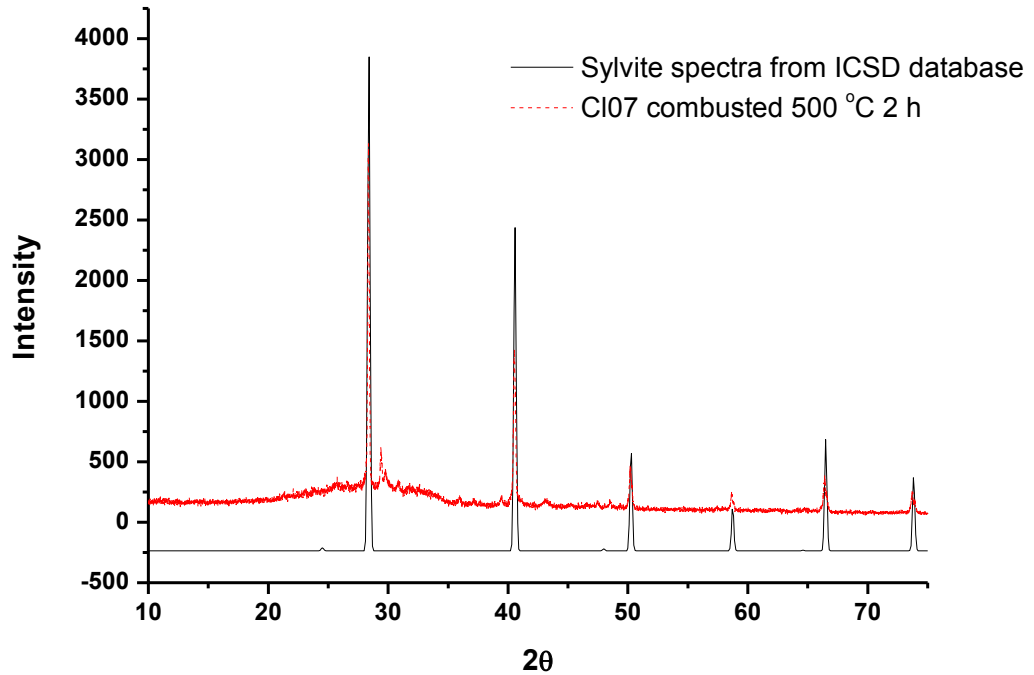


Figure A1: Powder XRD spectrum of sylvite from the ICSD database<sup>1</sup> compared to CI07 wheat straw ash combusted at 500 °C for 2 h (as shown in Figure 2.5b)

### 2. Calcite (CaCO<sub>3</sub>)

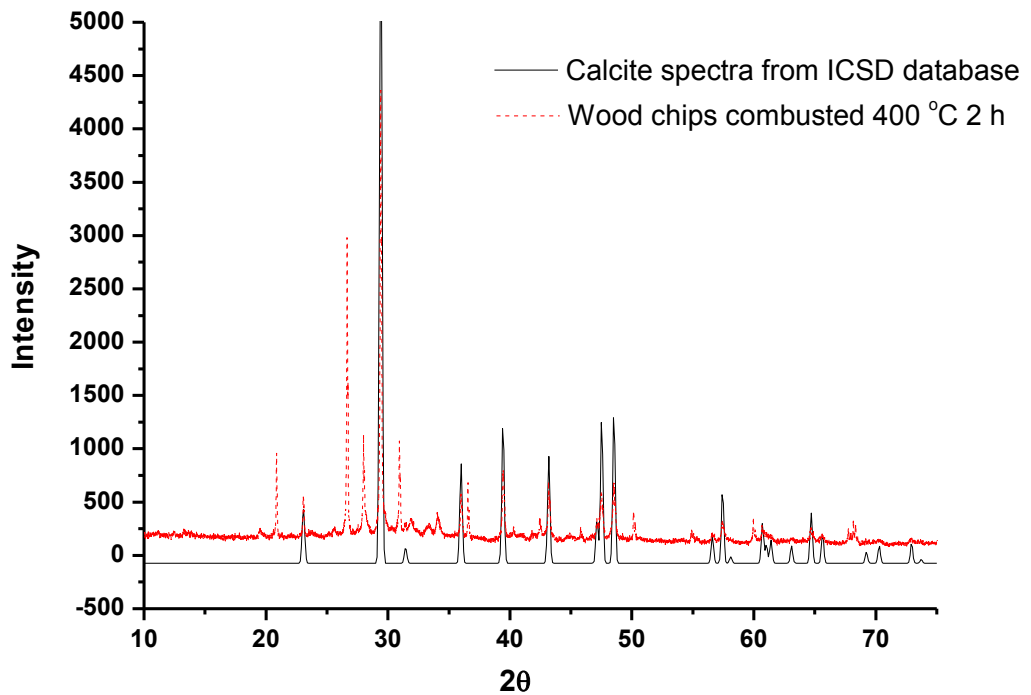


Figure A2: Powder XRD spectrum of calcite from the ICSD database<sup>2</sup> compared to wood chip ash combusted at 400 °C for 2 h (as shown in Figure 5.5)

### 3. Arcanite ( $K_2SO_4$ )

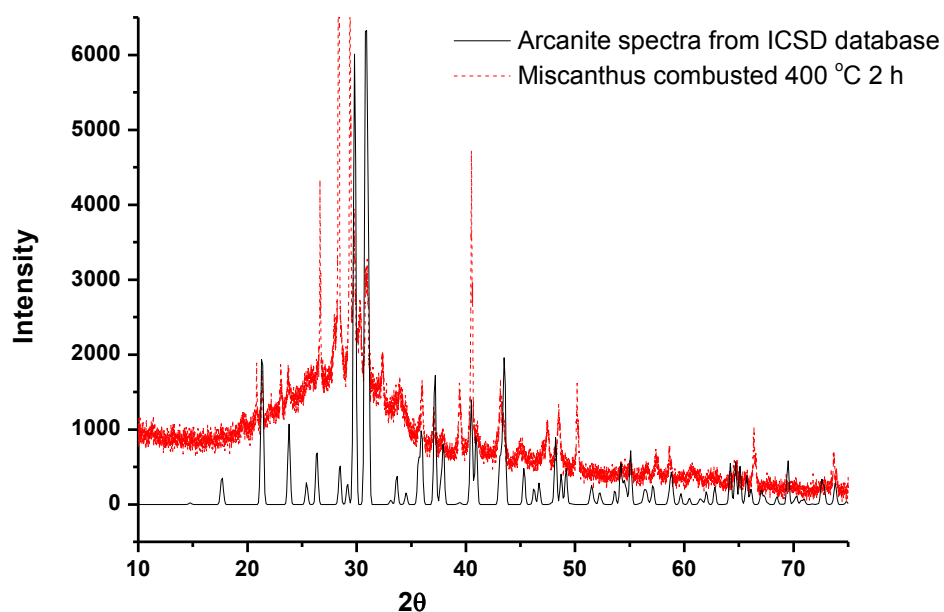


Figure A3: Powder XRD spectrum of arcanite from the ICSD database<sup>3</sup> compared to wood chip ash combusted at 400 °C for 2 h (as shown in Figure 5.5)

### 4. Anhydrite ( $CaSO_4$ )

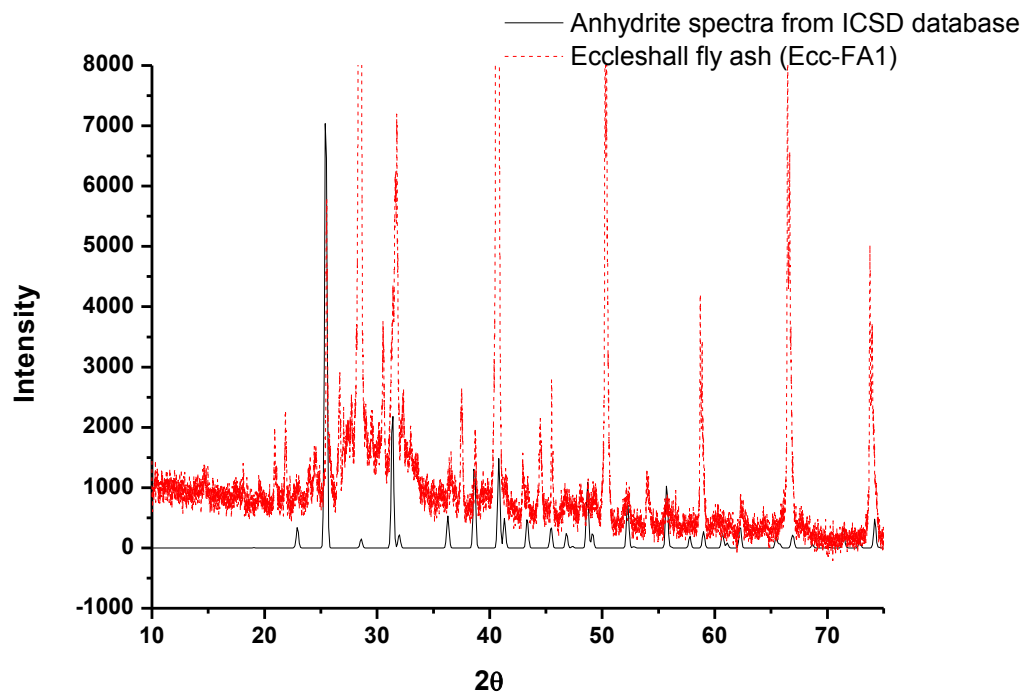


Figure A4: Powder XRD spectrum of anhydrite from the ICSD database<sup>4</sup> compared to Eccleshall fly ash (as shown in Figure 5.7)

## 5. Quartz ( $\text{SiO}_2$ )

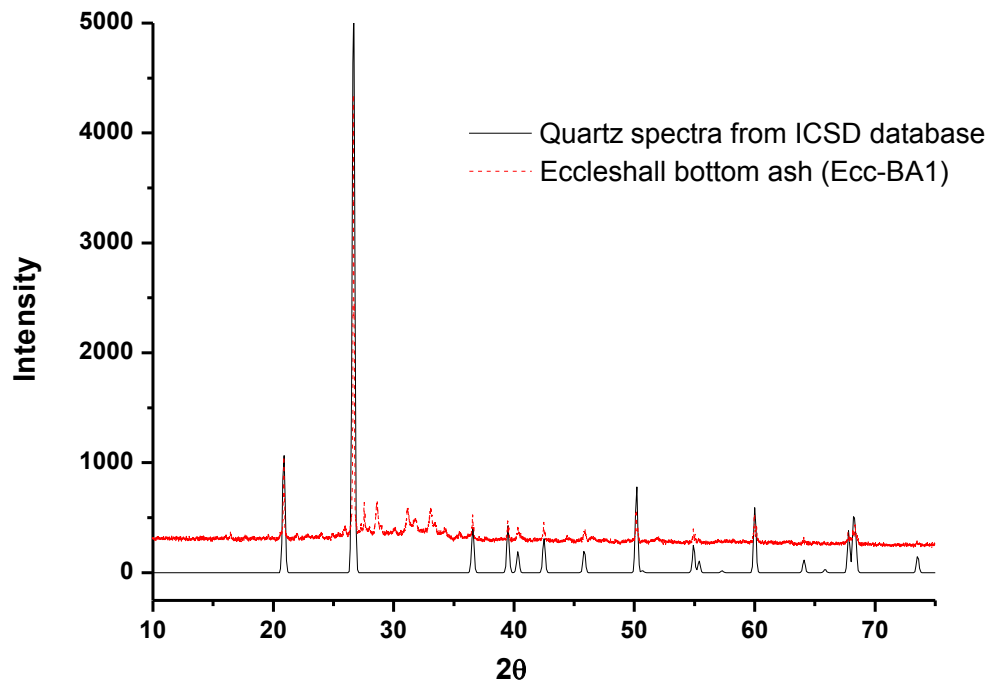


Figure A4: Powder XRD spectrum of quartz from the ICSD database<sup>5</sup> compared to Eccleshall bottom ash (as shown in Figure 5.7)

## 6. Calcium silicate ( $\text{CaSiO}_3$ )

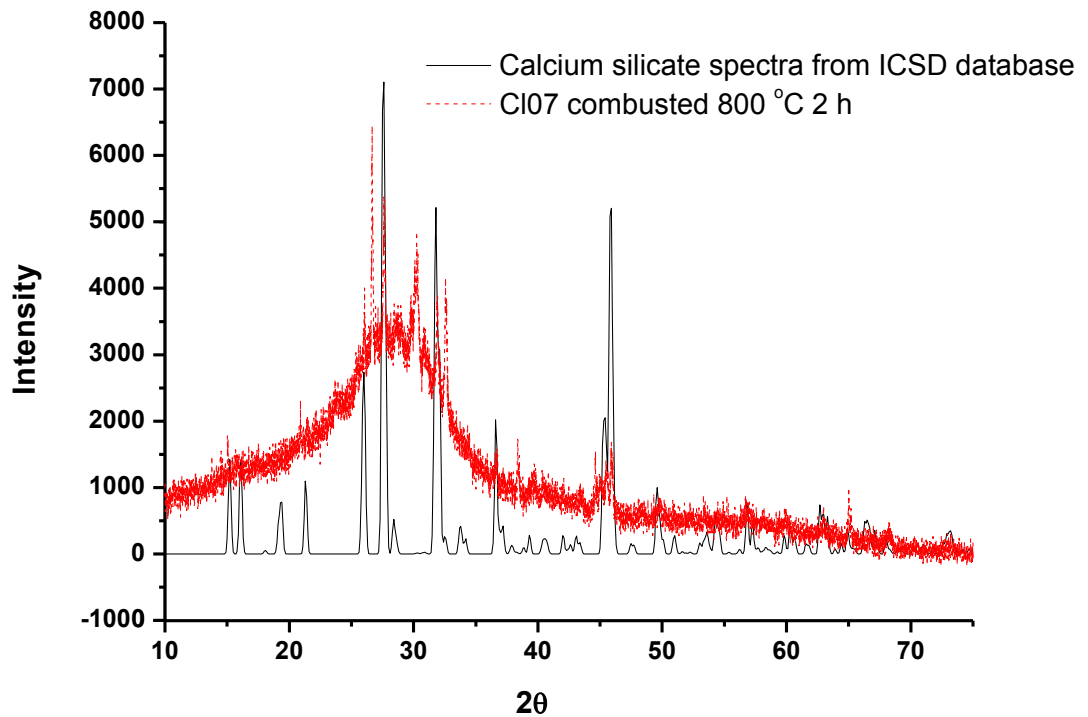


Figure A6: Powder XRD spectrum of calcium silicate from the ICSD database<sup>6</sup> compared to Cl07 wheat straw ash combusted at 800 °C for 2 h (as shown in Figure 2.5b)

## 7. Fairchildite ( $K_2Ca(CO_3)_2$ )

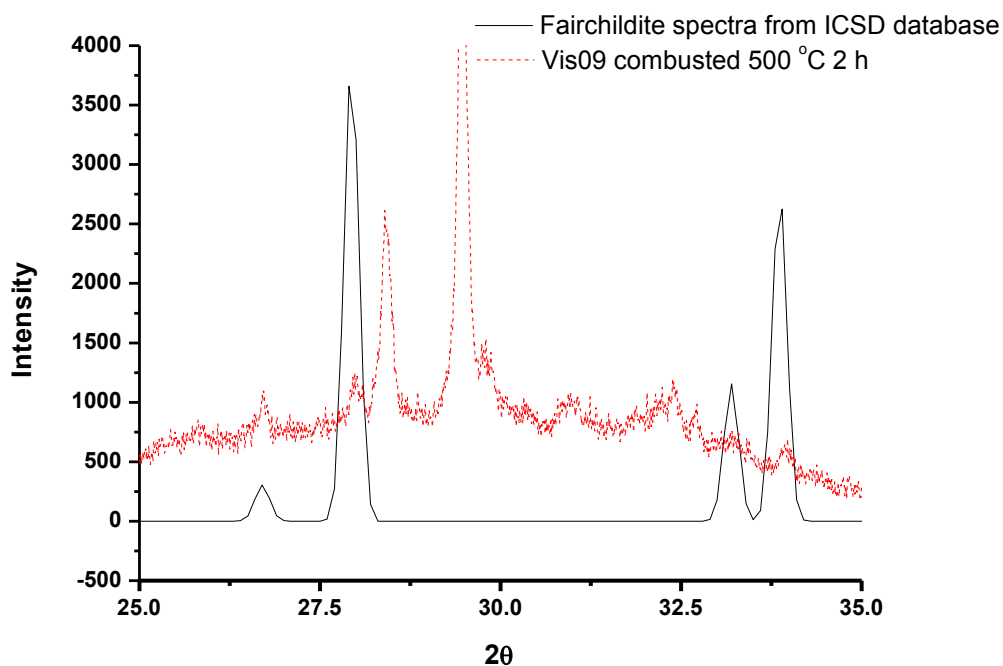


Figure A7: Powder XRD spectrum of fairchildite from the ICSD database<sup>7</sup> compared to Viscount 09 wheat straw ash combusted at 500 °C for 2 h (as shown in Figure 2.8)

## 8. $\alpha$ -Cristobalite ( $SiO_2$ )

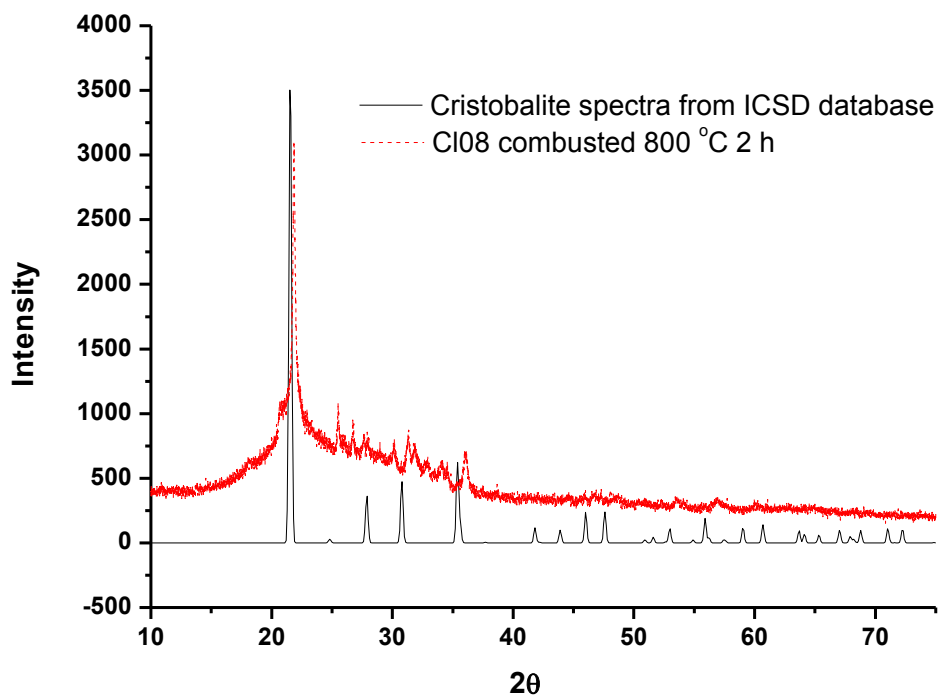


Figure A8: Powder XRD spectrum of  $\alpha$ -cristobalite from the ICSD database<sup>8</sup> compared to Claire 08 wheat straw ash combusted at 800 °C for 2 h (as shown in Figure 2.9)

## 9. Calcium silicate ( $\text{Ca}_2(\text{SiO}_4)$ )

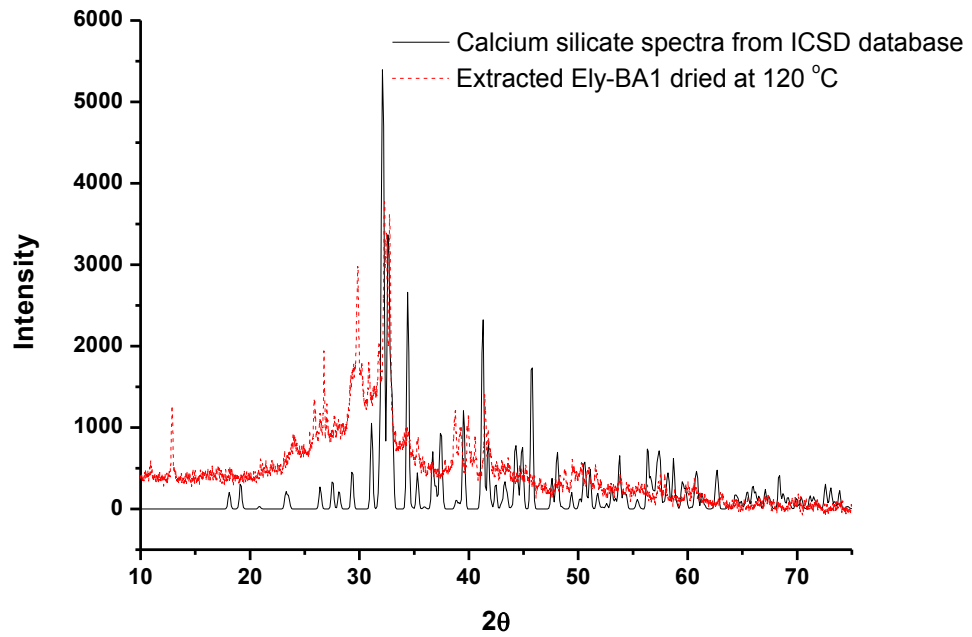


Figure A9: Powder XRD spectrum of calcium silicate from the ICSD database<sup>9</sup> compared to extracted Ely-BA1 ash dried at 120 °C (as shown in Figure 5.24)

## 9. Potassium carbonate ( $\text{K}_2\text{CO}_3$ )

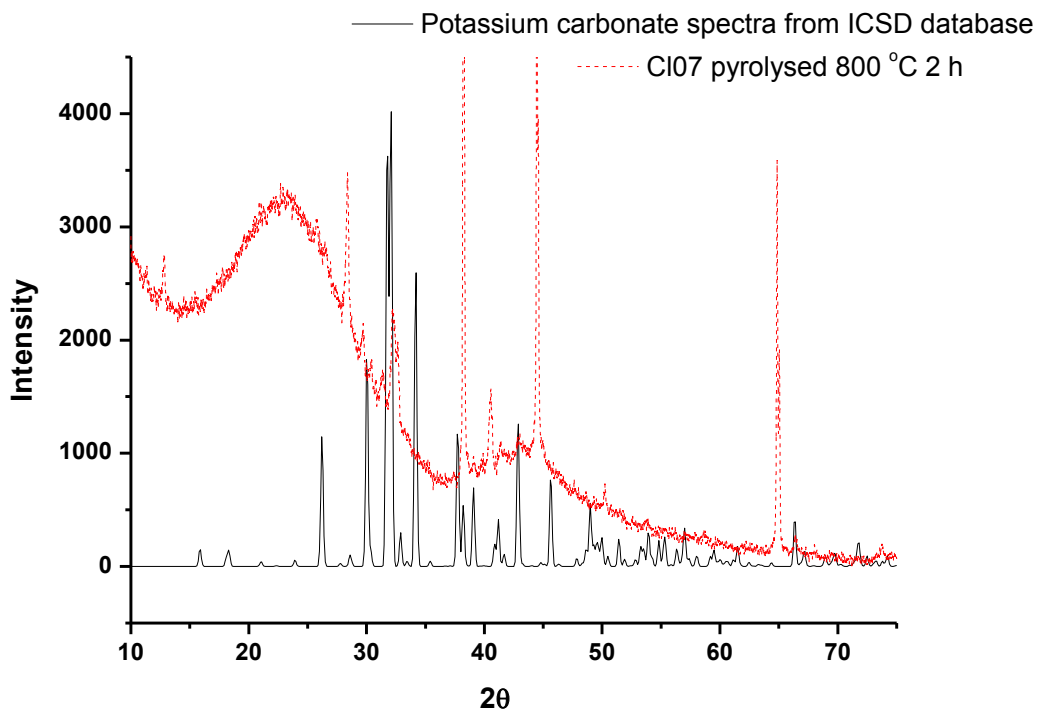


Figure A10: Powder XRD spectrum of potassium carbonate from the ICSD database<sup>10</sup> compared to Claire 07 wheat straw pyrolysed at 800 °C for 2 h (as shown in Figure 4.15)

## 10. Calcium oxide (CaO)

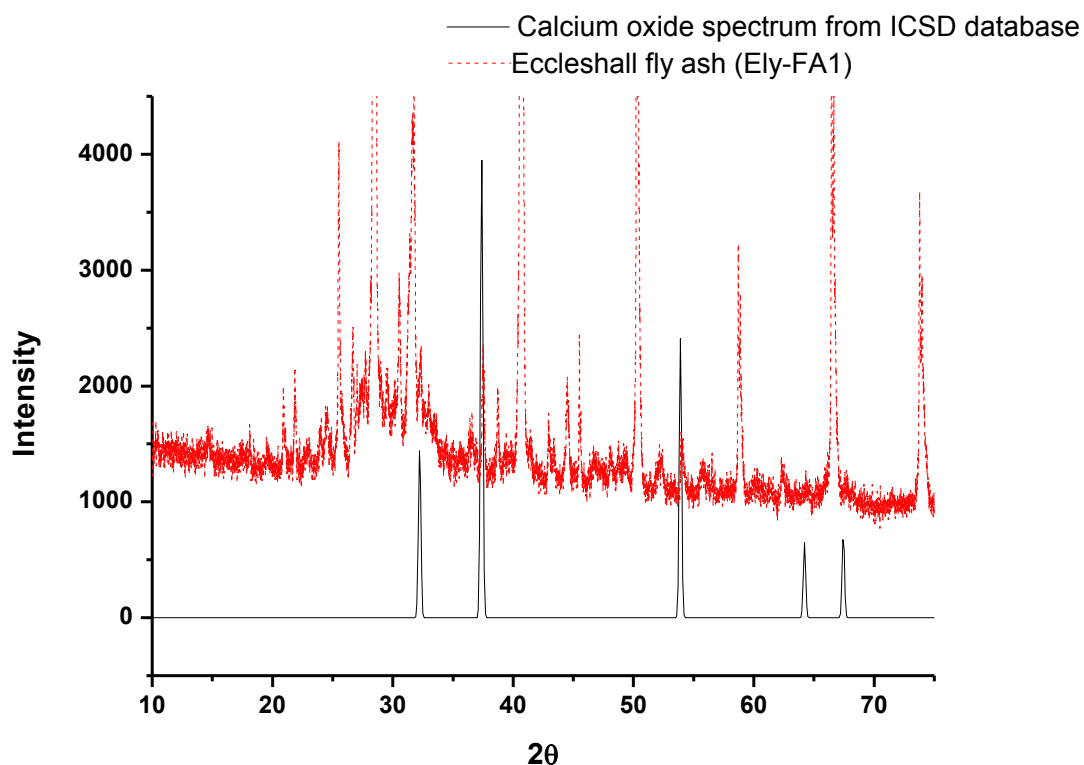


Figure A11: Powder XRD spectrum of calcium oxide from the ICSD database<sup>11</sup> compared to Ecc-FA1 (as shown in Figure 5.7)

## 11. Portlandite ( $\text{Ca}(\text{OH})_2$ )

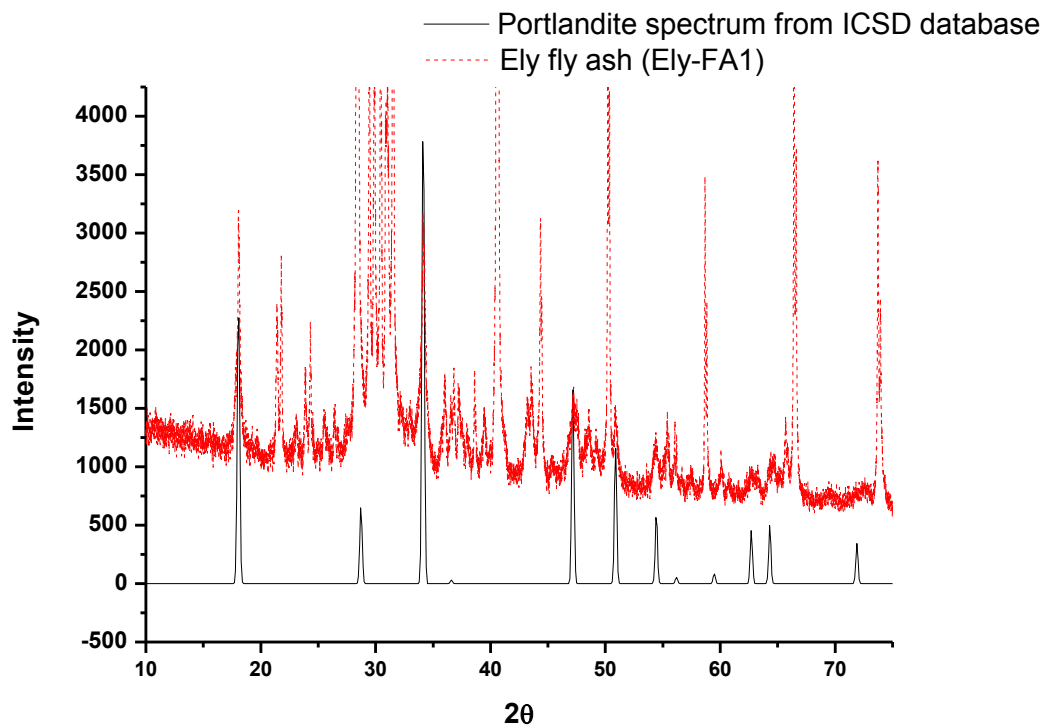


Figure A12: Powder XRD spectrum of portlandite from the ICSD database<sup>12</sup> compared to Ely-FA1 (as shown in Figure 5.6)

## 12. Aphthitalite ( $K_3Na(SO_4)_2$ )

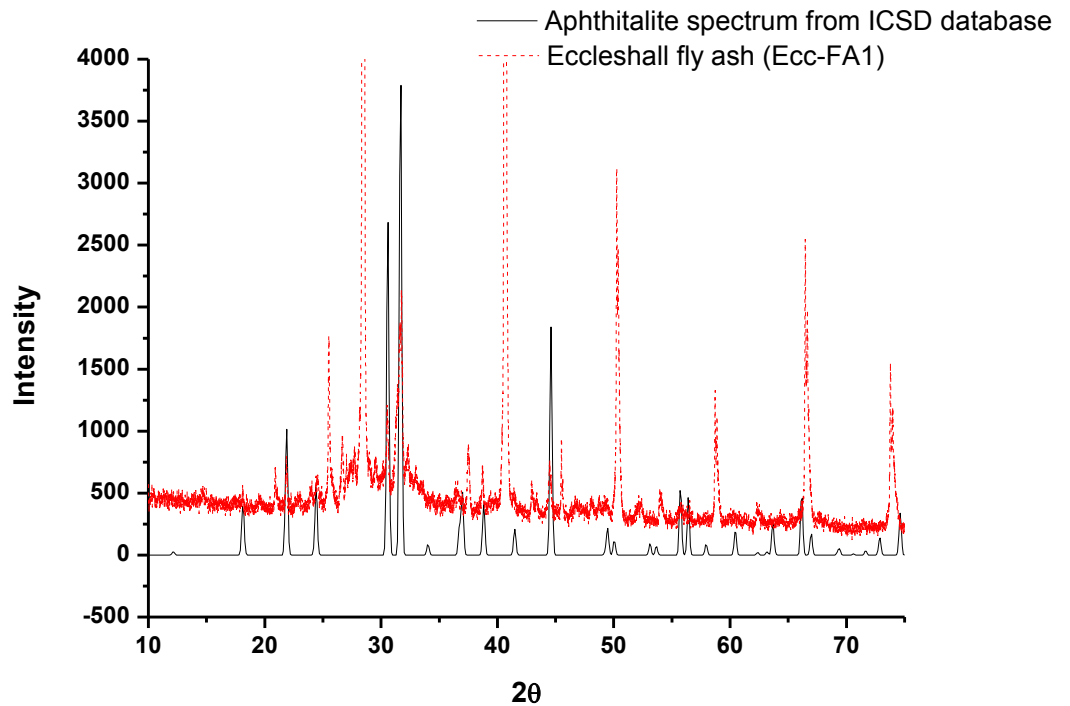


Figure A13: Powder XRD spectrum of aphthitalite from the ICSD database<sup>13</sup> compared to Ely-FA1 (as shown in Figure 5.7)

## Sh. Sample holder (Aluminium)

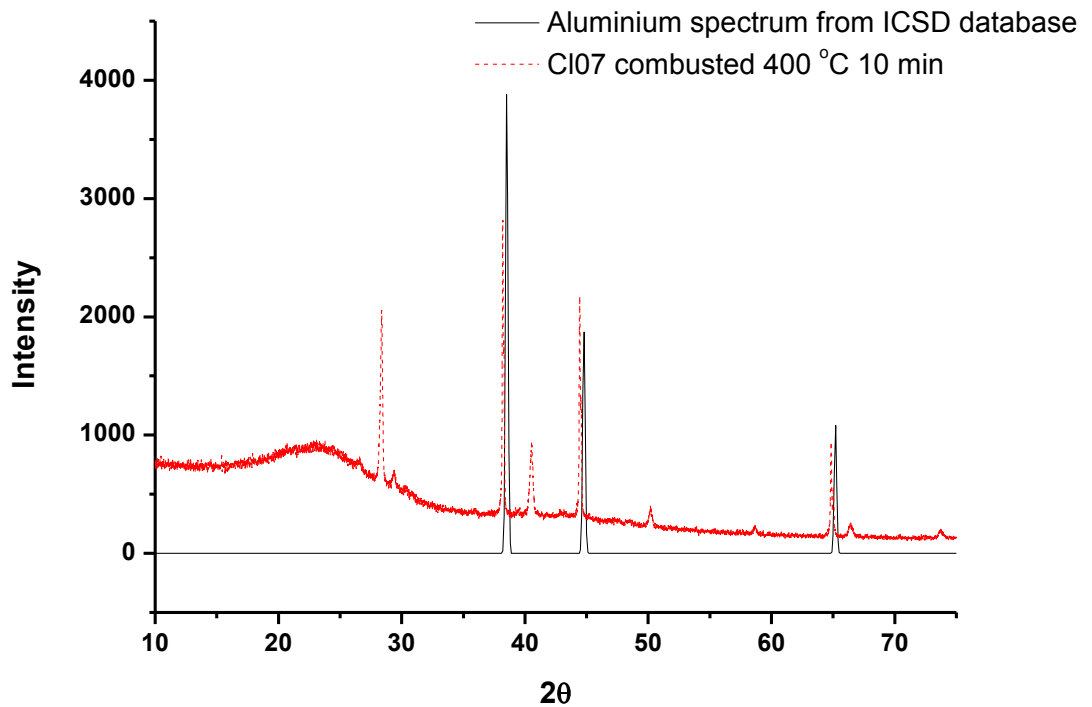


Figure A14: Powder XRD spectrum of aluminium from the ICSD database<sup>14</sup> compared to Claire 07 wheat straw combusted at 400 °C for 10 min (as shown in Figure 2.5)

## References

1. D. Walker, P. K. Verma, L. M. D. Cranswick, R. L. Jones, S. M. Clark and S. Buhre, *American Mineralogist*, 2004, **89**, 204-210.
2. H. Sitepu, *Powder Diffraction*, 2009, **24**, 315-326.
3. J. A. McGinnety, *Acta Crystallographica B*, 1972, **28**, 2845-2852.
4. A. Kirfel and G. Will, *Acta Crystallographica B*, 1980, **36**, 2881-2890.
5. S. M. Antao, I. Hassan and W. Jun., *Canadian Mineralogist* 2008, **46**, 1501-1509.
6. H.-X. Yang and C. T. Prewitt, *American Mineralogist*, 1999, **84**, 1902-1905.
7. F. Pertlik, *Zeitschrift fur Kristallographie*, 1981, **157**, 199-205.
8. S. Coh and D. Vanderbilt, *Physical Review, Series 3. B - Condensed Matter*, 2008, **74**, 54117-54111-54117-54114
9. K. Mori, R. Kiyonagi and M. Yonemura, 2006.
10. R. E. Dinnebier, S. Vensky, M. Jansen and J. C. Hanson, *Chemistry - A European Journal*, 2005, **11**, 1119-1129.
11. M. C. Verbraeken, E. Suard and J. T. Irvine, *Journal of Materials Chemistry* 2009, **19**, 2766-2770
12. L. Desgranges, D. Grebille, G. Calvarin, G. Chevrier, N. Floquet and J. C. Niepce, *Acta Crystallographica B*, 1993, **49**, 812-817.
13. B. Gossner, *Neues Jahrbuch fuer Mineralogie, Geologie und Palaeontologie. Beilage*, 1928, **57**, 89-116.
14. B. Predel and K. Huelse, *Zeitschrift fur Metallkunde*, 1978, **69**, 690-696.

# Glossary



AAS	Atomic Absorption Spectroscopy
AC	Activated Carbon
APD	Average Pore Diameter
APR	Average Pore Radius
ATR FTIR	Attenuated Total Reflectance Fourier Transform Infrared
BA	Bottom Ash
BET	Brunauer, Emmett and Teller
BJH	Barrett, Joyner and Helenda
CEC	Cation Exchange Capacity
CHN	Carbon, hydrogen, nitrogen
CI07	Wheat straw variety Claire from the year 2007
CI08	Wheat straw variety Claire from the year 2008
CI09	Wheat straw variety Claire from the year 2009
dab	Dry ash-free basis
db	Dry basis
DCM	Dichloromethane
DSC	Differential Scanning Calorimetry
dTG	Change in mass loss
$E_{DA}$	Surface energy
EU	European Union
FA	Fly Ash
FBC	Fluidised Bed Combustion
GC-MS	Gas Chromatography Mass Spectrometry
h	hour
HGCA	Homegrown Cereal Association
HTT	Heat Treatment Temperature
IC	Ion Chromatography
ICP-AES	Inductively Coupled Plasma – Atomic Emissions Spectroscopy
ICSD	International Crystal Structural Database
IR	Infrared
IUPAC	International Union of Pure and Applied Chemistry
K60	Kieselgel (60 Å)

LCD	Liquid Crystal Display
MDF	Medium Density Fibreboard
min	minutes
Mis	Miscanthus
MP	Micropore
Nij08	Wheat straw variety Nijinsky from the year 2008
NMR	Nuclear Magnetic Resonance
NQ	Not quenched in extractant (air cooled)
O <sub>nb</sub>	Non-bridging oxygen atoms
P	Pressure
ppm	parts per million
Q	Quenched in extractant
RED	Renewable Energy Directive
RHA	Rice Hull Ash
Rob08	Wheat straw variety Robigus from the year 2008
Rob09	Wheat straw variety Robigus from the year 2009
S <sub>BET</sub>	Specific surface area
scCO <sub>2</sub>	Supercritical carbon dioxide
SCF	Supercritical Fluid
SRC	Short Rotation Coppice
STA	Simultaneous Thermal Analysis
T	Temperature
TEM	Transmission Electron Microscopy
TG	Thermogravimetric
UF	Urea Formaldehyde
UK	United Kingdom
V	Volume
V <sub>micro</sub>	Micropore volume
Vis09	Wheat straw variety Viscount from the year 2009
V <sub>m</sub>	Monolayer volume
WC	Wood Chips
WS	Wheat Straw

wt	Weight
WSA	Wheat Straw Ash
w/v	weight/volume
XRD	X-Ray Diffraction
XRF	X-Ray Fluorescence

